# A BAYESIAN PROBABILISTIC APPROACH TO DAMAGE DETECTION FOR CIVIL STRUCTURES

A DISSERTATION
SUBMITTED TO THE DEPARTMENT OF CIVIL AND ENVIRONMENTAL ENGINEERING
AND THE COMMITTEE ON GRADUATE STUDIES
OF STANFORD UNIVERSITY
IN PARTIAL FULFILLMENT OF THE REQUIREMENTS
FOR THE DEGREE OF
DOCTOR OF PHILOSOPHY

Hoon Sohn
December 1998

I certify that I have read this thesis and that in my opinion it is fully adequate, in scope and in quality, as a dissertation for the degree of Doctor of Philosophy.

Kincho H. Law
(Principal Advisor)

I certify that I have read this thesis and that in my opinion it is fully adequate, in scope and in quality, as a dissertation for the degree of Doctor of Philosophy.

Anne S. Kiremidjian

I certify that I have read this thesis and that in my opinion it is fully adequate, in scope and in quality, as a dissertation for the degree of Doctor of Philosophy.

H. Allison Smith

I certify that I have read this thesis and that in my opinion it is fully adequate, in scope and in quality, as a dissertation for the degree of Doctor of Philosophy.

Steven R. Winterstein

Approved for the University Committee on Graduate Studies:

# Abstract

There have been increased economic and societal demands to periodically monitor the safety of structures against long-term deterioration, and to ensure their safety and adequate performance during the life span of the structures.

In this work, a Bayesian probabilistic framework for damage detection is proposed for the continuous monitoring of structures. The idea is to search for the most probable damage event by comparing the relative probabilities for different damage scenarios. The formulation of the relative posterior probability is based on an output error, which is defined as the difference between the estimated vibration parameters and the theoretical ones from the analytical model. The Bayesian approach is shown (1) to take into account the uncertainties in the measurement and the analytical modeling, (2) to perform damage diagnosis with a relatively small number of measurement points and a few modes, and (3) to systematically extract information from continuously obtained test data. A branch-and-bound search scheme is devised to expedite the search for the most likely damage event without exhaustively examining all possible damage cases.

As an alternative to modal vectors, load-dependent Ritz vectors are incorporated into the Bayesian framework. The following advantages of Ritz vectors over modal vectors are shown: (1) in general, load-dependent Ritz vectors are more sensitive to damage than the corresponding modal vectors, and (2) by a careful selection of load patterns, substructures of interest can be made more observable. Furthermore, a procedure to extract Ritz vectors from vibration test is proposed, and the procedure is successfully demonstrated using experimental test data.

Data from vibration tests of civil structures indicate that the environmental effects such as temperature, traffic loading, humidity can often mask subtle structural changes caused by damage. A linear adaptive filter is presented to discriminate the changes of modal parameters due to temperature changes from those caused by structural damage or other environmental effects. Results based on the field vibration test of a bridge indicate that the filter can reproduce the temporal variability of the frequencies so that the thermal effects on the vibration parameters can be differentiated from other environmental effects or potential structural damage.

# Acknowledgments

There are many people who assisted me in my completion of the doctoral program. I wish to acknowledge the support each has shown me during my four-year journey at Stanford University.

I would like to express my sincere gratitude and appreciation to my advisor, Professor Kincho H. Law, for his enthusiastic guidance and his encouragement throughout the course of my research. His level of involvement with my work and his enthusiasm for my research were unparalleled and his innovation will continue to influence me throughout my career. It has truly been a privilege to learn under his guidance.

I thank Professor Anne S. Kiremidjian for her insightful comments, teaching, and knowledge. Professor Kiremidjian inspired me to develop a branch-and-bound search scheme for this work. She was another advisor with whom I could speak freely when I needed advice. I would also like to thank all of my professors for the excellent education they provided me during my graduate studies, including the reading and defense committee members, Professor H. Allison Smith and Doctor Steven R. Winterstein.

This research was supported by the National Science Foundation Grant No. CMS-95261-2 and the Pohang Iron & Steel Corporation (POSCO) Scholarship Society. I express my sincere appreciation for the support provided by these organizations. Doctors Charles R. Farrar and Scott W. Doebling of the Los Alamos National Laboratory provided a plethora of test data for this study. I am also indebted to them for their consistent interest in this study and for acting as mentors during my last two years. Hyundai Engineering & Construction Co. and University of California, Irvine also

deserve special recognition. Some of the experimental results presented in this dissertation were obtained at the Hyundai Institute of Construction Technology in Korea or at the Structural Engineering Test Hall of the University of California, Irvine. Without the support of the laboratories and their personnel, this dissertation could not have been completed.

So much of what I have learned during the last four years has been through interactions with my colleagues. All of my peers are recognized for the depth of their friendships, the memorable experiences we shared, and the hours of companionship. In addition, I am grateful to my friends for providing great distractions. I cannot begin to individually acknowledge all the people who have made my time at Stanford University enjoyable.

Last but certainly not least, I wish to dedicate this dissertation to my parents who have never considered this pursuit to be anything less than invaluable. I would like to express my deepest gratitude to my parents for their countless sacrifices, support, and understanding through all of the challenges I have faced.

# Contents

# List of Tables

# List of Figures

# Chapter 1

# INTRODUCTION

## 1.1 Motivation

The monitoring of civil structures has received increasing interest in the research community. Also, there have been increased economic and societal demands to periodically monitor the safety of structures against long term deterioration, and to immediately assess the condition after extreme events such as earthquakes. The condition assessment of civil structures after extreme events is of great importance for emergency management officials to properly allocate resources for prompt emergency response. An equally important task is the continuous/periodic monitoring of civil structures to ensure their safety and adequate performance during the life span of the structures. Damage assessment can be categorized into the following four levels [129]:

Level 1. Determine the presence of damage within the structure.
Level 2. Locate the regions of damage.
Level 3. Quantify the severity of damage.
Level 4. Predict the remaining service life of the structure.

One common approach is to employ the vibration characteristics of a structure to assess the damage locations and to estimate the amount of damage [43]. These vibration-based methods typically determine the dynamic characteristics through forced or ambient vibration test. Damage detection is, then, based on the premise that damage in the structure will cause changes in the measured vibration test data.

Since modal parameters such as frequencies, modal vectors, and modal damping are functions of the physical properties of the structure, changes of the modal parameters will indicate changes in the physical properties such as stiffness, mass and damping. However, it has been shown that changes in the modal parameters might not be apparent at an early stage of damage [48,88].

The vibration-based methods can be further divided into *model-based* and *non-model-based* methods [75]. Model-based damage detection methods locate and quantify damage by correlating an analytical model with test data of the damaged structure. Non-model-based methods assess damage by comparing the measurements from the undamaged and damaged structures. Model-based methods can provide quantitative information of damage as well as damage locations (level 3 assessment). However, these methods are computationally intensive and require a finite element model, which should be carefully refined with test data of the undamaged structure. While non-model-based methods are simple and straightforward, these methods generally do not provide quantitative information about structural damage (level 2 assessment).

In this study, our discussions are mainly focused on the model-based methods since our final goal of damage assessment is to estimate the severity of damages (i.e. level 3 assessment). Many of the existing damage detection and monitoring algorithms have been originally developed in the field of aerospace industry for the monitoring of space-station-like structures such as truss structures [85,69,133]. These algorithms do not fully address the issues that arise in the monitoring of civil structures. The main challenges for the development of a robust damage detection and monitoring system for civil structures are as follows:

1. Civil structures typically display more complicated geometry; consist of variety of materials such as steel, concrete, cable and asphalt; and involve more redundancy in the design than space structures. In addition, the uncertainty involved in the estimation of the strength and stiffness of structural components are significantly higher than that of truss members commonly used for space structures. These issues make the accurate modeling of civil structures very difficult. Model updating and refinement techniques [8,83,80,137] can be employed prior to damage detection. However, the practical applications of these

techniques remain primarily to research activities. Model updating and refinement techniques assume that the degrees of freedom (DOFs) of the measured modal vectors match identically to the DOFs of the analytical model. This assumption can be met when measurements are conducted at all DOFs of the analytical model or when mode shape expansion or model reduction techniques are employed. However, damage generally smears into the undamaged DOFs when the mode shape expansion or model reduction techniques are applied. Furthermore, many model updating techniques utilize the connectivity information of the structural members to obtain a baseline model. On the other hand, the connectivity information is lost when a model reduction technique is applied. Model reduction techniques are commonly employed for the dynamic analysis of civil structures since the modeling of civil structures produce large system matrices and the rotational DOFs are typically condensed out from dynamic analyses. (Note that truss members do not contain any rotational DOFs.)

2. The size of civil structures does not permit the instrumentation of a large number of sensors and actuators, and the excitation of higher modes. Furthermore, the application of forced vibration tests, which are commonly used for system identification, is difficult for civil structures in service because of the economic and social ramification caused by service interruption due to road closure and evacuation of buildings. Ambient vibration tests are more suitable for civil structures since the tests can be conducted under normal operation of structures and can be easily repeated to collect additional modal data sets. One problem with ambient tests is the difficulty of exciting higher modes. Therefore, most of damage detection for civil structures would suffer from lack of data that may not be available in practical testing of a structure: only a small number of measurement points and a few fundamental modes would be available.

3. Civil structures involve a significant amount of uncertainties caused by environmental effects such as temperature, traffic loading, humidity and so on. These environmental effects can impede the reliable identification of damage [49,42]. For example, an experimental study shows that several concrete bridges in

the United Kingdom absorbed considerable amount of moisture during damp weather, and consequently increased the mass of the bridges [151]. Experimental modal analyses conducted on the Alamosa Canyon Bridge demonstrate that the ambient temperature caused more that 5% variation in the estimated fundamental frequency within a 24-hour vibration test [49,139]. The environmental effects are shown to possibly cause changes of modal properties several times larger than expected from damage. Therefore, for reliable damage detection, the damage would need to cause significant changes in the dynamic characteristics that are beyond the natural variability caused by non-damage effects.

The aforementioned problems, that would arise for the monitoring of civil structures, formed the motivation for this study, which is intended to cope with some of the problems.

## 1.2 Objectives

This study is intended to develop a global damage diagnosis framework for continuous monitoring of civil structures. Particularly, a Bayesian probabilistic damage detection method is proposed aiming at the global localization of damage regions (level 2 assessment) [141,140]. The proposed method is a probability-based and model-based approach that does not necessarily require an accurate analytical model. Bayesian probabilistic approaches have been applied to damage detection problems by previous researchers [16,15,56]. While most previous studies focused on the use of modal parameters (i.e. natural frequencies and modal vectors), this study introduces load-dependent Ritz vectors to damage detection problems. Furthermore, an attempt is made to discriminate environmental effects on the dynamic characteristics of the structure from potential damage in order to reliably determine the presence of damage within the structure (level 1 assessment). The objectives of this dissertation are:

1. To develop a systematic Bayesian framework for the damage detection and monitoring of civil structures, considering (1) uncertainties in the measurement noise and the analytical modeling and (2) the cases when only a small number

of degrees of freedom are measured and a few modes are estimated.

2. To develop and demonstrate procedures to extract load-dependent Ritz vectors from vibration tests, and to incorporate load-dependent Ritz vectors into the proposed Bayesian probabilistic approach for damage detection problems.

3. To address the environmental effects on the modal parameters of civil structures and to propose a linear adaptive model which discriminates the effects of environment from potential structural damage.

## 1.3 Overview

Figure 1.1 shows the schematic diagram of the proposed framework for damage detection. The damage detection procedure can be outlined as follows:

1. Model Construction: The objective is to construct an analytical model and to identify structural parameters which closely represent the actual structure.

2. Modal Testing: Based on the experimental data accumulated through either forced or ambient vibration tests, the modal parameters (i.e. the natural frequencies and the modal vectors) or load-dependent Ritz vectors are estimated.

3. Model Updating and Refinement: Utilizing the dynamic characteristics of the undamaged structure estimated from modal tests, the corresponding analytical model is refined to match as close as possible the measured vibration data.

4. Damage Diagnosis: A Bayesian approach is proposed to search for the most probable damage event by comparing the relative probabilities for different damage scenarios. The formulation of the relative posterior probability is based on the output error, which is defined as the difference between the estimated modal parameters (or experimental Ritz vectors) and the theoretical modal parameters (or analytical Ritz vectors) from the analytical model. Using an output error approach, we avoid the aforementioned problem introduced by either mode shape expansion or model reduction techniques. To reduce the potentially intensive

computational cost of the Bayesian approach, this study employs a branch-and-bound search scheme and a simplified approach for the modeling of multi-story frame structures.

5. Diagnosis Report and Continuous Updating: The proposed method reports the relative damage possibilities of different damage scenarios as well as the most likely damaged locations. The damage probabilities are continuously updated when new test data are obtained from the structure. The Bayesian approach provides a heuristic means to combine previous experimental data with newly available test data.

The organization of this thesis follows closely the procedure described in Figure 1.1. Chapter 2 describes the theoretical framework for the Bayesian probabilistic damage detection. Chapter 3 introduces the use of load-dependent Ritz vectors for damage detection in the Bayesian framework. The existing model updating techniques and the related issues are discussed in Chapter 4. Chapter 5 describes the application of the proposed Bayesian damage detection to the simulated data of two frame structures and the experimental data of a reinforced concrete bridge column tested at the University of California, Irvine. Chapter 5 also focuses on the issue of damage detection using simplified analytical models.

Chapter 6 presents the results of an experimental test for a grid-type bridge structure tested at Hyundai Engineering & Construction Co., Seoul, Korea. In this chapter, the procedure for the extraction of Ritz vectors is demonstrated and the damage diagnoses using modal properties and Ritz vectors are compared.

Chapter 7 addresses the thermal effects on the modal properties estimated from the Alamosa Canyon Bridge in New Mexico. A linear adaptive filtering technique is applied to reproduce the temporal variation of modal parameters and to discriminate the changes of modal parameters due to temperature changes from those caused by structural damage or other environmental effects. Finally, Chapter 8 summarizes the results and contributions of this study and presents the conclusions and suggestions for future work in this research area.

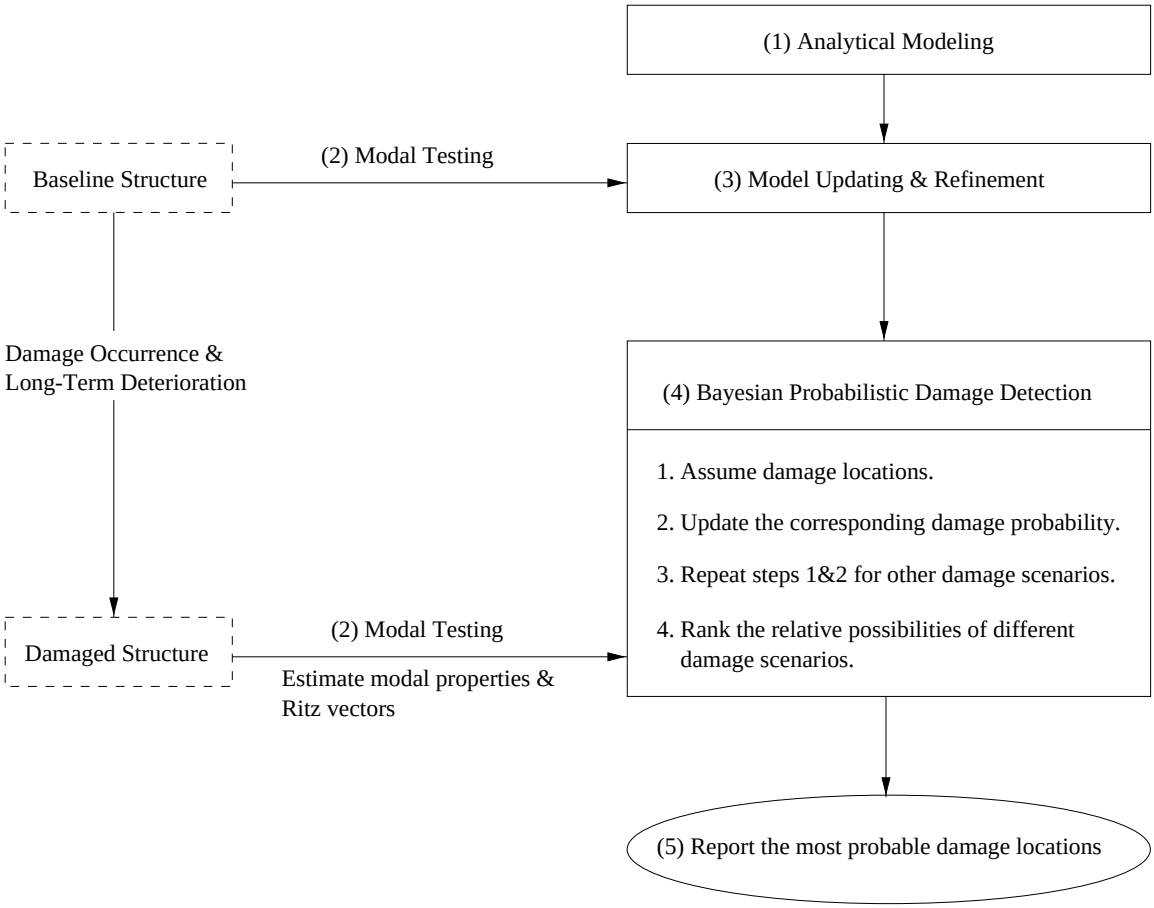


Figure 1.1: A framework of damage detection

# Chapter 2

# A Bayesian Probabilistic Approach for Damage Detection

This chapter presents a damage detection method based on a Bayesian probabilistic approach using the modal parameters (i.e., the natural frequencies and modal vectors). We first derive a general formulation of the Bayesian probabilistic approach to determine the most probable damage event by comparing the relative damage probabilities of different damage events. The relative probability of a damage event is defined as the difference between the estimated modal parameters and the theoretical modal parameters from the analytical model. The proposed Bayesian approach (1) explicitly considers both modeling and noise errors, (2) is able to detect multiple damage locations, and (3) updates the damage probabilities whenever new data become available. A branch-and-bound search scheme is employed to identify the most probable damage event without searching through all possible damage events. Finally, a six-story shear frame structure is employed to illustrate the Bayesian approach.

## 2.1 Theoretical Formulation

### 2.1.1 Notation and Assumption

For an analytical model of a structure, we represent the system stiffness matrix $\mathbf{K}$ as an assembly of substructure stiffness matrices. For a model with $N_{sub}$ substructures, the overall stiffness matrix can be expressed as:

$$\mathbf{K}(\Theta) = \sum_{i=1}^{N_{sub}} \theta_i \mathbf{K}_{si} \tag{2.1}$$

where $\mathbf{K}_{si}$ is the stiffness matrix of the $i$th substructure and $\theta_i$ $(0 \leq \theta_i \leq 1)$ is a non-dimensional parameter which represents the contribution of the $i$th substructure stiffness to the system stiffness matrix. The non-dimensional parameter $\theta_i$ is a damage indicator and is introduced to allow the modeling of damage in the $i$th substructure. A substructure is said to have been damaged when the $\theta$ value is less than a specified threshold. As damage locations and amount are determined according to the $\theta$ values, the system stiffness matrix in Equation (2.1) is expressed as a function of $\Theta = \left\{\theta_i; i = 1, ..., N_{sub}\right\}$.

Modal data sets are assumed to be collected and estimated from repeated or continuous vibration tests. When vibration tests are repeated $N_s$ times, the total collection of $N_s$ modal data sets is denoted as:

$$\hat{\Psi}_{N_s} = \left\{\hat{\psi}(n); n = 1, ..., N_s\right\} \tag{2.2}$$

A modal data set $\hat{\psi}(n)$ in Equation (2.2) consists of both the frequencies and the modal vectors estimated from the $n$th vibration test, i.e.,

$$\hat{\psi}(n) = \left[\hat{\omega}_1^n, ..., \hat{\omega}_{N_m}^n, \hat{\mathbf{v}}_1^{nT}, ..., \hat{\mathbf{v}}_{N_m}^{nT}\right]^T \in \mathbf{R}^{N_t} \tag{2.3}$$

where $\hat{\omega}_i^n$ and $\hat{\mathbf{v}}_i^n$ respectively denote the $i$th estimated frequency and modal vector in the $n$th data set. The modal vector $\hat{\mathbf{v}}_i^n$ $(\in \mathbf{R}^{N_d})$ has components corresponding to the instrumented DOFs. The variables $N_t$, $N_d$ and $N_m$ represent the total number of components in a data set $\hat{\psi}(n)$, the number of the measured DOFs and the number of the measured modes, respectively.

Let $H_j$ denote a hypothesis for a damage event which can contain any number of substructures as damaged, and the initial degree of belief about the hypothesis $H_j$ is represented with a prior probability $P(H_j)$. Using Bayes Theorem, the posterior probability $P(H_j|\hat{\Psi}_{N_s})$, after observing a set of estimated modal parameters $\hat{\Psi}_{N_s}$, can be represented as:

$$P(H_j|\hat{\Psi}_{N_s}) = \frac{P(\hat{\Psi}_{N_s}|H_j)}{P(\hat{\Psi}_{N_s})} P(H_j) \tag{2.4}$$

The most likely damaged substructures are the ones included in the hypothesis $H_{max}$ which has the largest posterior probability, i.e.

$$P(H_{max}|\hat{\Psi}_{N_s}) = \max_{\forall H_j} P(H_j|\hat{\Psi}_{N_s}) \tag{2.5}$$

Since the objective is to determine the most probable damage hypothesis, the relative posterior probabilities of alternative hypotheses are of interest. We attempt to avoid the explicit expression of a posterior probability $P(H_j|\hat{\Psi}_{N_s})$ and the examination of all hypotheses. The precise calculation of $P(\hat{\Psi}_{N_s}|H_j)$ is a difficult task. Furthermore, the calculation of the denominator $P(\hat{\Psi}_{N_s})$ in Equation (2.4) involves summing $P(\hat{\Psi}_{N_s}|H_j) \cdot P(H_j)$ over every possible hypothesis. The number of all possible damage events (the size of hypothesis space) for a structure with $N_{sub}$ substructures is equal to $2^{N_{sub}}$. For a large structure, the size of the hypothesis space easily becomes intractable and the computational cost is prohibitive.

### 2.1.2 Determination of the Most Probable Damage Event

When applying Equation (2.4) to calculate the posterior probability $P(H_j|\hat{\Psi}_{N_s})$, the only undefined term is $P(\hat{\Psi}_{N_s}|H_j)$. The prior probability of a hypothesis $P(H_j)$ is the prior information given by users and the probability of estimated modal data $P(\hat{\Psi}_{N_s})$ is simply a normalizing constant.

As shown in Equation (2.1), less than a unity value for $\theta_i$ reflects the stiffness decrease in the $i$th substructure. As noted earlier, when $\theta_i$ is less than a specified threshold $\theta_i^*(< 1)$, the $i$th substructure is defined as *damaged*. If we define $\Theta^1_{H_j}$ as the

set of $\theta_i$'s corresponding to the damaged substructures in a hypothesis $H_j$ and $\Theta^2_{H_j}$ as the rest of $\theta_i$'s, the conditional probability $P(\hat{\Psi}_{N_s}|H_j)$ can be interpreted as the probability of obtaining $\hat{\Psi}_{N_s}$, when $\theta_i$'s in $\Theta^1_{H_j}$ are less than or equal to their threshold $\theta^*_i$'s and the remaining $\theta_i$'s stay within $\theta^*_i < \theta_i \leq 1$. Denoting $\Omega^*_{H_j}$ as the range of $\Theta_{H_j}$ such that $0 \leq \Theta^1_{H_j} \leq \Theta^{1,*}_{H_j}$ and $\Theta^{2,*}_{H_j} < \Theta^2_{H_j} \leq 1$, the conditional probability $P(\hat{\Psi}_{H_j}|H_j)$ becomes:

$$\begin{aligned} P(\hat{\Psi}_{N_s}|H_j) = P(\hat{\Psi}_{N_s}|\Theta_{H_j} < \Omega^*_{H_j}) &= \frac{P(\hat{\Psi}_{N_s}, \Theta_{H_j} < \Omega^*_{H_j})}{P(\Theta_{H_j} < \Omega^*_{H_j})} \\ &= \frac{P(\Theta_{H_j} < \Omega^*_{H_j}|\hat{\Psi}_{N_s})\ P(\hat{\Psi}_{N_s})}{P(\Theta_{H_j} < \Omega^*_{H_j})} \\ &= \frac{P(\hat{\Psi}_{N_s})}{P(\Theta_{H_j} < \Omega^*_{H_j})} \int_{\Theta_{H_j} < \Omega^*_{H_j}} f(\Theta_{H_j}|\hat{\Psi}_{N_s}) d\Theta_{H_j} \end{aligned} \tag{2.6}$$

where $\Theta^{1,*}_{H_j}$ and $\Theta^{2,*}_{H_j}$ are the sets of damage thresholds for $\Theta^1_{H_j}$ and $\Theta^2_{H_j}$, respectively, and $f(\Theta_{H_j}|\hat{\Psi}_{N_s})$ is a conditional probability density function (PDF) of $\Theta_{H_j}$ given $\hat{\Psi}_{N_s}$. Furthermore, $\Theta_{H_j} < \Omega^*_{H_j}$ indicates that $\Theta_{H_j}$ are within the range of $\Omega^*_{H_j}$ such that $0 \leq \Theta^1_{H_j} \leq \Theta^{1,*}_{H_j}$ and $\Theta^{2,*}_{H_j} < \Theta^2_{H_j} \leq 1$.

If we define the most probable parameter values $\Theta^{max}_{H_j}$, given a hypothesis $H_j$, such that:

$$f(\Theta^{max}_{H_j}|\hat{\Psi}_{N_s}) = \max_{\Theta_{H_j} < \Omega^*_{H_j}} f(\Theta_{H_j}|\hat{\Psi}_{N_s}) \tag{2.7}$$

Then, the upper bound of $P(\hat{\Psi}_{N_s}|H_j)$ in Equation (2.6) becomes:

$$P_U(\hat{\Psi}_{N_s}|H_j) = \frac{P(\hat{\Psi}_{N_s})}{P(\Theta_{H_j} < \Omega^*_{H_j})} \int_{\Theta_{H_j} < \Omega^*_{H_j}} f(\Theta^{max}_{H_j}|\hat{\Psi}_{N_s}) d\Theta_{H_j}$$

$$= \frac{P(\hat{\Psi}_{N_s})}{P(\Theta_{H_j} < \Omega^*_{H_j})}\ f(\Theta^{max}_{H_j}|\hat{\Psi}_{N_s}) \int_{\Theta_{H_j} < \Omega^*_{H_j}} 1\ d\Theta_{H_j} \tag{2.8}$$

For simplification, we assume if damage occurs, it could have any arbitrary amount with equal probability. That is, we assign a uniform probability density function to $\theta_i$ such that:

$$f(\theta_i) = \begin{cases} 1 & \text{if } 0 \leq \theta_i \leq 1 \\ 0 & \text{otherwise} \end{cases} \tag{2.9}$$

Furthermore, if $\theta_i$'s are assumed to be independent, the following two equations hold:

$$f(\Theta_{H_j}) = \prod_{\forall\ \theta_i \in \Theta_{H_j}} f(\theta_i) = 1 \tag{2.10}$$

$$\frac{1}{P(\Theta_{H_j} < \Omega^*_{H_j})} = \frac{1}{\int_{\Theta_{H_j} < \Omega^*_{H_j}} f(\Theta_{H_j}) d\Theta_{H_j}} = \frac{1}{\int_{\Theta_{H_j} < \Omega^*_{H_j}} 1\ d\Theta_{H_j}} \tag{2.11}$$

Substituting Equation (2.11) into Equation (2.8), $P_U(\hat{\Psi}_{N_s}|H_j)$ can be simplified as:

$$P_U(\hat{\Psi}_{N_s}|H_j) = f(\Theta^{max}_{H_j}|\hat{\Psi}_{N_s})\ P(\hat{\Psi}_{N_s}) \tag{2.12}$$

The computation of $f(\Theta^{max}_{H_j}|\hat{\Psi}_{N_s})$ will be explained later in the following subsection.

### 2.1.3 Consideration of Measurement Noise and Modeling Error

The next step is to compute the conditional PDF, $f(\Theta^{max}_{H_j}|\hat{\Psi}_{N_s})$. Here, $f(\Theta^{max}_{H_j}|\hat{\Psi}_{N_s})$ is defined considering both measurement noise and modeling error. First, let's define a modal error $e(n, \Theta_{H_j})$ as:

$$e(n, \Theta_{H_j}) = \hat{\psi}(n) - \psi(\Theta_{H_j});\ n = 1, ..., N_s \tag{2.13}$$

where $\hat{\psi}(n)$ is defined in Equation (2.3). Given $\Theta_{H_j}$, an analytical modal data set $\psi(\Theta_{H_j})$ is defined similar to Equation (2.3) and is obtained by solving an eigenvalue

problem, $\mathbf{K}(\Theta_{H_j})\,\mathbf{v}_i(\Theta_{H_j}) = \omega_i^2(\Theta_{H_j})\mathbf{M}\,\mathbf{v}_i(\Theta_{H_j})$:

$$\psi(\Theta_{H_j}) = \left[\omega_1(\Theta_{H_j}), ..., \omega_{N_m}(\Theta_{H_j}), \mathbf{v}_1^T(\Theta_{H_j}), ..., \mathbf{v}_{N_m}^T(\Theta_{H_j})\right]^T \in \mathbf{R}^{N_t} \tag{2.14}$$

It should be noted that, for a modal vector $\mathbf{v}_i(\Theta_{H_j})$ in Equation (2.14), only the components associated with the measured DOFs are included.

The modal error reflects the discrepancy between the measured response of the structure and the response of the associated analytical model. Two types of uncertainties account for this discrepancy. The first type of uncertainty is the measurement uncertainty caused by the presence of noise during vibration tests. The noise specifically accounts for the difference between the unknown true response and the measured response of the structure. The second type of uncertainty arises from the assumptions and simplifications introduced in the modeling process. Thus, the modal error defined in Equation (2.13) can be divided into two parts:

$$e(n, \Theta_{H_j}) = e_N(n) + e_M(\Theta_{H_j}) \tag{2.15}$$

where $e_N(n)$ is the modal error caused by the measurement noise in the $n$th vibration data set and $e_M(\Theta_{H_j})$ is the modal error caused by the modeling error. Assuming that each entry or component of $e_N(n)$ is a normal distribution with zero mean, the expectation on both sides of Equation (2.15) with respect to $N_s$ data sets becomes:

$$\mathbf{E}[e(n, \Theta_{H_j})] = \mathbf{E}[e_N(n)] + \mathbf{E}[e_M(\Theta_{H_j})] = e_M(\Theta_{H_j}) \tag{2.16}$$

where $e_M(\Theta_{H_j})$ is assumed to be constant for all $N_s$ data sets. That is, the modeling error is caused only by the inherent difference between the analytical model and the structure regardless of the noise existence.

It appears that $e_M(\Theta_{H_j})$ changes according to the damage locations and amount. However, when damage is not severe, the modeling error can be assumed not to change significantly. In other words, the modal error caused by the modeling error $e_M(\Theta_{H_j})$ can be assumed to be constant and be approximated by $e_M(\Theta_{H_o})$, which is the modal error caused by the modeling error in the healthy (undamaged) state of

the structure:

$$e_M(\Theta_{H_j}) \cong e_M(\Theta_{H_o});\ \forall \Theta_{H_j} \tag{2.17}$$

where $H_o$ is a null hypothesis that there is no damage in the structure and the $\theta$ values of the healthy structure are calibrated to have unity values before any damage occurs. From the definition of the modal error and Equation (2.16), $e_M(\Theta_{H_o})$ can be evaluated from the estimated and the analytical modal parameter sets:

$$e_M(\Theta_{H_o}) = \mathbf{E}[e(n, \Theta_{H_o})] = \mathbf{E}[\hat{\psi}^h(n)] - \mathbf{E}[\psi(\Theta_{H_o})] \cong \hat{\psi}^h_m - \psi(\Theta_{H_o}) \tag{2.18}$$

where the superscript $h$ denotes the properties of the healthy structure. Since $\psi(\Theta_{H_j})$ is constant with respect to the $N_s$ data sets, $\mathbf{E}[\psi(\Theta_{H_o})] = \psi(\Theta_{H_o})$. Furthermore, the sample mean $\hat{\psi}^h_m$ is used to approximate the expectation, $\mathbf{E}[\hat{\psi}^h(n)]$. The $i$th component of $\hat{\psi}^h_m$ is calculated such that:

$$\mathbf{E}[\hat{\psi}^h_i(n)] \cong \hat{\psi}^h_{m,i} = \frac{1}{N^h_s} \sum_{n=1}^{N^h_s} \hat{\psi}^h_i(n) \tag{2.19}$$

where $i = 1, ..., N_t$ and $N^h_s$ is the number of modal data sets before damage occurrence. As a result, $e_M(\Theta_{H_j})$ can be evaluated from the measured modal parameter set $\hat{\psi}^h(n)$ of the healthy structure and the modal parameter set $\psi(\Theta_{H_o})$ of the initial analytical model:

$$e_M(\Theta_{H_j}) \cong e_M(\Theta_{H_o}) = \hat{\psi}^h_m - \psi(\Theta_{H_o})\ ;\ \forall \Theta_{H_j} \tag{2.20}$$

From the results of Equations (2.16) and (2.17), the $i$th compoments $e_i(n, \Theta_{H_j})$ $(n = 1, ..., N_s)$ of the error vector $e(n, \Theta_{H_j})$ become a multivariate normal distribution with mean $e_{M,i}(\Theta_{H_o})$ and variance $\sigma_i^2$. The variance $\sigma_i^2$ can be evaluated from the observation of the estimated modal parameter sets. When a large number of experimental data sets are available, sample standard deviations (or variances) can be extracted from the data set. When modal data sets available are not sufficient

to estimate the variances, we assign uniform coefficient of variation (COV) to all modal parameters. Assuming that the components of the modal error $e(n, \Theta_{H_j})$ are independent, the conditional joint PDF of $\Theta_{H_j}$ becomes:

$$f(\Theta_{H_j}|\hat{\Psi}_{N_s}) = f(e(n, \Theta_{H_j})|\hat{\Psi}_{N_s}) = k \cdot exp\{ - J(\hat{\Psi}_{N_s}, \Theta_{H_j})\} \tag{2.21}$$

where $k = \frac{1}{[2\pi]^{\frac{N_s}{2}}} \frac{1}{\|\mathbf{C}_{\hat{\Psi}}\|^{\frac{1}{2}}}$ and $\|\mathbf{C}_{\hat{\Psi}}\| = det|diag[\sigma_1^2, ..., \sigma_{N_t}^2]| = \prod_{i=1}^{N_t} \sigma_i^2$. Furthermore, the error function $J(\hat{\Psi}_{N_s}, \Theta_{H_j})$ is:

$$J(\hat{\Psi}_{N_s}, \Theta_{H_j}) = \tag{2.22}$$
$$\frac{1}{2} \sum_{n=1}^{N_s} [\hat{\psi}(n) - \psi(\Theta_{H_j}) - e_M(\Theta_{H_o})]^T \mathbf{C}_{\hat{\Psi}}^{-1} [\hat{\psi}(n) - \psi(\Theta_{H_j}) - e_M(\Theta_{H_o})]$$

From Equations (2.4), (2.12) and (2.21), the upper bound of $P(H_j|\hat{\Psi}_{N_s})$ becomes:

$$P_U(H_j|\hat{\Psi}_{N_s}) = f(\Theta_{H_j}^{max}|\hat{\Psi}_{N_s}) P(H_j) = exp\{ - J(\hat{\Psi}_{N_s}, \Theta_{H_j}^{max})\} \cdot P(H_j) \cdot k \tag{2.23}$$

From Equation (2.23) and the fact that the relative comparison of $P_U(H_j|\hat{\Psi}_{N_s})$ is independent of the constant $k$, the following relationships hold:

$$\begin{aligned} \max \left[P_U(H_i|\hat{\Psi}_{N_s}), P_U(H_j|\hat{\Psi}_{N_s})\right] &= \max \left[ln\, P_U(H_i|\hat{\Psi}_{N_s}), ln\, P_U(H_j|\hat{\Psi}_{N_s})\right] \\ &= \min \left[J(\hat{\Psi}_{N_s}, \Theta_{H_i}^{max}) - lnP(H_i), J(\hat{\Psi}_{N_s}, \Theta_{H_j}^{max}) - lnP(H_j)\right] \end{aligned} \tag{2.24}$$

where $ln$ denotes a natural logarithm. Therefore, the most probable hypothesis $H_{max}$ in Equation (2.5) satisfies:

$$J(\hat{\Psi}_{N_s}, \Theta_{H_{max}}^{max}) - lnP(H_{max}) = \min_{\forall H_j} \left[J(\hat{\Psi}_{N_s}, \Theta_{H_j}^{max}) - lnP(H_j)\right] \tag{2.25}$$

Now, the search of the most probable damage event in Equation (2.5) can be conducted by examining only the error function $J(\hat{\Psi}_{N_s}, \Theta_{H_j}^{max})$ and the prior probability $P(H_j)$. It should be noted that $P_U(H_j|\hat{\Psi}_{N_s})$ is employed rather than $P(H_j|\hat{\Psi}_{N_s})$ in Equation (2.24). The use of $P_U(H_j|\hat{\Psi}_{N_s})$ can be justified as follows: First, assume

that $H_d$ and $\Theta_{H_d}^{max}$ correspond to the actual damage locations and amount. Then, we can expect an inequality $f(\Theta_{H_d}^{max}|\hat{\Psi}_{N_s}) \geq f(\Theta_{H_j}|\hat{\Psi}_{N_s})$ for any $H_j$ and $\Theta_{H_j}$. That is, the conditional PDF of observing $H_d$ and $\Theta_{H_d}^{max}$ is expected to be higher than or equal to any other damage cases (the equality holds when $H_j = H_d$ and $\Theta_{H_j} = \Theta_{H_d}^{max}$). From this observation and the fact that $P_U(H_j|\hat{\Psi}_{N_s}) = \int_{\Theta_{H_j} < \Omega_{H_j}^*} f(\Theta_{H_j}^{max}|\hat{\Psi}_{N_s}) d\Theta_{H_j}$, $P_U(H_d|\hat{\Psi}_{N_s}) \geq P_U(H_j|\hat{\Psi}_{N_s})$ holds for all $H_j$. However, if $\Theta_{H_d}$ differs from $\Theta_{H_d}^{max}$, the conditional PDF $f(\Theta_{H_d}|\hat{\Psi}_{N_s})$ can be less than other conditional PDFs even though $H_d$ corresponds to the actual damage locations. In other words, the PDF of *correct* damage locations and *incorrect* damage amount can be lower than the PDFs of some other damage cases ($f(\Theta_{H_d}|\hat{\Psi}_{N_s}) < f(\Theta_{H_j}|\hat{\Psi}_{N_s})$ for some $H_j$ and $\Theta_{H_j}$). Consequently, $P(H_d|\hat{\Psi}_{N_s})$ can be less than $P(H_j|\hat{\Psi}_{N_s})$ for some $H_j$. In this case, we may fail to identify the actual damage event. Therefore, the use of $P_U(H_j|\hat{\Psi}_{N_s})$ appears to increase the chance of identifying the actual damage locations and amount.

### 2.1.4 Computational Issues

For given modal data, while we are interested in the probability $P_U(H_j|\hat{\Psi}_{N_s})$ of the assumed damage locations, the approach in Reference 16 calculates the conditional PDF $f(\Theta|\hat{\Psi}_{N_s})$ where $\Theta = \{\theta_1, ..., \theta_{N_{sub}}\}$, and $\theta_i$ is defined as a continuous variable with states ranging from 0 to 1. To obtain the probability for some parameter set $\Theta$, a multi-dimensional integration for a desired $\Theta$ space is required. Here, the total number of substructures becomes the dimension of integration. This multi-dimensional integral may not be feasible for a large scale model. This problem can be simplified by assuming that damage is localized in only a single substructure [16]. As an alternative, an asymptotic approach is proposed in Reference 15. However, the asymptotic approach requires the calculation of all the maxima of $f(\Theta|\hat{\Psi}_{N_s})$, which is also a computationally expensive task.

In this study, the computational effort to find the most likely non-dimensional parameter value $\Theta_{H_j}^{max}$ in Equation (2.7) increases with the number of potentially damaged substructures included in the hypothesis $H_j$. The dimension of search space $\Theta_{H_j} < \Omega_{h_j}^*$ depends mainly on the number of damaged substructure $\Theta_{H_j}^1$ (the set

of $\theta$'s corresponding to the damaged substructures in a hypothesis $H_j$) rather than the total number of substructures. The search space is evaluated at the intersections of the grid lines which discretize the search domain with an incremental step $\Delta\theta$. Figure 2.1 shows a typical search space of $f(\Theta_{H_j}|\hat{\Psi_{N_s}})$ when $\theta_1$ and $\theta_2$ correspond to $\Theta^1_{H_j}$ and an incremental step is 0.1. Since the Bayesian approach is developed for a continuous monitoring of a structure, we intend to detect damage at its early stage. Therefore, for a continuous monitoring, we can assume that damage is localized in small regions and the search space of Equation (2.7) remains small. However, the computation could become prohibitive when $\Theta^{max}_{H_j}$ is calculated for a hypothesis $H_j$ which assumes a large number of substructures as damaged. Further effort is required to develop an efficient method to evaluate $\Theta^{max}_{H_j}$.

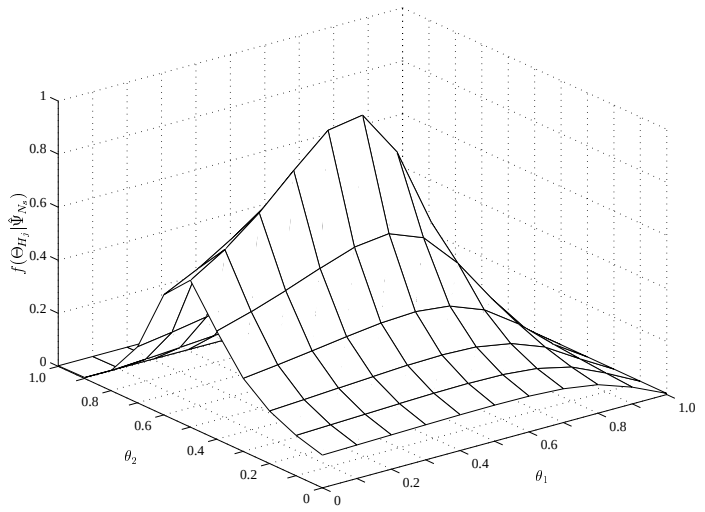


Figure 2.1: A typical search space of $f(\Theta_{H_j}|\hat{\Psi}_{N_s})$

The approach described here is analogous to pattern recognition using a Bayes classifier [55]. The goal of the pattern recognition approach is to make a decision, when a new measurement is observed, whether the measurement comes from a normal (healthy) or abnormal (damaged) state of a system. To make this decision, the Bayes classifier assumes a probabilistic distribution of each class, and estimates the characteristic parameters of each distribution from observations. However, the difficulty of obtaining the sample observations hampers the application of the Bayes classifier to

damage detection problems; the collection of sample observations corresponding to the damaged state of the specific location is practically infeasible unless the structure is intentionally damaged. To overcome this difficulty, Garcia and Stubbs [56] estimate the properties of the undamaged and damaged classes from a finite element (FE) model of the structure with simulated damages. The performance of this approach depends on the selection of the simulated data sets used to estimate the class properties. Theoretically, for a structure with $n$ number of substructures, $2^{(n-1)}$ different damage scenarios need to be simulated to correctly estimate the properties of a single class. This process needs to be repeated for the damaged/undamaged classes for all the substructures. Furthermore, if different damage amount for each substructure is considered, the computation becomes practically prohibitive.

The proposed approach eliminates the parameter estimation process by defining each damage scenario as a separate class, and the state of a substructure as *damaged* or *undamaged*. The binary states make it possible to construct a tree representation of all possible damage scenarios. The *damage tree* starts with a null hypothesis (scenario) $H_o$ that no damage is present. From the root, the first level branches are extended by adding a substructure as damaged one at a time. For a system with $N_{sub}$ substructures, the number of the first level branches becomes ${}_{N_{sub}}C_1$. Here, we define ${}_NC_K (= \frac{N!}{K!(N-K)!})$ as the number of combinations of $K$ items out of a population $N$. From each first level branch, the second level branches are extended by adding another substructure as damaged. The total number of the second level branches becomes ${}_{N_{sub}}C_2$. For a system with $N_{sub}$ substructures, the damage tree has a total $N_{sub}$ levels of branches and the total number of branches is $2^{N_{sub}} = {}_{N_{sub}}C_0 + {}_{N_{sub}}C_1 + ... + {}_{N_{sub}}C_{N_{sub}}$. Clearly, the number of alternatives remains large. The complexity can be significantly reduced by a branch-and-bound search scheme, which is originally proposed for the diagnosis of multiple diseases [70].

## 2.2 A Branch-and-Bound Search Scheme

A branch-and-bound search scheme is proposed to expedite the search for the most likely damage case without exhaustively examining all the possible combinations of

damaged substructures. Starting from the null hypothesis $H_o$ that no damage is present, one substructure is added as a possible damage location at a time to generate extended hypotheses. The posterior probabilities of hypotheses are examined in terms of their error functions and the prior probabilities as defined in Equation (2.25). Each hypothesis keeps extending by adding a new substructure as damaged until the further addition of substructures does not lead to a more probable hypothesis. The key requirement is a bounding heuristic which allows us to rule out further extensions of a hypothesis. In this study, the following two pruning heuristics are adopted: [1]

1. Let $H_j + D_i$ denote an extension of hypothesis $H_j$ by adding the $i$th substructure as damaged. (Note that, in the extended hypothesis $H_j + D_i$, the other substructures, except the damaged substructures in $H_j$ and the $i$th substructure, are assumed undamaged.) If a posterior probability of $H_j + D_i$ is less than that of $H_j$, then further extension of $H_j + D_i$ is ruled out; i.e.

$$\text{if } P(H_j + D_i|\hat{\Psi}_{N_s}) < P(H_j|\hat{\Psi}_{N_s}), \text{ stop extending } H_j + D_i. \tag{2.26}$$

2. If a posterior probability of $H_j$ is less than $P_{max}$, which is the largest posterior probability among all the hypotheses examined so far, then further extension of $H_j$ is ruled out; i.e.

$$\text{if } P(H_j|\hat{\Psi}_{N_s}) < P_{max}, \text{ stop extending } \ H_j. \tag{2.27}$$

Using Equation (2.26), we can exclude the extension of $H_j + D_i$ when the addition of the $i$th substructure as damaged is found not to lead to a more probable hypothesis. In addition, when the first $H_j$ is found such that $P(H_j|\hat{\Psi}_{N_s}) > P(H_j + D_i|\hat{\Psi}_{N_s})$ for all substructures not included in $H_j$ ($\forall D_i \notin H_j$), $P(H_j|\hat{\Psi}_{N_s})$ is the first local maximum posterior probability in the current branching direction of damage events. That is, the criterion in Equation (2.26) guarantees that the first local maximum posterior probability in every branching direction is found. Unfortunately this pruning heuristic

[1] In Chapter 3, an additional heuristic based on the sensitivity analysis of modal parameters to stiffness changes is also presented.

is not a strong criterion for the system with a large number of substructures since all branches are subject to further extensions until the first local maximum point is found.

As a complementary criterion, Equation (2.27) excludes the further branching of the newly extended hypotheses which have posterior probabilities less than the largest posterior probability among the hypotheses examined so far. The second criterion can be easily modified to include $n$ number of the newly extended hypotheses for the further branching by replacing $P_{max}$ in Equation (2.27) with the $n$th largest posterior probability $P^n_{max}$.

Damage detection techniques, which rely only on the modal parameter information such as the one described in this study, might have the drawback that the damage locations and amount may not be uniquely determined from the estimated modal data [147]. Models with differently assumed damage locations and amount can produce identical modal parameters. These models are referred to as *output equivalent* models [89]. The exhaustive search of all possible models (hypotheses) is infeasible, and a branch-and-bound search scheme may identify only some models (hypotheses with assumed damage locations and amount), which locally maximize the posterior probability $P(H_j|\hat{\Psi}_{N_s})$ in Equation (2.5), and may not detect the global maximum points.

In real applications, multiple hypotheses need to be examined for the following reasons:

1. Since the modal testing measures the dynamic responses at limited points and estimates only a few fundamental modes, the number of output equivalent models can increase.

2. In the presence of the modeling error and the measurement noise, some erroneous models could have modal parameters closer to the estimated modal parameters than the model with the correct damage locations and amount.

Therefore, in practice, multiple hypotheses should be examined to find local maximum posterior probabilities and potentially to identify the correct damage event.

In the proposed method, a larger subspace of the hypothesis space can be examined by replacing $P_{max}$ in Equation (2.27) with $P^n_{max}$, where $P^n_{max}$ is the $n$th largest posterior probability among the hypotheses examined so far. This approach allows us to make an explicit trade-off between the computational cost and the better diagnosis. However further research is required to provide a systematic guideline for choosing "$n$" in $P^n_{max}$ . Using the two pruning heuristics, Figure 2.2 depicts an example of the branch-and-bound search for the most likely damage events of a structure which is divided into five substructures.

## 2.3 Application to a Six-Story Shear Structure

This section illustrates the Bayesian probabilistic approach using a six-story shear frame structure shown in Figure 2.3. The system stiffness matrix is represented as an assembly of the substructure stiffness matrices and a non-dimensional parameter $\theta_i$ is introduced to model the stiffness contribution of the $i$th substructure [see Equation (2.1)]. The mass matrix is assumed to be known and invariant. For all examples, a uniform prior probability is assigned to all hypotheses. Therefore, the determination of the most probable hypothesis in Equation (2.25) depends only on the error function $J(\hat{\Psi}_{N_s}, \Theta^{max}_{H_j})$. The search space $\Theta_{H_j} < \Omega^*_{H_j}$ in Equation (2.7) is evaluated at the intersections of grid lines which discretize the search domain with an incremental step $\Delta\theta$. For the presented numerical examples, we use an incremental step $\Delta\theta = 0.1$. In addition, a value of 0.9 is used for the damage threshold $\theta^*$ for every substructure, that is, decreases in the stiffness over 10% are defined as *damage*.

Instead of the largest posterior probability $P_{max}$, we use the third largest posterior probability $P^3_{max}$ ($< P^2_{max} < P^1_{max} = P_{max}$) in Equation (2.27) to investigate a larger subspace of the hypothesis space. The branch-and-bound search in the presented examples follows a depth-first/best-first search strategy. Each modal vector is normalized with respect to the absolute maximum component in the modal vector. Since one component is used for normalization, only $N_d - 1$ pieces of information exist for each mode.

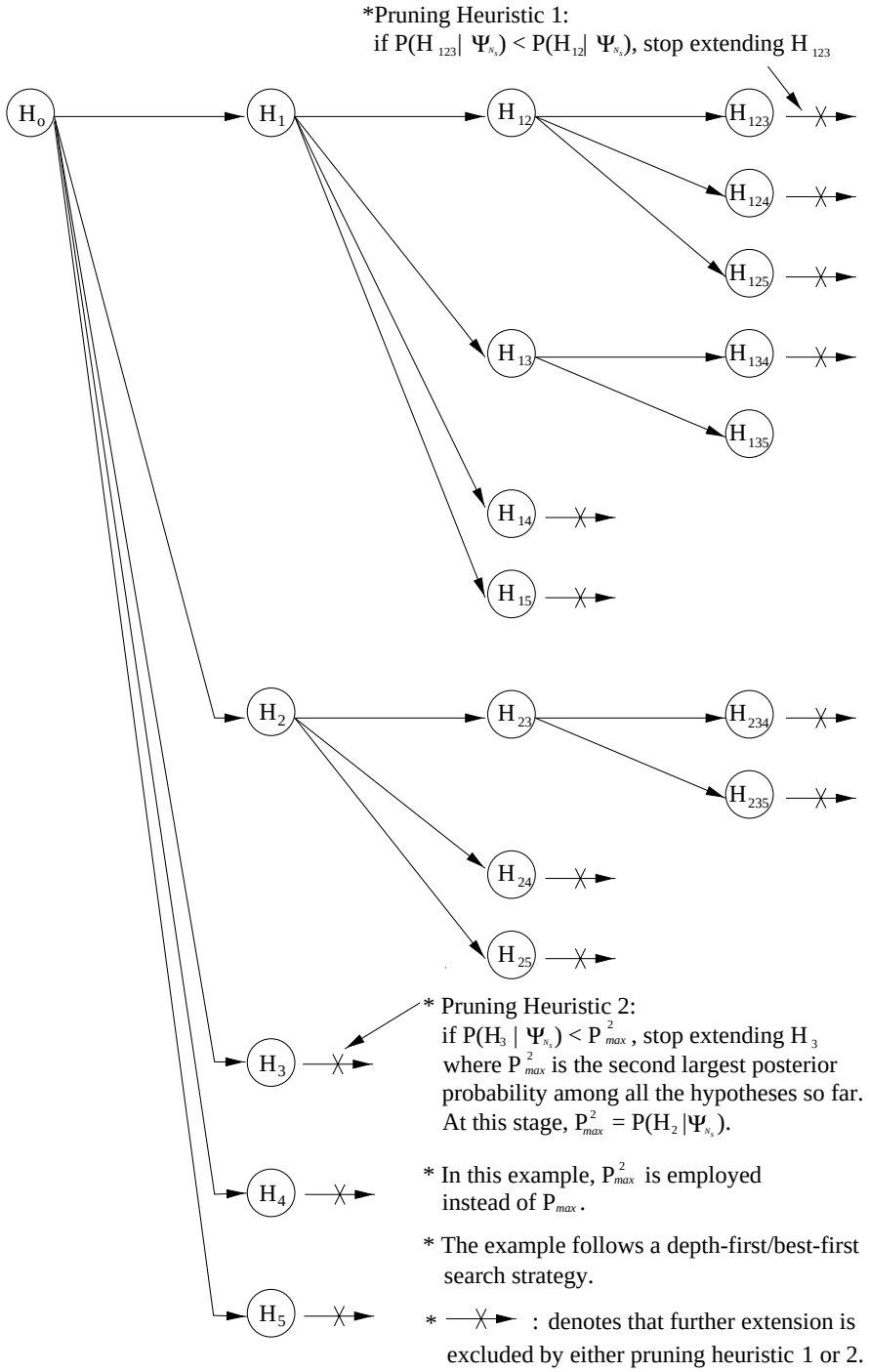


Figure 2.2: An example of branch-and-bound search for a structure with five substructures

For the examples shown below, $L_{dam}$ and $D_{dam}$ denote the actual damage locations and the associated damage amount, respectively. $\hat{L}_{dam}$ and $\hat{D}_{dam}$ denote the most probable damage locations and the associated damage amount estimated by the proposed method. In addition, the measured DOFs and the estimated modes are denoted by DOFm and MODEm, respectively.

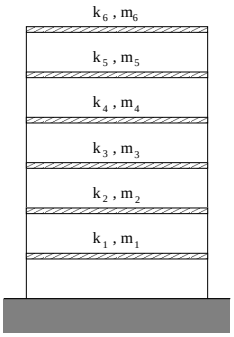


Figure 2.3: A six-story shear frame model

The frame structure consists of six DOFs and six substructures corresponding to each floor story. To simulate measurement uncertainties in the estimated modal parameters, the exact modal parameters, obtained from the analytical model with the assumed damage, are perturbed with noise. More explicitly, the estimated modal parameter set $\hat{\psi}(n)$ in Equation (2.3) is constructed such that:

$$\hat{\psi}(n) = \psi \ (1 + \frac{\mathcal{N}}{100} \mathcal{R}) \tag{2.28}$$

where $\psi$ is the exact modal parameter set obtained from the analytical model, $\mathcal{N}$ is a specified noise level in terms of percentage, and $\mathcal{R}$ is a normally distributed random number with zero mean and a variance of 1.0. This process is repeated $N_s$ times to simulate the $N_s$ modal data sets.

Since the estimated modal parameters are simulated by adding noise to the exact modal parameters, the modal error defined in Equation (2.15) arises only from noise error, i.e. $e(n, \Theta_{H_j}) = e_N(n, \Theta_{H_j})$. Therefore the error function shown in Equation (2.22) is simplified as:

$$J(\hat{\Psi}_{N_s}, \Theta_{H_j}) = \frac{1}{2}\sum_{n=1}^{N_s}[\hat{\psi}(n) - \psi(\Theta_{H_j})]^T \mathbf{C}_{\hat{\Psi}}^{-1}[\hat{\psi}(n) - \psi(\Theta_{H_j})] \tag{2.29}$$

This example investigates the applicability of the proposed method subject to the effects of (1) the noise level in the estimated modal data, (2) the number and the selection of estimated modes and measured DOFs, (3) the locations and the amount of damage, and (4) the number of modal data sets.

### 2.3.1 Effect of Noise Level in the Estimated Modal Data

The proposed method is first tested to show that it does not give a false-positive indication of damage (the case of indicating damage when in fact damage does not exist). Three cases are conducted assuming 3%, 5% and 10% noise levels. For each case, 10 sets of modal parameters are simulated from the *undamaged* structure, the DOFs corresponding to the second and fourth stories are measured, and the first and second modes are identified. For all cases, the proposed method does not provide a false-positive indication.

Next, the effect of noise in the measured data is investigated. Four cases are conducted by varying the noise levels from 0.5% to 10%. For all cases, the stiffnesses of the second and sixth stories are decreased by 30% and 10%, respectively, i.e. $L_{dam} = \{2,\ 6\}$ and $D_{dam} = \{30\%,\ 10\%\}$. The measurements are made at the second and fourth stories, and the first and second modes are identified, i.e. DOFm=$\{2,\ 4\}$ and MODEm=$\{1,\ 2\}$. Three sets of modal parameters are collected ($N_s$=3). Table 2.1 summarizes the results. The *rank* in the table indicates the rank of the actual damage event when the posterior probabilities of all examined hypotheses are sorted in descending order. As the noise level increases from case 1 to cases 2, 3 and 4, the rank of the actual damage event decreases.

Table 2.1: Effect of noise level

| Case | Noise level | Rank |
|---|---|---|
| 1 | 0.5% | 1 |
| 2 | 1.0% | 5 |
| 3 | 5.0% | 8 |
| 4 | 10.0% | 10 |

$L_{dam}$={2,6}, $D_{dam}$={30%,10%}, $N_s$=3
Measured DOFs={2,4}, Estimated Modes={1,2}

### 2.3.2 Effect of Measured DOFs

The effect of measured DOFs is examined by changing the number and locations of the measured DOFs. Five cases are conducted by assuming $L_{dam} = \{2,\ 6\}$, $D_{dam} = \{30\%,\ 10\%\}$, $N_s = 5$ and a 10% noise level for the estimated modal parameters. Table 2.2 shows the results. When the modal vectors are obtained from the measurements on all DOFs (case 1) or on alternative floors (case 2), the proposed method correctly identifies the damage locations even in the presence of a 10% noise. As the number of measured DOFs decreases to two or one (cases 3, 4 and 5), the proposed method fails to rank the actual damage event as the most likely one. In case 5 of Table 2.2 (where only one DOF is measured), the proposed method uses only the estimated frequency information. No information is provided from modal vectors since the normalization of modal vectors requires the measurements of more than two DOFs. If a larger number of modal data sets were available, the diagnosis result could be improved. This is true even for the cases where only a limited number of locations are measured, and the data have relatively high noise level. The effect of the number of modal data sets is investigated in Section 2.3.6.

### 2.3.3 Effect of Multiple Damage Locations

One salient feature of this work is that multiple damage locations in a structure can be detected. As noted earlier, a branch-and-bound search scheme is employed to facilitate the search of multiple damage locations. Figure 2.4 presents a typical result of the branch-and-bound search. In this figure, 10%, 20% and 30% damages are

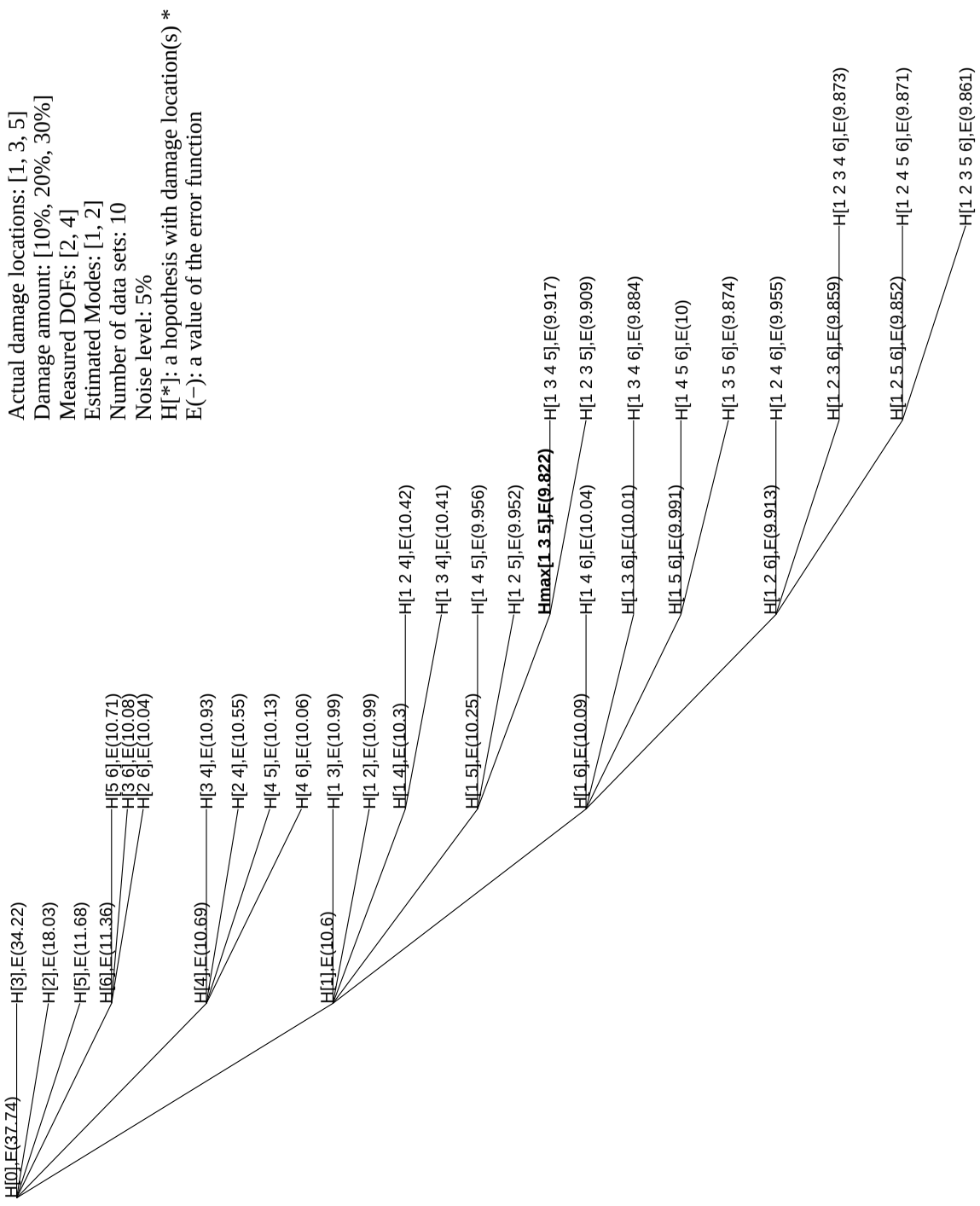


Figure 2.4: A branch-and-bound search for damage locations of a six-story shear frame structure

Table 2.2: Effect of measured DOFs

| Case | DOFm | Rank |
|---|---|---|
| 1 | all | 1 |
| 2 | 1,3,5 | 1 |
| 3 | 3,5 | 15 |
| 4 | 2,4 | 14 |
| 5 | 3 | 13 |

$L_{dam}$={2,6}, $D_{dam}$={30%,10%}, $N_s$=5
Estimated Modes={1,2}, Noise=10%

assumed in the first, the third and the fifth stories, respectively ($L_{dam}$={1, 3, 5} and $D_{dam} = \{10\%,\ 20\%,\ 30\%\}$). The first two modes are estimated by the measurements on the second and fourth stories (DOFm=[2, 4] and MODEm=[1, 2]). In addition, 10 modal data sets are simulated by assuming a 5% noise level ($N_s$=10 and Noise=5%).

Figure 2.4 shows that the proposed method finds the actual damage locations after searching 39 hypotheses out of the 64 possible hypotheses. The first story is detected as damaged immediately in the first step of branching. Since the decrease of the first story stiffness has a significant effect on all modal parameters, the first story is easily detected as a damaged substructure. In the next step, the fifth story, which has the largest damage amount, is detected. Finally, the third story is added as one of the possible damage locations. The correct damage hypothesis is extended one more step and bounded for further branching because the posterior probabilities of the extended hypotheses are lower than that of the correct hypothesis.

The branch-and-bound search scheme shown in Figure 2.4 follows a depth-first/ best-first search strategy. After the first extension of H[0] to H[1], H[4], H[6], H[5], H[2] and H[3], $P(\text{H[6]}|\hat{\Psi}_{N_s})$ is assigned to $P^3_{max}$. Since the posterior probabilities of H[1], H[4] and H[6] are larger or equal to the current $P^3_{max}$, only these three branches remain for further extensions. Next, H[1] is extended since H[1] has the highest posterior probability among H[1], H[4] and H[6] (best-first search). After this extension, $P^3_{max}$ is changed to $P(\text{H[1,4]}|\hat{\Psi}_{N_s})$. Among the subtrees of H[1], only H[1,6], H[1,5] and H[1,4] remain for further extensions. In the next step, since we employ a depth-first search scheme, H[1,6] is first extended rather than H[4]. When we extend H[4] to H[4,6], H[4,5], H[2,4] and H[3,4], all branches below H[1] are already extended.

That is, at this stage, $P^3_{max}$ has been changed to $P(\mathrm{H}[1,2,5,6]|\hat{\Psi}_{N_s})$ which is the third largest posterior probability among the hypotheses examined so far. Since the posterior probabilities of H[4,6], H[4,5], H[2,4] and H[3,4] are less than the current $P^3_{max}$, further extensions are excluded.

In place of the largest posterior probability in Equation (2.27), the search scheme shown in Figure 2.4 uses the third largest posterior probability among the hypotheses examined so far as the pruning criterion. If the largest posterior probability were used as the pruning criterion, the branching from hypothesis H(1) to H(1,5) would have been excluded. For the detection of multiple damage locations, the pruning heuristic in the branch-and-bound search scheme should be loosened to include a larger subspace of the hypothesis space. Examining more hypotheses increases the chance of capturing the actual damage event. In real situations, the proposed method may not find *all* the damaged substructures, but, very likely it can find the damage locations which have *significant* effect on the modal parameters.

### 2.3.4 Effect of Damage Amount

For all three cases in Table 2.3, we assume a 5% noise level, five sets of modal data, and the estimation of the first and second modes with the measurement on the second and fourth stories. The proposed method identifies the actual damage event for case 1, where 30% and 10% decreases in the stiffness are simulated in the second and sixth stories, respectively. As damage in the second and sixth stories respectively increases to 60% and 20% (case 2), the rank of the actual damage event decreases. When more severe damage is assumed for case 3 ($\hat{L}_{dam}$={2,6} and $\hat{D}_{dam}$={90%, 30%}), the rank of the actual damage event becomes lower. In spite of the absolute increase of damage in both the stories from case 1 to cases 2 and 3, the diagnosis result worsens. This phenomenon can be explained as follows: Since, in the current example structure, the second story stiffness has more significant effect on the modal parameters and larger damage than the sixth story stiffness, the second story becomes more detectable than the sixth story (for all cases, the branch-and-bound search identifies the second story first). On the other hand, the sixth story becomes less detectable as the difference

of damage between the second and sixth stories increases. This implies that, for the detection of multiple damage locations, the proposed method depends on the *relative* damage amount among the damaged substructures as well as the *absolute* damage amount of each substructure. The cases shown in Table 2.3 use a value of 0.9 as the

Table 2.3: Effect of damage amount

| | Damage Amount | | |
|---|---|---|---|
| Case | 2nd story | 6th story | Rank |
| 1 | 30% | 10% | 1 |
| 2 | 60% | 20% | 21 |
| 3 | 90% | 30% | 28 |

Measured DOFs={2,4}, $N_s$=5
Estimated Modes={1,2}, Noise=5%

damage threshold value $\theta^*$ for all substructures. That is, damaged substructures with less than 10% stiffness decrease may not be detected. If a higher damage threshold value ($> 0.9$) and a smaller $\Delta\theta$, which is an incremental value implemented to search the non-dimensional parameter space $\Theta_{H_j} < \Theta^*_{H_j}$ in Equation (2.7), are used, the proposed method can identify smaller damage. For the cases shown in Table 2.4, we

Table 2.4: Detection of small damage

| Case | $L_{dam}$ | $D_{dam}$ | Noise | $N_s$ | Rank |
|---|---|---|---|---|---|
| 1 | {3} | {3%} | 2% | 20 | 1 |
| 2 | {1,3} | {5%,5%} | 2% | 100 | 1 |
| 3 | {2,6} | {5%,3%} | 5% | 100 | 1 |
| 4 | {2,3} | {5%,3%} | 5% | 50 | 1 |

Measured DOFs={2,4}, Estimated Modes={1,2}

set the damage threshold value $\theta^*$ to 0.99 and the incremental value $\Delta\theta$ to 0.01. Four cases are conducted by changing the damage locations and amount. For all cases, less than 10% stiffness decrease is assumed. In spite of a small damage amount, all cases converge to the actual damage event. The problem is that the smaller the incremental value $\Delta\theta$, the more the computation time is required. Also the measured data with lower noise level is necessary for the detection of small damage.

### 2.3.5 Effect of Mode Selection

To study the effect of mode selection, the estimated modes are changed for each case. For all cases, the damage amount of the second and sixth stories is assumed to be 30% and 10% respectively. Three modal data sets are collected and a 5% noise level is assumed. Measurements are assumed to be made on the second and fourth stories.

Table 2.5: Effect of mode selection

| Case | Estimated Modes | Rank |
|---|---|---|
| 1 | all | 1 |
| 2 | 1, 2 | 8 |
| 3 | 3, 4 | 1 |
| 4 | 5, 6 | 7 |

$L_{dam}$={2,6}, $D_{dam}$={30%,10%}, $N_s$=3
Measured DOFs={2,4}, Noise=5%

Table 2.5 presents the diagnosis results obtained by using four different mode selection strategies. When all six modes are estimated in case 1, the proposed method ranks the actual damage event as the most probable one. From the results of cases 2, 3 and 4, where two different modes are estimated for each case, it appears that the selection of the third and fourth modes yields better assessment than the other two selection strategies for the detection of the assumed damage locations $L_{dam}$={2, 6}.

What modes should be selected depends on the specified damage locations. Unfortunately, for the damage detection of civil structures, selecting specific modes may not be practical because (1) usually only a few fundamental modes can be estimated from the vibration test of a structure, and (2) the contribution of a mode for the damage detection depends on the actual damage locations which are unknown when modes are selected. [2]

[2]This issue motivates the use of load-dependent Ritz vectors for damage detection problems as described in Chapter 3.

### 2.3.6 Effect of the Number of Modal Data Sets

Better damage assessment can be achieved by accumulating modal data sets from vibration tests. To investigate the effect of the number of modal data sets $N_s$, four cases are conducted by increasing $N_s$ from 1 to 10. For all cases, $L_{dam} = \{2,\ 6\}$, $D_{dam} = \{30\%,\ 10\%\}$ and a 5% noise level are assumed. The first and second modes are estimated by the measurements on the second and fourth stories. The diagnosis results presented in Table 2.6 show that the proposed method identifies the actual damage locations when $N_s \geq 5$. For case 1, since the branch-and-bound search does not find the actual damage event, the rank of the actual damage event is denoted as *not found* in Table 2.6.

Table 2.6: Effect of data set number

| Case | $N_s$ | Rank |
|---|---|---|
| 1 | 1 | not found |
| 2 | 3 | 8 |
| 3 | 5 | 1 |
| 4 | 10 | 1 |

$L_{dam}$={2,6}, $D_{dam}$={30%,10%}, Noise=5%
Measured DOFs={2,4}, Estimated Modes={1,2}

Table 2.7 shows the results of the re-diagnosis of the previous cases, which failed to rank the actual damage event as the most probable one, by increasing the number of data sets. For the previous case 3 of Table 2.1, the rank of the actual damage event changes from eighth to first after increasing the number of data sets $N_s$ from 3 to 5. Table 2.7 also shows the other cases in which the actual damage locations are properly detected after increasing $N_s$. However, for the previous case 5 of Table 2.2, where only one DOF is measured, the proposed method fails to identify the actual damage locations even after increasing $N_s$ to 20. This illustrates that sufficient measured DOFs and number of data sets are required for damage detection.

Table 2.7: Improvement of diagnosis results by increasing data set number

| Case | $D_{dam}$ | Noise | MODEm | DOFm | $N_s$ | Rank |
|---|---|---|---|---|---|---|
| case 2 of table 2.1 | {30%,10%} | 1% | {1,2} | {2,4} | 3→5 | 5→1 |
| case 3 of table 2.1 | {30%,10%} | 5% | {1,2} | {2,4} | 3→5 | 8→1 |
| case 4 of table 2.1 | {30%,10%} | 10% | {1,2} | {2,4} | 3→20 | 10→1 |
| case 2 of table 2.3 | {60%,20%} | 5% | {1,2} | {2,4} | 5→10 | 21→1 |
| case 3 of table 2.3 | {90%,30%} | 5% | {1,2} | {2,4} | 5→10 | 28→1 |
| case 4 of table 2.5 | {30%,10%} | 5% | {5,6} | {2,4} | 3→20 | 7→1 |
| case 3 of table 2.2 | {30%,10%} | 10% | {1,2} | {3,5} | 5→20 | 15→1 |
| case 4 of table 2.2 | {30%,10%} | 10% | {1,2} | {2,4} | 5→20 | 14→1 |
| case 5 of table 2.2 | {30%,10%} | 10% | {1,2} | {3} | 5→20 | 13→9 |

For all cases, $L_{dam}$={2, 6}

## 2.4 Summary and Discussions

In this chapter, a Bayesian probabilistic approach has been formulated to detect the most likely locations and amount of damage in a structure using the estimated modal parameters. The system stiffness matrix is represented as an assembly of the substructure stiffness matrices and a non-dimensional parameter $\theta_i$ is introduced to model the stiffness contribution of the $i$th substructure. The mass matrix is assumed to be known and invariant. Assuming a uniform probability density function for the non-dimensional parameter $\theta_i$ ($0 \leq \theta_i \leq 1$), we formulate the relative posterior probability of an assumed damage event and apply a branch-and-bound search scheme to identify the most likely damage event. The measurement noise and modeling error between the structure and the analytical model are explicitly considered within the Bayesian probabilistic framework.

A shear frame structure is employed to assess the potential applicability of the proposed method. As long as sufficient modal data sets are available, the proposed method is able to identify the actual damage locations and amount in most cases when (1) low noise levels are achieved in the estimated modal parameters, (2) a small number of degrees of freedom are measured, and (3) only several fundamental modes are estimated. The computational cost of the method is also significantly reduced by using a branch-and-bound search scheme.

# Chapter 3

# Load-Dependent Ritz Vectors for Damage Detection

In this chapter, the Bayesian-based damage detection framework is extended to incorporate load-dependent Ritz vectors as a possible alternative to modal parameters. Recent research has shown that it is possible to extract Ritz vectors from vibration tests [28]. The first Ritz vector is the static deformation of a structure due to a particular load applied to the structure. The subsequent vectors account for the inertial effects of the loading and are generated by iterative matrix multiplication and orthogonalization. Ritz vectors (or Lanczos vectors) have been shown very effective for eigenvalue problems, dynamic and earthquake analyses, and model reductions [150,94,111]. However, very few studies have applied Ritz vectors to damage detection or system identification problems [27,91].

The incorporation of Ritz vectors for damage detection problems is motivated by the following potential advantages of Ritz vectors over modal vectors: (1) Ritz vectors can be made more sensitive to damage than the corresponding modal vectors, (2) substructures of interest can be made more observable using the Ritz vectors generated from particular load patterns, (3) the computation of Ritz vectors is less expensive than that of modal vectors (eigenvectors) and (4) while the practical difficulties of modal testing impede the extraction of a large number of meaningful modes, multiple sets of Ritz vectors can be extracted by imposing different load patterns on a

structure.

This chapter is organized as follows: First, the basic formulation to incorporate the Ritz vectors into the Bayesian framework is described in Section 3.1. In Section 3.2, a weighting scheme is introduced into the Bayesian framework to measure the relative significance of Ritz or modal vectors to damage [44]. Sensitivity analysis of modal vectors [127,88,17,39,64,52] reveals that only members (or substructures) which cause significant changes in the estimated modal parameters can be detected and the identification of higher modes is necessary for damage detection of complex structures. Similarly, we measure the relative significance of Ritz vectors to the assumed damage locations for the computation of the posterior probability. The sensitivity analysis of the modal parameters and Ritz vectors are described in Sections 3.3 and 3.4, respectively. Finally, in Section 3.5, the potential applicability of Ritz vectors to damage detection of structures is demonstrated using a three-dimensional truss structure.

## 3.1 Basic Formulation

In this section, the Bayesian framework presented in Chapter 2 is extended to incorporate load-dependent Ritz vectors as a possible alternative to modal parameters. Again, test data sets are assumed to be collected from repeated vibration tests. When vibration tests are repeated $N_s$ times, the total collection of $N_s$ data sets is denoted as:

$$\hat{\Psi}_{N_s} = \left\{ \hat{\psi}(n) \ : \ n = 1, ..., N_s \right\} \tag{3.1}$$

A data set $\hat{\psi}(n)$ in Equation (3.1) is composed of Ritz vectors estimated from the $n$th vibration test:

$$\hat{\psi}(n) = \left[ \hat{\mathbf{r}}_1^{nT}, ..., \hat{\mathbf{r}}_{N_r}^{nT} \right]^T \in \mathbf{R}^{N_t} \tag{3.2}$$

where $\hat{\mathbf{r}}_i^n$ denotes the $i$th estimated Ritz vector in the $n$th data set. The Ritz vector $\hat{\mathbf{r}}_i^n$ ($\in \mathbf{R}^{N_d}$) has components corresponding to the instrumented DOFs. The variables $N_t$, $N_d$ and $N_r$ represent the total number of components in a data set $\hat{\psi}(n)$,

the number of the measured DOFs and the number of the estimated Ritz vectors, respectively.

Given $\Theta_{H_j}$, an analytical data set $\psi(\Theta_{H_j})$ is defined similar to Equation (3.2):

$$\psi(\Theta_{H_j}) = \left[\mathbf{r}_1^T(\Theta_{H_j}), ..., \mathbf{r}_{N_r}^T(\Theta_{H_j})\right]^T \in \mathbf{R}^{N_t} \tag{3.3}$$

It should be noted that a Ritz vector $\mathbf{r}_i(\Theta_{H_j})$ in Equation (3.3) has only the components associated with the measured DOFs. The rest of derivation is identical to the discussion in Section 2.1. The most probable hypothesis $H_{max}$ has the identical form given in Equation (2.25) as:

$$J(\hat{\Psi}_{N_s}, \Theta_{H_{max}}^{max}) - lnP(H_{max}) = \min_{\forall H_j} \left[J(\hat{\Psi}_{N_s}, \Theta_{H_j}^{max}) - lnP(H_j)\right] \tag{3.4}$$

where the error function $J(\hat{\Psi}_{N_s}, \Theta_{H_j})$ is:

$$J(\hat{\Psi}_{N_s}, \Theta_{H_j}) = \tag{3.5}$$
$$\frac{1}{2}\sum_{n=1}^{N_s}[\hat{\psi}(n) - \psi(\Theta_{H_j}) - e_M(\Theta_{H_o})]^T \mathbf{C}_{\hat{\Psi}}^{-1}[\hat{\psi}(n) - \psi(\Theta_{H_j}) - e_M(\Theta_{H_o})]$$

and

$$e_M(\Theta_{H_j}) \cong e_M(\Theta_{H_o}) = \hat{\psi}_m^h - \psi(\Theta_{H_o}) \; ; \; \forall \Theta_{H_j} \tag{3.6}$$

The incorporation of Ritz vectors to the Bayesian framework is completed by simply replacing the modal parameters with the Ritz vectors. Therefore, the branch-and-bound search scheme in Section 2.2 can be also applied without any modification.

## 3.2 A Weighting Scheme Based on Sensitivity

Previous works have suggested the importance in selecting the appropriate modes which are sensitive to the critical members [44,88] for damage detection. However, the ignorance of the actual damage locations hinders the selection process. Since the

posterior probabilities of the assumed damage events are of interest in the Bayesian approach, the Ritz vectors, which are more sensitive to the stiffness changes of substructures in each assumed damage event, can be weighted for each case. In other words, the Ritz vectors, which are sensitive not to the unknown actual damage but to the assumed damage, can be weighted for the computation of the error function. In this section, a weighting scheme is introduced into the Bayesian framework to measure the relative significance of Ritz or modal vectors to damage.

Realizing that $\mathbf{C}_{\hat{\Psi}}^{-1}$ in Equation (2.22) is one form of a weighting matrix, we modify the error function $J(\hat{\Psi}_{N_s}, \Theta_{H_j})$ such that each term of the error function is weighted to take into account the sensitivities of Ritz vectors to the assumed damage as well as the measurement uncertainties:

$$J(\hat{\Psi}_{N_s}, \Theta_{H_j}) = \tag{3.7}$$
$$\frac{1}{2}\sum_{n=1}^{N_s}\left[\hat{\psi}(n) - \psi(\Theta_{H_j}) - e_M(\Theta_{H_o})\right]^T \mathbf{W}_{\mathbf{r}}\left[\hat{\psi}(n) - \psi(\Theta_{H_j}) - e_M(\Theta_{H_o})\right]$$

where a diagonal weighting matrix $\mathbf{W}_{\mathbf{r}}$ replaces the inverse of the covariance matrix $\mathbf{C}_{\hat{\Psi}}^{-1}$ in Equation (3.5). $\mathbf{W}_{\mathbf{r}}$ is a diagonal matrix given as:

$$\mathbf{W}_{\mathbf{r}} = \mathrm{diag}\left[W_{\mathbf{r}_{11}}\ W_{\mathbf{r}_{12}}\ ...\ W_{\mathbf{r}_{1N_d}}, W_{\mathbf{r}_{21}}, ..., W_{\mathbf{r}_{2N_d}}, ..., W_{\mathbf{r}_{N_r N_d}}\right] \tag{3.8}$$

where $\mathbf{r}_{pk}$ denotes the $k$th component of the $p$th analytical Ritz vector and each diagonal entry $W_{\mathbf{r}_{pk}}$ is defined as follows:

$$W_{\mathbf{r}_{pk}}(\Theta_{H_j}) = \frac{w_{\mathbf{r}_{pk}}(\Theta_{H_j})}{\sigma^2_{\hat{\mathbf{r}}_{pk}}} \tag{3.9}$$

$w_{\mathbf{r}_{pk}}(\Theta_{H_j})$ weights the corresponding error term in Equation (3.7) considering the sensitivity of $\mathbf{r}_{pk}$ to the assumed damage. $\sigma_{\hat{\mathbf{r}}_{pk}}$ is the standard deviation of the $k$th component of the $p$th estimated Ritz vector and considers the measurement noise.

The definition of $w_{\mathbf{r}_{pk}}$ first requires the computation of the Ritz vector derivative, $\frac{\partial \mathbf{r}_{pk}}{\partial \theta_i}$. A closed form solution of $\frac{\partial \mathbf{r}_{pk}}{\partial \theta_i}$ is derived in Section 3.4.2. It should be noted that $\Theta_{H_j}$ contains all the information regarding the current damage state. The damaged

substructures are the ones included in $H_j$ as damaged and the damage amount of the $i$th substructure, $\Delta\theta_i$, is $1-\theta_i$. Since it is difficult to find the sensitivities of the Ritz vectors for multiple damage locations, we define the sensitivity of $\mathbf{r}_{pk}$ with respect to the current damage state as the rate of $\Delta\mathbf{r}_{pk}$ (the change of $\mathbf{r}_{pk}$ from the undamaged state) to the average change of $\theta_i$ ($\in \Theta^1_{H_j}$). For simplicity, $\mathbf{r}_{pk}$ is assumed to change linearly with the change of $\theta_i$. Thus, $\Delta\mathbf{r}_{pk}$ at the current damage state can be approximated as:

$$\Delta\mathbf{r}_{pk} \cong \sum_{\theta_i \in \Theta^1_{H_j}} \frac{\partial \mathbf{r}_{pk}}{\partial \theta_i} \Delta\theta_i \tag{3.10}$$

The sensitivity of $\mathbf{r}_{pk}$ at the current damage state, $S(\mathbf{r}_{pk}|\Theta_{H_j})$, is defined as:

$$S(\mathbf{r}_{pk}|\Theta_{H_j}) = \frac{\Delta\mathbf{r}_{pk}}{\Delta\bar{\theta}} \cong \sum_{\theta_i \in \Theta^1_{H_j}} \frac{\partial \mathbf{r}_{pk}}{\partial \theta_i} \frac{\Delta\theta_i}{\Delta\bar{\theta}} = \sum_{\theta_i \in \Theta^1_{H_j}} \frac{\partial \mathbf{r}_{pk}}{\partial \theta_i} \beta_i \tag{3.11}$$

where $\Delta\bar{\theta} = \frac{1}{N_{\theta^1}} \sum_{\theta_i \in \Theta^1_{H_j}} \Delta\theta_i$, $\beta_i = \frac{\Delta\theta_i}{\Delta\bar{\theta}}$ and $N_{\theta^1}$ is the number of damaged substructures in a hypothesis $H_j$. The sensitivity of a Ritz vector is defined as:

$$S(\mathbf{r}_p|\Theta_{H_j}) = \frac{[\ \sum_{k=1}^{N} S^2(\mathbf{r}_{pk}|\Theta_{H_j})\ ]^{\frac{1}{2}}}{[\ \sum_{k=1}^{N} \mathbf{r}^2_{pk}(\Theta_{H_j})\ ]^{\frac{1}{2}}} \tag{3.12}$$

where $N$ is the total number of DOFs in the analytical model. Finally, the weighting $w_{\mathbf{r}_{pk}}(\Theta_{H_j})$ is related to $S(\mathbf{r}_p|\Theta_{H_j})$ as:

$$w_{\mathbf{r}_{pk}}(\Theta_{H_j}) = \frac{S(\mathbf{r}_p|\Theta_{H_j})}{\sum_{i=1}^{N_r} S(\mathbf{r}_i|\Theta_{H_j})} \quad \text{for all } k \tag{3.13}$$

As mentioned earlier, the weighting scheme described in this section can also be applied for modal parameters. In this case, the diagonal weighting matrix in Equation (3.7) is computed based on the derivatives of the natural frequencies and modal vectors, which are derived in the next section.

## 3.3 Sensitivity of Modal Parameters

The partial derivatives of modal parameters are defined as sensitivity coefficients. Statistical-based system identification methods [29,39,59,127,146] generally involve the minimization of the errors employing the generalized least squares methods to update/modify a structural model using modal test data. The covariance matrix required by the generalized least squares is based on the sensitivity of modal parameters. Different formulations of the sensitivity are employed in these statistical-based methods [107,65,40,52]. The method described in Reference 40 requires a full modal matrix and is computationally expensive for a large system. When the derivative of one modal vector is computed, the method described in Reference 52 requires only the knowledge of the corresponding eigenvalue and modal vector. However, the second method requires the solution of a set of simultaneous equations equal to the size of the mass and stiffness matrices. In this study, the procedure described in References 107 and 65 is employed because of its simplicity.

Once the mass and stiffness matrices of the structure are formulated, the eigenvalues and eigenvectors of a $N$ degree-of-freedom system are obtained by solving the following eigenvalue problem:

$$\mathbf{K}\mathbf{v}_r - \omega_r^2 \mathbf{M}\mathbf{v}_r = \mathbf{0} \quad \text{for} \quad r = 1, ..., N \tag{3.14}$$

We start by taking the derivative of Equation (3.14) with respect to the non-dimensional damage parameter $\theta_i$:

$$\frac{\partial \mathbf{K}}{\partial \theta_i}\mathbf{v}_r + \mathbf{K}\frac{\partial \mathbf{v}_r}{\partial \theta_i} = \frac{\partial \omega_r^2}{\partial \theta_i}\mathbf{M}\mathbf{v}_r + \omega_r^2 \mathbf{M}\frac{\partial \mathbf{v}_r}{\partial \theta_i} \tag{3.15}$$

Then, pre-multiplying Equation (3.15) by $\mathbf{v}_s^T$ gives:

$$\begin{aligned} \mathbf{v}_s^T\frac{\partial \mathbf{K}}{\partial \theta_i}\mathbf{v}_r + \mathbf{v}_s^T\mathbf{K}\frac{\partial \mathbf{v}_r}{\partial \theta_i} = \frac{\partial \omega_r^2}{\partial \theta_i}\mathbf{v}_s^T\mathbf{M}\mathbf{v}_r + \omega_r^2\ \mathbf{v}_s^T\mathbf{M}\frac{\partial \mathbf{v}_r}{\partial \theta_i} = 0 \\ \rightsquigarrow \frac{\partial \omega_r^2}{\partial \theta_i}\mathbf{v}_s^T\mathbf{M}\mathbf{v}_r = \mathbf{v}_s^T\frac{\partial \mathbf{K}}{\partial \theta_i}\mathbf{v}_r + (\omega_s^2 - \omega_r^2)\mathbf{v}_s^T\mathbf{M}\frac{\partial \mathbf{v}_r}{\partial \theta_i} \end{aligned} \tag{3.16}$$

where, the transpose of Equation (3.14), $\mathbf{v}_s^T\mathbf{K} = \omega_s^2\mathbf{v}_s^T\mathbf{M}$, is used to obtain the second equality from the first one (i.e. $\mathbf{K}$ and $\mathbf{M}$ are assumed to be symmetric).

Equation (3.16) can be divided into the following two cases.

$$\frac{\partial\omega_r^2}{\partial\theta_i} = \left(\frac{1}{\mathbf{v}_r^T\mathbf{M}\mathbf{v}_r}\right)\mathbf{v}_r^T\frac{\partial\mathbf{K}}{\partial\theta_i}\mathbf{v}_r \quad \text{for } s = r, \tag{3.17}$$

and

$$\mathbf{v}_s^T\frac{\partial\mathbf{K}}{\partial\theta_i}\mathbf{v}_r + (\omega_s^2 - \omega_r^2)\mathbf{v}_s^T\mathbf{M}\frac{\partial\mathbf{v}_r}{\partial\theta_i} = 0 \text{ for } s \neq r \tag{3.18}$$

Now $\frac{\partial\omega_r}{\partial\theta_i}$is computed from Equation (3.17) such that:

$$\frac{\partial\omega_r}{\partial\theta_i} = \left(\frac{1}{2\omega_r}\right)\left(\frac{1}{\mathbf{v}_r^T\mathbf{M}\mathbf{v}_r}\right)\left(\mathbf{v}_r^T\frac{\partial\mathbf{K}}{\partial\theta_i}\mathbf{v}_r\right) \tag{3.19}$$

where $\frac{\partial\mathbf{K}}{\partial\theta_i}$ is computed by differentiating Equation (2.1) with respect to $\theta_i$ and is equal to the $i$th substructure stiffness $\mathbf{K}_{si}$. Note that the $r$th frequency derivative only requires the $r$th modal vector. However, the derivative of the $r$th modal vector requires the knowledge of other modal vectors. Assume that $\frac{\partial\mathbf{v}_r}{\partial\theta_i}$ can be expressed in a series of eigenvectors [107]:

$$\frac{\partial\mathbf{v}_r}{\partial\theta_i} = \sum_{j=1}^{N} C_{rij}\mathbf{v}_j \tag{3.20}$$

Substituting Equation (3.20) into Equation (3.18), we obtain the following equations:

$$\mathbf{v}_s^T\frac{\partial\mathbf{K}}{\partial\theta_i}\mathbf{v}_r + (\omega_s^2 - \omega_r^2)\mathbf{v}_s^T\mathbf{M}\left(\sum_{j=1}^{N} C_{rij}\mathbf{v}_j\right) = 0$$

$$\mathbf{v}_s^T\frac{\partial\mathbf{K}}{\partial\theta_i}\mathbf{v}_r + (\omega_s^2 - \omega_r^2)\mathbf{v}_s^T\mathbf{M}\mathbf{v}_s C_{ris} = 0$$

$$\rightsquigarrow C_{ris} = \left(\frac{1}{\omega_r^2 - \omega_s^2}\right)\left(\frac{1}{\mathbf{v}_s^T\mathbf{M}\mathbf{v}_s}\right)\left(\mathbf{v}_s^T\frac{\partial\mathbf{K}}{\partial\theta_i}\mathbf{v}_r\right) \quad \text{where } s \neq r \tag{3.21}$$

Substituting Equation (3.21) into Equation (3.20), we have

$$\frac{\partial \mathbf{v}_r}{\partial \theta_i} = \sum_{j=1}^{N} \left( \frac{1}{\omega_r^2 - \omega_j^2} \right) \left( \frac{1}{\mathbf{v}_j^T \mathbf{M} \mathbf{v}_j} \right) \left( \mathbf{v}_j^T \frac{\partial \mathbf{K}}{\partial \theta_i} \mathbf{v}_r \right) \mathbf{v}_j (1 - \delta_{rj}) \tag{3.22}$$

where

$$\delta_{rj} = \begin{cases} 1 & \text{if } r = j \\ 0 & \text{if } r \neq j \end{cases} \tag{3.23}$$

It has been shown that only a small number of terms are necessary in the summation of Equation (3.22) to obtain a reasonable accuracy [66].

## 3.4 Generation and Sensitivity of Ritz Vectors

### 3.4.1 Analytical Generation of Ritz Vectors

This subsection introduces a generation procedure of Ritz vectors [94,28]. Assume that the dynamic loading $\mathbf{F}(t)$ can be separated into a spatial vector $\mathbf{f}$ and a time function $u(t)$:

$$\mathbf{F}(t) = \mathbf{f}\, u(t) \tag{3.24}$$

Then, the first Ritz vector is a static deformation caused by the spatial distribution of the dynamic load vector $\mathbf{f}$:

$$\mathbf{K}\bar{\mathbf{r}}_1 = \mathbf{f} : \text{ solve for } \bar{\mathbf{r}}_1 \ (= \tilde{\mathbf{r}}_1) \tag{3.25}$$

the first Ritz vector is then mass-normalized as:

$$\mathbf{r}_1 = \frac{\tilde{\mathbf{r}}_1}{[\tilde{\mathbf{r}}_1^T \mathbf{M} \tilde{\mathbf{r}}_1]^{\frac{1}{2}}} \tag{3.26}$$

The following Ritz vectors are recursively generated. Assuming the mass matrix times the previous Ritz vector $\mathbf{M}\mathbf{r}_{p-1}$ as a load, the recurrence relationship computes the next Ritz vector $\bar{\mathbf{r}}_p$:

$$\mathbf{K}\bar{\mathbf{r}}_p = \mathbf{M}\mathbf{r}_{p-1} : \quad \text{solve for } \bar{\mathbf{r}}_p \tag{3.27}$$

The linear independence of Ritz vectors is achieved using the Gram-Schmidt orthogonalization. That is, the current Ritz vector is mass-orthogonalized with respect to all the previous Ritz vectors:

$$\tilde{\mathbf{r}}_p = \bar{\mathbf{r}}_p - \sum_{q=1}^{p-1} (\mathbf{r}_q^T \mathbf{M} \bar{\mathbf{r}}_p)\mathbf{r}_q \tag{3.28}$$

Finally, the current Ritz vector is mass-normalized:

$$\mathbf{r}_p = \frac{\tilde{\mathbf{r}}_p}{[\tilde{\mathbf{r}}_p^T \mathbf{M} \tilde{\mathbf{r}}_p]^{\frac{1}{2}}} \tag{3.29}$$

### 3.4.2 Sensitivity of Ritz Vectors

A procedure to compute the sensitivity of the $p$th Ritz vector with respect to the $i$th substructure stiffness $\frac{\partial \mathbf{r}_p}{\partial \theta_i}$ is now presented. The sensitivity of a Ritz vector is also formulated as a recurrence relationship. To compute the sensitivity of Ritz vectors, each Ritz vector is differentiated with respect to the non-dimensional damage parameter $\theta_i$. Taking the derivative on both sides of Equation (3.25) with respect to $\theta_i$ yields:

$$\frac{\partial \bar{\mathbf{r}}_1}{\partial \theta_i} = -\mathbf{K}^{-1} \frac{\partial \mathbf{K}}{\partial \theta_i} \bar{\mathbf{r}}_1 \tag{3.30}$$

where $\frac{\partial \mathbf{K}}{\partial \theta_i}$ is computed by differentiating Equation (2.1) with respect to $\theta_i$ and is equal to the $i$th substructure stiffness $\mathbf{K}_{si}$. Equation (3.26) is differentiated in a

similar manner to produce the sensitivity of the first Ritz vector:

$$\frac{\partial \mathbf{r}_1}{\partial \theta_i} = \frac{1}{[\tilde{\mathbf{r}}_1^T \mathbf{M} \tilde{\mathbf{r}}_1]^{\frac{1}{2}}} \frac{\partial \tilde{\mathbf{r}}_1}{\partial \theta_i} - \frac{[\tilde{\mathbf{r}}_1^T \mathbf{M} \frac{\partial \tilde{\mathbf{r}}_1}{\partial \theta_i}]}{[\tilde{\mathbf{r}}_1^T \mathbf{M} \tilde{\mathbf{r}}_1]} \mathbf{r}_1 \tag{3.31}$$

where, $\frac{\partial \tilde{\mathbf{r}}_1}{\partial \theta_i}$ is computed in Equation (3.30).

The sensitivities of the additional Ritz vectors ($\mathbf{r}_p : p \neq 1$) are computed in a similar manner by differentiating Equations (3.27), (3.28) and (3.29) with respect to $\theta_i$:

$$\frac{\partial \bar{\mathbf{r}}_p}{\partial \theta_i} = \mathbf{K}^{-1} \left[ -\frac{\partial \mathbf{K}}{\partial \theta_i} \bar{\mathbf{r}}_p + \mathbf{M} \frac{\partial \mathbf{r}_{p-1}}{\partial \theta_i} \right] \tag{3.32}$$

$$\frac{\partial \tilde{\mathbf{r}}_p}{\partial \theta_i} = \frac{\partial \bar{\mathbf{r}}_p}{\partial \theta_i} - \sum_{q=1}^{p-1} \left[ \left( \frac{\partial \mathbf{r}_q^T}{\partial \theta_i} \mathbf{M} \bar{\mathbf{r}}_p + \mathbf{r}_q^T \mathbf{M} \frac{\partial \bar{\mathbf{r}}_p}{\partial \theta_i} \right) \mathbf{r}_q + \left( \mathbf{r}_q^T \mathbf{M} \bar{\mathbf{r}}_p \right) \frac{\partial \mathbf{r}_q}{\partial \theta_i} \right] \tag{3.33}$$

$$\frac{\partial \mathbf{r}_p}{\partial \theta_i} = \frac{1}{[\tilde{\mathbf{r}}_p^T \mathbf{M} \tilde{\mathbf{r}}_p]^{\frac{1}{2}}} \frac{\partial \tilde{\mathbf{r}}_p}{\partial \theta_i} - \frac{[\tilde{\mathbf{r}}_p^T \mathbf{M} \frac{\partial \bar{\mathbf{r}}_p}{\partial \theta_i}]}{[\tilde{\mathbf{r}}_p^T \mathbf{M} \tilde{\mathbf{r}}_p]} \mathbf{r}_p \tag{3.34}$$

The derived sensitivity reveals how the sensitivity of a Ritz vector is related to that of the previous Ritz vectors. The validity of the derived sensitivities of Ritz vectors is demonstrated in Section 3.5.1.

## 3.5 Application to an Eight-Bay Truss Structure

This section demonstrates the potential applicability of Ritz vectors to damage detection of structures and the better sensitivity of Ritz vectors over modal vectors. The example structure is an eight-bay truss structure from the NASA dynamic scale model technology (DSMT) program of Langley Research Center [87]. As shown in Figure 3.1, the structure is fixed at one end. The structure is modeled using 104 truss elements, and consists of 36 nodes and 96 DOFs. Five truss members at the fixed

end are not included in the model. Furthermore, each truss member is assigned as a substructure. The numbering of substructures are shown in Figure 3.2.

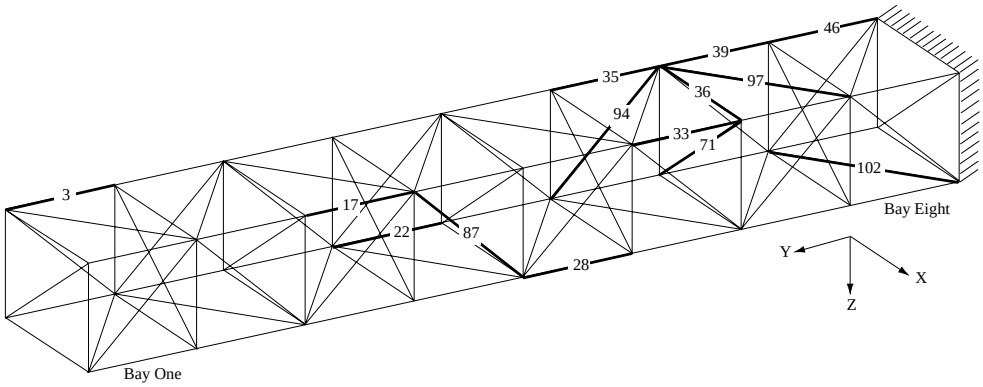


Figure 3.1: An eight-bay truss structure

Table 3.1 classifies the truss members into four different lacing patterns: longeron, batten, face diagonal and side diagonal. The truss members which belong to each lacing pattern are shown in Figure 3.3. A detailed description of the example structure can be found in Reference 87. This section is organized as follows: First, sensitivity analysis of Ritz vectors is conducted and the sensitivities of Ritz vectors are compared to those of modal vectors. Second, the damage detection of the eight-bay truss structure is conducted by changing damage locations and load patterns. Furthermore, the damage detection using Ritz vectors is compared to the damage detection using modal parameters.

Table 3.1: Classification of truss members into four lacing patterns

| | Longeron | Batten | | Face Diag | Side Diag | | | |
|---|---|---|---|---|---|---|---|---|
| Bay # | | X | Y | | Top | Bottom | Right | Left |
| 1 | 3,4,5,7 | 1,2 | 49,50 | 65 | 74 | 76 | 73 | 75 |
| 2 | 9,10,11,13 | 6,8 | 51,52 | 66 | 77 | 80 | 79 | 78 |
| 3 | 15,16,17,19 | 12,14 | 53,54 | 67 | 81 | 84 | 82 | 83 |
| 4 | 21,22,23,25 | 18,20 | 55,56 | 68 | 85 | 88 | 87 | 86 |
| 5 | 27,28,29,31 | 24,26 | 57,58 | 69 | 89 | 92 | 90 | 91 |
| 6 | 33,34,35,37 | 30,32 | 59,60 | 70 | 93 | 96 | 95 | 94 |
| 7 | 39,40,41,43 | 36,38 | 61,62 | 71 | 97 | 100 | 98 | 99 |
| 8 | 45,46,47,48 | 42,44 | 63,64 | 72 | 103 | 102 | 101 | 104 |

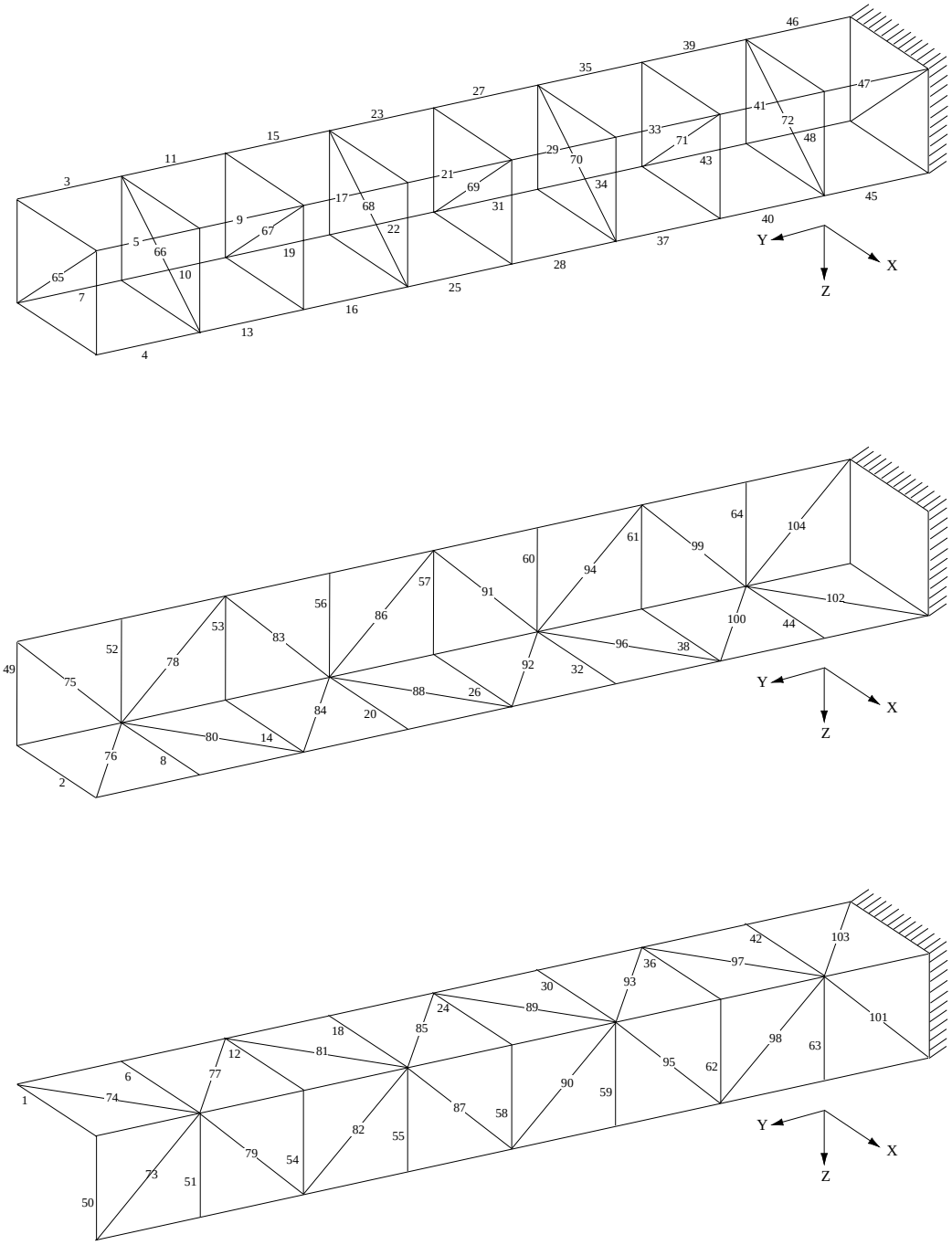


Figure 3.2: Substructures of an eight-bay truss structure

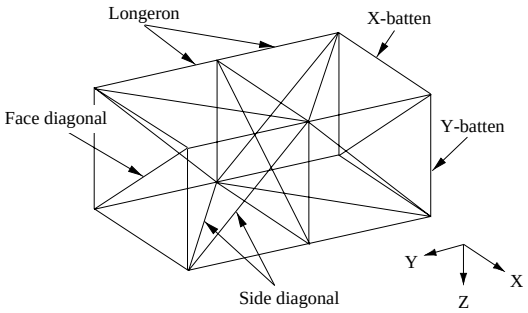


Figure 3.3: Lacing patterns of an eight-bay truss structure

### 3.5.1 Sensitivity Comparison of Ritz & Modal Vectors

In this subsection, a sensitivity analysis of Ritz vectors for the truss structure shown in Figure 3.1 is conducted. First, the validity of the Ritz vector sensitivity derived in Section 3.4 is evaluated. Then, the sensitivities of Ritz vectors are compared with those of modal vectors. In the sensitivity analysis, load pattern 1 shown in Figure 3.4 (a) is employed for the generation of Ritz vectors.


(a) Load Pattern 1 (b) Load Pattern 2

Figure 3.4: Load patterns applied to an eight-bay truss structure

The derived sensitivity is validated by comparing the analytical changes of Ritz vectors, which are computed using the derived sensitivity, with the actual changes of Ritz vectors. Figures 3.5 and 3.6 present selected results for comparison. In these figures, $\mathbf{r}_j^h$ and $\mathbf{r}_j^d$ represent the $j$th Ritz vector before and after the stiffness changes, respectively. Imposing load pattern 1 on the healthy structure, the first five successive Ritz vectors are generated from the procedures described in Equations (3.25) $\sim$ (3.29). After decreasing the stiffness of each member by 1%, the actual changes of the Ritz vectors from the healthy state are computed to arrive at $\mathbf{r}_j^h - \mathbf{r}_j^d$. The corresponding analytical changes of the Ritz vectors are computed as $(\frac{\partial \mathbf{r}_j}{\partial \theta_i})\Delta\theta_i$. Here $(\frac{\partial \mathbf{r}_j}{\partial \theta_i})$ is the derived sensitivity from Equations (3.31) $\sim$ (3.34) and $\Delta\theta_i$ is set to 0.01. As shown in

Figures 3.5 and 3.6, the analytical changes of the Ritz vectors are in good agreement with the actual changes of the Ritz vectors.

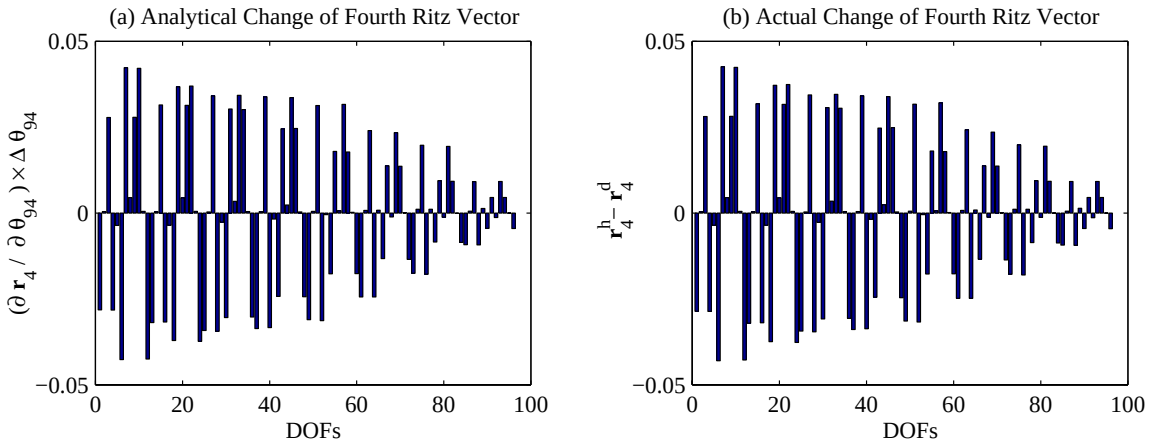


Figure 3.5: Change of the fourth Ritz vector caused by 1% decrease of the 94th member stiffness

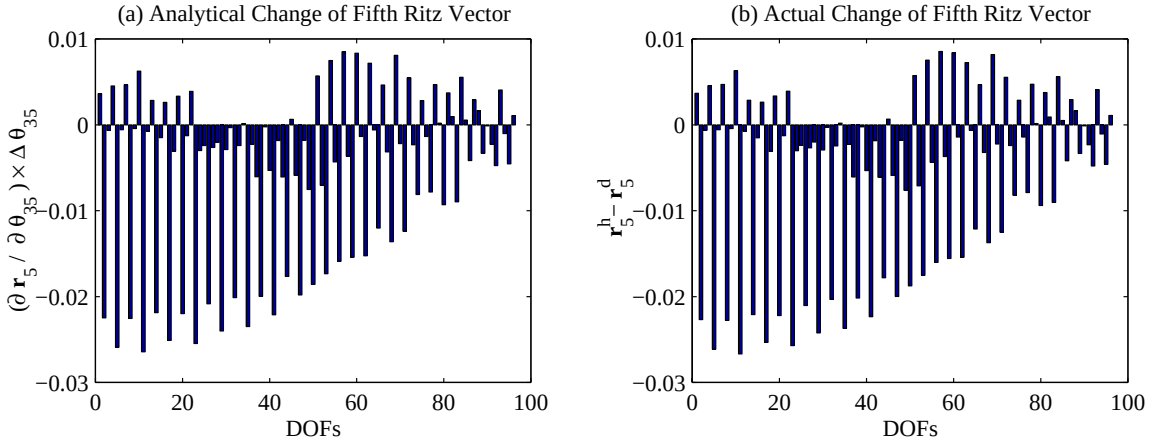


Figure 3.6: Change of the fifth Ritz vector caused by 1% decrease of the 35th member stiffness

Next, the sensitivities of Ritz vectors are compared to the sensitivities of modal vectors. The comparison of the first five Ritz and modal vectors as shown in Figure 3.7 reveals that the Ritz vectors, particularly the higher Ritz vectors, produce more complicated deformed shapes. This implies intuitively that Ritz vectors might be more sensitive to the stiffness changes of substructures. This observation can be justified by a detailed sensitivity analysis. The sensitivity analysis is conducted by

comparing the changes of the Ritz and modal vectors as the stiffness of each substructure (member) deteriorates. Selected results from the comparisons are presented in Figures 3.8, 3.9 and 3.10. Figure 3.8 (a) shows how the first five Ritz vectors change as the stiffness loss of the 33rd member (a longeron in bay six) varies from 0% to 100%. For a simple graphical representation, the ratio of $\|\mathbf{r}_r^h - \mathbf{r}_r^d\|$ to $\|\mathbf{r}_r^h\|$ is computed to indicate the change of a Ritz vector as damage progresses in the 33th member. Here, $\|\cdot\|$ denotes the Euclidean norm and $\mathbf{r}^h$ and $\mathbf{r}^d$ denote the Ritz vectors before and after damage occurs, respectively. Figure 3.8 (b) shows similar quantities for the first five modal vectors, where $\mathbf{v}^h$ and $\mathbf{v}^d$ present the modal vectors before and after stiffness changes, respectively. The shaded portion of the plot indicates that if each component of a modal vector has a 5% uncertainty, no measurable change in any modal vector are apparent unless the stiffness loss exceeds 75%. On the other hand, 10% change of stiffness results in perceivable changes in the second and third Ritz vectors in the presence of a 5% uncertainty.

As a second example, Figure 3.9 presents the sensitivity comparison for the stiffness change of the 94th member (a side diagonal in bay six). While the fourth and fifth Ritz vectors are very sensitive to the stiffness change of the 94th member, the change of modal vectors is not apparent until the stiffness loss reaches about 40%. Figure 3.10 shows that the stiffness change of the face diagonal member 71 does not change the first five modal vectors at all and causes very little change in the Ritz vectors. Similar insensitivity is observed for all face diagonal members. This insensitivity of face diagonal members to Ritz/modal vectors is largely due to the redundancy of the example truss structure.

Based on the sensitivity analysis conducted here, several observations can be made: (1) In many cases, stiffness changes in the model lead to larger changes in the Ritz vectors than in the modal vectors, (2) face diagonals do not cause significant changes to either the Ritz or modal vectors, and (3) in many cases, Ritz and modal vectors are more sensitive to the stiffness losses of side diagonals and longerons than those of battens. The sensitivity analysis presented here allows one to determine detectable damage amount for each substructure before the actual damage detection. Detectable damage should cause significant changes of Ritz vectors greater than what can be

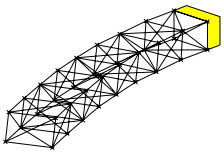

First Ritz Vector

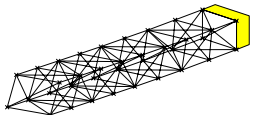

First Modal Vector

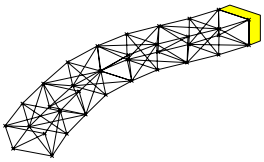

Second Ritz Vector

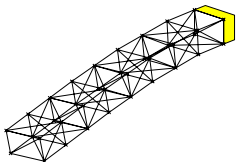

Second Modal Vector

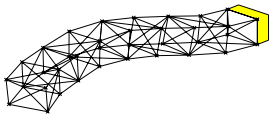

Third Ritz Vector

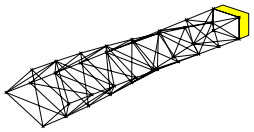

Third Modal Vector

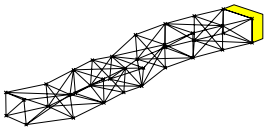

Fourth Ritz Vector

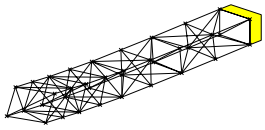

Fourth Modal Vector

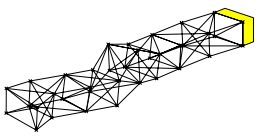

Fifth Ritz Vector

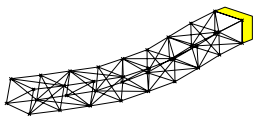

Fifth Modal Vector

Figure 3.7: Comparison of Ritz vectors and modal vectors of an eight-bay truss structure

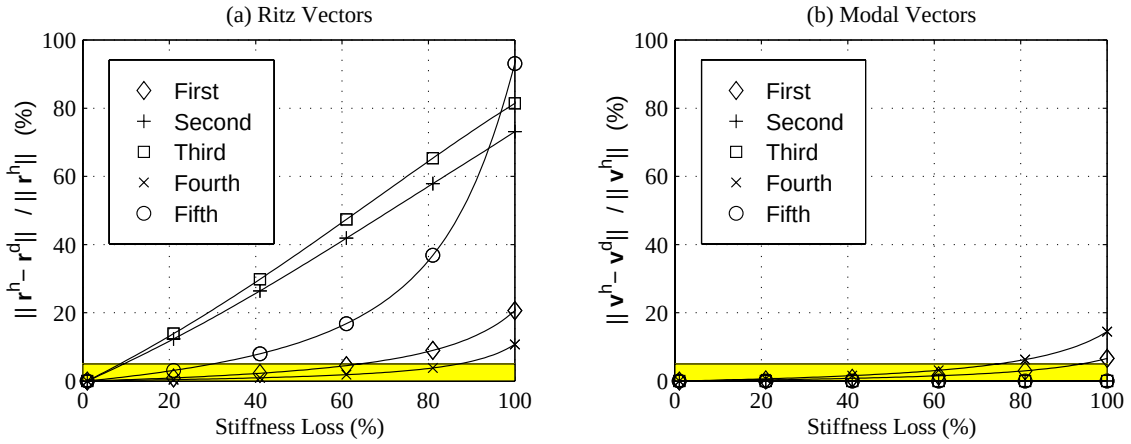


Figure 3.8: Sensitivity comparison of Ritz and modal vectors for progressive damage in Member 33

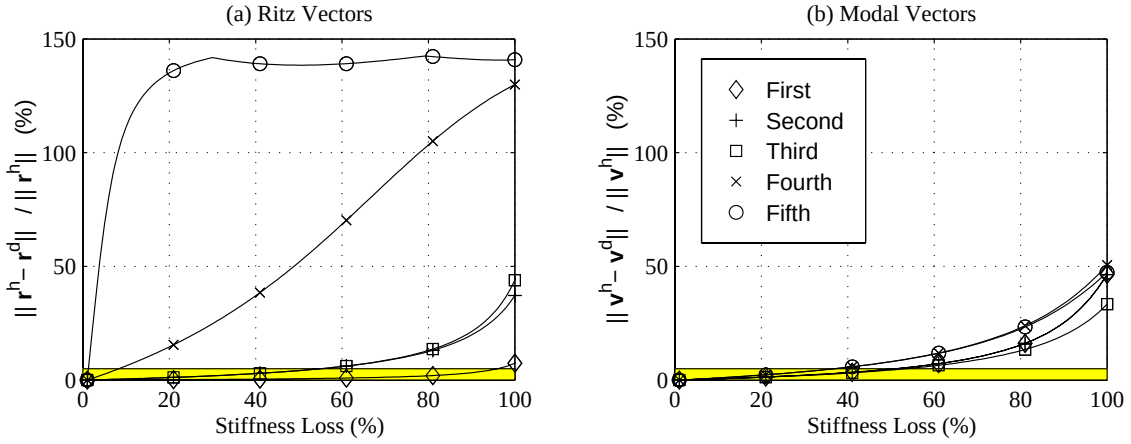


Figure 3.9: Sensitivity comparison of Ritz and modal vectors for progressive damage in Member 94

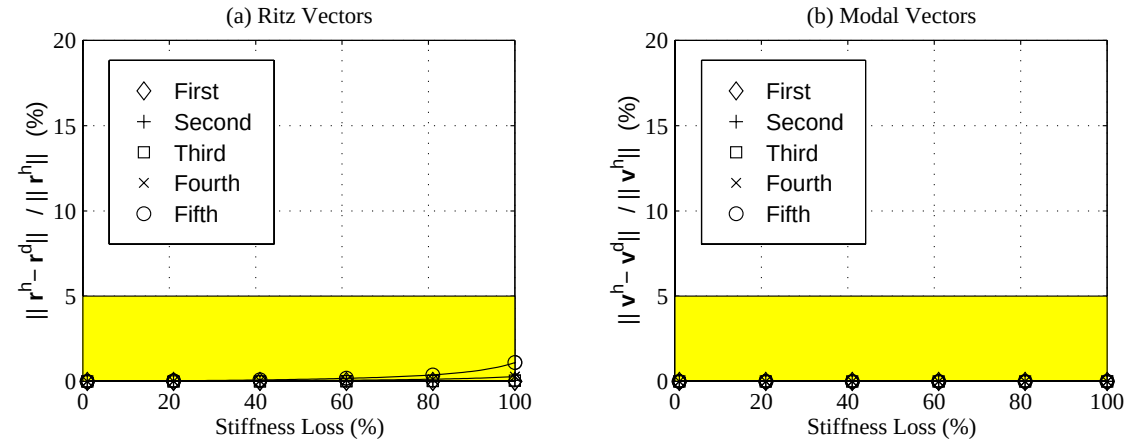


Figure 3.10: Sensitivity comparison of Ritz and modal vectors for progressive damage in Member 71

attributed to measurement uncertainties, modeling error or environmental effects.

### 3.5.2 Comparison of Ritz & Modal Vectors for Damage Diagnosis

This subsection presents the diagnostic results of an eight-bay truss structure conducted under different damage scenarios. For all examples, a uniform prior probability is assigned to all hypotheses. Therefore, the determination of the most probable hypothesis in Equation (2.25) depends only on the error function $J(\hat{\Psi}_{N_s}, \Theta_{H_j}^{max})$. The search space $\Theta_{H_j} < \Omega_{H_j}^*$ in Equation (2.7) is evaluated at the intersection of grid lines which discretize the search domain with an increment of $\Delta\theta$. For all numerical examples, we use an incremental step $\Delta\theta = 0.1$. The branch-and-bound search in the presented examples follows a depth-first/best-first search strategy. Instead of the largest posterior probability $P_{max}$, the third largest posterior probability $P_{max}^3$ ($< P_{max}^2 < P_{max}^1 = P_{max}$) is employed in Equation (2.27) for the branch-and-bound search to investigate a larger subspace of the hypothesis space. Furthermore, the extension of the branch-and-bound search is limited such that a maximum of three substructures can be examined.

Each Ritz vector is normalized with respect to a reference point. The DOF which has the absolute maximum magnitude in each Ritz vector of the healthy structure, is assigned as a reference point. All the other DOFs are normalized with respect to this reference point. Since one component is used for normalization, only $N_r - 1$ pieces of information exist for each Ritz vector. To simulate measurement uncertainties in the estimated Ritz vectors, the exact Ritz vectors obtained from Equations (3.25) to (3.29) are perturbed with noise. More explicitly, the estimated Ritz vector set $\hat{\psi}(n)$ in Equation (2.3) is constructed such that:

$$\hat{\psi}(n) = \psi \, (1 + \frac{\mathcal{N}}{100} \, \mathcal{R}) \tag{3.35}$$

where $\psi$ is the exact Ritz vector set obtained from the analytical model, $\mathcal{N}$ is a specified percentage of noise level, and $\mathcal{R}$ is a normally distributed random number

with zero mean and a variance of 1.0. This process is repeated $N_s$ times to simulate the $N_s$ data sets.

Excitation is assumed to be a swept sine excitation generated from electrodynamics or hydraulic shakers [45]. All actuators are assumed to generate forces with the same magnitude and phase. According to Equation (3.24), the spatial distribution of forces is defined by a vector $\mathbf{f}$ and an identical input excitation is given to all actuators by a scalar function $u(t)$. The spatial vector $\mathbf{f}$ is assumed not to vary with time. Load patterns are selected to maximize the sensitivities of the first five Ritz vectors over all substructures. However, a systematic scheme for the selection of load patterns is not provided in this study. For all examples, $L_{dam}$ and $D_{dam}$ denote the actual damage locations and the associated damage amount, respectively. $\hat{L}_{dam}$ and $\hat{D}_{dam}$ denote the most probable damage locations and the associated damage amount estimated by the proposed method. In addition, the measured DOFs and the estimated modes are denoted by DOFm and MODEm, respectively. First, twelve damage cases with a single damage location are investigated using a uniform damage threshold for every substructure. Then, fourteen damage cases, including the previous twelve damage cases, are re-diagnosed using different damage threshold values for substructures. Finally, six damage cases with either two or three damaged substructures are examined.

### Diagnosis Using Uniform Damage Thresholds

Twelve different damage cases are investigated employing Ritz vectors and the proposed weighting scheme. For the purpose of comparison, the same damage cases are re-diagnosed using Ritz vectors but without the weighting scheme. Furthermore, the diagnosis results using modal vectors are presented. Sensitivity analysis which is similar to Figures 3.8, 3.9 and 3.10, are conducted for load patterns 1 and 2 to compute a minimum detectable damage. The *minimum detectable damage* of each substructure is defined as the minimum damage amount for which the estimated Ritz vectors from a given load pattern can detect when each component of a Ritz vector is contaminated by a certain level of noise. The minimum detectable damage of each substructure is presented in Table 3.2 assuming that, because of noise, each component of a Ritz vector is perturbed by 5% of its magnitude.

Table 3.2: Minimum detectable damage amount of each substructure for a given load pattern

| | Bay # | Sub. # | Load Pattern | | | Modal | Sub. # | Load Pattern | | | Modal |
|---|---|---|---|---|---|---|---|---|---|---|---|
| | | | (1) | (2) | (3) | Vector | | (1) | (2) | (3) | Vector |
| Longeron | 1 | 3 | 50% | 10% | 90% | 80% | 5 | 70% | - | 40% | 100% |
| | | 4 | 50% | 20% | 70% | 80% | 7 | 70% | - | 90% | 100% |
| | 2 | 9 | 10% | 20% | 60% | 60% | 11 | 40% | 10% | 90% | 80% |
| | | 10 | 10% | 20% | 60% | 60% | 13 | 40% | 20% | 70% | 80% |
| | 3 | 15 | 30% | 10% | 40% | 50% | 17 | 10% | 20% | 60% | 60% |
| | | 16 | 30% | 10% | 30% | 50% | 19 | 10% | 20% | 50% | 60% |
| | 4 | 21 | 10% | 10% | 20% | 60% | 23 | 20% | 10% | 40% | 50% |
| | | 22 | 20% | 10% | 20% | 60% | 25 | 20% | 10% | 30% | 50% |
| | 5 | 27 | 10% | 10% | 10% | 60% | 29 | 10% | 10% | 20% | 50% |
| | | 28 | 10% | 10% | 10% | 50% | 31 | 20% | 10% | 20% | 50% |
| | 6 | 33 | 10% | 10% | 10% | 80% | 35 | 10% | 10% | 10% | 50% |
| | | 34 | 10% | 10% | 10% | 80% | 37 | 10% | 10% | 10% | 50% |
| | 7 | 39 | 10% | 10% | 10% | 80% | 41 | 10% | 10% | 10% | 80% |
| | | 40 | 10% | 10% | 10% | 70% | 43 | 10% | 10% | 10% | 80% |
| | 8 | 45 | 10% | 10% | 10% | 70% | 47 | 10% | 10% | 10% | 60% |
| | | 46 | 10% | 10% | 10% | 70% | 48 | 10% | 10% | 10% | 60% |
| Batten | 1 | 1 | 40% | 20% | 90% | 100% | 49 | 40% | 10% | 90% | 100% |
| | | 2 | 10% | 10% | 80% | 100% | 50 | 40% | 10% | 60% | 100% |
| | 2 | 6 | 30% | 60% | - | - | 51 | 40% | 50% | 90% | - |
| | | 8 | 40% | 60% | - | - | 52 | 60% | 50% | - | - |
| | 3 | 12 | 30% | 100% | 100% | - | 53 | 80% | 90% | 100% | - |
| | | 14 | 30% | 100% | 100% | - | 54 | 70% | 90% | 90% | - |
| | 4 | 18 | 30% | 70% | 100% | - | 55 | 70% | 60% | - | - |
| | | 20 | 40% | 70% | 100% | - | 56 | 60% | 70% | 100% | - |
| | 5 | 24 | 50% | 30% | - | - | 57 | 10% | 20% | 100% | - |
| | | 26 | 40% | 30% | - | - | 58 | 40% | 30% | 100% | - |
| | 6 | 30 | 50% | 80% | 10% | 100% | 59 | 60% | 70% | - | 100% |
| | | 32 | 60% | 80% | 90% | 100% | 60 | 60% | 70% | 10% | 100% |
| | 7 | 36 | 70% | 80% | 10% | - | 61 | 80% | 90% | 10% | - |
| | | 38 | 70% | 80% | 90% | - | 62 | 80% | 90% | 10% | - |
| | 8 | 42 | 90% | 100% | 70% | - | 63 | 90% | 90% | 80% | - |
| | | 44 | 90% | 100% | 60% | - | 64 | 90% | 90% | 70% | - |
| Side Diagonal | 1 | 73 | 10% | 10% | 40% | 70% | 75 | 10% | 10% | 90% | 70% |
| | | 74 | 10% | 10% | 80% | 70% | 76 | 10% | 10% | 70% | 70% |
| | 2 | 77 | 10% | 10% | 80% | 60% | 79 | 10% | 10% | 60% | 60% |
| | | 78 | 10% | 10% | 70% | 60% | 80 | 10% | 10% | 70% | 60% |
| | 3 | 81 | 10% | 10% | 70% | 60% | 83 | 10% | 10% | 70% | 60% |
| | | 82 | 10% | 10% | 70% | 60% | 84 | 10% | 10% | 60% | 60% |
| | 4 | 85 | 10% | 10% | 70% | 60% | 87 | 10% | 10% | 70% | 60% |
| | | 86 | 10% | 10% | 60% | 60% | 88 | 10% | 10% | 60% | 60% |
| | 5 | 89 | 10% | 10% | 60% | 60% | 91 | 10% | 10% | 60% | 60% |
| | | 90 | 10% | 10% | 60% | 60% | 92 | 10% | 10% | 60% | 60% |
| | 6 | 93 | 10% | 10% | 50% | 40% | 95 | 10% | 10% | 50% | 40% |
| | | 94 | 10% | 10% | 60% | 40% | 96 | 10% | 10% | 50% | 40% |
| | 7 | 97 | 10% | 10% | 40% | 20% | 99 | 10% | 10% | 50% | 20% |
| | | 98 | 10% | 10% | 40% | 20% | 100 | 10% | 10% | 40% | 20% |
| | 8 | 101 | 10% | 10% | 30% | 20% | 103 | 10% | 10% | 40% | 20% |
| | | 102 | 10% | 10% | 20% | 20% | 104 | 10% | 10% | 30% | 20% |
| Face Diag | 1,2 | 65 | 80% | 20% | 30% | - | 66 | - | 90% | 30% | - |
| | 3,4 | 67 | - | - | 30% | - | 68 | - | 100% | 30% | - |
| | 5,6 | 69 | 80% | 30% | 30% | - | 70 | - | 100% | 30% | - |
| | 7,8 | 71 | - | - | 30% | - | 72 | - | - | 40% | - |

"-" denotes that damage is undetectable.

Table 3.2 shows that a stiffness loss larger than 10% is detectable from load patterns 1 and 2 for most side diagonals and longerons. Battens undergo a 10%∼100% loss of stiffness before the changes of Ritz vectors become observable. However, the stiffness changes of most face diagonals are undetectable from both load patterns. Based on this preliminary sensitivity analysis, the detection of 10% stiffness loss in most face diagonals and battens seems difficult from the assumed load patterns. Therefore, the face diagonals and battens are precluded from the branch-and-bound search in the examples presented here.[1] That is, only longerons and side diagonals are investigated for potential damage. For comparison, the minimum detectable damage amount from modal vectors is also presented in Table 3.2. Again, the better sensitivity of Ritz vectors is clearly shown in Table 3.2. For load pattern 3, 16 actuators are assumed to be placed at both ends of all face diagonals to produce tensile forces in the face diagonals. This load pattern is presented here just to show that this load pattern can make the face diagonals more detectable (larger than 30% stiffness loss is detectable from the Ritz vectors generated from load pattern 3). However, since this loading is not realistic, only the first two load patterns are employed for damage detection.

Twelve damage cases with a single damaged substructure are simulated by assuming a 10% stiffness loss, a 5% noise level and one data set ($N_s$=1). The damaged substructures used in the examples are shown in Figure 3.1 by solid lines. Furthermore, all DOFs are assumed to be measured and a value of 0.9 is used for the damage threshold $\theta^*$ of each substructure. The damage locations are identical to some of the damage cases which are experimentally tested in Reference 87. It should be noted that while the damage cases in Reference 87 refer to the total removal of a truss member, only a 10% stiffness loss is considered in this study. Table 3.3 shows the diagnosis results of the twelve damage cases using load pattern 2. For all damage cases, the most probable damage event computed by the proposed method includes the actually damaged substructure. In some cases, however, undamaged substructures are also included in the most probable damage event. For example, the 7th

[1] The pruning heuristics of the branch-and-bound search scheme are presented in Section 2.2.

Table 3.3: Damage diagnoses of an eight-bay truss structure using a uniform threshold

| | Actual Damage | | | Most Probable Damage | |
|---|---|---|---|---|---|
| Case[1] | $L_{dam}$ | $D_{dam}$ | Rank[2] | $\hat{L}_{dam}$ | $\hat{D}_{dam}$ |
| A | {46} | {10%} | 3/313 | {7,46} | {80%,10%} |
| B | {102} | {10%} | 1/251 | {102} | {10%} |
| C | {39} | {10%} | 3/313 | {7,39} | {80%,10%} |
| D | {97} | {10%} | 3/313 | {5,97} | {80%,10%} |
| G | {33} | {10%} | 2/313 | {5,33} | {30%,10%} |
| H | {35} | {10%} | 3/313 | {5,35} | {80%,10%} |
| I | {94} | {10%} | 3/313 | {5,94} | {70%,10%} |
| J | {28} | {10%} | 3/313 | {5,28} | {80%,10%} |
| K | {87} | {10%} | 1/251 | {87} | {10%} |
| L | {22} | {10%} | 3/313 | {5,22} | {80%,10%} |
| M | {17} | {10%} | 3/313 | {5,17} | {70%,10%} |
| N | {3} | {10%} | 3/313 | {3,5} | {10%,70%} |

1. Damage locations are defined identical to ones presented in Reference 87.
2. The first number is the rank of the actual damage event and the second is the total number of the examined hypotheses.
3. The first five Ritz vectors are estimated from load pattern 2.
4. $N_s$=1, Noise=5%, and all DOFs are measured.

substructure is included as a potentially damaged substructure in case A. Table 3.2 shows that the Ritz vectors employed in this diagnosis set (the Ritz vectors generated from load pattern 2) are insensitive to the stiffness changes of the 7th substructure. Therefore, a small stiffness change of the 7th substructure may not result in a noticeable change of the error function value in Equation (2.22) or actually can reduce the error function value when Ritz vectors are noise contaminated. For similar reasons, the 5th substructure is also included in the most probable damage event for other damage cases.

Table 3.4: Comparison of diagnosis results using Ritz or modal vectors

| | Actual Damage | | Rank[4] | | |
|---|---|---|---|---|---|
| Case | $L_{dam}$ | $D_{dam}$ | Scheme 1[1] | Scheme 2[2] | Scheme 3[3] |
| A | {46} | {10%} | 3/313 | 3/313 | 350/434 |
| B | {102} | {10%} | 1/251 | 4/374 | 30/434 |
| C | {39} | {10%} | 3/313 | 6/313 | 350/434 |
| D | {97} | {10%} | 3/313 | 3/313 | 55/434 |
| G | {33} | {10%} | 2/313 | 3/313 | 372/434 |
| H | {35} | {10%} | 3/313 | 3/313 | 219/434 |
| I | {94} | {10%} | 3/313 | 3/313 | 356/434 |
| J | {28} | {10%} | 3/313 | 7/374 | 382/434 |
| K | {87} | {10%} | 1/251 | 3/313 | 405/434 |
| L | {22} | {10%} | 3/313 | 4/374 | 320/434 |
| M | {17} | {10%} | 3/313 | 3/252 | 428/494 |
| N | {3} | {10%} | 3/313 | 3/313 | 213/494 |

1. The first five Ritz vectors are estimated from load pattern 2 and the proposed weighting scheme is employed.
2. Same as Scheme 1 except that the weighting scheme is not used.
3. The first five modal vectors are employed instead of Ritz vectors.
4. The first number is the rank of the actual damage event and the second is the total number of the examined hypotheses.
5. $N_s$=1, Noise=5%, and all DOFs are measured.
6. Only longeron and side diagonal members are examined for damage.

To validate the use of Ritz vectors and the proposed weighting scheme, the twelve damage cases are re-diagnosed using modal vectors or without the weighting scheme in Table 3.4. All other conditions remain the same as for the previous example. The rank of the actual damage event is shown in columns $4 \sim 6$ of Table 3.4. Scheme 1

uses the first five Ritz vectors and the proposed weighting, scheme 2 uses the same Ritz vectors without the weighting scheme. The first five modal vectors are employed in scheme 3 instead of the Ritz vectors. Table 3.4 shows that scheme 1 provides the best diagnoses among the three schemes. Comparing schemes 1 and 2, we observe that the weighting in scheme 1 slightly improves the diagnoses. Scheme 3 using modal vectors fails to detect most damage cases. These results show the superiority of Ritz vectors to modal vectors for damage detection.

### Diagnosis Using Different Damage Thresholds

In this example, fourteen damage cases (including the previous twelve cases) are diagnosed using a different threshold value for each substructure. The other conditions are unchanged (Noise=5%, $N_s$=1 and all DOFs are measured). We prevent unnecessary extensions of the proposed branch-and-bound search by employing preliminary sensitivity analysis. The branch-and-bound search is conducted including only substructures with damage larger or equal to the pre-assigned minimum detectable damage.

Table 3.2 and the previous diagnoses show that Ritz vectors have different sensitivities for different substructures. This observation motivates the use of a different threshold for each substructure. The damage thresholds in this subsection are assigned based on the minimum detectable damage computed in Table 3.2. For example, since the minimum detectable damage amount assigned to the first substructure is 20% (when load pattern 2 is employed), the corresponding damage threshold is set to 0.8 $(1 - 0.2)$. The damage thresholds for other substructures are determined in the same fashion. It should be noted that when the total removal of a substructure does not cause a perceivable change in Ritz vectors, the substructure is defined as undetectable and excluded from the diagnosis. For example, the 67th member is defined as undetectable since the total removal of the member (100% stiffness loss) does not yield significant changes in Ritz vectors beyond the assumed variation caused by uncertainties. Therefore, the 67th member is excluded from the diagnosis.

Table 3.5 shows that the redefined damage threshold improves the diagnoses. Comparing the most probable events (hypothesis) of case A in Tables 3.3 and 3.5, one

Table 3.5: Damage diagnoses of an eight-bay truss structure using different threshold values

| | Actual Damage | | | Most Prob. Damage | |
|---|---|---|---|---|---|
| Case | $L_{dam}$ | $D_{dam}$ | Rank[1] | $\hat{L}_{dam}$ | $\hat{D}_{dam}$ |
| A | {46} | {10%} | 1/371 | {46} | {10%} |
| B | {102} | {10%} | 1/552 | {102} | {10%} |
| C | {39} | {10%} | 1/371 | {39} | {10%} |
| D | {97} | {10%} | 1/461 | {97} | {10%} |
| E | {36} | {10%} | 17/95 | no damage | |
| F | {71} | {10%} | -/95 | no namage | |
| G | {33} | {10%} | 1/371 | {33} | {10%} |
| H | {35} | {10%} | 1/461 | {35} | {10%} |
| I | {94} | {10%} | 1/462 | {94} | {10%} |
| J | {28} | {10%} | 1/371 | {28} | {10%} |
| K | {87} | {10%} | 1/371 | {87} | {10%} |
| L | {22} | {10%} | 1/461 | {22} | {10%} |
| M | {17} | {10%} | 9/95 | no damage | |
| N | {3} | {10%} | 1/461 | {3} | {10%} |

1. The first number is the rank of the actual damage event and the second is the total number of the examined hypotheses. "-" denotes that actual damage is not detected.
2. The first five Ritz vectors are estimated from load pattern 2 and the proposed weighting scheme is employed.
3. $N_s$=1, Noise=5%, and all DOFs are measured.
4. Different damage threshold value is assigned to each substructure.

can observe that the undamaged 7th substructure is removed from the most probable hypothesis, making the actual damage case the most probable one. In case E, the proposed method indicates that most likely there is no damage. Considering the fact that the damage threshold of the 36th substructure is set to 0.2, the 10% stiffness loss in the 36th substructure is not detectable. The proposed method ranks the 36th substructure as the 17th most probable damage location with 80% damage. Similar results are observed for cases F and M. Sensitivity analysis in Table 3.2 shows that the stiffness deterioration of the 71st substructure, which is a face diagonal in the 7th bay, does not yield any noticeable changes to the estimated Ritz vectors. Therefore the 71st substructure is precluded from the diagnosis and the proposed method provides a false-negative indication of damage. For case M, the damage threshold of the 17th substructure is set to 0.8. Again the proposed method indicates that most likely there is no damage and ranks the event of 20% damage in the 17th substructure as the 9th most probable damage case.

**Diagnosis of Damage in Multiple Locations**

In this example, we focus on the detection of damage in multiple locations. Table 3.6 presents diagnosis results of six different damage cases. In cases O $\sim$ R, 10% stiffness decrease is simulated in two substructures. Cases S and T present damage cases with three damaged substructures. The six damage cases are repeatedly diagnosed under different conditions. In the fourth column of Table 3.6, the first five Ritz vectors are generated from load pattern 1 and employed for damage detection along with the proposed weighting scheme. In the fifth column, load pattern 2 is employed instead of load pattern 1. In the last column of the table, a total of ten Ritz vectors are generated from load patterns 1 and 2 (the first five Ritz vectors are generated from each load pattern). For all cases in Table 3.6, all DOFs are measured and one set of Ritz vectors is simulated assuming a 5% noise level ($N_s$=1 and Noise=5%). Furthermore, the proposed weighting scheme is employed.

When the first five Ritz vectors are generated from load pattern 1, the proposed method identifies the actual damage event of cases O, P, Q and T. However, the actual damage locations are not detected for cases R and S. While the use of load

pattern 2 yields the detection of actual damage locations in cases P, Q and R, load pattern 2 fails to identify damage of cases O, S and T. Finally, when a total of ten Ritz vectors are generated from load patterns 1 and 2, the proposed method identifies the actual damage locations for all cases (cases O $\sim$ T). It is shown that each damage case has different sensitivity to different load patterns and by including more Ritz vectors from different load patterns, diagnosis results can be improved.

Table 3.6: Damage diagnoses of an eight-bay truss structure with multiple damage locations

| | Actual Damage | | Rank[4] | | |
|---|---|---|---|---|---|
| Case | $L_{dam}$ | $D_{dam}$ | F1[1] | F2[2] | F1, F2[3] |
| O | {35,94} | {10%,10%} | 1/672 | -/371 | 1/686 |
| P | {39,46} | {10%,10%} | 1/483 | 1/644 | 1/686 |
| Q | {28,102} | {10%,10%} | 1/861 | 2/914 | 1/974 |
| R | {39,87} | {10%,10%} | -/672 | 1/644 | 1/679 |
| S | {22,35,97} | {10%,10%,10%} | -/672 | -/644 | 1/686 |
| T | {17,35,97} | {10%,10%,10%} | 1/577 | -/554 | 1/986 |

1. The first five Ritz vectors are estimated from load pattern 1.
2. The first five Ritz vectors are estimated from load pattern 2.
3. Load Patterns 1 and 2 are employed and the first five Ritz vectors are estimated from each load pattern (i.e. a total of ten Ritz vectors).
4. The first number is the rank of the actual damage event and the second is the total number of the examined hypotheses. "-" denotes that actual damage is not detected.
5. $N_s$=1, Noise=5%, all DOFs are measured and the proposed weighting scheme is employed.
6. Different damage threshold value is assigned to each substructure.

## 3.6 Summary and Discussions

In this chapter, load-dependent Ritz vectors are employed in the Bayesian probabilistic framework to detect the locations and amount of damage. Several damage scenarios using an eight-bay truss structure illustrate the potential use of load-dependent Ritz vectors for damage detection. Sensitivity analyses show that the derived derivative of a load-dependent Ritz vector with respect to a substructure stiffness is a good approximation of the actual sensitivity and the sensitivity analyses allow us to identify detectable substructures before actual diagnoses. It is shown that most face

diagonals and battens of the eight-bay truss structure are secondary members, making the truss structure a highly redundant system. Diagnosis examples of the truss and frame structures show that, (1) load-dependent Ritz vectors are able to identify the actual damage locations for most damage cases when the estimated Ritz vectors are contaminated by low level noise, only one set of Ritz vectors are estimated, and a small amount of stiffness deterioration is assumed, (2) by a careful selection of load patterns, substructures of interest can be made more observable using the Ritz vectors generated from the particular load patterns, (3) the proposed weighting scheme, which weights Ritz vectors according to their sensitivity to the assumed damage locations, improves the diagnosis results, and (4) if load patterns are selected carefully and a large number of data set are available, the proposed method can identify most of the damage locations, even in the presence of modeling error and measurement noise.

Derivatives of load-dependent Ritz vectors with respect to substructure stiffnesses are derived and employed to weight the load-dependent Ritz vectors which are more sensitive to the assumed damage locations. A minimum detectable damage of each substructure is defined as the minimum damage amount which the estimated Ritz vectors from a given load pattern can detect when each component of a Ritz vector is contaminated by a certain level of noise. Furthermore, the damage threshold is assigned according to the minimum detectable damage. By assigning a different damage threshold to each substructure, a substructure which causes small changes to the estimated Ritz vectors needs to undergo large stiffness deterioration before the substructure can be detected as damaged and the very insensitive substructures are precluded from a branch-and-bound search. The computational cost of the proposed method is significantly reduced by using a branch-and-bound search scheme and the modeling simplification technique.

While this chapter has illustrated the potential applicability of load-dependent Ritz vectors to damage detection, many interesting research issues remain. First, even though a procedure to experimentally extract load-dependent Ritz vectors is proposed [28] and the effect of noise on the estimated load- dependent Ritz vectors is studied [154], real testing should be conducted to validate the experimental procedure.

This issue will be examined in Section 6.2, where experimental results are employed to validate the possibility of extracting Ritz vectors. Second, the physical issue of the actuator placement should be addressed to make the extraction of load-dependent Ritz vectors practical. In this chapter, we assume that the amplitudes and phases among actuators can be fully controlled and the power requirement to generate the desired excitation forces is not addressed. Third, it is worth while to develop a systematic scheme to find load patterns, which yield better detection of damage in substructures of interest. While it is shown that a careful selection of load patterns can make the substructures of interest more observable, a systematic selection scheme for the load patterns has not been addressed in this study.

Note that while normal modal vectors are characterized only by a system itself (the stiffness and mass matrices of a structure), load-dependent Ritz vectors are a function of the spatial distribution of loading as well as the system. Therefore, it appears that by imposing an excitation in a particular way, substructures of interest or vulnerable to damage might be made more observable using the load-dependent Ritz vectors from the specific loading. While the first load-dependent Ritz vector is simply a static deformation of a structure cause by a particular load, a higher load-dependent Ritz vector is orthogonalized with respect to the previous Ritz vectors during the generation procedure, and the relationship between a load pattern and a higher Ritz vector may become obscure. This fact makes the load pattern selection scheme difficult.

# Chapter 4

# Model Updating and Refinement

This chapter addresses the issues of updating an analytical model by employing data from a vibration test of a structure. Model refinement or updating is required to validate an analytical model of structures, to accurately predict dynamic responses and to diagnose damages within a structure. For these purposes, highly accurate analytical models of structures are necessary. The system property matrices can be adjusted to produce more reliable system matrices using experimental test data. The purpose of model refinement in this study is to obtain a modified baseline model which improves the correlation of such model to the structure. Then, the updated model is employed as a baseline model for damage detection. This chapter is organized as follows: Section 4.1 reviews the existing updating methods. Section 4.2 describes the modification of an existing updating scheme for the cases when multiple sets of vibration test data are available. Section 4.3 addresses the issues of the model reduction and mode shape expansion that arise when limited number of transducers are employed to measure the response of a structure. Finally, Section 4.4 discusses different matrix updating schemes that are used to obtain a baseline model for the damage detection.

## 4.1 Previous Work

Based on their mathematical frameworks, most model updating methods can be categorized into three basic approaches: (1) optimal matrix update (direct method), (2)

sensitivity-based update, and (3) statistical parameter identification. There are many different techniques that have been proposed for the model updating problem. An literature review on model updating methods and the related issues can be found in References 105 and 54, respectively. A detailed review of all the existing methods is beyond the scope of this study. Instead, emphasis is placed on the methods relevant to the first two approaches since they represent the main approaches employed in this study.

### 4.1.1 Optimal Matrix Update Method

In optimal update methods, the entire stiffness matrix (and/or mass matrix) is updated in a single step. The objective of the optimal matrix update is to assess the perturbation matrices $\Delta\mathbf{K}$ and $\Delta\mathbf{M}$ such that a given error function $J(\Delta\mathbf{K}, \Delta\mathbf{M})$ is minimized:

$$\min_{\Delta\mathbf{K},\Delta\mathbf{M}} J(\Delta\mathbf{K}, \Delta\mathbf{M}) \tag{4.1}$$

The most common criterion is to minimize the difference between the measured and analytical modal parameters:

$$J(\Delta\mathbf{K}, \Delta\mathbf{M}) = \|\hat{\psi} - \psi(\Delta\mathbf{K}, \Delta\mathbf{M})\| \tag{4.2}$$

where $\hat{\psi}$ is the measured modal parameters, $\psi(\Delta\mathbf{K}, \Delta\mathbf{M})$ is the corresponding modal parameters from the analytical model, and $\|\cdot\|$ denotes an Euclidean or Frobenius norm. Berman and Nagy [24] and Kammer [83] observe that the criterion shown in Equation (4.2) has a tendency to produce an updated model far different from the original model. This difficulty is resolved by adding the following minimum change criterion:

$$J(\Delta\mathbf{K}, \Delta\mathbf{M}) = \|\Delta\mathbf{K}\| + \|\Delta\mathbf{M}\| \tag{4.3}$$

The equation of motion allows a direct comparison between the measured modal

parameters and the analytical model:

$$J(\Delta\mathbf{K}, \Delta\mathbf{M}) = \sum_{i=1}^{N_m} \|(\mathbf{K} + \Delta\mathbf{K})\hat{\mathbf{v}}_i - \hat{\omega}_i^2(\mathbf{M} + \Delta\mathbf{M})\hat{\mathbf{v}}_i\| \tag{4.4}$$

where $N_m$ is the number of measured modes and, $\hat{\mathbf{v}}_i$ and $\hat{\omega}_i$ denote the $i$th measured modal vector and natural frequency, respectively. Physically, Equation (4.4) represents a set of unbalanced forces resulted from the comparison of the measured modal parameters and the analytical model.

The models updated using Equations (4.2) to (4.4) are observed to loose some of its fundamental properties such as symmetry, positivity or sparsity pattern. To enforce these conditions to the updated model, constraints are added to Equation (4.1) using Lagrange multipliers or penalty techniques [81,24,137]:

$$\min_{\Delta\mathbf{K},\Delta\mathbf{M}} J(\Delta\mathbf{K}, \Delta\mathbf{M}) + \lambda C(\Delta\mathbf{K}, \Delta\mathbf{M}) \tag{4.5}$$

where $C(\Delta\mathbf{K}, \Delta\mathbf{M})$ denotes the additional constraint and $\lambda$ is either a Lagrange multiplier or a given constant when a penalty technique is used. There are three commonly used constraints:

1. The symmetry of the perturbation matrices:

$$\Delta\mathbf{K}^T = \Delta\mathbf{K} \text{ and } \Delta\mathbf{M}^T = \Delta\mathbf{M} \tag{4.6}$$

2. The positivity:

$$\mathbf{x}^T\Delta\mathbf{K}\mathbf{x} \geq 0 \text{ and } \mathbf{x}^T\Delta\mathbf{M}\mathbf{x} \geq 0 \ \ \forall\mathbf{x} \tag{4.7}$$

3. The preservation of the sparsity pattern (connectivity) of the original matrices:

$$\begin{aligned} \text{sparsity}(\mathbf{K} + \Delta\mathbf{K}) &= \text{sparsity}(\mathbf{K}) \\ \text{sparsity}(\mathbf{M} + \Delta\mathbf{M}) &= \text{sparsity}(\mathbf{M}) \end{aligned} \tag{4.8}$$

Table 4.1 summarizes different optimal updating methods. These methods involve only simple matrix computation, have the advantage of computational efficiency, and

Table 4.1: Comparison of optimal updating methods reported by Hemez [69]

| Method | Criterion[1] | Constraint[1] | Test data[2] | Scheme[3] |
|---|---|---|---|---|
| Baruch [8,10,12,9] | M | S, EOM | D | D |
| Berman [23,22,25] | M | S, EOM | D | D |
| Berman and Nagy [24] | M | S, EOM | D | D |
| Chou and O'Callahan [36,114] | EOM | S, P | D | D |
| Kabe [80,81] | M | S, EOM, C | D | D |
| Kammer [83] | M | S, EOM, C | D | D |
| Lin [98] | M | S, EOM | D | D |
| Smith and Beattie [137,136] | M, EOM | S, C | D | I |
| Hajela and Soeiro [64,63] | TAC | S, P, | D, S, H | I |
| Zhang and Zhang [152] | M | S, EOM | D | D |
| Zimmerman and Kaouk [158,156,155] | EOM | S, P, C | D | I |

1. C=connectivity, EOM=equation of motion, M=minimum change, P=positivity, S=symmetry, TAC=comparison between test and analysis quantities
2. D=dynamic, S=static, H=hybrid
3. D=direct, I=iterative

are able to reproduce the modal parameters employed for the model updating. However, it is often difficult to interpret the physical meaning on the resulting changes to the mass and stiffness coefficients. In addition, the methods require that the DOFs of the measured modal vectors need to agree with those of the analytical model in terms of the size and locations. The main disadvantage with these methods is the lack of control over the parameters that are subject to updating. Considering the limited amount of information contained in the measured data, a model updating method should keep the number of updating parameters small in order to achieve a physically meaningful refinement.

In this study, we focus on optimal stiffness matrix updating methods. A brief comparison of the stiffness updating methods [137,80,83,11] is summarized in Table 4.2 and briefly reviewed here.

Baruch and Bar Itzhack [11] developed an procedure to orthogonalize the measured modes and to update an initial stiffness matrix using the measured frequencies and the orthogonalized modal vectors. The updated stiffness matrix is found such that the matrix represents as closely as possible the initial model and is consistent with the observed modal data. A constrained optimization problem is solved to find

Table 4.2: Comparison of different optimal stiffness matrix updating methods

| Method | cost function & constraint(s) | | | PD | SP | EC |
|---|---|---|---|---|---|---|
| Baruch [11] | $\|\mathbf{M}^{-\frac{1}{2}}(\mathbf{K}-\mathbf{K}^{\circ})\mathbf{M}^{-\frac{1}{2}}\|$ | s.t. | $\mathbf{K}\Phi = \mathbf{M}\Phi\Omega$ | ∘ | × | × |
| Kabe [80] | $\|(\mathbf{K}-\mathbf{K}^{\circ}) \odot \mathbf{W_1}\|$ | s.t. | $\mathbf{K}\Phi = \mathbf{M}\Phi\Omega$ | × | ∘ | × |
| Kammer [83] | $\|\mathbf{K}\Phi - \mathbf{M}\Phi\Omega\|$ | s.t. | other conditions | × | ∘ | × |
| Smith [137] | $\|\mathbf{D}^{-1}(\mathbf{K}-\mathbf{K}^{\circ})\mathbf{D}^{-1}\|$ | s.t. | $\mathbf{K}\Phi = \mathbf{M}\Phi\Omega$ | × | ∘ | × |
| Smith2 [137] | $\|\mathbf{D}^{-1}(\mathbf{K}-\mathbf{K}^{\circ})\mathbf{D}^{-1}\| + \|(\mathbf{K}\Phi - \mathbf{M}\Phi\Omega)\Lambda^{-1}\|$ | | | ∘ | ∘ | ∘ |
| Smith3 [134] | $\|\mathbf{M}^{-\frac{1}{2}}(\mathbf{K}-\mathbf{K}^{\circ})\mathbf{M}^{-\frac{1}{2}}\|$ | s.t. | iteratively enforce sparsity | ∘ | ∘ | × |

* PD: maintenance of positive definiteness, SP: preservation of the sparsity pattern of the original matrix and EC: consideration of error compensation
* $\odot$ denotes an element-by-element matrix multiplication operator
* The $(i,j)$ component of $\mathbf{W_1} = (\mathbf{K^o_{ij}})^{-1}$ and $\mathbf{D} = diag(\sqrt{\mathbf{K^o_{ii}}})$

the updated stiffness matrix that is closest to an initial stiffness matrix and that exactly satisfies the dynamic constraints imposed by the test data. This method adjusts a stiffness matrix such that the updated matrix contains more non-zero coefficients than the initial stiffness matrix. The new non-zero coefficients created in the updated stiffness matrix are interpreted as the fictitious load paths that do not exist in the real structure. Berman and Nagy [24] extended the same approach to optimally update a mass matrix.

Kabe [80] presented an updating procedure which preserves the physical connectivity of the original model in the updated stiffness. The confidence or reliability of the adjusted model is increased by preserving the actual load paths of a structure. An optimally updated stiffness matrix is closest to the original matrix, and satisfies the constraints imposed by the estimated modal parameters and the symmetricity. The closeness to the original stiffness matrix is measured by summing the relative change of non-zero coefficients in the updated stiffness matrix. However, Kabe's method requires solution of an auxiliary linear system of equations, demanding a large amount of computational effort. Kammer [83] reformulated Kabe's method by minimizing the residual forces obtained from the measured modal data, and imposing the matrix sparsity and the symmetricity as constraints. The method by Kammer is reported to produce equivalent results as that by Kabe in many circumstances.

Smith and Beattie [137] addressed the analogy of the optimal stiffness matrix update with optimal secant update used in nonlinear optimization. They also presented

a generalized secant method to produce an updated stiffness matrix which preserves the structural connectivity and requires minimal storage. However, it is reported that these sparsity-preserving methods could result in a non-positive definite matrix when test data contains noises. It appears that the preservation of sparsity and the constraints imposed by the noise-contaminated modal parameters provide inconsistent information for the stiffness updating. In practice, there may not exist an update which satisfies both the desired sparsity pattern and the hard constraint imposed by the test data. Smith proposed an error compensation version to circumvent this problem [14]. Imposing test data as a hard constraint yields an adjusted model which exactly reproduces the noise-contaminated test data. In this error compensation approach, the dynamic constraint imposed by modal parameters is included in the cost function permitting deviation of the updated modal parameters from the measured ones.

As an alternative, an iterative approach to force the sparsity pattern was proposed [134]. First, the stiffness matrix is updated using any of the previous updating methods. Then, the sparsity is imposed by discarding the generated non-zero values. These two-steps are repeated until the model converges to a solution. This two step iteration alternates between the optimal solution which matches the test data and the other solution which satisfies the sparsity pattern. However, it appears that this approach does not guarantee the positive definiteness of the updated stiffness matrix nor the convergence to an unique solution.

### 4.1.2 Sensitivity-Based Methods

Similar to the optimal matrix updating, sensitivity-based methods seek to minimize an objective function which is usually based on Equations (4.2) to (4.4) and constraints (4.6) to (4.8). The main difference between sensitivity-based methods and the optimal matrix updating methods is that the objective function is expressed as a function of a set of parameters $\mathbf{p}$ instead of the direct matrix perturbations, $\Delta\mathbf{K}$ and $\Delta\mathbf{M}$:

$$\min_{\mathbf{p}} J(\mathbf{p}) + \lambda C(\mathbf{p}) \tag{4.9}$$

where the updating parameter set $\mathbf{p}$ may represent mass and stiffness entries, boundary conditions, or design parameters. Since the objective function in Equation 4.9 is generally a nonlinear function of updating parameters, the updated model is sought in an iterative manner. The iterative scheme requires the computation of the sensitivity matrix $\frac{\partial J}{\partial \mathbf{p}}$. A broad range of methods are available with different formulations of error functions and sensitivity derivatives. Table 4.3 summarizes several sensitivity-based methods identified in Reference 69.

Table 4.3: Comparison of sensitivity-based methods reported by Hemez [69]

| Method | Criterion[1] | Constraint[1] | Test data[2] | Scheme[3] |
|---|---|---|---|---|
| Chen and Garba [32,31] | M | EOM | D | I |
| Soeiro and Hajela [138] | TAC | EOM, S, P, C | D, S | I |
| Haug and Choi [67] | EOM | S | D, S | D |
| Norris and Meirovitch [110] | EOM | S, C | D | I |
| Ojalvo [116] | EOM | S | D | D |
| Ricles and Kosmatka [127] | EOM | S | D | I |
| Sanayei and Onipede [130,131] | EOM | S, P, C | S | I |
| Berger and Ohayon [21,20] | EOM | S, P, C | D | I |
| Bernitsas and Tawekal [26] | TAC | EOM, S, P, C | D | I |
| Chen and Garba [33] | EOM | S, P, C | D, S | I |
| Chou and Wu [37] and Baruh [13] | EOM | S, C | D | D |
| Dupuis, Roy and Girard [128,58] | EOM | S, P, C | D | I |
| Ladeveze, Reynier and Nedjar [93,126] | EOM, TAC | S, P, C | D, S, H | I |
| Piranda, Lallement and Cogan [124] | EOM | S, P, C | D, S | I |
| Lim [97,96] | EOM | S, P, C | D | I |
| Olhoff and Rasmussen [117] | EOM | S, C | S | D |

1. C=connectivity, EOM=equation of motion, M=minimum change, P=positivity, S=symmetry, TAC=comparison between test and analysis quantities
2. D=dynamic, S=static, H=hybrid
3. D=direct, I=iterative

Note that, the choice of updating parameters is a crucial step in the sensitivity-based updating methods. For example, when the updating parameters represent a set of design parameters, the adjusted matrices are automatically symmetric and positive-definite since the update is carried out at the structural element level. These parameterization methods are reviewed and summarized in Reference 53.

### 4.1.3 Statistical Parameter Identification

Statistical parameter identification derives from the first order Taylor's expansion of the modal output error $\Delta\psi = \hat{\psi} - \psi(\mathbf{p})$:

$$\Delta\psi = \mathbf{S}\ \delta\mathbf{p} + \varepsilon \tag{4.10}$$

where $\mathbf{S}$, $\delta\mathbf{p}$ and $\varepsilon$ represents the generalized sensitivity matrix, the unknown change of the updating parameters and the measurement noise, respectively. The sensitivity matrix $\mathbf{S}$ is estimated similar to those of the sensitivity-based methods. The unknown changes in the parameters are sought by an iterative nonlinear generalized least-squares (NGLS) scheme [59]:

$$\delta\mathbf{p} = [\mathbf{S}^T\mathbf{W}^{-1}\mathbf{S}]^{-1}[\mathbf{S}^T\mathbf{W}^{-1}]\Delta\psi \tag{4.11}$$

where $\mathbf{W}$ is the covariance matrix of the measurement noise $\varepsilon$. Obtaining an accurate estimation of the covariance matrix $\mathbf{W}$ is a critical step in the statistical parameter identification methods. Assuming a Gaussian normal distribution for $\varepsilon$, the experimental identification of the covariance matrix $\mathbf{W}$ is estimated in References 39,40. A performance comparison of three different covariance matrices has been conducted and reported in Reference 59. Reference 59 concludes that a diagonal covariance matrix obtained by assuming uncorrelated Gaussian distributions achieves a satisfactory updating for small measurement noise. For larger measurement noises, other estimates of the covariance matrix are proposed. The statistical treatment requires large amount of data and assumptions for the probability density function of noise or the covariance matrix. However, the statistical methods provide a measure of the updating's quality as well as the adjustment itself.

## 4.2 Model Updating with Multiple Test Data Sets

In general, the measured test data is not sufficient to obtain an unique updated model. The incomplete measurement produces a smaller number of modes from modal analyses of a structure than that of the analytical model, and the modal vectors are

estimated only at limited measurement points. One way to address the problem is to test a structure in different configurations by adding masses or stiffnesses to the structure or by changing boundary conditions [106,157]. In this section, the error compensation model of Reference 137 is extended for the cases where multiple test data sets are available. The use of multiple test data sets can be one possible way of overcoming the lack of measurement and circumventing the uncertainty in measurements. Multiple test data sets can be collected by testing a structure under different configurations. Different configurations can be achieved by changing boundary conditions, and the redistribution of mass and stiffness throughout the structure. The proposed method extracts only meaningful information from the multiple test data sets and results in the update of the stiffness matrix which is physically plausible. That is, this method is relatively insensitive to noises in the test data and results in an updated stiffness such that the physical load paths, the positive definitiveness and the sparsity of the initial stiffness matrix are maintained.

First, the Multiple-Secant Marwil-Toint (MSMT) method with error compensation is presented and then extended for the cases where dynamic tests are repeated in several configurations. The procedure closely follows the development reported in Reference 137. The analytical mass matrix is assumed to be accurate. In the original MSMT method, an updated stiffness matrix is found such that the following objective function with constraints is minimized:

$$\begin{aligned} &\min \|\mathbf{S}^{-1}(\mathbf{K}-\mathbf{K}^o)\mathbf{S}^{-1}\| + \|(\mathbf{K}\Phi - \mathbf{M}\Phi\Omega)\Lambda^{-1}\| \\ &\text{subject to } \mathbf{K}=\mathbf{K}^T \text{ and } \text{sparse}(\mathbf{K}) = \text{sparse}(\mathbf{K}^o) \end{aligned} \tag{4.12}$$

where $\mathbf{K}$ and $\mathbf{K}^o$ are, respectively, the updated and the initial stiffness matrix, $\mathbf{M}$ is the mass matrix, $\|\cdot\|$ denotes the Frobenius norm, and $\mathbf{S}$=diag($\mathbf{S}_i$)=diag($\sqrt{\mathbf{K}^o_{ii}}$). $\Phi$ and $\Omega$ are the modal vector matrix and the diagonal eigenvalue matrix obtained from experimental modal analysis, respectively. A diagonal matrix $\Lambda$ can be assigned to weigh the confidence levels on each modal vector. The optimization of this objective function yields an updated stiffness matrix which is as close as possible to the original matrix, and as consistent as possible with the test data preserving the structural

connectivity and symmetricity.

If $\Delta\mathbf{K}$ is defined as the difference between $\mathbf{K}$ and $\mathbf{K}^o$ ($\Delta\mathbf{K} = \mathbf{K} - \mathbf{K}^o$), Equation (4.12) can be rewritten for $\Delta\mathbf{K}$ as follows:

$$\begin{gathered} \min \|\mathbf{S}^{-1}\Delta\mathbf{K}\mathbf{S}^{-1}\| + \|(\Delta\mathbf{K}\Phi - \mathbf{R})\Lambda^{-1}\| \\ \text{subject to } \Delta\mathbf{K} = \Delta\mathbf{K}^{\mathbf{T}} \text{ and } \text{sparse}(\Delta\mathbf{K}) = \text{sparse}(\mathbf{K^o}) \end{gathered} \tag{4.13}$$

where $\mathbf{R}$ is a collection of dynamic residual force vectors and is defined as follows:

$$\mathbf{R} = \mathbf{M}\Phi\Omega - \mathbf{K}^o\Phi \tag{4.14}$$

By minimizing the Lagrangian function with respect to $\Delta\mathbf{K}$ (in the Lagrangian function the constraints are incorporated into the objective function by employing Lagrange multipliers), the stiffness coefficients of the updated stiffness matrix are related to those of the original stiffness matrix and the estimated modal parameters:

$$\mathbf{K}_{ij} = \mathbf{K}^o_{ij} + \mathbf{S}_i\mathbf{S}_j[(\mathbf{J}_i\mathbf{S}\Phi, {}_i)_j + (\mathbf{J}_j\mathbf{S}\Phi, {}_j)_i] \quad \text{for } i,\ j\text{=1, 2, .., N} \tag{4.15}$$

where $\mathbf{K}_{ij}$ and $\mathbf{K}^o_{ij}$ are the $(i, j)$ component of the updated and original stiffness matrices, respectively. N is the number of degrees of freedom (DOFs) in the stiffness matrix. The projection matrix $\mathbf{J}$ has the same sparsity of the original stiffness matrix $\mathbf{K}^o$ and contains only ones and zeros:

$$\mathbf{J}_{ij} = \begin{cases} 1 & \text{if } \mathbf{K}^o_{ij} \neq 0 \\ 0 & \text{if } \mathbf{K}^o_{ij} = 0 \end{cases} \tag{4.16}$$

$, {}_i$ in Equation (4.15) is a subvector of $,$ $(= [, {}^T_1, {}^T_2 \ldots, {}^T_N]^T)$, which is a collection of the Lagrange multipliers and the solution of the following auxiliary equation. An auxiliary equation is established by taking the partial derivative of the Lagrangian function with respect to each Lagrange multiplier and setting the equation equal to zero. This auxiliary equation is solved for the Lagrange multipliers which are needed for the stiffness matrix update in Equation (4.15):

$$\mathbf{H}^T(\mathbf{I} + \mathbf{II})\mathbf{H}, \ = \mathbf{D} \tag{4.17}$$

where $\mathbf{I}$ ($\in \mathbf{R}^{N^2 \times N^2}$) is an identity matrix and $\mathbf{II}$($\in \mathbf{R}^{N^2 \times N^2}$) is a permutation matrix which transforms a columnwise listing of an $N \times N$ matrix to a columnwise listing of its transpose, that is

$$\mathbf{II}[x_{11}x_{12}...x_{1N}x_{21}...x_{2N}...x_{NN}]^T = [x_{11}x_{21}...x_{N1}x_{12}...x_{N2}...x_{NN}]^T \tag{4.18}$$

In Equation (4.17), $\mathbf{H}$ is a block diagonal matrix and has the dimension of $N^2 \times NN_m$ (where $N_m$ is the number of the estimated modal vectors):

$$\mathbf{H} = \begin{bmatrix} \mathbf{J}_1\mathbf{S}\Phi & & & \\ & \mathbf{J}_2\mathbf{S}\Phi & & \\ & & \ddots & \\ & & & \mathbf{J}_N\mathbf{S}\Phi \end{bmatrix} \tag{4.19}$$

$\mathbf{J}_i$ is the $i$th column vector of $\mathbf{J}$. A subvector $\mathbf{D}_i$ of $\mathbf{D}$ ($= [\mathbf{D}_1^T\ \mathbf{D}_2^T\ ...\ \mathbf{D}_N^T]^T$) corresponds to the $i$th row of the dynamic residual forces, $\mathbf{R} = \mathbf{M}\Phi\Lambda - \mathbf{K}^o\Phi$, weighted with $\mathbf{S}_i^{-1}$:

$$\mathbf{D}_i = \mathbf{S}_i^{-1}[\mathbf{R}_{i1}\ \mathbf{R}_{i2}\ ...\ \mathbf{R}_{iN_m}]^T \tag{4.20}$$

The solution of Equation (4.17) requires storing a large sparse matrix $\mathbf{H}^T(\mathbf{I} + \mathbf{II})\mathbf{H}$ ($\in \mathbf{R}^{N^2 \times NN_m}$). Taking advantage of the repetitive pattern of the right-hand side matrix of Equation (4.17), an iterative procedure for computing , is presented in Reference 137. This iteration procedure requires no more than the storage size of the system stiffness matrix.

In practice, due to the limited installation of sensors and difficulties of exciting a structure above a certain frequency, the number of identifiable modes is limited. One possible way to provide additional information about the structure is to conduct a series of vibration tests under different conditions. When $t$ number of such tests are conducted, the dynamics residual force matrix $\mathbf{R}$ can be written as:

$$\mathbf{R} = [\mathbf{R}_1\mathbf{R}_2...\mathbf{R}_t] = \Delta\mathbf{K}[\Phi_1\Phi_2...\Phi_t] \tag{4.21}$$

where $\Phi_i$ are modal vectors from the $i$th vibration test and $\mathbf{R}_i$ are the associated

dynamic residual forces:

$$\mathbf{R}_i = [\mathbf{M} + \Delta\mathbf{M}_i]\Phi_i\Omega_i - [\mathbf{K} + \Delta\mathbf{K}_i]\Phi_i \tag{4.22}$$

where $\Delta\mathbf{M}_i$ and $\Delta\mathbf{K}_i$ are the mass and stiffness perturbations made to the original structure for the $i$th test. The mass and stiffness matrices of the structure can be altered by placing additional masses and members on the structure, changing boundary conditions and so on. It should be noted that in most cases the rank of $\mathbf{R}$ is smaller than the column size of $\mathbf{R}$. The rank of $\mathbf{R}$ can be smaller than the column size of $\mathbf{R}$ when (1) the actual rank of the stiffness perturbation (modeling error) matrix $\Delta\mathbf{K}$ is less than the column size and (2) some of the column vectors in $\mathbf{R}$ are linearly dependent. Since modeling errors tend to spread throughout the structure, the rank of the stiffness perturbation is generally large (that is, the rank of $\Delta\mathbf{K}$ is normally larger than the column size of $\mathbf{R}$). Therefore, the rank deficiency of $\mathbf{R}$ is most likely caused by the linear dependence among the residual vectors (column vectors of $\mathbf{R}$). Since the mass and stiffness perturbations ($\Delta\mathbf{K_i}$ and $\Delta\mathbf{M_i}$ in Equation (4.22)) are likely to be small from one test configuration to another, all residual vectors (or modal vectors) from different configurations will not be linearly independent. Some of the residual vectors will not provide significantly new information or only introduce measurement noises. Therefore, a decision should be made on selecting appropriate residual vectors to be used for model updating.

To extract meaningful information from the residual vectors, a subspace selection scheme in Reference 157 is adopted in this study. When a series of tests are conducted, Equation (4.13) is modified such that $\|(\Delta\mathbf{K}\Phi\mathbf{Z} - \mathbf{R}\mathbf{Z})\Lambda^{-1}\|$ is minimized instead of $\|(\Delta\mathbf{K}\Phi - \mathbf{R})\Lambda^{-1}\|$:

$$\begin{gathered} \min \|\mathbf{S}^{-1}\Delta\mathbf{K}\mathbf{S}^{-1}\| + \|(\Delta\mathbf{K}\Phi\mathbf{Z} - \mathbf{R}\mathbf{Z})\Lambda^{-1}\| \\ \text{subject to } \Delta\mathbf{K} = \Delta\mathbf{K}^T \text{ and } \text{sparse}(\Delta\mathbf{K}) = \text{sparse}(\mathbf{K}^o) \end{gathered} \tag{4.23}$$

where $\mathbf{Z}$ ($\in \mathbf{R}^{N_m \times N_{\bar{m}}}$) is a selection matrix to extract useful information from the residual force matrix $\mathbf{R}$ and $N_{\bar{m}}$ is a reduced rank of $\mathbf{R}$. $N_{\bar{m}}$ is determined from the

singular value decomposition of $\mathbf{R}$:

$$\mathbf{R} = [\mathbf{U}_1|\mathbf{U}_2] \begin{bmatrix} \Sigma_1 & \mathbf{0} \\ \mathbf{0} & \mathbf{0} \end{bmatrix} [\mathbf{V}_1 \mid \mathbf{V}_2]^T \tag{4.24}$$

where the diagonal matrix $\Sigma_1 (\in \mathbf{R}^{N_{\bar{m}} \times N_{\bar{m}}})$ contains $\bar{m}$ number of the singular values which are larger than a user-specified threshold, and the left and right singular vectors $\mathbf{U}$ and $\mathbf{V}$ are partitioned according to the partitions of the singular values. Since the range of $\mathbf{R}$ is mainly spanned by $\mathbf{U}_1$, $\mathbf{Z}$ is found such that:

$$\mathbf{RZ} = \mathbf{U}_1 \tag{4.25}$$

Taking a pseudo-inverse of $\mathbf{R}$, $\mathbf{Z}$ becomes

$$\mathbf{Z} = \mathbf{R}^+\mathbf{U}_1 = (\mathbf{V}_1\Sigma^{-1}\mathbf{U}_1^T)\mathbf{U}_1 = \mathbf{V}_1\Sigma^{-1} \tag{4.26}$$

where $\mathbf{R}^+$ is the pseudo-inverse of $\mathbf{R}$. From Equation (4.26), one can retain significant information and reduce the effect of measurement noises by spanning the range of $\mathbf{R}$ with $\mathbf{U_1}$. Physically feasible update is enforced in Equation (4.23) to minimize the generalized residual forces, $\Delta\mathbf{K}\Phi\mathbf{Z} - \mathbf{RZ}$.

In Section 4.4, the performance of the proposed method is compared to other optimal update methods employing a numerical example and an experimental test data from an eight-bay truss structure.

## 4.3 Model Reduction and Mode Shape Expansion

For most model updating techniques presented in the previous section, the DOFs in the analytical model should coincide with those in the estimated modal vectors. When only a small number of sensors are installed, one can use either system condensation techniques or mode shape expansion techniques. System condensation techniques reduce the DOFs defined in the analytical model to the measured DOFs. Reduction techniques often produce a condensed matrix that does not resemble the member connectivity of the original model. As a result, locating damaged members from the residual force vectors of the reduced system becomes very difficult [24,68].

Model reduction techniques include the static reduction, dynamic reduction, Improved Reduced System (IRS) and System Equivalent Reduction Expansion Process (SEREP) [53]. Static or Guyan reduction [61] is the simplest method. This method divides the mass and stiffness matrices into submatrices relating to the master DOFs and the slave DOFs. Here, the master DOFs are related to the measured DOFs and retained. The slave DOFs are eliminated to produce a reduced model assuming that no force is applied to the slave DOFs and neglecting the inertial forces relating to the slave DOFs. Since the inertia forces neglected in the slave DOFs become more significant for higher frequency, the accuracy of higher modes drastically deteriorates in the static reduction method.

The dynamic reduction method [120] modifies the static reduction method to include the inertia forces, which are neglected in the static reduction method, at a specified frequency. The choice of the frequency is, however, not obvious. The IRS [112] improves the static reduction method by including the inertial terms into the transformation matrix as pseudo static forces. The transformation matrix here relates the full DOFs to the master DOFs. The SEREP [112] uses the analytical eigenvectors to produce the transformation matrix. This method reproduces the lower natural frequencies of the full model. References 6 and 7 compare these reduction methods and Reference 60 considers the effect of model reduction in model updating.

An alternative is to expand the modal vectors, based on the measurements at the instrumented DOFs, to the size of the analytical model [54]. The mode shape expansion techniques can be categorized into three approaches [74]. First, geometrical expansion [149] involves the interpolation/extrapolation of the measured degrees of freedom to those of the full model. This approach is rarely applied to structural dynamic problems since this approach is highly sensitive to the distribution of measurement points, the changes of boundary conditions and the energy localization. Second, the subspace rotation algorithm (SRA) or the modal coordinate expansion (MCE) [82,113,115,135] assume that the measured modal vectors can be expressed as a linear combination of the analytical modal vectors. Usually, the analytical modal vectors that correlate well with the measured modal vectors are considered although,

in theory, any number of modal vectors could be included. Third, the dynamic expansion or the physical expansion (PE) [90,24,21] is inverse to the Guyan reduction where the slave DOFs are reconstructed from the master DOFs. This approach directly uses the analytical mass and stiffness matrices to compute the unmeasured DOFs in the measured modal vectors. This method avoids the direct comparison of the measured and analytical modal vectors. However, this method may require large storage space for all the system matrices.

Mode shape expansion invariably requires a finite element model to fill the unmeasured part of the modal vectors, and works only when the analytical model is already a good representation of the structure. Mode shape expansion methods generally do not produce the results that are accurate enough to provide reliable information about the damaged DOFs or the damaged structural members. Comparison of mode shape expansion methods is presented in References 62, 74, and 95.

The mode shape expansion methods are often employed with optimal model updating methods [137,80,83,11,24], damage detection methods [69,86] as well as test/analysis correlation. Many model refinement and damage detection methods require the orthogonality of modal vectors with respect to the structure mass matrix. References 11 and 144 present the subsequent orthogonalization process of the expanded modal vectors. The orthogonal Procrustes expansion method [135] simultaneously expands and orthogonalizes the modal vectors.

## 4.4 Application to an Eight-Bay Truss Structure

An example structure is presented to demonstrate and compare the proposed method to the previously published optimal update methods. The structure employed in this section is an eight-bay truss structure from the NASA dynamic scale model technology (DSMT) program of Langley Research Center described in Section 3.5. As shown in Figure 4.1, the structure is fixed at one end and ninety-six accelerometers are instrumented to all thirty-two unconstrained nodes to measure all three translational DOFs of each node (note that the measurements at the DOFs 43, 44 and 45 are reported to be defective [84]). Experimental modal analysis was conducted under

the undamaged condition of the structure and several damage cases. For each test, the first five modes were estimated. For fourteen damage cases, one strut in different locations is completely removed from the structure, respectively, and for one case, two struts are removed simultaneously. In the last case, one strut is buckled to simulate a partial damage. Throughout the whole example, the mass matrix of the analytical model is assumed to be an accurate representation of the true mass matrix. The structure is modeled using 104 truss elements, 36 nodes and 96 DOFs. Five truss members at the fixed end are not included in the model. Furthermore, each truss member is defined as a substructure. In the analytical model, a lumped mass matrix is used and an additional concentrated mass is added to each node to take into account the joint and instrumentation masses. A detailed description of the example structure can be found in Reference 87.

This section is organized as follows: First, a comparison of stiffness matrix updating methods (Baruch's [11], Kabe's [80], Smith's [137] and MRPT [84] methods) is conducted using simulated modal parameter data. The MRPT method is not an optimal updating method but investigated here since the MRPT method was used for the model updating of the eight-bay truss reported in Reference 84. Second, the updating of an initial finite element model of the eight-bay truss structure is conducted using the experimental test data from the undamaged state of the truss structure. Three previously published methods (Baruch's, MRPT methods and the error compensation version described in Reference 137) and the modified version of

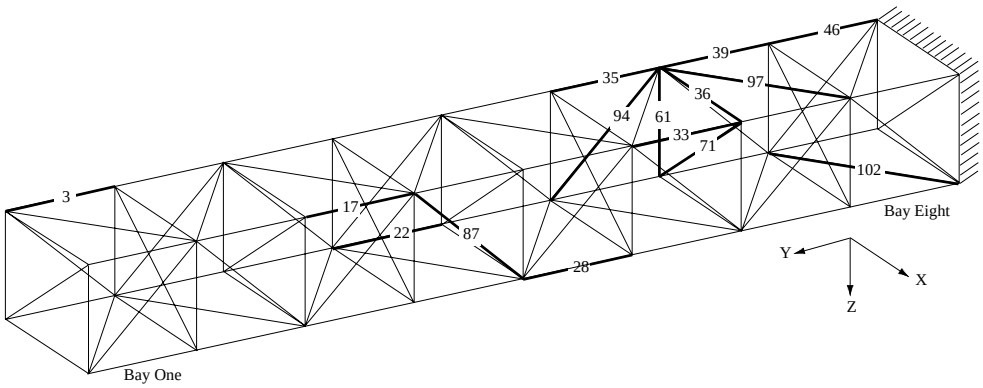


Figure 4.1: An eight-bay truss structure

the multiple-secant Marwil-Toint (MSMT) method presented in Section 4.2 are employed for the updating. Finally, the Bayesian probabilistic approach is employed to diagnose ten actual damage cases. In the Bayesian approach, the previously adjusted stiffness matrix from each updating method is used as an initial analytical model for damage detection of ten different damage cases, and the performance of diagnoses is compared to investigate which model produces a better representation of the real structure.

### 4.4.1 Model Refinement using Simulated Test Data

The finite element model obtained from the NASA Langley Research Center is assumed to be an exact model in this simulation. An initial stiffness matrix is generated by perturbing the exact stiffness matrix. The initial stiffness matrix is obtained by assembling the following perturbed element stiffness matrix $\hat{\mathbf{K}}_{si}$:

$$\hat{\mathbf{K}}_{si} = \mathbf{K}_{si}\,(1 + \frac{\mathcal{N}}{100}\,\mathcal{R}) \tag{4.27}$$

where $\hat{\mathbf{K}}_{si}$ and $\mathbf{K}_{si}$ are the element stiffness matrices after and before the perturbation, respectively, $\mathcal{N}$ is a specified noise level in terms of percentage, and $\mathcal{R}$ is a normally distributed random number with zero mean and a variance of 1.0. Here, the value of 10% noise level is used for $\mathcal{N}$. The initial model, however, preserves the sparsity pattern of the exact model. Four previously published methods (Baruch's, Kabe's, MRPT, and Smith's methods) are employed for the model refinement. Each method updates the initial stiffness matrix using the first five natural frequencies and modal vectors of the exact model.

Table 4.4 presents the first ten natural frequencies from each updated stiffness matrix. In addition, the modal assurance criterion (MAC) of the corresponding modal vectors are computed as [45]:

$$\mathrm{MAC}(i,j) = \frac{(\Phi_i^T \bar{\Phi}_j)^2}{(\Phi_i^T \Phi_i)(\bar{\Phi}_j^T \bar{\Phi}_j)} \tag{4.28}$$

where $\Phi_i$ is the $i$th modal vector of the exact model and $\bar{\Phi}_j$ is the $j$th modal vector of an updated model. If two modal vectors used in the calculation of the MAC are

Table 4.4: Comparison of different updating methods using simulated data: without noise

| | Exact | Initial | Baruch | Kabe | Smith | MPRT |
|---|---|---|---|---|---|---|
| | | | (a) Natural Frequencies (Hz) | | | |
| 1* | 13.9245 | 14.1893 | 13.9245 | 13.9245 | 13.9245 | 13.9245 |
| 2* | 14.4407 | 14.3048 | 14.4407 | 14.4407 | 14.4407 | 14.4407 |
| 3* | 46.7445 | 47.0348 | 46.7445 | 46.7445 | 46.7445 | 46.7445 |
| 4* | 66.0067 | 67.3592 | 66.0067 | 66.0067 | 66.0067 | 66.0067 |
| 5* | 71.1420 | 70.7437 | 71.1420 | 71.1420 | 71.1420 | 71.1420 |
| 6 | 117.3227 | 117.3367 | 117.3300 | 126.2192 | 113.6756 | 118.9687 |
| 7 | 137.3942 | 136.1062 | 136.0681 | 137.3942 | 137.3942 | 134.5062 |
| 8 | 144.4354 | 145.2038 | 145.1855 | 144.4354 | 144.4354 | 143.7498 |
| 9 | 154.8468 | 155.3103 | 155.3010 | 154.8468 | 154.8468 | 154.6907 |
| 10 | 216.2318 | 215.4142 | 215.4027 | 216.2318 | 216.2318 | 215.2313 |
| | | | (b) Modal Assurance Criterion | | | |
| 1 | | 0.9965 | 1.0000 | 1.0000 | 1.0000 | 1.0000 |
| 2 | | 0.9965 | 1.0000 | 1.0000 | 1.0000 | 1.0000 |
| 3 | | 0.9974 | 1.0000 | 1.0000 | 1.0000 | 1.0000 |
| 4 | | 0.9988 | 1.0000 | 1.0000 | 1.0000 | 1.0000 |
| 5 | | 0.9973 | 1.0000 | 1.0000 | 1.0000 | 1.0000 |
| 6 | | 0.9985 | 0.9987 | 0.9985 | 0.9984 | 0.9887 |
| 7 | | 0.8841 | 0.8865 | 1.0000 | 1.0000 | 0.9287 |
| 8 | | 0.8860 | 0.8872 | 1.0000 | 1.0000 | 0.9354 |
| 9 | | 0.9881 | 0.9881 | 1.0000 | 1.0000 | 0.9958 |
| 10 | | 0.6546 | 0.6548 | 1.0000 | 1.0000 | 0.4506 |

* These modes used for updating

identical, the value of the MAC becomes a unity. If they correspond to two different modes (if two modal vectors are orthogonal to each other), the MAC value becomes zero.

The first column of Table 4.4 shows the natural frequencies of the exact model and the second column presents the natural frequencies obtained from the initial model and the corresponding MAC values. The remaining columns show the frequencies and the MAC values obtained from the models updated by four different methods. The first five natural frequencies and modal vectors, which are used for updating, are exactly reproduced by all updating methods. Baruch's method shows a slight improvement in the sixth, eighth and ninth natural frequencies and in all modal vectors. Kabe's and Smith's methods also significantly improve the remaining modal parameters which are not used for the updating. In Kabe's method, the number of independent coefficients of the stiffness matrix (the number of diagonal terms in the stiffness matrix and non-zero coefficients on one side of the diagonal) should be less than the number of constraints (the number of modal vectors times the number of DOFs in one modal vector) to obtain the exact stiffness matrix. However, because of the redundancy of a structure, more constraints are required in most cases [81]. Kabe's method is found to need a minimum of six modal vectors to exactly reproduce the stiffness matrix of the eight-bay truss structure. In Kabe's and Smith's methods, the preservation of the zero and non-zero patterns of the stiffness matrix enables the better updating with the same number of modal parameters. The eighth, ninth and tenth natural frequencies, and all modal vectors (except the tenth modal vectors) are improved in the MRPT method. In theory, the MRPT method should be employed only when the rank of the stiffness perturbation is equal or less than that of the used modal vectors.

Next, the same procedure is repeated considering measurement noises. To simulate measurement uncertainties in the estimated modal vectors, the exact modal vectors obtained from the exact stiffness matrix are perturbed with noise. More explicitly, the estimated modal vector is constructed such that

$$\hat{\Phi}_i = \Phi_i \left(1 + \frac{\mathcal{N}}{100}\, \mathcal{R}\right) \tag{4.29}$$

where $\hat{\Phi}$ is the $i$th measured modal vector simulated from the exact model. $\mathcal{N}$ is a specified noise level in terms of percentage, and $\mathcal{R}$ is a normally distributed random number with zero mean and a variance of 1.0. Similarly, the natural frequencies are also constructed assuming that they are noise-contaminated. Since the modal parameters are noise-contaminated, the modal vectors do not satisfy a mass-orthogonality condition ($\Phi_i^t \mathbf{M} \Phi_i = 1$). Therefore, it is necessary to adjust the modal vectors such that the orthogonality condition is satisfied. In this study, the weighted orthogonalization procedure by Baruch is employed [11] . Note that Baruch's method is based on the assumption that the measured modal parameters are orthogonalized with respect to the mass matrix of the structure. Furthermore, the MRPT method guarantees the symmetricity of the updated model only when the measured modal parameters are mass-orthogonalized.

The first ten natural frequencies of the exact model are shown in the first column of Table 4.5 and the frequencies in parenthesis are the noise-contaminated ones. The noise-contaminated frequencies and the associated noise-corrupted modal vectors (the measured modal parameters) are employed for model refinement. The rest of columns shows the frequencies from each updated stiffness matrix as well as the MAC values.

The updated natural frequencies of Baruch's method exactly match the noise contaminated frequencies, which are used for the updating. The remaining modes are also slightly improved. Kabe's, Smith's and MRPT methods fail to update the stiffness matrix. It appears that there is no physically feasible update of the stiffness matrix satisfying all the constraints provided by the noise-contaminated modal parameters and the sparsity pattern. Furthermore, Kabe's or Smith's methods do not guarantee the positive definiteness of the updated matrix and several imaginary eigenvalues are produced by both methods (this possibility of a non-positive definite update is also reported in References 137 and 81).

This difficulty is overcome by the error compensation version described in Reference 137 where the stiffness matrix is updated as consistent as possible (but not exactly match) with the measured test data while preserving the connectivity of the structure. This method improves both the natural frequencies and the MAC values. However, the improved modal parameters do not exactly match the measured modal

Table 4.5: Comparison of different updating methods using simulated data: with 10% noise

| | Exact | Baruch | Kabe | Smith | MPRT | Smith2 |
|---|---|---|---|---|---|---|
| | | | (a) Natural Frequencies (Hz) | | | |
| 1 | 13.9245(13.8973*) | 13.8973 | 9.6388 | 11.0311 | 13.8973 | 14.0283 |
| 2 | 14.4407(14.3405*) | 14.3405 | 16.8531 | 21.3090 | 14.3405 | 14.2897 |
| 3 | 46.7445(46.9954*) | 46.9954 | 26.7688 | 26.6711 | 45.8764 | 47.0479 |
| 4 | 66.0067(66.4243*) | 66.4243 | 28.5706 | 28.7817 | 46.9954 | 67.3375 |
| 5 | 71.1420(71.3151*) | 71.3151 | 34.5585 | 31.8033 | 66.4243 | 70.7341 |
| 6 | 117.3227 | 117.3314 | 40.0831 | 40.4220 | 71.3151 | 117.3361 |
| 7 | 137.3942 | 136.0066 | 43.3671 | 43.6058 | 87.9210 | 136.1078 |
| 8 | 144.4354 | 145.1335 | 44.5334 | 44.2145 | 117.3834 | 145.2017 |
| 9 | 154.8468 | 155.2229 | 49.5919 | 48.9827 | 129.3925 | 155.3070 |
| 10 | 216.2318 | 215.2845 | 52.9519 | 51.7119 | 147.4479 | 215.4127 |
| | | | (b) Modal Assurance Criterion | | | |
| 1 | | 0.9929 | 0.0070 | 0.0004 | 0.9929 | 0.9435 |
| 2 | | 0.9881 | 0.0047 | 0.0378 | 0.9881 | 0.9438 |
| 3 | | 0.9888 | 0.0019 | 0.0000 | 0.0001 | 0.9974 |
| 4 | | 0.9907 | 0.0014 | 0.0007 | 0.0000 | 0.9988 |
| 5 | | 0.9932 | 0.0004 | 0.0045 | 0.0001 | 0.9973 |
| 6 | | 0.9986 | 0.0001 | 0.0000 | 0.0000 | 0.9985 |
| 7 | | 0.8880 | 0.0818 | 0.0620 | 0.0475 | 0.8839 |
| 8 | | 0.8879 | 0.0051 | 0.0563 | 0.0011 | 0.8858 |
| 9 | | 0.9865 | 0.0356 | 0.0210 | 0.1189 | 0.9881 |
| 10 | | 0.6590 | 0.0000 | 0.0017 | 0.0099 | 0.6550 |

* These are noise-contaminated frequencies and used for updating

parameters employed for the updating. The weighting matrix in this method ($\Lambda$ in Equation (4.13)) is determined such that the updated stiffness matrix is positive definite and close to the initial model. The values of the weighting matrix is somehow determined by a trial-and-error process. The selection of appropriate weighting matrix for the best performance requires further study.

It is observed that the natural frequencies and the MAC values updated by Baruch's method are slightly closer to the exact values than those from the error compensation version. However, it is not clear whether the updated stiffness matrix from Baruch's method is a better representation of the exact stiffness matrix than one from the compensation method. While the updated stiffness matrix by the error compensation method preserves the sparsity pattern, the stiffness adjustment in Baruch's method is spread throughout the stiffness matrix.

### 4.4.2 Model Refinement using Experimental Test Data

The same update methods are applied to the experimental test data obtained from the NASA Langley Research Center [87]. Same as the previous simulation, the first five natural frequencies and modal vectors are estimated from the experimental test. Again, the modal vectors are mass-orthogonalized using the method in Reference 11. The original finite element (FE) model provided by the NASA Langley Research Center is employed as an initial analytical model of the eight-bay truss. Since Kabe's and Smith's methods yield unrealistically updated stiffness matrices (both methods produce more than ten negative eigenvalues), the results from Kabe's and Smith's methods are not presented here.

Table 4.6 summarizes the results of different updating methods. In the first column of Table 4.6, the measured natural frequencies from the NASA Langley Research Center are presented. The second column shows the natural frequencies of the initial analytical model and the MAC values between the measured modal vectors and the analytical modal vectors. The measured frequencies and modal vectors are again matched exactly by using Baruch's method (see the third columns of Table 4.6).

The first column under the heading "MRPT" in Table 4.6 is obtained using the extended MRPT method described in Reference 157. The extended MRPT updates

Table 4.6: Comparison of different updating methods using experimental data

| | Test | Initial | Baruch | MPRT* | Smith2 | Proposed |
|---|---|---|---|---|---|---|
| | | | (a) Natural Frequencies (Hz) | | | |
| 1 | 13.8760 | 13.9245 | 13.8760 | 13.6721(13.8760) | 13.0166 | 13.7120 |
| 2 | 14.4780 | 14.4407 | 14.4780 | 14.2918(14.4780) | 14.1974 | 14.5932 |
| 3 | 48.4120 | 46.7445 | 48.4120 | 46.6641(48.4120) | 46.9382 | 46.7528 |
| 4 | 64.0330 | 66.0067 | 64.0330 | 63.9088(64.0330) | 65.1356 | 65.9931 |
| 5 | 67.4630 | 71.1420 | 67.4630 | 69.8608(67.4630) | 72.2335 | 71.1495 |
| | | | (b) Modal Assurance Criterion | | | |
| 1 | | 0.8774 | 1.0000 | 0.9964(1.0000) | 0.9178 | 0.9906 |
| 2 | | 0.8816 | 1.0000 | 0.9965(1.0000) | 0.9229 | 0.9905 |
| 3 | | 0.9945 | 1.0000 | 0.9920(1.0000) | 0.9945 | 0.9888 |
| 4 | | 0.9622 | 1.0000 | 0.9679(1.0000) | 0.9628 | 0.9763 |
| 5 | | 0.9647 | 1.0000 | 0.9641(1.0000) | 0.9652 | 0.9768 |

* The first one is the extended MRPT method in Reference 157 and the second one in parenthesis is the original MRPT method in Reference 84. The second method produces three imaginary natural frequencies $204.49i$, $126{,}01i$ and $16.54i$, respectively. However these values are not presented in this table.

the stiffness matrix when tests with different configurations are available. Different configurations can be achieved by changing boundary conditions, the redistribution of mass and stiffness throughout the structure. Here, test data from the undamaged state and from damage cases E and F (damage cases E and F are resulted from the removal of struts 36 and 71 in Figure 4.1, respectively) are considered different configurations of testing. Since five modes are estimated from each configuration, a total of fifteen modes are employed for the extended MRPT method. The second column under the heading "MRPT" (the one in parenthesis) is obtained using the original MPRT method in Reference 84. While the extended MRPT method does not exactly match the measured modal parameters, the original MRPT method reproduces the test data exactly. However, it should be noted that the updated stiffness matrix from the original MRPT method contains three negative eigenvalues (-16.51$\times 10^6$, -6.27$\times 10^6$ and -0.108$\times 10^6$). Therefore, it appears that the updated stiffness matrix is not realistic although the stiffness matrix exactly reproduces the measured modal parameters.

The original MRPT method forces the rank of the stiffness change to be less than or equal to the number of measured modal vectors. For model correction (not for damage detection), modeling error might be spread throughout all members making the rank of the stiffness perturbation large. However, the use of the MRPT method for the eight-bay truss is justified in Reference 84 presuming that modeling errors are mainly localized (1) near the actuators, whose dynamic effects were not modeled in the FE model, and (2) at the cantilever ends. The extended MRPT method requires estimating the rank of residual force matrix in Equation (4.24). The rank estimation schemes in Reference 76 are adopted here. The first scheme keeps only $\bar{m}$ singular values $(\sigma(1), \sigma(2), ..., \sigma(\bar{m}))$ when $\sigma(\bar{m}+1)/\sigma(1)$ becomes less than a tolerance. The second scheme sets the rank of the residual force to be $\bar{m}$ where the decrease of $\sigma(\bar{m}+1)/\sigma(\bar{m})$ is smallest. In the third scheme, $\bar{m}$ is selected at the point where the accumulation of $\sigma(i)$ reaches a certain value. Finally, the estimated rank is taken to be the minimum rank from the three schemes. When fifteen modal vectors (five modal vectors are obtained from three cases: undamaged case and damage cases E and F) are employed for the extended MRPT method, the rank of the residual force

matrix is approximately close to five. It implies that only some of the modal vectors provide reliable information or the actual rank of perturbation is close to five.

In the fifth column of Table 4.6, the error compensation version described in Reference 137 is employed for the updating (In the table, this method is labelled as "Smith2"). This method improves the MAC values significantly but natural frequencies obtained are far away from the measured ones. The results from the extended MSMT method is presented in the last column of Table 4.6. Similar to the extended MRPT method, the data sets from undamaged case and damage cases E and F are employed for the extended MSMT method. The proposed method clearly provides better agreement with the test data (both frequencies and MAC values) by employing multiple test data sets. The proposed method appears to extract only meaningful information from the noise-contaminated test data and conduct updating that is physically possible.

Since the testing of the truss structure is well controlled in the laboratory, the element stiffness of each truss member (EA/L) is believed to be reasonably accurate. It seems that errors mainly come from (1) the mismodeling of the boundary conditions and member joints, (2) neglecting the mass and dynamic effects of actuators (two electro-magnetic shakers are placed near the free end to vibrate the structure), and (3) the unreliable responses obtained from defective sensors at DOFs 43, 44 and 45 (note that the measurements at the DOFs 43, 44 and 45 are reported to be defective [84]). It is difficult to judge which updated stiffness matrix is closer to the real stiffness matrix of the eight-bay truss. It should be noted that the updated model which matches the measured modal parameters more closely is not necessary the better representation of the real structure. For examples, although the updated stiffness matrix by the original MRPT method exactly reproduces the measured modal parameters, it also contains three negative eigenvalues. It is difficult to justify that the updated stiffness matrix is an appropriate representation of the real stiffness matrix of the eight-bay truss. To answer this question, we employ each updated stiffness matrix for the damage detection presented in Section 6.1.3. We presume that the updated stiffness matrix which is closer to the actual stiffness of the structure would provide better indication of damage for most damage cases.

### 4.4.3 Application to Damage Detection

To determine which updated model is closer to the actual stiffness, each updated stiffness matrix from the previous subsection is employed as an initial analytical stiffness matrix for the Bayesian damage detection. In this study, ten damage cases out of fourteen damage cases, that have a single removed strut, are investigated (damage cases E and F are used for model updating and we did not receive data sets for damage cases B and G). For each damage case, damage is caused by completely removing a strut. The Bayesian probabilistic approach employed here examines all possible damage cases with a single damaged location.

Table 4.7: Damage detection of an eight-bay truss structure using the Bayesian approach

| | Actual Damage | | Rank | | | |
|---|---|---|---|---|---|---|
| Case | $L_{dam}$ | $D_{dam}$ | Baruch | MRPT* | Smith2 | Proposed |
| A | {46} | {100%} | 3 | 2(1) | 2 | 1 |
| C | {39} | {100%} | 41 | 45(70) | 1 | 1 |
| D | {97} | {100%} | 1 | 1(1) | 1 | 1 |
| H | {35} | {100%} | 2 | 5(3) | 4 | 2 |
| I | {94} | {100%} | 4 | 23(9) | 1 | 1 |
| J | {28} | {100%} | 15 | 27(38) | 1 | 1 |
| K | {87} | {100%} | 3 | 13(5) | 1 | 1 |
| L | {22} | {100%} | 23 | 65(22) | 16 | 3 |
| M | {17} | {100%} | 13 | 30(11) | 32 | 2 |
| N | {3} | {100%} | 42 | 13(57) | 24 | 11 |

* The first one is the extended MRPT method in Reference 157 and the second one in parenthesis is the original MRPT method in Reference 84.

Table 4.7 summarizes the diagnosis results of the ten damage cases. Baruch's and MRPT methods fail to identify the actual damage location for most damage cases. The error compensation method improves the diagnoses significantly. Employing the updated stiffness matrix from the error compensation method, the Bayesian probabilistic approach identifies the actual locations for five damage cases out of ten.

Finally, the Bayesian probabilistic approach provides the best diagnosis result when the extended MSMT method is employed. In six out of the ten damage cases, the Bayesian approach ranks the actual damage location as the most probable damage

location. For cases H, L and M, the actual damage locations are ranked at the second or third most probable locations. Only for case H, the proposed method does not detect the actual damage location.

## 4.5 Summary and Discussions

Several optimal stiffness update methods are investigated and compared using simulated and experimental test data from an eight-bay truss structure. Furthermore, a model updating method is proposed extending the Multiple-Secant Marwil-Toint (MSMT) method with error compensation [135] for the cases where dynamic tests are repeated in several configurations. The proposed method is applicable when multiple test data are obtained from different configurations of a structure. The proposed method extracts meaningful information from noise-contaminated test data and updates the stiffness matrix such that the adjusted stiffness matrix is as close as possible to the original stiffness matrix and as consistent as possible with the vibration test data. In addition, the symmetricity, the structural connectivity information and the positive definitiveness of the original stiffness matrix are preserved in the proposed method.

A numerical example without errors in simulated modal parameters indicates that Kabe's and Smith's methods provide significantly better updated stiffness matrices than Baruch's and MRPT methods. The preservation of zero and non-zero pattern provides additional constraints for Kabe's and Smith's methods and enables the better update of a stiffness matrix using a small number of modal vectors. However, when the experimental test data or simulated data contaminated with noise are employed, Kabe's and Smith's method produce non-positive definite stiffness matrices. It appears that the test data provide inconsistent constraints with the structural connectivity information of the structure. Although Baruch's and MRPT methods exactly reproduce the modal parameters used in the stiffness updating, the adjustment is spread throughout all the coefficients of the stiffness matrix. The physical load paths are not reserved in Baruch's and MRPT methods. On the other hand, the MSMT method with error compensation and the proposed method preserves the

sparsity pattern of the stiffness matrix and minimize the residual forces. The updated stiffness matrix from the proposed method provides the best diagnosis results for the ten damage cases examined. Damage detection using a Bayesian probabilistic approach implies that the updated model from the proposed method is a better representation of the unknown system stiffness of the eight-bay truss structure. Finally, model refinement requires the application of considerable physical insight to select parameters subject to updating and the arrangement of constraints.

# Chapter 5

# Damage Detection with Simplified Models

As a model-based method, the proposed Bayesian approach requires an analytical model for damage diagnosis. The construction of an analytical model introduces modeling error (the discrepancy between the analytical model and the actual structure). The modeling error is inevitable even when the model is updated with test data using the methods presented in the previous chapter. The computational cost involved for using a detailed FE model of a large scale structure in damage diagnosis is significant. Furthermore, the proposed probabilistic based approach and the branch-and-bound search scheme require repetitive computation of modal parameters/Ritz vectors. Therefore, the size of the analytical model and the number of updating parameters, which reflect damage changes in a structure, should be kept to a minimum. If there are too many updating parameters compared to the amount of test data available, most damage detection methods will suffer from ill-conditioning problems, divergence of updating parameters and the existence of too many output equivalent models. (The output equivalent models are those that have different physical parameter values but produce identical vibration data.) Therefore, the construction of an appropriate analytical model is a crucial step for damage diagnosis. The purpose of this chapter is to study the modeling issues where simplified models are employed, and modeling error and measurement noise are considered.

This chapter is organized as follows: Section 5.1 reviews an approach that is commonly employed to simplify the modeling of multi-story frame structures [35].

In Sections 5.2 and 5.3, damage diagnoses are conducted explicitly considering the modeling error as well as the noise error. Section 5.4 presents the detection of plastic hinge deformation for a reinforced-concrete bridge column using the modal parameters experimentally obtained from vibration tests.

## 5.1 Simplified Modeling Technique for Multi-Story Frame Structures

The modeling of a multi-story frame structure can be simplified by assuming that (1) the floor diaphragm is rigid in its own plane and only flexible in the vertical direction, (2) the rotational and vertical DOFs of the lateral frames can be condensed out of the dynamic analysis, and (3) the axial deformations of beams and columns are negligible [35]. The system stiffness matrix of a multi-story frame structure is determined from the lateral stiffness matrices of individual planar frames. The modeling process can be summarized as follows:

1. Using the same notation as in Equation (2.1), the stiffness matrix of a frame $j$ can be written as:

$$\mathbf{K}(\Theta)_j = \sum_{\forall i \in j} \theta_i \mathbf{K}_{si} \tag{5.1}$$

   where the assembly is performed for each substructure $i$ in the $j$th planar frame ($\forall i \in j$). Neglecting the axial deformations in the columns and beams, the model of a planar frame has one in-plane rotational DOF at each node and one lateral DOF at each floor level [see Figure 5.1 (a)].

2. The stiffness matrix of the planar frame can be partitioned according to the lateral ($l$) and rotational ($r$) DOFs, respectively:

$$\mathbf{K}(\Theta)_j = \begin{bmatrix} \mathbf{K}_{ll,j} & \mathbf{K}_{lr,j} \\ \mathbf{K}_{rl,j} & \mathbf{K}_{rr,j} \end{bmatrix} \tag{5.2}$$

   Since the inertial effects associated with the rotational DOFs are usually small, the rotational DOFs can be statically condensed and removed from the dynamic

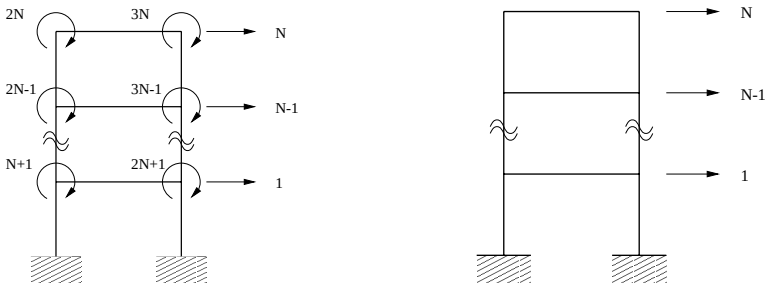


(a) complete DOFs (b) reduced DOFs

Figure 5.1: Calculation of lateral stiffness by condensing out rotational DOFs

analysis [see Figure 5.1 (b)]. Using static condensation, the lateral stiffness of the planar frame $\bar{\mathbf{K}}(\theta)_j$ becomes:

$$\bar{\mathbf{K}}(\Theta)_j = \mathbf{P}(\Theta)_j^T \, \mathbf{K}(\Theta)_j \, \mathbf{P}(\Theta)_j \tag{5.3}$$

where

$$\mathbf{P}(\Theta)_j = \begin{bmatrix} \mathbf{I} \\ -\mathbf{K}_{rr,j}^{-1} \, \mathbf{K}_{rl,j} \end{bmatrix} \tag{5.4}$$

and $\mathbf{I}$ is an identity matrix. It should be noted that the transformation matrix $\mathbf{P}(\Theta)_j$ is expressed as a function of $\Theta$.

3. Using compatibility conditions, the displacement transformation matrix $\mathbf{G}_j$ can be defined to relate the lateral displacements of the $j$th frame to the global DOFs of the system:

$$\mathbf{u}_j = \mathbf{G}_j \mathbf{u}; \; j = 1, ..., N_f \tag{5.5}$$

where $N_f$ is the number of planar frames, $\mathbf{u}$ is the global displacement vector and $\mathbf{u}_j$ is the displacement vector for lateral DOFs of the $j$th planar frame. Figure 5.2 (a) shows the global DOFs of the system and the lateral DOFs of planar frames in the $i$th floor of a multi-story building. An example of the displacement transformation matrix is shown in Figure 5.2 (b).

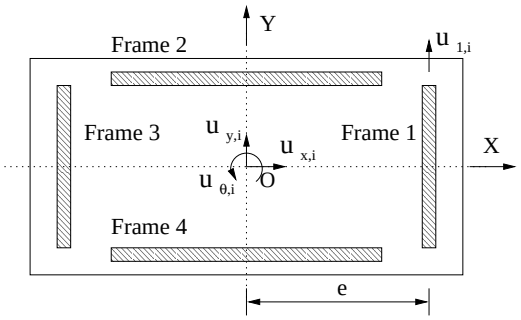


(a) the $i$th floor plan

$$\mathbf{u}_1 = \mathbf{G}_1 \left\{ \begin{array}{c} \mathbf{u}_x \\ \mathbf{u}_y \\ \mathbf{u}_\theta \end{array} \right\}$$

where

$$\mathbf{G}_1 = \left[ \begin{array}{ccc} \mathbf{0} & \mathbf{I} & \mathbf{eI} \end{array} \right]$$

(b) displacement transformation

Figure 5.2: Global DOFs of a system and lateral DOFs of planar frames

4. Finally, the system stiffness matrix of the simplified model is obtained by assembling the transformed stiffness matrices of all the planar frames:

$$\begin{aligned} \mathbf{K}(\Theta) &= \sum_{j=1}^{N_f} \mathbf{G}_j^T \bar{\mathbf{K}}_j \mathbf{G}_j = \sum_{j=1}^{N_f} \mathbf{G}_j^T \mathbf{P}(\Theta)_j^T \mathbf{K}(\Theta)_j \mathbf{P}(\Theta)_j \mathbf{G}_j \\ &= \sum_{j=1}^{N_f} \mathbf{T}(\Theta)_j^T \mathbf{K}(\Theta)_j \mathbf{T}(\Theta)_j \end{aligned} \tag{5.6}$$

where $\mathbf{T}(\Theta)_j$=$\mathbf{P}(\Theta)_j \mathbf{G}_j$. After substituting Equation (5.1) into Equation (5.6) and some manipulations, the stiffness matrix of the simplified model can be represented in a similar form as in Equation (2.1):

$$\mathbf{K}(\Theta) = \sum_{j=1}^{N_f} \sum_{\forall i \in j} \theta_i \mathbf{T}(\Theta)_j^T \mathbf{K}_{si} \mathbf{T}(\Theta)_j = \sum_{i=1}^{N_{sub}} \theta_i \bar{\mathbf{K}}(\Theta)_{si} \tag{5.7}$$

where the effective stiffness contribution of the $i$th substructure is:

$$\bar{\mathbf{K}}(\Theta)_{si} = \sum_{\forall j \ni i} \mathbf{T}(\Theta)_j^T \mathbf{K}_{si} \mathbf{T}(\Theta)_j \tag{5.8}$$

To obtain the effective stiffness contribution of the $i$th substructure, the assembly is performed for all planar frames which include the $i$th substructure ($\forall j \ni i$). For example, when the $i$th substructure is common to planar frames 1 and 2, the stiffness contribution of the $i$th substructure to the system stiffness

matrix is $\theta_i(\mathbf{T}(\Theta)_1^T\mathbf{K}_{si}\mathbf{T}(\Theta)_1 + \mathbf{T}(\Theta)_2^T\mathbf{K}_{si}\mathbf{T}(\Theta)_2)$.

This approach neglects compatibility of deformations in columns which are common to more than one frame. The assumption is acceptable except for tall slender buildings or tube type structures [1]. The system mass matrix is diagonalized by lumping the floor mass and the half masses of columns connected to the floor. The mass moment of inertia of the floor diaphragm is calculated about the vertical axis through the center of mass. Since the proposed Bayesian approach requires repeated solutions of the eigenvalue problem, the computational cost is significantly reduced by using the simplified model.

## 5.2 A Two-Story Three-Dimensional Frame Structure

A two-story frame structure, shown in Figure 5.3, is employed to validate the proposed Bayesian approach for three-dimensional problems. The analytical model is assumed to be identical to the actual structure, and has 48 DOFs (24 rotational DOFs and 24 translational DOFs). Each beam and column is modeled as a substructure. Altogether, the system consists of 16 substructures. For all the cases considered in this example, five fundamental modes are estimated. The modal parameters are measured at 5 DOFs out of the total 48 DOFs. Two configurations of the measured DOFs are shown in Figure 5.4. In addition, three sets of the estimated modal parameters are simulated by perturbing the exact modal parameters with a 5% noise level.

As shown in Table 5.1, the four cases are conducted by changing the damage locations and amount. The modal parameters are measured at the DOFs shown in Figure 5.4 (a). For case 1, the first substructure is subject to a 20% decrease in the stiffness. Case 2 assumes 20% and 40% stiffness decreases in the 10th and 11th substructures, respectively. Case 3 assumes 20% and 40% stiffness decreases in the 1st and 14th substructures, respectively. All the damaged substructures are shown as circled numbers in Figure 5.3.

For cases 1 and 2, the Bayesian method finds the exact damage locations as well as the exact damage amount. Case 3 ranks the actual damage event as the second most

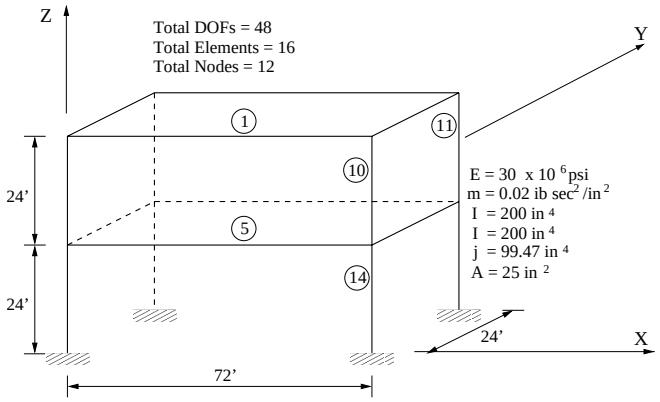


Figure 5.3: A two-story frame structure

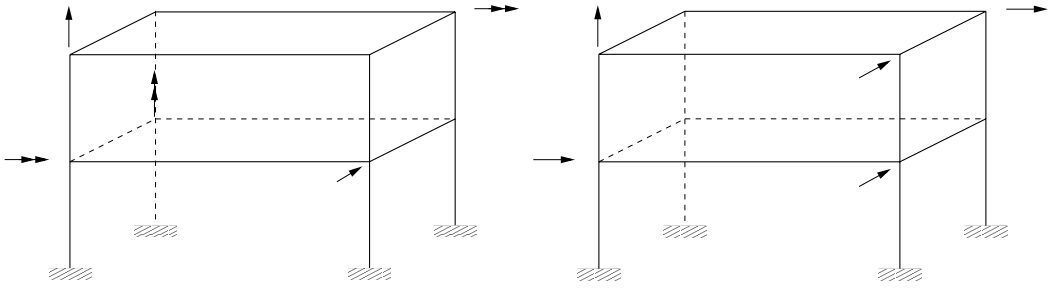

(a) measurement configuration 1
DOFm={3, 16, 28, 32, 48}

(b) measurement configuration 2
DOFm={8, 13, 20, 25, 32}

Figure 5.4: Two different configurations of measured DOFs

probable event; the most probable event corresponds to the actual damage locations (the 1st and 14th substructures) with one extra location (the 11th substructure). After increasing the number of modal data sets from 5 to 10, the actual damage event is properly identified as the most likely one as shown in case 4.

Table 5.1: Diagnosis results of a two-story frame structure

| | Actual Damage | | Estimated Damage | | | |
|---|---|---|---|---|---|---|
| Case | $L_{dam}$ | $D_{dam}$ | $\hat{L}_{dam}$ | $\hat{D}_{dam}$ | $N_s$ | Rank |
| 1 | {1} | {20%} | {1} | {20%} | 5 | 1 |
| 2 | {10,11} | {20%,40%} | {10,11} | {20%,40%} | 5 | 1 |
| 3 | {1,14} | {20%,40%} | {1,11,14} | {20%,20%,40%} | 5 | 1 |
| | | | {1,14} | {20%,40%} | | 2 |
| 4 | {1,14} | {20%,40%} | {1,14} | {20%,40%} | 10 | 1 |

Measured DOFs={3,16,28,32,48}, Estimated Modes={1,2,3,4,5}, Noise=2%, $N_s$=5

Table 5.2: Comparison of two measurement strategies

| Case | DOFm | Rank |
|---|---|---|
| 5 | {3,16,28,32,48} | not found |
| 6 | {8,13,20,25,32} | 1 |

Estimated Modes={1,2,3,4,5}, Noise=2%, $N_s$=5
$L_{dam}$={1,5}, $D_{dam}$={20%,40%}

Table 5.2 investigates the effect of measured DOFs on damage detection by comparing two different configurations of measured DOFs as shown in Figure 5.4. For both cases, 20% and 40% damages are assumed in the first and fifth substructures. Since the actual damage event is not found by the branch-and-bound search for case 5, the rank of the actual damage event is represented as *not found* in Table 5.2. In dynamic analysis, the inertial effects associated with rotational DOFs are usually small. In addition, the axial deformations of beams and columns can be ignored in many cases. As a result, lateral DOFs provide more information than rotational and vertical DOFs. For case 5, three rotational, one vertical and one horizontal DOFs (DOFm={3, 16, 28, 32, 48}) are measured, and for case 6 the measured DOFs {8, 13, 20, 25, 32} are all lateral DOFs. The results of Table 5.2 show that the measured

DOFs in case 6 are more appropriate for the detection of damage in the first and fifth substructures.

## 5.3 A Five-Story Three-Dimensional Frame Structure

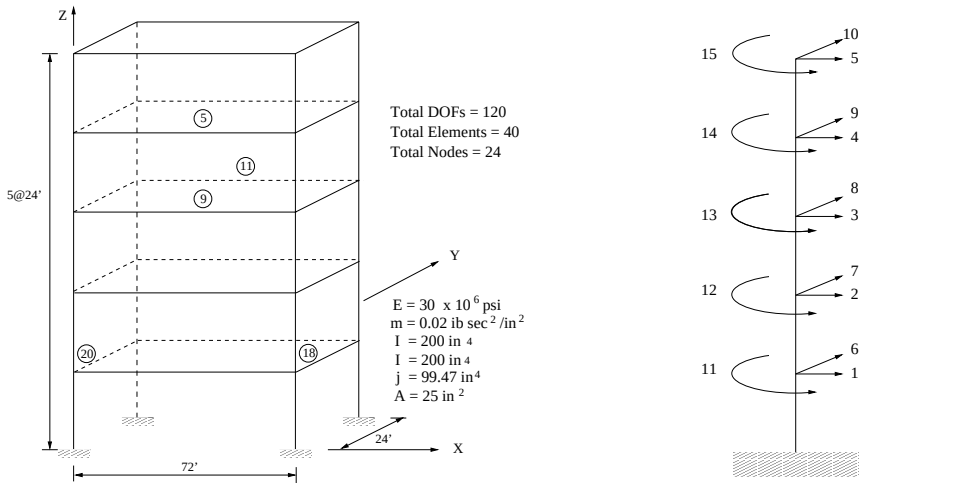


(a) the baseline structure (b) the simplified model

Figure 5.5: The baseline structure and the simplified model of a five-story frame structure

The applicability of the Bayesian probabilistic approach is illustrated when differences exist between the baseline structure and the simplified model. In this example, a finite element (FE) model of a five-story frame structure serves as the baseline structure. The term *baseline structure* is used to represent a structure from which the experimental modal parameters are simulated. The simplified model, which the proposed method works with, is constructed as described in Section 5.1. The system mass matrix is diagonalized by lumping the floor mass and the half masses of columns connected to the floor. The moment of inertia of the floor diaphragm is calculated about the vertical axis through the center of mass. Figure 5.5 (a) and (b) show the baseline structure and the simplified model, respectively. While the baseline structure has 6 DOFs at each node (three translational and three rotational DOFs), the

simplified model has only 3 DOFs at the mass center of each floor. For the current five-story example, the baseline structure has 120 DOFs and the simplified model has 15 DOFs.

### 5.3.1 Damage Detection using Modal Parameters

First, the damage diagnoses are conducted using the modal parameters. The first example neglects the measurement noise to highlight the effect of modeling error, and the second example considers both modeling and noise errors. Furthermore, for the calculation of $e_M(\Theta_{H_o})$ in Equation (2.18), $\hat{\psi}_m^h$ is simulated by perturbing the modal parameters of the initial FE model with noise. $\psi(\Theta_{H_o})$ is obtained by solving an eigenvalue problem of the simplified model. That is, $e_M(\Theta_{H_o})$ is defined as the modal error caused by the difference between the baseline structure and the simplified model.

To simulate the estimated modal vectors of a structure, the modal vector of the FE model is reconstructed at the mass center of every floor. (In many vibration tests of building structures, modal vectors are evaluated at the mass center of the floor diaphragm.) That is, the components of the estimated modal vector correspond directly with those of the simplified model. The first six fundamental modes are assumed to be estimated. The first and fourth modes are the first and second bending modes, respectively, in the X-direction. The second and fifth modes are the first and second bending modes, respectively, in the Y-direction. Furthermore, the third and sixth modes correspond to the first and second torsional modes, respectively.

#### Consideration of Modeling Error

Table 5.3 shows the diagnosis results of three different damage scenarios, considering the difference between the baseline structure and the simplified model. Case 1 assumes a 50% stiffness decrease in the 5th and the 9th substructures. For case 2, 40% and 60% decreases in the stiffness are imposed on the 9th and 11th substructures, respectively. Case 3 assumes 20% and 10% stiffness decreases in the 18th and 20th substructures, respectively. Figure 5.5 (a) shows the damaged substructures as circled numbers. Beams and columns in the baseline structure are defined as substructures.

Since the stiffness matrix of the simplified system is represented as an assembly of the effective stiffness contribution of each substructure [see Equation (5.7)], damage locations can be tracked at the substructure level of the baseline structure. That is, damage locations are identified in the baseline structure, not in the simplified model.

For all cases, the Bayesian approach properly identifies the actual damage locations. The estimated damage amount is, however, slightly different from the actual damage amount for cases 1 and 2. This result can be explained as follows: We search for the most likely hypothesis $H_{max}$ and the corresponding non-dimensional parameter value $\Theta_{H_{max}}^{max}$ which minimize the approximated error function $J(\hat{\Psi}_{N_s}, \Theta_{H_j})$ defined in Equation (2.22). For the exact definition of $J(\hat{\Psi}_{N_s}, \Theta_{H_j})$, the modal error caused by the modeling error after damage occurrence $e_M(\Theta_{H_d})$ should be evaluated. However, the actual damage locations and amount, which are required to evaluate $e_M(\Theta_{H_d})$, are unknown. Therefore, $e_M(\Theta_{H_d})$ is approximated by $e_M(\Theta_{H_o})$, which is the modal error caused by the modeling error before damage occurrence, assuming that the modeling error is constant for arbitrary damage locations and amount ($e_M(\Theta_{H_j}) \cong e_M(\Theta_{H_o})$; $\forall \Theta_{H_j}$).

Table 5.3: Effect of modeling error in a five-story frame structure

| | Actual Damage | | Estimated Damage | | |
|---|---|---|---|---|---|
| case | $L_{dam}$ | $D_{dam}$ | $\hat{L}_{dam}$ | $\hat{D}_{dam}$ | $N_s$ |
| 1 | {5,9} | {50%,50%} | {5,9} | {60%,50%} | 1 |
| 2 | {9,11} | {40%,60%} | {9,11} | {50%,70%} | 1 |
| 3 | {18,20} | {20%,10%} | {18,20} | {20%,10%} | 1 |

Noise=0%, Measured DOFs={1,2,...,15}, Estimated Modes={1,2,...,6}

For comparison of $e_M(\Theta_{H_o})$ and $e_M(\Theta_{H_j})$, the selected components of $e_M(\Theta_{H_o})$ and $e_M(\Theta_{H_j})$ are listed in Table 5.4. The error components corresponding to the first six frequencies are shown in part (a) of Table 5.4. Next the error components corresponding to the measured modal vectors are presented in part (b) of the table. For simplicity, only the components corresponding to the DOFs 1 - 5 are tabulated for the first and fourth modal vectors (the first two bending modes along the X-direction). Similarly, the components corresponding to the DOFs 6 - 10 are presented

Table 5.4: Comparison of $e_M(\Theta_{H_o})$ and $e_M(\Theta_{H_j})$

| | $\psi_i(\Theta_{H_o})$ | $e_{M,i}(\Theta_{H_o})$ | $e_{M,i}(\Theta_{H_j})$ | | |
|---|---|---|---|---|---|
| | | | Case 1 | Case 2 | Case 3 |
| | | (a) Components corresponding to the frequencies | | | |
| Mode | $\omega_i$ | | | | |
| 1 | 1.7313 | 0.0030 | 0.0053 (0.13%) | 0.0035 (0.02%) | 0.0030 (0.00%) |
| 2 | 2.4566 | 0.0281 | 0.0282 (0.00%) | 0.0282 (0.00%) | 0.0281 (0.00%) |
| 3 | 2.9106 | 0.0070 | 0.0079 (0.03%) | 0.0082 (0.04%) | 0.0076 (0.02%) |
| 4 | 5.7511 | 0.0157 | 0.0014 (0.30%) | 0.0078 (0.14%) | 0.0157 (0.00%) |
| 5 | 7.6658 | 0.0935 | 0.0943 (0.01%) | 0.0948 (0.02%) | 0.0948 (0.02%) |
| 6 | 9.1053 | 0.0956 | 0.0557 (0.44%) | 0.0415 (0.59%) | 0.0981 (0.03%) |
| | | (b) Components corresponding to the modal vectors | | | |
| DOF | $\mathbf{v}_1$ | | | | |
| 1 | 0.1559 | 0.0003 | 0.0002 (0.06%) | 0.0002 (0.05%) | 0.0003 (0.00%) |
| 2 | 0.4274 | 0.0009 | 0.0004 (0.12%) | 0.0006 (0.05%) | 0.0009 (0.00%) |
| 3 | 0.6865 | 0.0013 | 0.0001 (0.17%) | 0.0011 (0.03%) | 0.0013 (0.00%) |
| 4 | 0.8822 | 0.0012 | 0.0007 (0.06%) | 0.0011 (0.02%) | 0.0012 (0.00%) |
| 5 | 1.0000 | 0.0000 | 0.0000 (0.00%) | 0.0000 (0.00%) | 0.0000 (0.00%) |
| DOF | $\mathbf{v}_2$ | | | | |
| 6 | 0.1998 | 0.0014 | 0.0014 (0.00%) | 0.0014 (0.00%) | 0.0015 (0.03%) |
| 7 | 0.4834 | 0.0029 | 0.0029 (0.00%) | 0.0029 (0.00%) | 0.0031 (0.02%) |
| 8 | 0.7312 | 0.0032 | 0.0032 (0.00%) | 0.0032 (0.00%) | 0.0033 (0.01%) |
| 9 | 0.9077 | 0.0018 | 0.0018 (0.00%) | 0.0018 (0.00%) | 0.0019 (0.01%) |
| 10 | 1.0000 | 0.0000 | 0.0000 (0.00%) | 0.0000 (0.00%) | 0.0000 (0.00%) |
| DOF | $\mathbf{v}_3$ | | | | |
| 11 | 0.1987 | 0.0001 | 0.0002 (0.03%) | 0.0002 (0.02%) | 0.0002 (0.05%) |
| 12 | 0.4849 | 0.0022 | 0.0019 (0.07%) | 0.0018 (0.08%) | 0.0020 (0.04%) |
| 13 | 0.7345 | 0.0029 | 0.0027 (0.02%) | 0.0031 (0.04%) | 0.0029 (0.01%) |
| 14 | 0.9102 | 0.0013 | 0.0016 (0.03%) | 0.0019 (0.06%) | 0.0014 (0.01%) |
| 15 | 1.0000 | 0.0000 | 0.0000 (0.00%) | 0.0000 (0.00%) | 0.0000 (0.00%) |
| DOF | $\mathbf{v}_4$ | | | | |
| 1 | 0.4996 | 0.0005 | 0.0006 (0.04%) | 0.0005 (0.01%) | 0.0005 (0.00%) |
| 2 | 0.9619 | 0.0022 | 0.0011 (0.11%) | 0.0002 (0.21%) | 0.0022 (0.00%) |
| 3 | 0.6984 | 0.0084 | 0.0059 (0.36%) | 0.0071 (0.19%) | 0.0084 (0.00%) |
| 4 | -0.1532 | 0.0119 | 0.0103 (1.05%) | 0.0119 (0.01%) | 0.0119 (0.00%) |
| 5 | -1.0000 | 0.0000 | 0.0000 (0.00%) | 0.0000 (0.00%) | 0.0000 (0.00%) |
| DOF | $\mathbf{v}_5$ | | | | |
| 6 | 0.5963 | 0.0004 | 0.0003 (0.01%) | 0.0003 (0.01%) | 0.0013 (0.15%) |
| 7 | 1.0000 | 0.0000 | 0.0000 (0.00%) | 0.0000 (0.00%) | 0.0000 (0.00%) |
| 8 | 0.6238 | 0.0017 | 0.0016 (0.02%) | 0.0016 (0.02%) | 0.0024 (0.11%) |
| 9 | -0.2603 | 0.0020 | 0.0022 (0.06%) | 0.0025 (0.18%) | 0.0025 (0.17%) |
| 10 | -0.9869 | 0.0071 | 0.0069 (0.03%) | 0.0062 (0.10%) | 0.0070 (0.09%) |
| DOF | $\mathbf{v}_6$ | | | | |
| 11 | 0.5824 | 0.0021 | 0.0180 (2.73%) | 0.0319 (5.12%) | 0.0038 (0.29%) |
| 12 | 0.9756 | 0.0053 | 0.0447 (4.04%) | 0.0748 (7.12%) | 0.0015 (0.39%) |
| 13 | 0.5881 | 0.0125 | 0.0529 (6.86%) | 0.0855 (12.4%) | 0.0095 (0.51%) |
| 14 | -0.2931 | 0.0164 | 0.0348 (6.30%) | 0.0466 (10.3%) | 0.0148 (0.54%) |
| 15 | -1.0000 | 0.0000 | 0.0000 (0.00%) | 0.0000 (0.00%) | 0.0000 (0.00%) |

*The value in ( ) represents the normalized error, $100 \times |e_{M,i}(\Theta_{H_o}) - e_{M,i}(\Theta_{H_j})|/\psi_i(\Theta_{H_o})$, in percentage

Table 5.5: Effect of modeling and noise errors in a five-story frame structure

| | Actual Damage | | Estimated Damage | | |
|---|---|---|---|---|---|
| case | $L_{dam}$ | $D_{dam}$ | $\hat{L}_{dam}$ | $\hat{D}_{dam}$ | $N_s$ |
| 1 | {5,9} | {50%,50%} | {5,9} | {60%,50%} | 5 |
| 2 | {9,11} | {40%,60%} | {9,11} | {50%,70%} | 10 |
| 3 | {18,20} | {20%,10%} | {18,20} | {20%,10%} | 10 |

Noise=5%, Measured DOFs={1,2,...,15}, Estimated Modes={1,2,...,6}

for the second and fifth modal vectors (the first two bending modes along the Y-direction), and the components corresponding to the DOFs 11 - 15 are presented for the third and sixth modal vectors (the first two torsional modes). $e_M(\Theta_{H_j})$ is computed for the three damage cases in Table 5.3. To provide a relative measure on the magnitude of $e_M(\Theta_{H_o})$, the components of $\psi(\Theta_{H_o})$ corresponding to those of $e_M(\Theta_{H_o})$ are presented in the first column of each table. Furthermore, a normalized error defined as $100 \times |e_{M,i}(\Theta_{H_o}) - e_{M,i}(\Theta_{H_j})|/\psi_i(\Theta_{H_o})$ is parenthesized next to each $e_{M,i}(\Theta_{H_j})$ value.

For cases 1 and 2 of Table 5.4, larger differences between $e_M(\Theta_{H_j})$ and $e_M(\Theta_{H_o})$ than those of case 3 are observed especially in the components corresponding to mode 6. This explains why the estimated damage amount is slightly different from the actual damage amount for cases 1 and 2. It appears that $|e_{M,i}(\Theta_{H_o}) - e_{M,i}(\Theta_{H_j})|$ increases for higher modes. However, the magnitude of $|e_{M,i}(\Theta_{H_o}) - e_{M,i}(\Theta_{H_j})|$ remains less than 1 % of the corresponding $\psi_i(\Theta_{H_o})$ for most components. Since the damage amount is small in case 3, the change of the modeling error is negligible, and the Bayesian approach identifies the exact damage amount as well as the correct damage locations. This example illustrates that it is possible to simplify a model and to reduce the size of the system without losing significant accuracy.

### Consideration of Modeling and Noise Errors

In the following example, the measurement noise and the modeling error are taken into account together to validate the robustness of the Bayesian approach. The same damage scenarios in Table 5.3 are re-investigated. The only difference from the previous cases is that the modal parameters of the FE model are corrupted with

5% noise. Table 5.5 summarizes the diagnosis results. After increasing the number of modal data sets to a certain number, the Bayesian approach identifies the actual damage locations even in the presence of the measurement noise and the discrepancy between the baseline structure and the simplified model.

### 5.3.2 Damage Detection using Ritz Vectors

The five-story three-dimensional frame structure shown in Figure 5.5 is employed again to illustrate the applicability of Ritz vectors to damage detection when differences exist between the baseline structure and the simplified model. Similar to modal vectors, the components of the estimated Ritz vector coincide with those of the simplified model. Loads applied to the baseline structure are also converted to equivalent forces in the simplified model using the displacement transformation matrix which relates the DOFs of the baseline structure to the mass center DOFs of the simplified model. Furthermore, for the calculation of the modeling errror $e_M(\Theta_{H_o})$ in Equation (2.20), the sample mean $\hat{\psi}_m^h$ is computed from the Ritz vectors of the initial FE model without damage. The analytical data set $\psi(\Theta_{H_o})$ is obtained from the simplified model following Equations (3.25) to (3.29). Six Ritz vectors are estimated from the load patterns shown in Figure 5.6. Compared to the previous eight-bay truss example, in which the estimated Ritz vectors are insensitive to most face diagonals and battens, the frame example in this subsection has less redundancy and the estimated Ritz vectors are reasonably sensitive to all substructures. Therefore, the damage threshold is set to 0.9 for every substructure.

The first example neglects the measurement noise to highlight the effect of modeling error. In the second example, both modeling error and measurement noise are considered.

#### Diagnosis of Damage Cases with Modeling Error

To highlight the effect of modeling error, the effect of measurement noise is neglected in this example. Table 5.6 summarizes the diagnoses of eight different damage cases using the first six Ritz vectors generated from load pattern 1 shown in Figure 5.6 (a). The damaged substructures in Table 5.6 are shown as circled numbers in Figure 5.5.

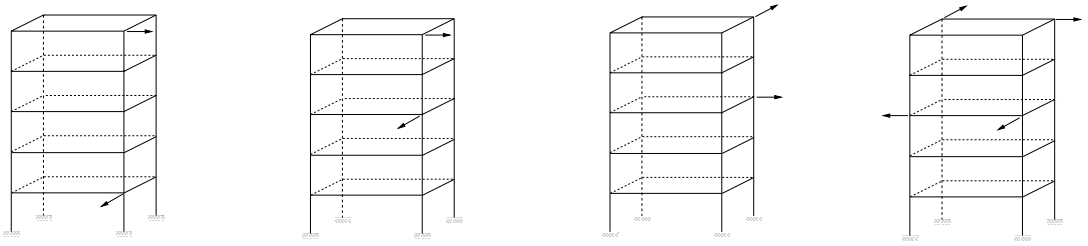

(a) Load Pattern 1 (b) Load Pattern 2 (c) Load Pattern 3 (d) Load Pattern 4

Figure 5.6: Load patterns applied to a five-story frame structure

For cases C, D, E and G of Table 5.6, the Bayesian approach ranks the actual damage

Table 5.6: Damage diagnoses of a five-story frame structure considering modeling error

| | Actual Damage | | | Most Prob. Damage | |
|---|---|---|---|---|---|
| Case | $L_{dam}$ | $D_{dam}$ | Rank[1] | $\hat{L}_{dam}$ | $\hat{D}_{dam}$ |
| A | {5} | {10%,10%} | 51/266 | {5,25} | {10%,10%} |
| B | {5,9} | {10%,10%} | 8/266 | {5,9,25} | {10%,10%,10%} |
| C | {13,20} | {10%,10%} | 1/303 | {13,20} | {10%,10%} |
| D | {25,28} | {10%,10%} | 1/193 | {25,28} | {10%,10%} |
| E | {25,30} | {10%,10%} | 1/266 | {25,30} | {20%,10%} |
| F | {9,25} | {10%,10%} | 2/266 | {9,25,28} | {10%,10%,10%} |
| G | {34,38} | {10%,10%} | 1/266 | {34,38} | {10%,10%} |
| H | {26,29} | {10%,10%} | 7/230 | {25,26,29} | {10%,10%,10%} |

1. The first number is the rank of the actual damage event and the second is the total number of the examined hypotheses.
2. The first six Ritz vectors are estimated from load pattern 1 in Figure 5.6.
3. $N_s$=1 and Noise=5%.
4. Damage threshold is set to 0.9 for all substructures.

event as the most likely damage event. In each of cases A, B, F and H, the actual damage locations are included in the most probable damage event, which the proposed method identifies. However, undamaged substructures are also mistakenly included in the most probable damage events. For example, in case B, the proposed Bayesian approach diagnoses that damage is most likely located in the 5th, 9th and 25th substructures. While the 5th and 9th substructures are actually damaged, the 25th substructure is mistakenly included. This result can be explained as follows: We

search for the most likely hypothesis $H_{max}$ and the corresponding nondimensional parameter value $\Theta_{H_{max}}^{max}$ which minimizes the approximated error function $J(\hat{\Psi}_{N_s}, \Theta_{H_j})$ defined in Equation (2.22). For the exact definition of $J(\hat{\Psi}_{N_s}, \Theta_{H_j})$, $e_M(\Theta_{H_d})$, which is the output error caused by the modeling error after damage occurrence, should be evaluated instead of $e_M(\Theta_{H_o})$. Since the actual damage locations and amount, which are required to evaluate $e_M(\Theta_{H_d})$, are unknown, $e_M(\Theta_{H_d})$ is approximated by $e_M(\Theta_{H_o})$. Here, $e_M(\Theta_{H_o})$ is the output error caused by the modeling error before damage occurrence, assuming that the modeling error is constant for arbitrary damage locations and damage amount. Since the Ritz vectors are very sensitive to the stiffness change, it appears that a relatively large difference between $e_M(\Theta_{H_d})$ and $e_M(\Theta_{H_o})$ may exist even for the small damage amount like the 10% stiffness loss presented in the example here. This difference explains why the undamaged substructures are mistakenly included in the most probable damage event in cases A, B, F and H. This also explains why the estimated damage amount is slightly different from the actual damage amount in case E. However, using the simplified model, we are able to reduce the size of the system from 120 DOFs to 15 DOFs without sacrificing significant accuracy.

The eight damage cases are re-diagnosed in Table 5.7 employing four different load patterns and a combination of the load patterns. For comparison, the results of diagnoses using modal vectors are also presented in the 6th column of Table 5.7 (denoted as MV in the table). Except for changing the load patterns, all the other conditions remain the same as the cases shown in Table 5.6. Table 5.7 shows that a careful selection of load patterns can improve diagnoses of damage and, in general, Ritz vectors provide better diagnoses than modal vectors. For example, by imposing load pattern 1 on the frame structure, the Bayesian approach identifies the actual damage locations in four out of eight cases (cases C, D, E and G). Even for the other four cases (cases A, B, F and H), all the actual damage locations are included in the most probable damage event. Load pattern 2 fails to detect the actual damage event in case H, load pattern 3 does not find the actual damage event of case E, and load pattern 4 ranks the actual damage event as the most probable one only for case G. When all four load patterns are employed simultaneously (the last column of

Table 5.7: Damage diagnoses of a five-story frame structure using different load patterns

| | The rank of the actual damage event[2] | | | | | |
|---|---|---|---|---|---|---|
| Case[1] | F1[3] | F2 | F3 | F4 | MV[4] | All F's[5] |
| A | 51/266 | 3/230 | 3/230 | 18/255 | 32/266 | 1/155 |
| B | 8/266 | 3/266 | 7/266 | 15/266 | 20/266 | 6/266 |
| C | 1/303 | 2/266 | 1/375 | 5/155 | 100/193 | 1/230 |
| D | 1/193 | 1/230 | 1/193 | 14/230 | -/155 | 2/155 |
| E | 1/266 | 4/266 | -/41 | 2/337 | -/41 | 1/266 |
| F | 2/266 | 2/266 | 1/266 | 2/266 | -/80 | 1/302 |
| G | 1/266 | 1/267 | 2/303 | 1/303 | 5/266 | 1/267 |
| H | 7/230 | -/41 | 3/266 | 2/338 | -/41 | 1/302 |

1. The damage cases here are identical to the damage cases in Table 5.6.
2. The first number is the rank of the actual damage event and the second is the total number of the examined hypotheses. "-" denotes that actual damage event is not detected.
3. In F1, F2, F3 and F4, the first six Ritz vectors are estimated from load patterns 1, 2, 3 and 4, respectively.
4. In MV, the first six modal vectors are estimated.
5. Load patterns 1 to 4 are employed and the first six Ritz vectors are generated from each load pattern.

Table 5.7), the rank of the actual damage event is improved for most damage cases.

### Diagnosis of Damage Cases with Modeling Error and Measurement Noise

In this example, both modeling error and measuring noise are included. To simulate the measurement noise, the analytical Ritz vectors generated from the baseline structure are perturbed with a 5% noise level using Equation (3.35). In addition, the number of data sets ($N_s$) is increased from 1 to 20. Since the use of all the four load patterns provides the best diagnosis in the previous examples, all of the load patterns are again employed in this example. Table 5.8 summarized the results for the eight cases, which have been diagnosed in the previous example. The results indicate that (1) the diagnoses provided by the proposed method improve as the number of data sets increases, and (2) if load patterns are selected carefully and a large number of data sets are available, the proposed method can identify the actual locations and amount of damage even in the presence of measurement noise and modeling error.

Table 5.8: Damage diagnoses of a frame structure considering modeling error and measurement noise

| | The Rank of The Actual Damage Event[2] | | | | Most Prob. Damage[3] | |
|---|---|---|---|---|---|---|
| Case[1] | $N_s = 1$ | $N_s = 5$ | $N_s = 10$ | $N_s = 20$ | $\hat{L}_{dam}$ | $\hat{D}_{dam}$ |
| A | 12/230 | 5/230 | 2/195 | 1/155 | {5} | {10%} |
| B | 65/303 | 4/266 | 2/266 | 2/266 | {4,5,9} | {10%,10%,10%} |
| C | 10/213 | 4/155 | 2/193 | 3/193 | {9,20} | {10%,10%} |
| D | 6/155 | 5/155 | 3/155 | 2/155 | {28} | {20%} |
| E | 1/303 | 1/299 | 1/266 | 1/303 | {25,30} | {10%,10%} |
| F | 2/303 | 1/266 | 1/374 | 1/303 | {9,25} | {10%,10%} |
| G | 1/230 | 1/267 | 1/267 | 1/267 | {35,38} | {10%,10%} |
| H | 1/337 | 1/337 | 1/337 | 1/266 | {25,26} | {10%,10%} |

1. The damage cases here are identical to the previous damage cases in Table 5.6.
2. The first number is the rank of the actual damage case and the second is the total number of the examined hypotheses.
3. $\hat{L}_{dam}$ and $\hat{D}_{dam}$ are identified using all the four load patterns and $N_s = 20$

## 5.4 A Reinforced-Concrete Bridge Column

In this section, the proposed Bayesian approach is applied to locate the plastic hinge of a concrete bridge column based on the data obtained from the vibration tests coducted at the University of California, Irvine (UCI).

A series of bridge column tests were conducted at the University of California, Irvine as a research project with the California Department of Transportation (CALTRANS). The main purpose of the tests was to study the relative strength and ductility provided by two seismic-retrofit procedures for reinforced-concrete bridge columns. The first procedure increased the diameter of an original column with cast-in-place concrete. The second procedure increased the diameter of the column using shotcrete sprayed onto the exterior of the original column. Incremental cyclic load tests were performed on the bridge columns with and without the retrofit procedures. Static lateral loads were incrementally applied to the top of a column until the ultimate load capacity of the column was reached. The column was cycled three times after each load increment and modal analysis was conducted after each cyclic load testing. The experimental modal analysis of the columns was performed by the Engineering

Analysis Group of the Los Alamos National Laboratory (LANL). [1]

### 5.4.1 Description of Experimental Setup

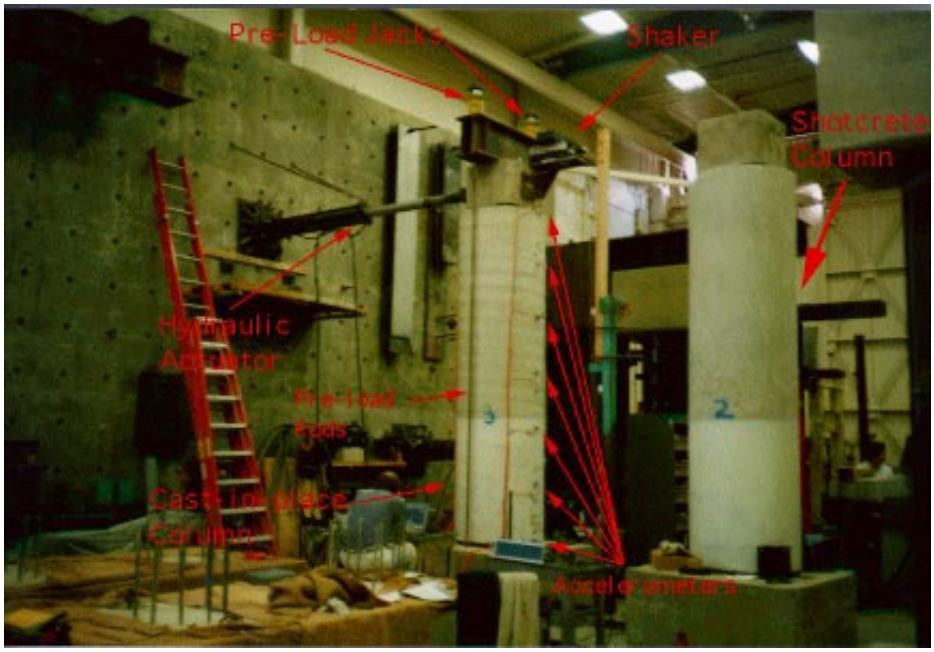


Figure 5.7: UC Irvine test configuration (Courtesy of the Los Alamos National Laboratory)

Two concrete bridge columns were employed in the test. The diameter of each column was retrofitted from 24 *in* (61.0 *cm*) to 36 *in* (91.4 *cm*). The first column was retrofitted by placing forms around the existing column and placing additional concrete within the form. The diameter of the second column was extended by spraying concrete in a process referred to as shotcreting. The shotcreted column was then polished with a trowel to obtain a circular cross section. The vibration test data obtained from the first column were employed for modal analysis and damage detection in this study.

Figure 5.7 shows the configuration of the test column. The column employed in this study was cast on top of a 56 $in^2$ (361.3 *cm*) concrete foundation with a height

[1] A detailed description of the columns and the data obtained from the tests are provided on the web site "http://esaea-www.esa.lanl.gov/damage_id".

of 25 *in* (63.5 *cm*). A 25 $in^2$ (161.3 *cm*) concrete block was placed on the top of the column, and a hydraulic actuator for the static cyclic testing and an electro-magnetic shaker for the modal analysis were attached to this block. As is typical of actual retrofit in the field, a 1.5 *in* (3.8 *cm*) gap was left between the top of the foundation and the bottom of the column part. Therefore, the vertical reinforcement in the retrofitted portion of the column did not extend into the foundation. Since the concrete foundation was bolted to the laboratory floor, the bottom of the foundation was not moved once testing started. An inner circle of 10 #6 vertical rebars with a yield strength of 74.9 ksi (516.4 MPa) were embedded within the initial 24 *in* (61.0 *cm*) column. These rebars were enclosed by a spiral cage of #2 rebars with a yield strength 30 ksi (206.9 MPa) and spaced at 7 *in* (17.8 *cm*) pitch. The retrofit jacket had 16 #8 vertical rebars with a yield strength of 60 ksi (414.0 MPa). These rebars were enclosed by a spiral cage of #6 rebars spaced at 6 *in* (15.2 *cm*) pitch.

Cyclic lateral loads were applied to the top of the column using an hydraulic actuator. The loads were first applied in a force-controlled manner to produce lateral deformations at the top of the column, corresponding to $0.25\Delta y_T$, $0.5\Delta y_T$, $0.75\Delta y_T$, and $\Delta y_T$, respectively. Here $\Delta y_T$ is the lateral deformation corresponding to the theoretical first yield of the longitudinal reinforcement. The structure was cycled three times at each load level. Based on the observation of these responses under force-controlled loadings, a lateral deformation corresponding to the actual first yield, $\Delta y$, was calculated. [2] Next, the loading was increased in a displacement-controlled manner corresponding to $\Delta y$, $1.5\Delta y$, $2.5\Delta y$, $4.0\Delta y$ and $7.0\Delta y$, respectively. The incremental loadings caused continuous deterioration of the column stiffness. The formation of a plastic hinge was observed between the top of the foundation and the bottom of the retrofit jacket.

For the modal analysis, the column was excited by an APS electro-magnetic shaker mounted at the top of the column. As shown in Figure 5.8, the shaker rested on a steel plate attached to the concrete top, and the shaker was mounted off the axis to excite torsional modes. Note that the actuator was operated in an open-loop mode

[2] A detailed summary of the calculation of the actual first yielding deformation can be found in "http://www.ics.uci.edu/~athomas/caltrans".

and there was a significant feedback to the actuator through the steel plate. This feedback resulted in a poor band-limited white noise excitation to the column and rendered the identification of modal parameters difficult.

The exciting force was measured with an accelerometer mounted to the sliding mass of the shaker 0.18 $lb\text{-}s^2/in$ (31.5 kg). The same magnitude of excitation was used in all tests. Figure 5.9 shows the locations of the forty accelerometers mounted. Locations 2, 39 and 40 had PCB 302A accelerometers with a nominal sensitivity 10mV/g. Since these accelerometers were found not to be sensitive enough to measure the desired vibration quantities, the acceleration data from these sensors were excluded for modal analysis. Wilcoxon 736t accelerometers with a nominal sensitivity of 100mV/g were placed in locations 33, 34, 35, 36 and 37. All other locations had PCB 336C accelerometers with a nominal sensitivity of 1V/g. Accelerometers 36 and 37 were located 8 $in$ (20.3 $cm$) off the axis in the y direction.

Data were sampled and processed with an HP 3566A dynamic data acquisition system. Frequency response functions (FRFs), auto and cross power spectra, and coherence functions were measured in the range of 0 to 400 Hz. Each spectrum was calculated from 30 averages of 2 second duration time histories with 2048 sampling points. This sampling rate produced a frequency resolution of 0.5 Hz. Time history measurements and FRF analysis were conducted after each cyclic load test was done at the deformation levels, $\Delta y$, $1.5\Delta y$, $2.5\Delta y$, $4.0\Delta y$, and $7.0\Delta y$, respectively. For simplicity, the tests corresponding to the deformation level, $\Delta y$, $1.5\Delta y$, $2.5\Delta y$, $4.0\Delta y$, and $7.0\Delta y$, are labeled hereafter as Test 1, Test 2, Test 3, Test 4, and Test 5, respectively. Furthermore, the vibration test prior to any cyclic loading is referred to as Test 0.

### 5.4.2 Analytical Modeling

Two analytical models are constructed for damage detection. The first model (Model 1) consists of 9 beam elements and the second model (Model 2) has 27 beam elements (see Figure 5.10 and Figure 5.11). Each node of a beam element has three translational DOFs and three rotational DOFs. Therefore, Models 1 and 2 have a total of 54 and 162 DOFs, respectively. An elastic modulus of $3.6\times10^6$ psi ($2.48\times10^4$ MPa), a mass

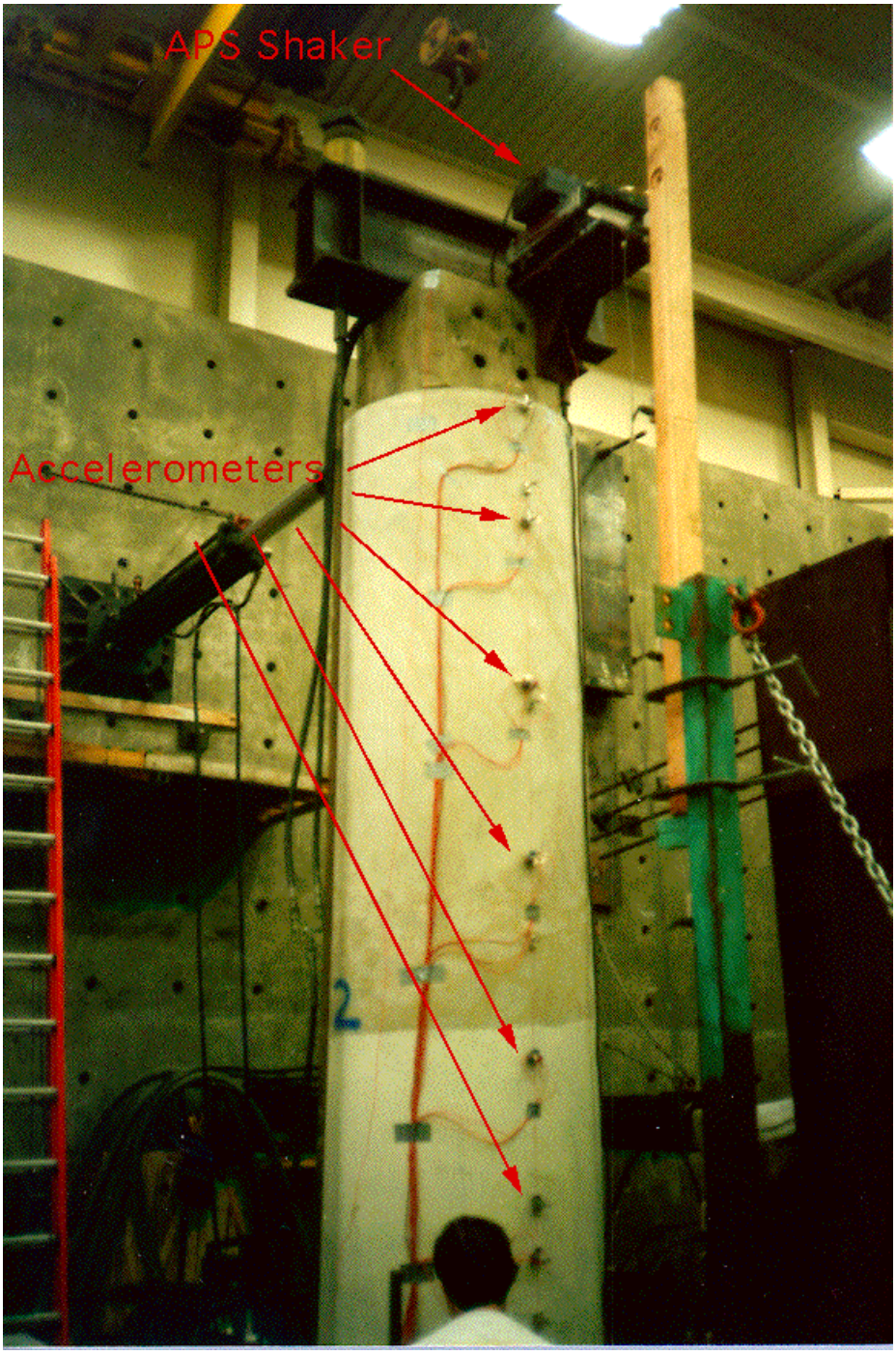


Figure 5.8: A shaker and accelerometers for UC Irvine test (Courtesy of the Los Alamos National Laboratory)

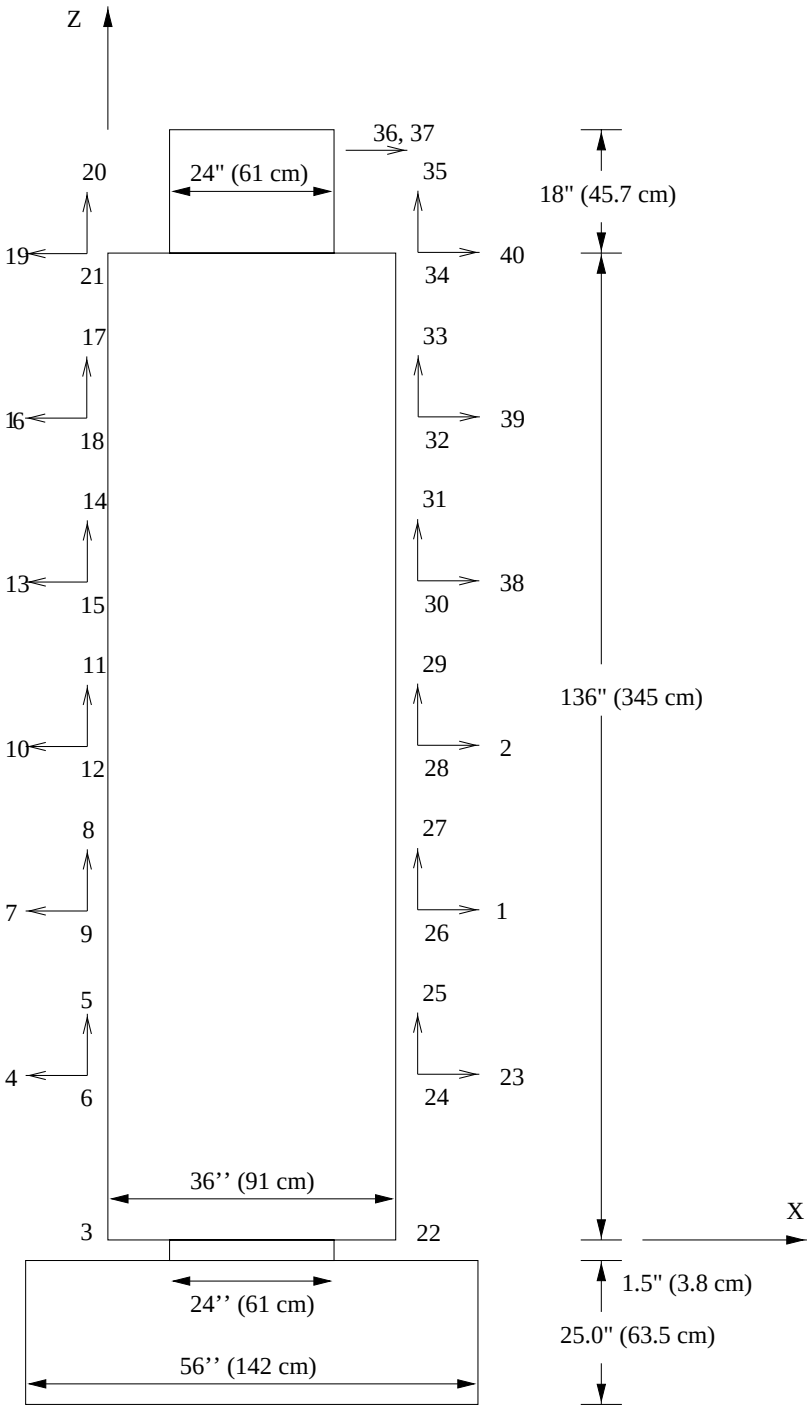


Figure 5.9: Dimensions and accelerometer locations of UC Irvine column test

density of $2.17\times10^{-4}$ $lb\text{-}s^2/in^4$ ($2.32\times10^{-3}$ $kg/cm^3$, and a Poission's ratio of 0.2 are specified in the models. The DOFs at the base of the foundation were constrained for translation and rotation.

To construct the system mass matrix, the lumped mass $m$ and the mass moments of inertia $I^M$ are computed as: $m = \gamma\times\pi r^2\times h$, $I_x^M$, $I_y^M = \frac{1}{12}m(3r^2+h^2)$ and $I_Z^M = \frac{1}{2}mr^2$. Here, $\gamma$ is a mass density of $2.17\times10^{-4}$ $lb\text{-}s^2/in^4$ ($2.32\times10^{-3}$ $kg/cm^3$), $r$ is the radius of the column, and $h$ is the height of the tributary area. Furthermore, the masses of the actuator and the steel plate are added to the top node of the column (Node 10 in Figure 5.10 and Node 28 in Figure 5.11, respectively). Next, the analytical models are slightly refined based on engineering judgment to match the measured model parameters. The refinement mainly focuses on the consideration of the reinforcement steel, the estimation of the mass moments of inertia of the steel plate and the actuator, and the connection modeling between the foundation and the column.

Table 5.9: Natural frequencies (Hz) from the test and the analytical models

| | Test 0 | Model 1* | Model 2* | Model 3† | Model 4† |
|---|---|---|---|---|---|
| 1st Bending | 27.82 | 26.55 | 25.38 | 19.10 | 25.60 |
| 1st Torsion | 110.42 | 115.87 | 116.04 | 114.00 | 131.00 |
| 2nd Bending | 147.51 | 150.62 | 146.37 | 124.00 | 136.00 |
| 1st Axial | - | 206.36 | 201.35 | 181.00 | 204.00 |
| 2nd Torsion | 272.83 | 276.04 | 276.63 | 351.00 | 389.00 |
| 3rd Bending | 340.71 | 374.03 | 362.36 | 306.00 | 319.00 |

* Models 1 and 2 are shown in Figures 5.10 and 5.11, respectively. † Models 3 and 4 are constructed at the Los Alamos National Laboratory.

The natural frequencies from the test data and two analytical models are summarized in Table 5.9. Table 5.9 shows the first three bending modes in the X direction, the first two torsional modes, and first axial mode. The second column of Table 5.9 shows the estimated natural frequencies from the experimental modal analysis of the undamaged column (Test 0). The experimental modal analysis fails to identify the first axial mode. The natural frequencies obtained from Models 1 and 2 are also tabulated. In addition, the natural frequencies of two additional models (Models 3 and 4) constructed at the LANL using a finite element analysis software, ABAQUS are also

presented in the table. Model 3 is constructed using 8-node continuum elements and has 20,979 DOFs. While Model 4 is constructed using 3-node beam elements and has 114 DOFs. Reinforcement is not incorporated into the LANL models. Because of the symmetry of the column, identical bending modes occur in both X and Y directions at the same natural frequencies. Only the bending modes in the X direction are presented here.

Note that the orders of the second torsion and third bending modes in Models 1 and 2 are switched for Models 3 and 4. It appears that the differences between the models in this study (Models 1 and 2) and the LANL models (Models 3 and 4) arise mainly from the differences in the consideration of reinforcement, the addition of actuator and steel plate masses, and the computation of the mass moment of inertia. We can observe that since the reinforcement is included in Models 1 and 2, the bending mode frequencies of these models are higher than those of the LANL models. In contrast, the torsional mode frequencies in the LANL models are higher than those of Models 1 and 2. The inclusion of the actuator and steel plate masses, and the mass moment of inertia computed for Models 1 and 2 seem to have lowered the frequencies of corresponding torsional modes.

Since the measurement points on the test column do not coincide with the DOFs of the analytical model, the displacements at the measurement points are reconstructed at the DOFs of the analytical model. Figure 5.12 shows the displacement transformation matrix that relates the acceleration measurement points ($X_l$, $Y_l$, $Z_l$, $X_r$, $Y_r$ and $Z_r$) to the DOFs of the analytical model ($X_c$, $Y_c$, $Z_c$, $R_x$, $R_y$ and $R_z$). All measured modal vectors are reconstructed at the analytical DOFs after the displacement transformation. However, it should be noted that there are not sufficient accelerometers installed to reconstruct the estimated modal vectors at all the DOFs in the analytical model. That is, the components of the estimated modal vectors corresponding to the nodes 2, 3 and 10 in the analytical model of Figure 5.10 could not be obtained from the measurement points. For a graphical display of the measured modal vectors, the uninstrumented DOFs corresponding to the nodes 2, 3 and 10 in Figure 5.10 are simply assumed to be identical to adjacent nodes. For example, the displacements at nodes 2, 3 and 10 are set identical to the displacements at nodes 1,

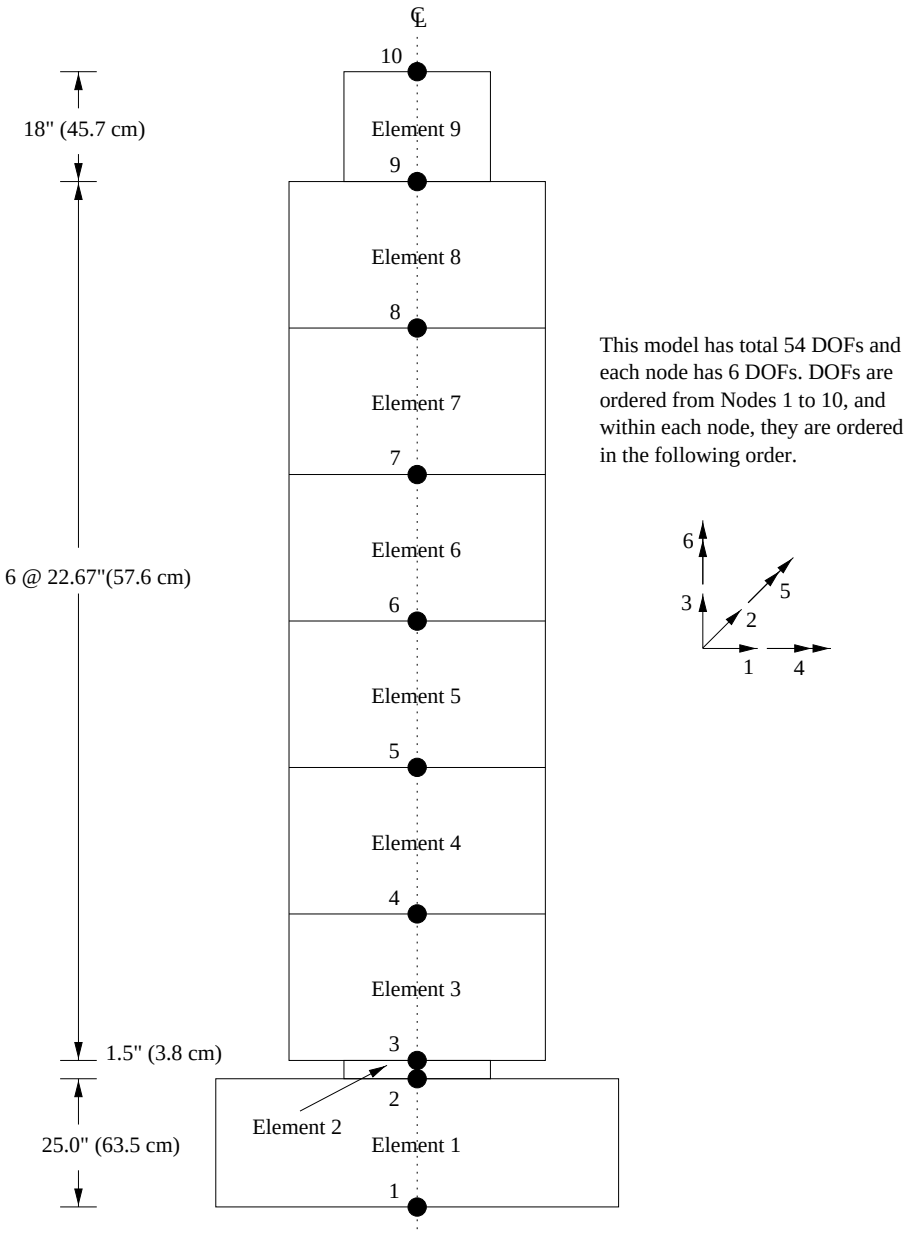


Figure 5.10: Analytical Model 1 of UC Irvine column test

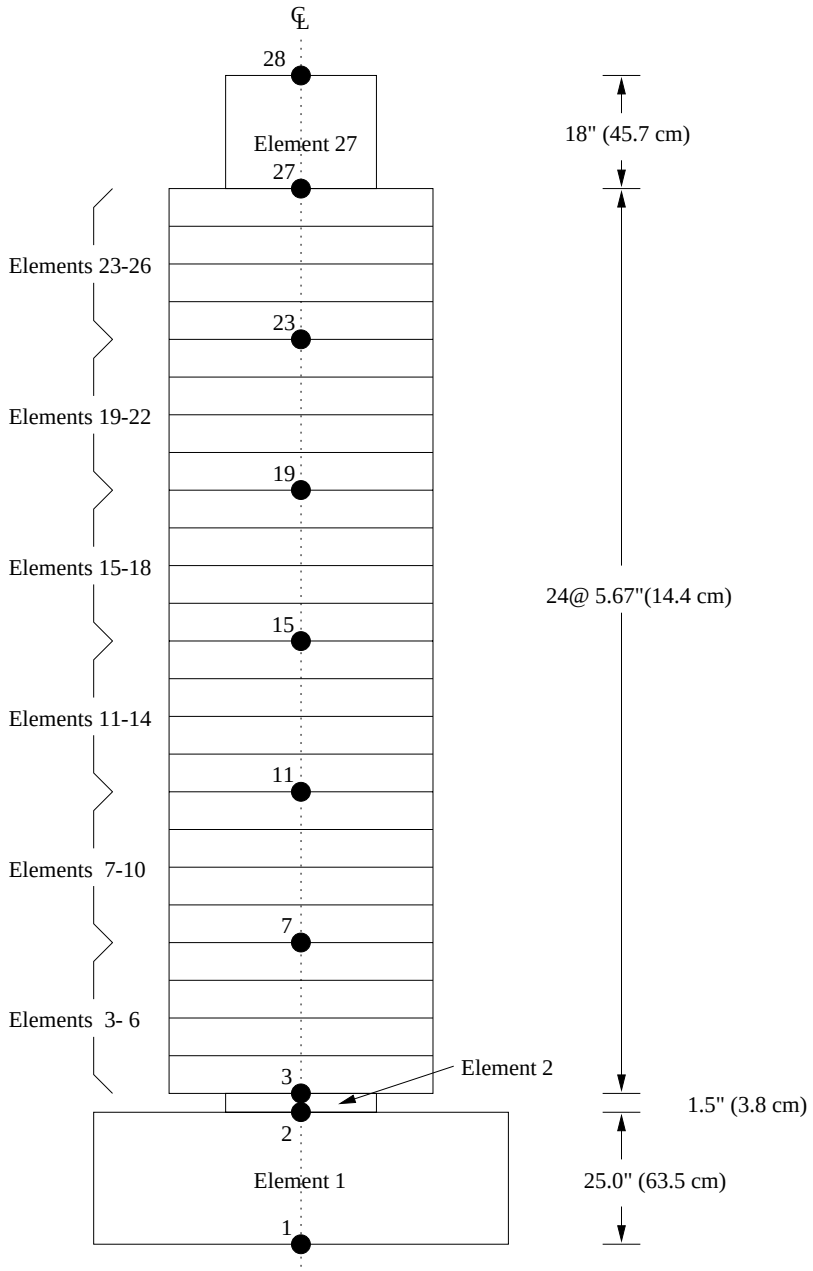


Figure 5.11: Analytical Model 2 of UC Irvine column test

4 and 9, respectively. Figures 5.13 to 5.16 show the analytical and measured modal vectors corresponding to the first bending and the first torsional modes in Table 5.9. The analytical modal vectors in Figures 5.13 and 5.15 are computed from Model 1 in Figure 5.10. The measured modal vectors in Figures 5.14 and 5.16 are computed from Test 0.

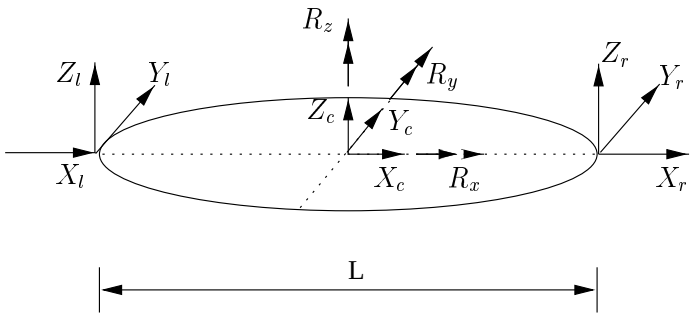


(a) the acceleration measurement points and the DOFs of the analytical model

$$\begin{Bmatrix} X_c \\ Y_c \\ Z_c \\ R_x \\ R_y \\ R_z \end{Bmatrix} = \begin{bmatrix} 1/2 & & & 1/2 & & \\ & 1/2 & & & 1/2 & \\ & & 1/2 & & & 1/2 \\ 1/L & & & -1/L & & \\ & & 1/L & & & -1/L \\ & -1/L & & & 1/L & \end{bmatrix} \begin{Bmatrix} X_l \\ Y_l \\ Z_l \\ X_r \\ Y_r \\ Z_r \end{Bmatrix}$$

(b) displacement transformation

Figure 5.12: Relating the acceleration measurement points to the DOFs of analytical model

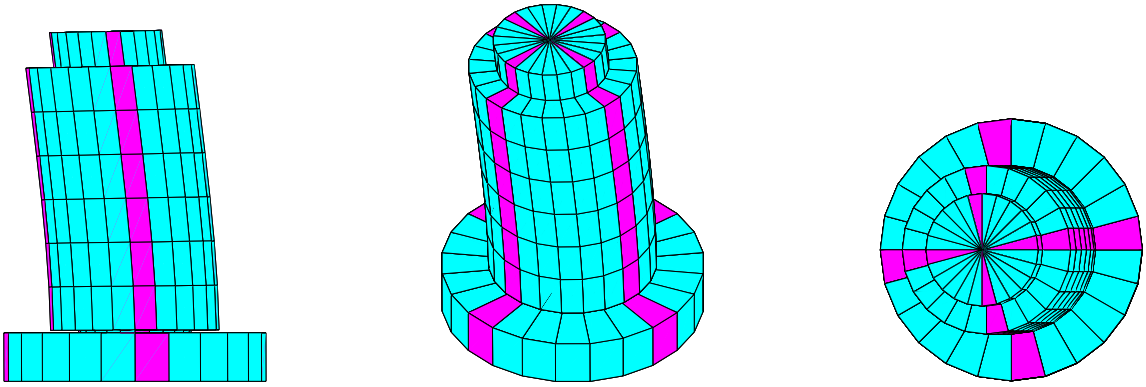

(a) X-Z plane view (b) 3D view (c) X-Y plane view

Figure 5.13: The first bending mode from Model 1 : 26.55 Hz

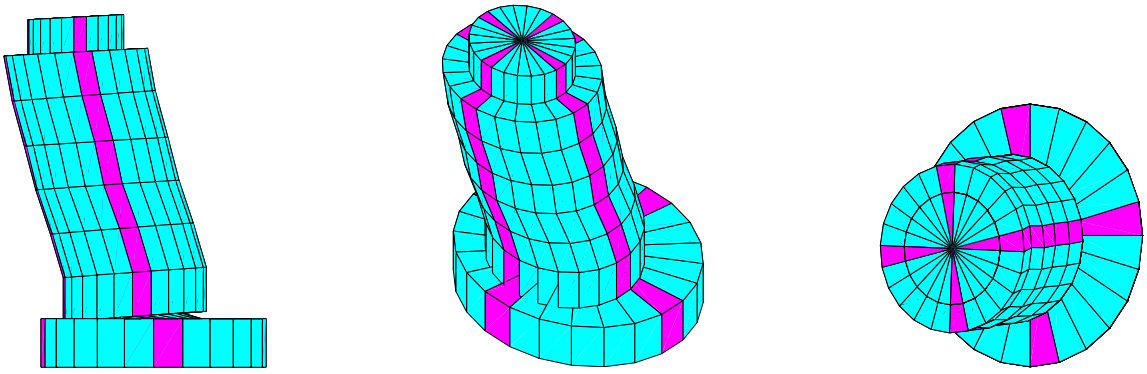

(a) X-Z plane view (b) 3D view (c) X-Y plane view

Figure 5.14: The first bending mode from test data: 27.82 Hz

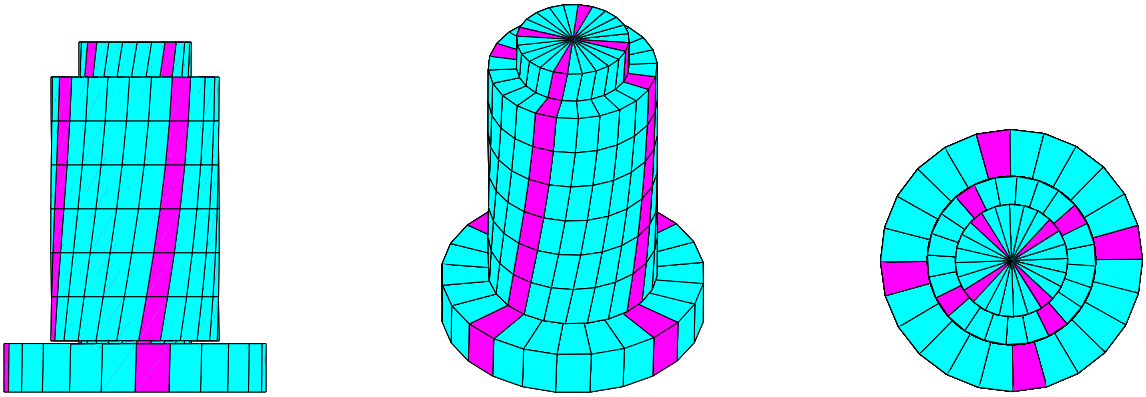

(a) X-Z plane view (b) 3D view (c) X-Y plane view

Figure 5.15: The first torsion mode from Model 1: 115.87 Hz

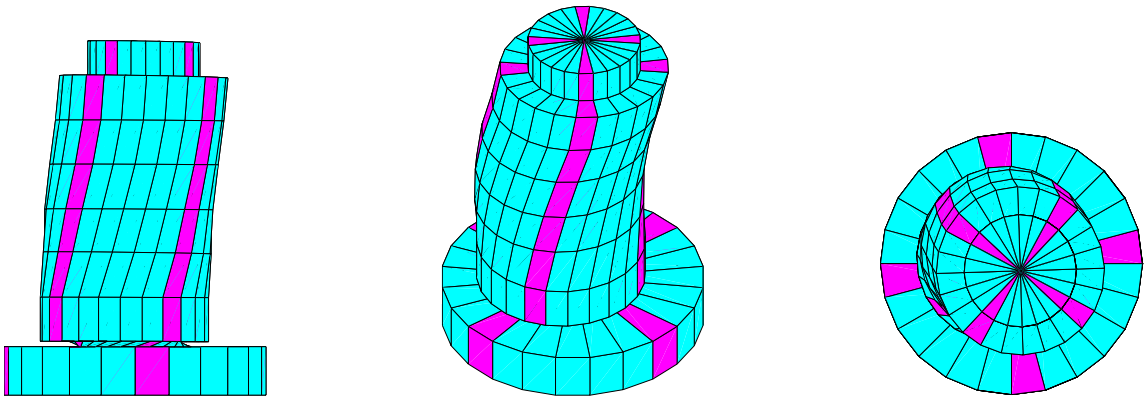

(a) X-Z plane view (b) 3D view (c) X-Y plane view

Figure 5.16: The first torsion mode from test data: 110.42 Hz

### 5.4.3 Application to Damage Detection

This subsection illustrates the Bayesian probabilistic approach for the detection of the plastic hinge location in the column tested. The natural frequencies and modal vectors estimated after each cyclic load test corresponding to $\Delta y$, $1.5\Delta y$, $2.5\Delta y$, $4.0\Delta y$ and $7.0\Delta y$ (Tests 1, 2, 3, 4 and 5, respectively) are employed. This incremental loading caused continuous stiffness deterioration of the column structure and simulated the condition for continuous monitoring. Table 5.10 shows the natural frequencies of the first bending and the first torsional modes at each displacement level. Note that only the first two modes are employed for damage detection since only the first two modes are reliably estimated from the experimental FRFs, and the discrepancies between the analytical modal vectors and the measured modal vectors become larger for higher modes. Deformation of plastic hinge was observed near the connection part between the foundation and the retrofitted portion of the column. It appears that this plastic hinge deformation was mainly responsible for the significant decreases in the first bending and torsional modes. This damage region approximately corresponds to elements 2 and 3 of the analytical models in Figures 5.10 and 5.11.

Table 5.10: Natural frequencies (Hz) estimated at different displacement levels

| Mode | initial | $\Delta y$ | $1.5\Delta y$ | $2.5\Delta y$ | $4.0\Delta y$ | $7.0\Delta y$ |
|---|---|---|---|---|---|---|
| 1st Bending | 27.82 | 12.80 | 7.31 | 6.15 | 5.61 | 5.21 |
| 1st Torsion | 110.42 | 109.97 | 50.20 | 36.90 | 20.32 | 19.04 |

In this study, only the simple models (Models 1 and 2) are employed. The measured and analytical modal vectors are normalized with respect to the analytical mass matrix. Each beam element is defined as a substructure. The main purpose is to demonstrate the continuous updating feature of the Bayesian approach. Starting from a uniform prior probability, $P(H_j)$, for every element (substructure), the posterior damage probability, $P(H_j|\hat{\Psi}_{N_s})$, is updated using Equation (2.4) when new modal parameters, $\hat{\Psi}_{N_s}$, are estimated after each cyclic load test. Also, damage is assumed to lie within a single element (substructure). For the examples presented here, we use an incremental step $\Delta\theta = 0.05$. In addition, a value of 0.9 is used for the damage threshold $\theta^*$ for every substructure. That is, an over 10% decrease in the

stiffness is defined as *damage*.

**Damage detection using the Bayesian Probabilistic Approach**

First, damage diagnosis is conducted using the first analytical model (Model 1). Substructures near the actual damage locations are shaded with darker color in Figures 5.17 and 5.18, respectively. The diagnosis results shown in Figures 5.17 and 5.18 are obtained by updating the damage probabilities either continuously or separately using the modal parameters measured at different deformation levels.

1. Figure 5.17 shows the continuous update of the damage probabilities using Model 1. Subtitles "Update $i$" ($i = 1, 2, .., 5$) in Figure 5.17 indicates that the corresponding damage probabilities are updated using modal parameters from Tests 1, 2,.., $i$. Figure 5.17 shows that the diagnosis result improves as more data sets are employed for damage detection.

2. For comparison, Figure 5.18 presents the diagnosis results obtained by using each individual data set separately. Subtitles "Test $i$" ($i = 1, 2, .., 5$) in Figure 5.18 indicate that the the corresponding damage probabilities are computed solely by using the modal parameters from Test $i$. When modal parameters from Tests 2 and 3 are employed separately (the counterparts to the figures with subtitles Update 2 and Update 3 in Figure 5.18), the Bayesian approach missed the actual damage locations. While the figures with subtitles Update 2 and Update 3 in Figure 5.17 identify the third substructure as the most probable damage location.

In both cases, the third substructure is diagnosed as the most likely damage location at the end. However, more strictly speaking, the actual plastic hinge was observed near the region where Elements 2 and 3 adjoin each other. To investigate if the proposed Bayesian approach approaches the hinge location, a refined model (Model 2) is employed next. All other conditions except the model remain the same as the previous diagnosis. While Model 1 has 9 elements, Model 2 consists of 27 elements to represent the test column. Figures 5.19 and 5.20 again illustrate that

the diagnosis using the proposed Bayesian approach converges to the actual damage locations (the actual damaged elements are distinguished by darker color in figures). At the end of the updating, the diagnosis result clearly shows that the column was very likely damaged between the top of the foundation and the bottom of the retrofit jacket.

The comparison of individual and continuous updating shows that the proposed Bayesian framework systematically combines the existing data with newly obtained data and the continuous updating is more stable in a sense that it is less sensitive to a single data set, and extracts consistent trends among the accumulated data. Furthermore, to provide information regarding the degree of damage for different damage stage, the values of the substructure stiffness reduction $(1 - \theta_i)$ at each damage stage are estimated from continuous updating and are reported in Table 5.11 for the actual damage locations (the second and third substructures). Continuous stiffness deterioration is observed in the actual damage locations (the second and third substructures).

Table 5.11: Estimated damage amount $(1 - \theta_i)$ at different damage stage

| | Test 1 | Test 2 | Test 3 | Test 4 | Test 5 |
|---|---|---|---|---|---|
| Model 1 | | | | | |
| $1 - \theta_2$ | 38% | 83% | 87% | 83% | 89% |
| $1 - \theta_3$ | 60% | 69% | 90% | 80% | 88% |
| Model 2 | | | | | |
| $1 - \theta_2$ | 59% | 88% | 92% | 87% | 92% |
| $1 - \theta_3$ | 72% | 78% | 94% | 91% | 93% |

### Damage detection using deterministic approaches

Two deterministic model updating or damage detection schemes are applied to the same test data of the column structure in order to compare the proposed probabilistic approach with some existing deterministic approaches. A Sensitivity-Based Element-By-Element (SB-EBE) method proposed by Hemez [69] and a Minimum Rank Perturbation Theory (MRPT) proposed by Kaouk and Zimmerman [85] are employed in this study as examples of the deterministic approaches. Both methods

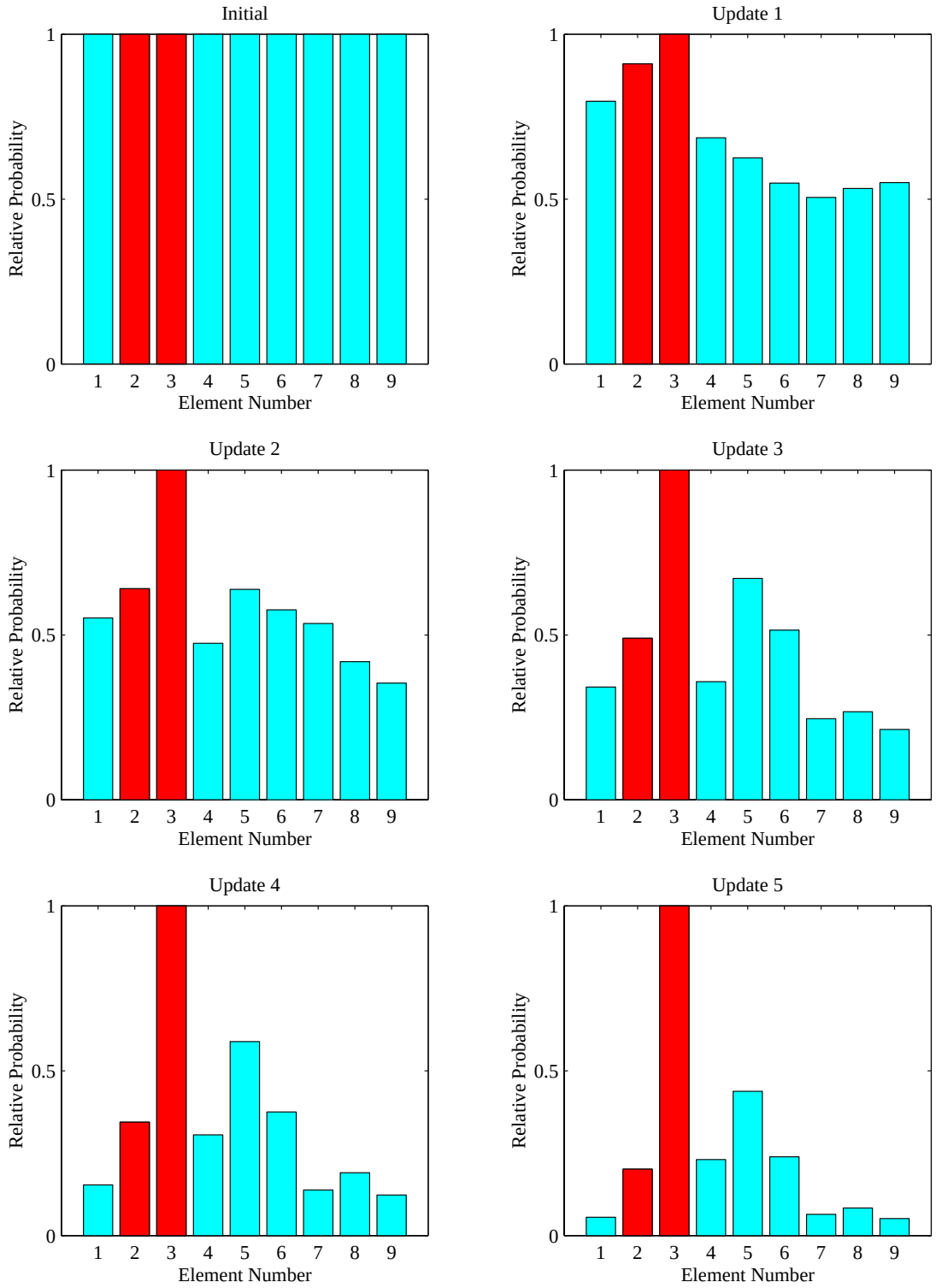


Figure 5.17: The damage probabilities after continuous updating (using Model 1)

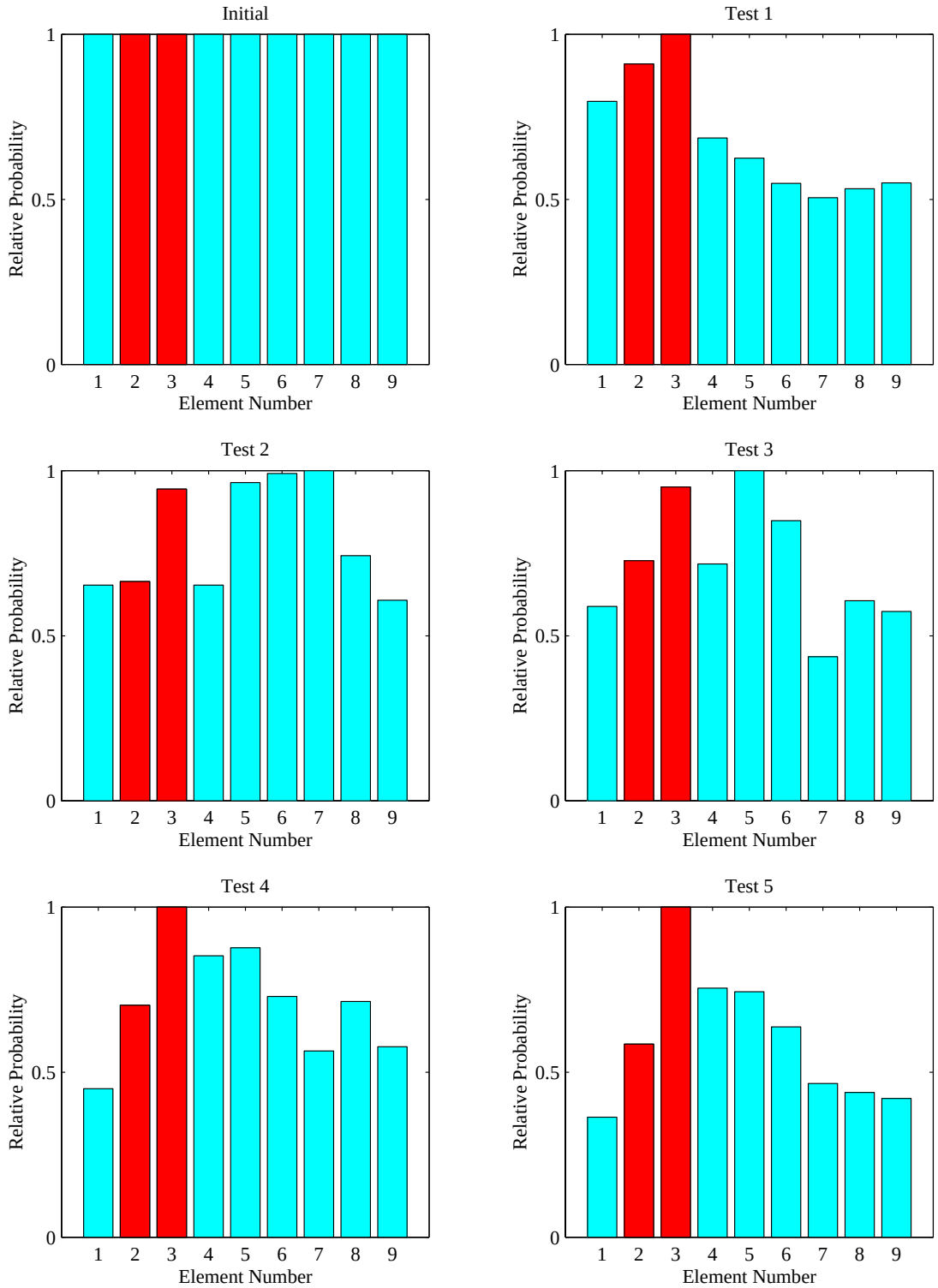


Figure 5.18: The damage probabilities computed from individual data set (using Model 1)

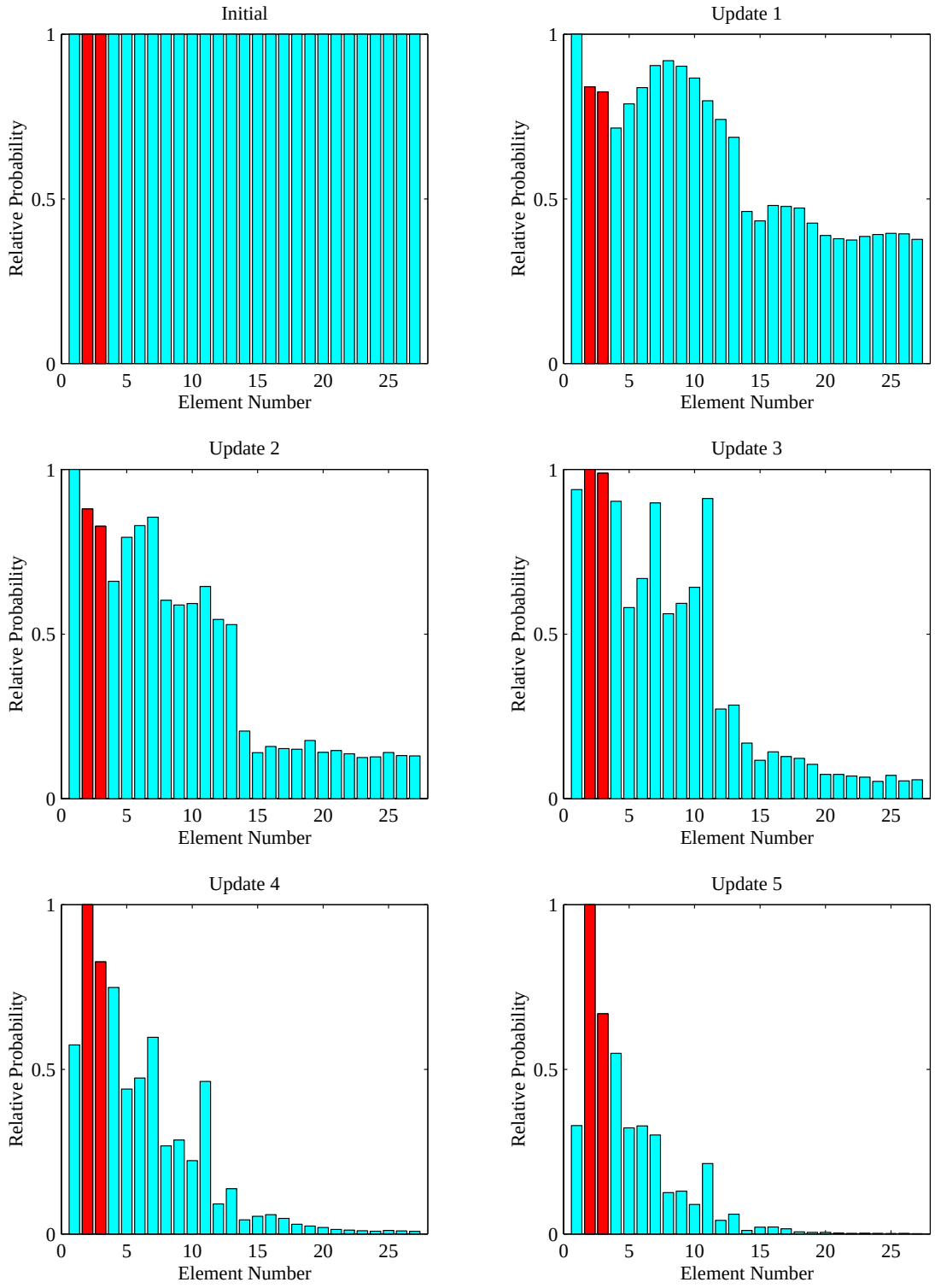


Figure 5.19: The damage probabilities after continuous updating (using Model 2)

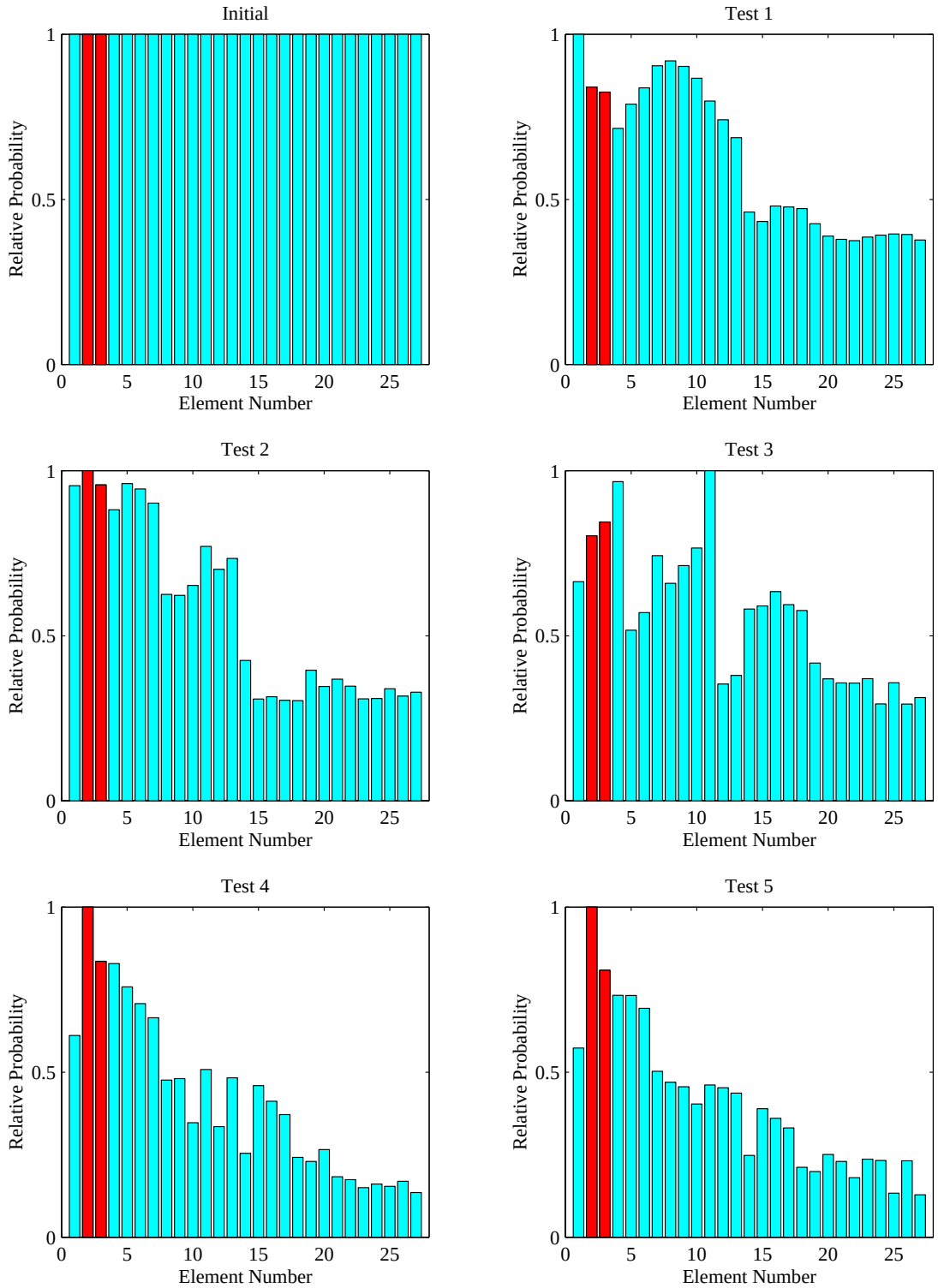


Figure 5.20: The damage probabilities computed from individual data set (using Model 2)

can be categorized as model-based methods that utilize estimated modal properties for damage diagnosis. The detailed development of these methods are described in References 69 and 85.

The SB-EBE method searches for the locations of potential errors between the finite element model and the measured modal data, and then updates the analytical model at the element-level by adjusting the elements' material properties. This method minimizes the squared norms of the modal dynamic residuals via a two-step iteration: At each iteration, the estimated modal vectors are first expanded, and, the parameters of the elements are corrected using the expanded modal vectors and natural frequencies. This approach has demonstrated the potential applicability to the damage detection of truss structures [46]. The SB-EBE method is employed here since the mode shape expansion scheme is built within the updating process and damage can be identified at each structural element level.

The MRPT proposed by Kaouk and Zimmerman decouples the localization and the quantification of damage [85]. First, dynamic residual forces (also known as damage vectors or residual force vectors) is employed to locate the most likely damaged regions which are mathematically expressed in terms of degrees of freedom (DOFs) in the analytical model [33,127,156]. Second, damage is quantified such that the rank of updating is minimized. The performance of this algorithm has been demonstrated using the NASA eight-bay truss structure [84]. This method is computationally efficient and does not require any iterations. However, the components of the estimated modal vectors should coincide with those of the analytical model, and the dimension of the modal vectors should be the same as the dimension of the analytical model. To satisfy these conditions, a mode shape expansion algorithm is applied prior to the application of the MRPT.

First, a numerical example is diagnosed by the SB-EBE method. For the numerical example, the stiffness of Element 2 in Figure 5.10 is decreased by 90% from the original analytical models (Models 1 or 2) and, then, the modal parameters are generated from the damaged model to simulate the measured modal parameters. Similar to the experimental test data in the previous example, only the modal parameters corresponding to the first bending and first torsional modes are used for damage detection,

and the DOFs corresponding to Nodes 4∼9 are assumed to be measured. Figure 5.21 shows the percent change of each element stiffness estimated by the SB-EBE method. Figures 5.21 (a) and (b) employ the first and second analytical models, respectively. Again, the actual damaged elements are distinguished by darker color in Figure 5.21. In theory, only the stiffness corresponding to Element 2 should be decreased by 90%. However, it is shown that the stiffness changes are spread throughout other elements. When Model 1 is employed, the stiffnesses of Elements 1, 2 and 3 are almost equally decreased by 70%. On the other hand, the stiffness deterioration is spread out to larger number of members when Model 2 is employed. The drop in the ratio of the measured DOFs to the unmeasured DOFs appears to aggravate the diagnosis results. Note that the SB-EBE method could not locate the actual damage location although no measurement noise is assumed in this numerical example and the analytical model is used to simulate the measured modal parameters. Then, the SB-EBE method is applied to the experimental test data (Test 1∼Test 5). This method was not successful in locating damage regions for all 5 test cases. Therefore, the diagnosis results are not presented in this study.

Next, the MRPT is applied to the simulated and experimental data. The MRPT does not directly identify damage at the element levels. The MRPT method estimates only the "damaged" DOFs that correspond to large dynamic residuals. Then, an analyst should infer the damaged elements based on the connectivity information of the structure. When the same numerical example as the SB-EBE method is employed, the damaged DOFs corresponding to Element 2 are easily determined. When the experimental data (Test 1∼Test 5) are employed, the damaged DOFs are not clearly noticeable until the last data set (Test 5) is used. Figure 5.22 shows the diagnosis result when Test 5 data are employed. The DOFs 1∼18 corresponding to Elements 2 and 3 are assumed to be damaged. Again, the actual damaged DOFs are distinguished by darker color in Figure 5.22. Figures 5.22 (a) and (b) show the normalized dynamic residual from the first bending and torsional modes, respectively. The Orthogonal Procrustes Expansion [135], Component Mode Synthesis [21] and Modal Coordinate Expansion [74] techniques are employed for mode shape expansion. Note

that when the mode shape expansion techniques other than the Orthogonal Procrustes Expansion are employed, the damaged DOFs are not clearly indicated. The selection of mode shape expansion techniques seems to be an essential factor for the success of damage diagnosis.

The poor performance of the two deterministic approaches can be attributed to the following:

1. Most mode shape expansion techniques including the ones used in this paper expand the measured modal vectors to the size of the analytical model based on the measurements at the instrumented DOFs and the corresponding analytical stiffness and mass matrices. These techniques work only when the analytical model is already a good representation of the structure. Mode shape expansion techniques generally do not produce the expanded modal vectors that are accurate enough to provide reliable information about damage. As previously mentioned, the discrepancy between the analytical model and the test data was large enve in the initial stage. This discrepancy produced additional errors into the two deterministic approaches presented. (Note that, the proposed Bayesian approach does not require any mode shape expansion or model reduction procedures.)

2. Both deterministic approaches basically update the system stiffness matrix so as to minimize the dynamic force residuals. However, for the frame structures as the one presented here, the order of magnitudes for the residual forces in rotational DOFs is significantly larger than that of translational DOFs. Therefore, the residual forces in the rotational DOFs are generally weighted more than those corresponding to the translational DOFs. The difference in magnitude of residual force for each DOF contributed to the poor performance of the deterministic approaches.

Alvin [4] addresses some of the aforementioned problems by employing dynamic displacement residuals, rather than force residuals. Furthermore, the Bayesian estimate is introduced to the SB-EBE method to incorporate the relative confidence measures for the parameters being updated and the test data used for updating. It

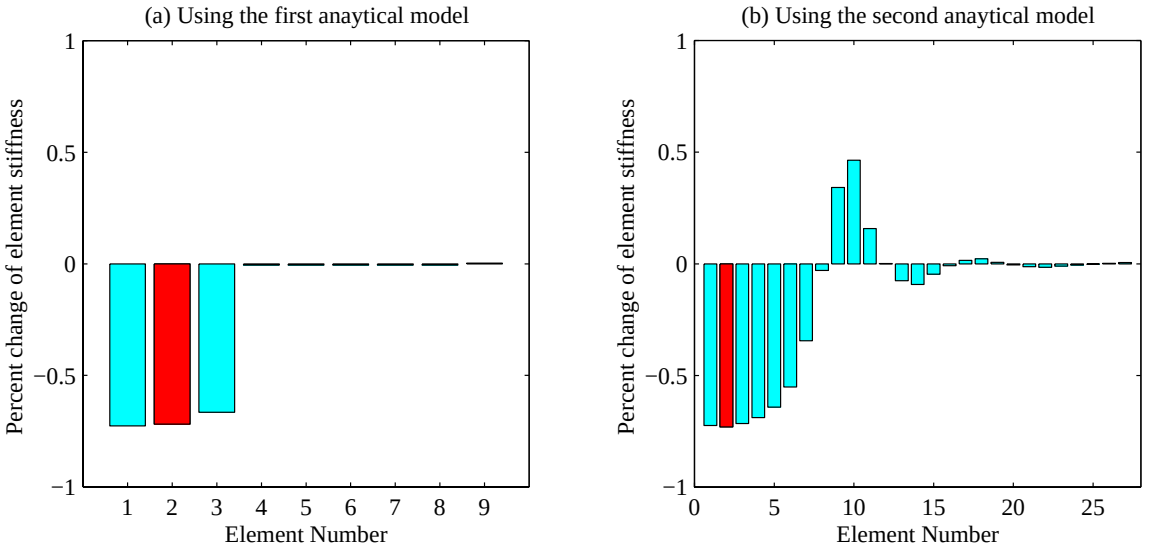


Figure 5.21: Damage diagnosis using the SB-EBE method: numerical example

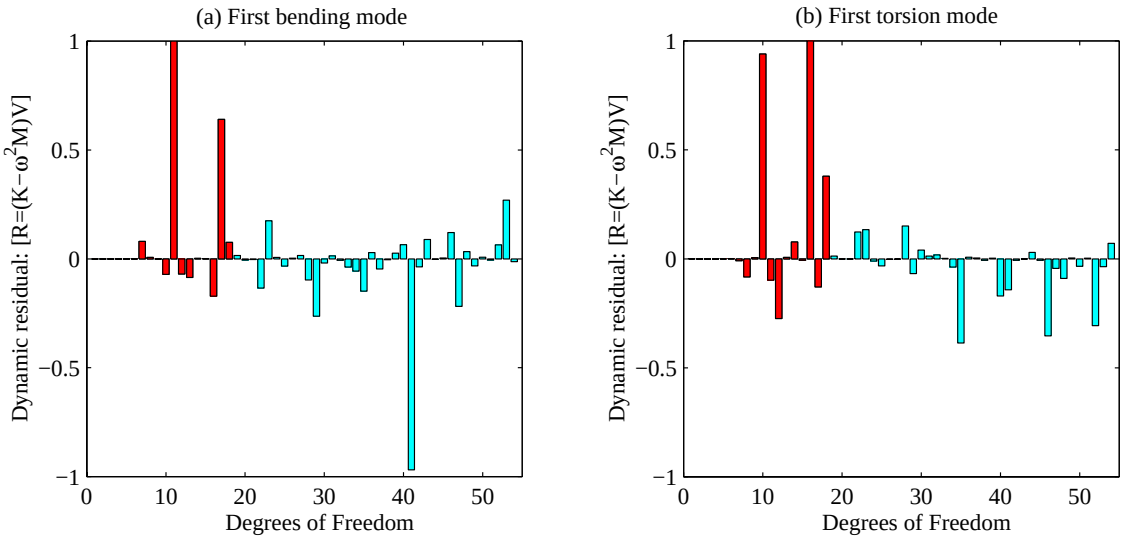


Figure 5.22: Damage diagnosis using the MRPT method: experimental example

would be an interesting research task to compare this approach with the one proposed in this study.

## 5.5 Summary and Discussions

This chapter illustrates the proposed Bayesian probabilistic approach for the cases when the analytical model differs from the test structure. The diagnosis results of the two-story and five-story frame structures show that, the proposed method identifies most of the damage locations, even in the presence of measurement noise and/or modeling error if a large number of data sets are available and load patterns are selected carefully when Ritz vectors are used. For the reinforced-concrete bridge column, the Bayesian damage detection method is able to locate the damaged region using a simplified analytical model and the modal parameters estimated from the vibration tests, although (1) only the first bending and first torsional modes were estimated from the experimental test data, (2) the locations where the accelerations were measured did not coincide with the degrees of freedom of the analytical model, and (3) there existed discrepancies between the undamaged test structure and the analytical model. The damage probabilities are systematically updated when new test data become available and better diagnosis is obtained by employing multiple data sets than just by using each test data set separately. Furthermore, the computational time required by the branch-and-bound search scheme is also significantly reduced by employing the simplified model.

# Chapter 6

# Experimental Applications

This chapter provides a comprehensive discussion on the verification of the damage detection process in an experimental study. The discussion is based on the author's experience participating in the design and experimental modal analysis at the Hyundai Engineering & Construction Co., Seoul, Korea. First, the experimental modal analysis procedure is described in detail. Then, numerical procedures that extract modal parameters and Ritz vectors are also described. An experiment for a grid-type bridge model is presented to illustrate the modal analysis procedure and the use of the experimentally measured modal and Ritz vectors for damage detection applications.

## 6.1 Experimental Modal Analysis

The purpose of experimental modal analysis is to determine the modal properties of a structure such as resonant frequencies, modal vectors and damping ratios from the response of the structure to a particular excitation. This section describes the experimental modal analysis procedure with special emphasis on practical issues. The theoretical and engineering developments of modal analysis can be found in many references. Ewins [45] gives a practical engineering perspective of modal analysis and its applications, Newland [108] and Bendat and Piersol [19] provide a good discussion on spectral analysis and measurement, and Bendat and Piersol 18 discuss some issues that are particularly relevant for practicing engineers and scientists. Finally, actual implementation issues are documented in Reference 118.

The quality of the identified modal properties is important for the success of vibration-based damage detection methods. Commonly used system identification techniques include the extended Kalman filters [79,72], the Polyrefence time domain method [153,34], the multivariate Auto-Regressive and Moving-Average (ARMA) model [123], the Q-Markov COVER algorithm [122,99] and the Eigensystem Realization Algorithm (ERA) [77,119,103]. This study employs the ERA because (1) the ERA is a robust procedure that is particularly appropriate to handle measurement data corrupted by noise, and (2) the indicators, which are used to qualify the estimated modal parameters, can be incorporated in the ERA. Since the ERA constructs a state-space model, the procedure can be extended for the extraction of load-dependent Ritz vectors.

A modal analysis procedure using the ERA method can be summarized as follows:

1. Determine the necessary parameters for the spectral analyzer such as sampling rate, frequency bandwidth of an excitation, and the total sampling time.
2. Apply excitations and measure responses of the structure.
3. Compute Frequency Response Functions (FRFs) and Coherence Functions.
4. Construct impulse response time history (Markov Parameters) from the FRFs.
5. Obtain a state-space model using the ERA.
6. Extract physical modal parameters and load-dependent Ritz vectors from the estimated state-space model.

In the following subsections, each step of the modal analysis procedure is discussed in detail.

### 6.1.1 State-Space Representation of Second-Order Differential Equations of Motion

We start with the state-space representation of second-order differential equations of motion. Let $\mathbf{M}$, $\mathbf{C}_\zeta$ and $\mathbf{K}$ denote the mass, damping and stiffness matrices of a

$N$-DOFs system, respectively, the equations of motion can be expressed as

$$\mathbf{M}\ddot{\mathbf{z}}(t) + \mathbf{C}_\zeta\dot{\mathbf{z}}(t) + \mathbf{K}\mathbf{z}(t) = \mathbf{B}_u\mathbf{u}(t) \tag{6.1}$$

where $\mathbf{z}$, $\dot{\mathbf{z}}$ and $\ddot{\mathbf{z}}$ are vectors of displacement, velocity and acceleration, respectively. $\mathbf{u}$ is a $r \times 1$ vector of input excitations and $\mathbf{B}_u$ is an $N \times r$ input influence matrix specifying the locations of inputs. Here, $r$ is the number of inputs. The second order differential equations can be recast into the first order differential equations in a number of ways. In classical control theory, the following representation is commonly used:

$$\dot{\mathbf{x}} = \mathbf{A}_c\mathbf{x} + \mathbf{B}_c\mathbf{u} \tag{6.2}$$

where

$$\mathbf{A}_c = \begin{bmatrix} \mathbf{0} & \mathbf{I} \\ \mathbf{M}^{-1}\mathbf{K} & \mathbf{M}^{-1}\mathbf{C}_\zeta \end{bmatrix},\ \mathbf{B}_c = \begin{bmatrix} \mathbf{0} \\ \mathbf{M}^{-1}\mathbf{B}_u \end{bmatrix} \text{ and } \mathbf{x} = \begin{bmatrix} \mathbf{z} \\ \dot{\mathbf{z}} \end{bmatrix} \tag{6.3}$$

When the response of a system is measured by the $m$ output quantities $\mathbf{y}(t)$ ($\in \mathcal{R}^{m\times 1}$) using sensors such as accelerometer, the measurement vector $\mathbf{y}(t)$ is related to the vectors $\mathbf{z}$, $\dot{\mathbf{z}}$ and $\ddot{\mathbf{z}}$ as follows:

$$\mathbf{y} = \mathbf{C}_a\ddot{\mathbf{z}} + \mathbf{C}_v\dot{\mathbf{z}} + \mathbf{C}_d\mathbf{z} \tag{6.4}$$

where $\mathbf{C}_a$, $\mathbf{C}_v$ and $\mathbf{C}_d$ are output influence matrices for acceleration, velocity and displacement, respectively. These output influence matrices convert the physical units in acceleration, velocity and displacement to the electrical units in the measurements. Solving for $\ddot{\mathbf{z}}$ from Equation (6.1) and substituting the result into Equation (6.4) produce

$$\mathbf{y} = \mathbf{C}\mathbf{x} + \mathbf{D}\mathbf{u} \tag{6.5}$$

where

$$\mathbf{C} = [\mathbf{C}_d - \mathbf{C}_a\mathbf{M}^{-1}\mathbf{K} \quad \mathbf{C}_v - \mathbf{C}_a\mathbf{M}^{-1}\mathbf{C}_\zeta] \quad \text{and} \quad \mathbf{D} = \mathbf{C}_a\mathbf{M}^{-1}\mathbf{B}_u \tag{6.6}$$

Here, $\mathbf{C}$ is an $m \times n$ output influence matrix for the state vector $\mathbf{x}$ which includes velocity and displacement. $\mathbf{D}$ is an $m \times r$ gain matrix and appears in Equation (6.6) only when accelerometers are used for the output measurements. Note that there exist an infinite number of state-space models that result in the same input and output relationship from $\mathbf{u}(t)$ to $\mathbf{y}(t)$.

In modal testing, an input signal, generated from a digital computer, is converted to an analog signal using a Digital-to-Analog (DA) converter. Conversely, the Analog-to-Digital (AD) converter receives the analog signal from a sensor and then converts the analog signal to the digital signal for use in computers. Typically, a zero-order hold, in which the signal remains constant in each of the sampling period, is assumed. Because experimental data are typically recorded in digital computers, a discretized linear-dynamic system with a sampling interval $\Delta t$ can be represented by the following discrete-time state-space model:

$$\begin{aligned} \mathbf{x}(k+1) &= \mathbf{A}\mathbf{x}(k) + \mathbf{B}\mathbf{u}(k) \\ \mathbf{y}(k) &= \mathbf{C}\mathbf{x}(k) + \mathbf{D}\mathbf{u}(k) \end{aligned} \quad \text{for } k = 0, 1, 2, ... \tag{6.7}$$

where $\mathbf{x}(k+1)$ denotes the state-space variable $\mathbf{x}$ at time $(k+1)\Delta t$. That is, $\mathbf{x}(k+1)$=$\mathbf{x}[(k+1)\Delta t]$, $\mathbf{x}(k)$=$\mathbf{x}[k\Delta t]$, and $\mathbf{u}(k)$=$\mathbf{u}[k\Delta t]$. Furthermore,

$$\mathbf{A} = e^{\mathbf{A}_c \Delta t} = \sum_{i=0}^{\infty} \frac{(\Delta t)^i}{i!} \mathbf{A}_c \;\text{ and }\; \mathbf{B} = \int_0^{\Delta t} e^{\mathbf{A}_c \tau} \mathbf{B}_c \, d\tau = [\mathbf{A} - \mathbf{I}]\mathbf{A}_c^{-1}\mathbf{B}_c \tag{6.8}$$

The second equalities in Equation (6.8) hold only if the state matrix $\mathbf{A}_c$ is asymptotically stable, in other words, if the real parts of all eigenvalues are negative. Note that matrices $\mathbf{C}$ and $\mathbf{D}$ are identical in both discrete and continuous state-space models.

### 6.1.2 Preparation of Modal Testing

The basic procedure for the digital spectral analysis is outlined below. With the recent development in spectral signal analyzers, most processes presented in this subsection have been automated using personal computers. Nevertheless, some parameters such as sampling rate, total length of sampling and the number of averaging for the modal testing still need to be tailored for a specific structure of interest. This subsection

aims to discuss the selection of these parameters and to facilitate the understanding of the subsequent sections.

Step 1: Estimate the frequency bandwidth of interest and the maximum frequency $f_{max}$ to be analyzed. The maximum frequency should exceed the natural frequency of the highest mode to be estimated. An approximate estimate of the natural (resonance) frequencies of the test structure can be obtained from a companion analytical model.

Step 2: Determine a sampling rate $f_s$ or sampling interval $\Delta t$. The sampling frequency $f_s$ is controlled mainly by the Nyquist criterion to avoid aliasing. Aliasing above the Nyquist frequency occurs due to the periodicity assumption in the Discrete Fourier Transformation (DFT). Theoretically, the Nyquist frequency $f_{nyq}$ should be higher than the maximum frequency to be analyzed:

$$f_{nyq}(= \frac{1}{2\Delta t}) \geq f_{max} \tag{6.9}$$

However, in real applications, the sampling frequency should be made much higher than $f_{max}$. A good "rule of thumb" is to sample at least ten points per period for the smallest period $T_{min}$ $(1/f_{max})$:

$$\Delta t \leq \frac{1}{10} T_{min} \quad \text{or} \quad f_s \geq 10 \times f_{max} \tag{6.10}$$

If the measurement quantity is a sinusoidal function, ten sampling points per the period are sufficient to capture the characteristic of the wave.

Step 3: Determine the total length of sampling $T_T$ and the number of data points $l$ $(= T_T/\Delta t)$. The desired frequency resolution $\Delta\omega$ determines $T_T$ since $\Delta\omega = 1/T_T$. (Note that the actual frequency resolution might change because of the zero padding of a time history.)

Step 4: Remove trends. Situations sometimes occur where the sample data include spurious trends or low frequency components with a wavelength longer than the record

length $T_T$. If such trends are not correctly removed from the original data, distortions may occur in the later FRF computations. The most common and easiest technique for trend removal is to subtract the mean value from the original data. For example, a discrete time series $\mu(k)$, $k$=0, 1,..., $l$, can be adjusted as:

$$\nu(k) = \mu(k) - \bar{\mu} \quad \text{where} \quad \bar{\mu} = \frac{1}{l}\sum_{r=1}^{l}\mu(r) \tag{6.11}$$

Now the modified sequences are employed for the subsequent frequency domain analysis. Instead of a mean value, higher-order polynomial fits may be employed [19]. However, the trends removal using an order of greater than 3 is not generally recommended. Note that higher-order trend removal should be conducted only when complex trends are clearly apparent.

Step 5: Extend the record length by *zero padding*. The Fast Fourier Transform (FFT) computes the DFT very efficiently when the length of a record is a power of 2. That is $l$=$2^p$, where $p$ is a positive integer. In many applications, the length of available records may not satisfy the condition, $l$=$2^p$. In this case, the length of the record can be increased to the next higher power of 2 by augmenting zeros at the end of the record. Note that this zero padding also brings other advantages such as improving the accuracy of correlation functions, frequency resolution and so on. Therefore, zero padding is recommended even when the original record has a length of $2^p$. Note that the zero padding should be conducted after trend removal.

Step 6: Select the amount of averaging. The accuracy and statistical reliability of spectral analysis can be improved by an *averaging* process, which averages the FRFs obtained from several individual time histories or different segments of a long time history. Detailed guidance for the selection of the averaging number can be found in References 19 and 45. However, in most applications, averaging of 30 time histories produces statistically reliable and smooth spectra.

### 6.1.3 Digital Signal Processing

The raw data obtained directly from instrumentation are rarely used for frequency domain analyses. The DFT of the raw data can yield erroneous results if the raw data are not properly treated. These errors are generally the result of discretization and of the limited length of the time history record. The discretization error causes *aliasing*, and the finite length of the time history yields *leakage* problem.

Discretization of the analog signals from sensors creates the aliasing problem. The discretization process with a given sampling rate $f_s$ cannot distinguish a signal with frequency $f(> f_s)$ and one with frequency $(f_s - f)$. Therefore, the actual spectrum above the Nyquist frequency $f_{nyq}$ $(=f_s/2)$ is reflected over the Nyquist frequency and the spectrum in the range of $[\ 0, f_s/2\ ]$ is distorted. As mentioned earlier, the Nyquist frequency can be raised by increasing the sampling rate. However, this does not eliminate the frequency distortion caused by the aliasing of high frequencies.

An *anti-aliasing* filter is commonly used to solve this problem. The anti-aliasing filter subjects the original continuous time history to a low- pass sharp cut-off filter and the filter results in a modified time history where the frequency content above a cut-off frequency $f_c$ is removed (or at least attenuated). Since the anti-aliasing is imperfect, frequencies near the Nyquist frequency are still susceptible to distortion. Therefore, in real applications, modal parameters are estimated only in the range of $[\ 0, 0.5 \text{ or } 0.8 f_{nyq}]$. Some of the available filters include the Butterworth filters (best flat response at low frequency), the Bessel filters (best flat delay at low frequency) and the Chebyschev filters (best uniformly bounded response at low frequency) [118]. Issues in choosing a filter are essentially its attenuation factor (ideally, large), the magnitude of its pass-band ripples (ideally, zero) and of its reject-band ripples (ideally, bounded), its phase shift (ideally, uniform) and the capability of the filter to minimize the energy spreading in the time domain [19]. The most common Butterworth filter is used in this study.

Sampling with a finite length of time history causes a *leakage* problem. The periodicity assumption $y(t) = y(t + T_T)$ in the sampled time history $y(t)$ causes a discontinuity at the beginning and the end of the sampling period. (Note that, this is also true for a periodic function $y_p(t) = y_p(t + T)$ unless $T_T = T$.) This discontinuity

causes a leakage of the energy content over several frequencies. For example, if the sampling period is identical to the inherent period of the function ($T_T$=$T$), the DFT of a periodic function $y_p(t)$ produces a single peak at the frequency $1/T$. However, if the sampling period is not identical to the inherent period of the function ($T \neq T_T$), the energy at the frequency $1/T$ leaks into the frequencies near the true frequency.

The application of *windowing* provides a practical solution to the leakage problem. Windowing modifies the original signal $y(t)$ by imposing a predetermined time function $w(t)$ on the original signal such that $\tilde{y}(t) = y(t)w(t)$. The selection of windowing depends on the energy content of the data, clustered or distant resonant peaks and so on. Rectangular ($w(t)$=$\delta(-T \leq t \leq T)$), Bartleft ($w(t)$=$|1 - t/T|$), Hanning ($w(t)$=$cos^2(\pi \times t/T)$) or exponential ($w(t)$=$e^{-|t|/T}$) are typical windows [118]. The same window is applied to both the input and response signals to corrupt them with the same distortion and to minimize noise in the FRF estimation.

### 6.1.4 Excitation of a Structure

There are essentially two types of vibration test. The first one is an ambient vibration test where responses are measured under normal operation of the structure and the structure is subject to ambient excitations such as wind, traffic excitation and wave. The second is a force vibration test where the structure is excited with a known input. Note that although the excitation is unknown for an ambient test, the ambient vibration test is becoming more attractive for the continuous monitoring of civil structure [51,43]. Recent development of many algorithms to extract modal parameters from ambient tests paves the way for more common application of this type of test. However, the force vibration test is still widely used for laboratory testing since the force vibration test is conducted under more closely controlled conditions and consequently yields more accurate information. Various types of excitation mechanism such as sinusoidal wave, random excitation and impulse excitation are available for force vibration test. Here, the impulse excitation by hammer impactor is mainly discussed since that is used in our experiment.

An excitation method using an impact hammer is simple in terms of testing. However, this is achieved at the price of greater data analysis later on. The sampling

of impulse responses should be continued until all transient response of a structure dies out. A lightly-damped structure may require a long sampling period and result in increased computation in the subsequent spectral analysis. A typical impact hammer consists of head, tip and force transducer. The magnitude of the impact is mainly controlled by the mass of the head and the initial velocity of the hammer when it hits the structure surface. In general, the change in the impact magnitude is not a critical problem since we are often interested in only the ratio of the output magnitude to the input magnitude. One main difficulty is to ensure that the position and the orientation of impact are essentially the same for repeated excitations. Otherwise, the frequency content of the excitation and the energy transformed to the structure drastically vary from one test to anther. Therefore, a single operator is recommended to repeat the impact excitation. The frequency content of the exciting force is controlled by the stiffness of the contact surface (the hammer tip) and the mass of the hammer head. A cut-off frequency $f_c$ is computed as (contact stiffness/the hammer mass)$^2$, above which the kinetic energy of the hammer is not delivered into the structure. Therefore, the stiffer the tip, the higher will be the frequency range covered by the impact. For civil structures, a very soft tip is typically used to focus all the energy input to a low-frequency range. The frequency content of a typical hammer excitation has a flat magnitude up to the cut-off frequency and then drastically diminishes after the cut-off frequency.

### 6.1.5 Frequency Response Function

A Frequency Response Function (FRF) is defined as the Fourier Transform of impulse or pulse response sequence (Markov Parameters):

$$\mathbf{G}(z) = \sum_{k=0}^{l-1} \mathbf{Y}_k e^{-j(\frac{2\pi z}{l})k} \tag{6.12}$$

where $\mathbf{G}(z)$ ($\in \mathcal{R}^{m\times r}$) is a FRF at frequency $z$, $\mathbf{Y}_k$ ($\in \mathcal{R}^{m\times r}$) is a sampled pulse response (Markov Parameters) at time $k$, and $l$ is the total number of sampled points. The dynamic characteristic of a linear time-invariant stable system can be sufficiently described by the FRF or Markov Parameters.

In the majority of modal testing, FRFs are computed prior to any system identification. Although many recent identification algorithms can directly analyze time histories, the construction of FRFs is still common in practice since (1) the FRF deduces the amount of data from a time history with no loss of useful information, (2) the computation in frequency domain is easier than in time domain, and (3) many traditional criteria and tools are available for the frequency domain analysis.

The computation of a FRF can be summarized in the following steps:

1. Compute the DFT of the input and output time histories.

2. The Auto-Spectral Density (ASD) of inputs, and Cross-Spectral Densities (CSD) of input and output signals are computed from the DFTs of the inputs and outputs.

3. From $N_a$ data records, which are obtained either from $N_a$ different experiments or from $N_a$ segments of a long record, the averaged auto- and cross-spectral densities are computed.

4. The FRF is computed from the averaged auto- and cross-spectral densities up to the Nyquist frequency.

Here, multiple inputs and multiple outputs (MIMO) case is considered for the construction of the FRF. First, the DFT of the input $\mathbf{u}(t)$ and output $\mathbf{y}(t)$ are computed as follows: [1]

$$\mathbf{u}(z) = \frac{1}{l}\sum_{k=0}^{l-1}\mathbf{u}(k)e^{-j(\frac{2\pi z}{l})k} \qquad (6.13)$$
$$\mathbf{y}(z) = \frac{1}{l}\sum_{k=0}^{l-1}\mathbf{y}(k)e^{-j(\frac{2\pi z}{l})k}$$

Note that this equation is based on the assumption that $\mathbf{u}(t)$ and $\mathbf{y}(t)$ are periodic. That is, $\mathbf{u}(k)$=$\mathbf{u}(k+l)$ and $\mathbf{y}(k)$=$\mathbf{y}(k+l)$. Furthermore, it can be shown that

[1] When the length of a data record is power of 2, the FFT can be employed to speed up the computation. The FFT requires approximately $p \times log(p) \times 2^p$ FLOPs for a record of length $2^p$.

$\mathbf{u}(-z)$=$\mathbf{u}^*(z)$ and $\mathbf{u}(z)$ $(z = l/2, l/2+1, ..., l)$ are the complex conjugates of $\mathbf{u}(z)$ $(z = l/2, l/2-1, ..., 0)$. Here, the superscript * denotes a complex conjugate of a complex number. Therefore, $\mathbf{u}(z)$ is uniquely determined from the value of $k$ over the interval $0 \leq k \leq l/2$. The same is true for $\mathbf{y}(z)$. Note that only $\mathbf{u}(z)$ and $\mathbf{y}(z)$ in the range of $0 \leq z \leq l/2$ need to be stored for the subsequent computation. Filtering is applied to $\mathbf{u}(z)$ and $\mathbf{y}(z)$ to eliminate spectral components above the Nyquist frequency.

Next, the ASD and CSD are computed from the DFT of the individual sequence in Equation (6.1.5):

$$\begin{aligned} \mathbf{S}_{uu}(z) &= \mathbf{u}(z)\mathbf{u}^*(z) \\ \mathbf{S}_{yu}(z) &= \mathbf{y}(z)\mathbf{u}^*(z) \end{aligned} \tag{6.14}$$

This computation is again based on the periodicity assumption of the data sequence. There is another way of computing spectral densities. One can first compute the auto- and cross-correlation and use the DFT to estimate the spectral densities. However, for a large number of $N_a$ and $l$, the latter procedure becomes computationally more expensive than the first one.

Assume that $N_a$ number of time histories are available, each record has a length of $l$, and possesses the ergodic property. The expected spectral densities $E[\mathbf{S}_{uu}]$ and $E[\mathbf{S}_{yu}]$ are approximated by the following averaged spectral densities.

$$\begin{aligned} \bar{\mathbf{S}}_{uu}(z) &= \frac{1}{N_a}\sum_{i=0}^{N_a}\mathbf{S}_{uu}^{(i)} = \frac{1}{N_a}\sum_{i=0}^{N_a}\mathbf{u}^{(i)}(z)\mathbf{u}^{*(i)}(z) \in \mathcal{R}^{r\times r} \\ \bar{\mathbf{S}}_{yu}(z) &= \frac{1}{N_a}\sum_{i=0}^{N_a}\mathbf{S}_{yu}^{(i)} = \frac{1}{N_a}\sum_{i=0}^{N_a}\mathbf{y}^{(i)}(z)\mathbf{u}^{*(i)}(z) \in \mathcal{R}^{m\times r} \end{aligned} \tag{6.15}$$

where $\mathbf{S}_{uu}^{(i)}$ and $\mathbf{S}_{yu}^{(i)}$ are the spectral densities from the $i$th time history data. Then, the frequency response function with a dimension of $m \times r$ can be estimated as:

$$\mathbf{G}(z) = \bar{\mathbf{S}}_{yu}(z)\bar{\mathbf{S}}_{uu}^{-1}(z) \tag{6.16}$$

However, in real practice, errors are introduced during the computation of $\mathbf{G}(z)$ in

Equation (6.16) due to the lack of periodicity of time sequences, and input and output noises. Therefore, it is necessary to qualify the estimated FRF.

The coherence function defined below is widely used to check the quality of the estimated FRF. Let $u_\nu(k)$ and $y_\mu(k)$ $(k = 0, 1, ..., l-1)$ be time histories generated from the $\nu$th exciting point and the $\mu$th measurement point, respectively. Then, the coherence function between the input $u_\nu$ and $y_\mu$ is defined as:

$$\gamma^2_{\mu\nu}(z) = \frac{\bar{S}_{y_\mu u_\nu}(z)\bar{S}^*_{y_\mu u_\nu}(z)}{\bar{S}_{y_\mu y_\mu}(z)\bar{S}_{u_\nu u_\nu}(z)} \tag{6.17}$$

where $\bar{S}_{y_\mu u_\nu}(z)$ is the averaged cross-spectral density between the $\nu$th input and the $\mu$th output and $\bar{S}_{u_\nu u_\nu}(z)$ is the averaged auto-spectral density of the $\nu$th input. Both $\bar{S}_{y_\mu u_\nu}(z)$ and $\bar{S}_{u_\nu u_\nu}(z)$ are defined in Equation (6.1.5). The coherence function estimates the signal to noise ratio achieved in the estimated frequency response function $\mathbf{G}(z)$. It can be shown that the coherence function satisfies:

$$0 \leq \gamma^2_{\mu\nu}(z) \leq 1 \tag{6.18}$$

Note that this inequality is useful only when a sufficient number of data are available. If only a single data set is available, the coherence function equals one for all $z$ values. When there are enough records to approximate the expected spectral density function by the averaged one, the coherence function approaches one if (1) the output signal $\mathbf{y}(k)$ becomes stronger than the noise levels, (2) the signals display more periodicity, or (3) the system has small nonlinearities. In general, the modes with above 0.9 value of the coherence function are considered reliable.

### 6.1.6 Markov Parameters

Once the FRF is estimated in the previous step, the Markov parameters in time domain are computed by a discrete Inverse Fourier Transform (IFT) of the FRF:

$$\mathbf{Y}_k = \sum_{z=0}^{l-1} \mathbf{G}(z) e^{j(\frac{2\pi k}{l})z} \tag{6.19}$$

where $\mathbf{Y}_0$=$\mathbf{D}$, $\mathbf{Y}_1$=$\mathbf{CB}$, $\mathbf{Y}_2$=$\mathbf{CAB}$,..., $\mathbf{Y}_k$=$\mathbf{CA}^{k-1}\mathbf{B}$ form a sequence of system Markov parameters. Physically, the system Markov parameters are nothing but the pulse response excited by a pulse input at the initial time period. However, in practice, the FRF is computed first and then the FRFs are converted to the Markov parameters on which many time-domain system identification methods are based. Note that the IFT imposes a periodicity on the converted time signal and cause a "leakage" of its energy content if a window is not applied prior to the IFT. Given the Markov parameters, a time-domain system identification is applied to construct minimum order state-space matrices $\mathbf{A}$, $\mathbf{B}$, $\mathbf{C}$, and $\mathbf{D}$. In this study, the ERA is employed and discussed next.

### 6.1.7 Eigensystem Realization Algorithm

The Eigensystem Realization Algorithm (ERA) is briefly presented here. First, the physical interpretation of the minimum order realization and the Hankel matrix is discussed. The order of the Hankel matrix is determined by the Singular Value Decomposition (SVD) of the Hankel matrix. The state matrices $\mathbf{A}$, $\mathbf{B}$, $\mathbf{C}$, and $\mathbf{D}$ are then related to the decomposed Hankel matrix. In addition, several indicators that assess the overall quality of the identification are presented.

The objective of a minimum order realization is to find a realization of $\mathbf{A}$, $\mathbf{B}$, $\mathbf{C}$, and $\mathbf{D}$ with minimum order that reproduces the measured input $\mathbf{u}(t)$ and output $\mathbf{u}(t)$ relationship:

$$\begin{aligned} \mathbf{x}(k+1) &= \mathbf{A}\mathbf{x}(k) + \mathbf{B}\mathbf{u}(k) \\ \mathbf{y}(k) &= \mathbf{C}\mathbf{x}(k) + \mathbf{D}\mathbf{u}(k) \end{aligned} \quad \text{for } k = 0, 1, 2, ... \tag{6.20}$$

The estimation of the minimum order realization is based on the following theorem, established by Ho and Kalman [71]:

**Theorem:** $\mathbf{Y}_k$ $(k = 0, 1, 2, ...)$ has a finite dimensional realization of order $n$ if and only if there exists $n$ nonzero constants $\{\alpha_1, \alpha_2, ..., \alpha_n\}$ such that:

$$\mathbf{Y}_{k+n} = \sum_{i=1}^{n} \alpha_i \, \mathbf{Y}_{n-i+k} \quad \text{for all } k \geq 0$$

That is, the minimum order $n$ is identical to the dimension of basis $[\mathbf{Y}_0, \mathbf{Y}_1, ..., \mathbf{Y}_{n-1}]$

which spans the space defined by sequence $\mathbf{Y}_k$ ($k$=0, 1, 2, ...). The minimum order $n$ is estimated by finding the minimum column rank of the left hand rectangular matrix in the following equation:

$$\begin{bmatrix} \mathbf{Y}_k & \cdots & \mathbf{Y}_{k+d-1} \\ \mathbf{Y}_{k+1} & \cdots & \mathbf{Y}_{k+d} \\ \vdots & \ddots & \vdots \\ \mathbf{Y}_{k+q-1} & \cdots & \mathbf{Y}_{k+q+d-2} \end{bmatrix} \begin{Bmatrix} \alpha_1 \\ \alpha_2 \\ \vdots \\ \alpha_d \end{Bmatrix} = \begin{Bmatrix} \mathbf{Y}_{k+d} \\ \mathbf{Y}_{k+d+1} \\ \vdots \\ \mathbf{Y}_{k+q+d-1} \end{Bmatrix} \tag{6.21}$$

The rectangular matrix in the left hand side of Equation (6.21) is defined as a Hankel matrix:

$$\mathbf{H}_{qd}(k-1) = \begin{bmatrix} \mathbf{Y}_k & \cdots & \mathbf{Y}_{k+d-1} \\ \mathbf{Y}_{k+1} & \cdots & \mathbf{Y}_{k+d} \\ \vdots & \ddots & \vdots \\ \mathbf{Y}_{k+q-1} & \cdots & \mathbf{Y}_{k+q+d-2} \end{bmatrix} \tag{6.22}$$

where $q$ and $d$ denote the number of block rows and columns, respectively. The Hankel matrix $\mathbf{H}_{qd}$ had a dimension of $(q \times m)$ rows by $(d \times r)$ columns. Since the order of the system is unknown, a very large size of Hankel matrix should be formed to extract the minimum order realization. The minimum column rank $n$ is also asymptotically equal to the rank of the Hankel matrix $\mathbf{H}_{qd}(0)$ as both $q$ and $d$ approach infinity:

$$n = \lim_{d\to\infty} \lim_{q\to\infty} Rank[H_{qd}(0)] \tag{6.23}$$

Note that the minimum order of the system ($Rank[\mathbf{A}]$) is identical to the minimum column rank $n$. It can be shown that the Hankel matrix in Equation (6.22) is related to the state-space matrices $\mathbf{A}$, $\mathbf{B}$ and $\mathbf{C}$:

$$\mathbf{H}_{qd}(k-1) = \mathbf{P}_q \mathbf{A}^{k-1} \mathbf{Q}_d \quad \text{for } k \geq 1 \tag{6.24}$$

where matrices $\mathbf{P}_q$ and $\mathbf{Q}_d$ are the observability and controllability matrices, respectively, defined as:

$$\mathbf{P}_q = \begin{bmatrix} \mathbf{C} \\ \mathbf{CA} \\ \vdots \\ \mathbf{CA}^{q-1} \end{bmatrix} \quad \text{and} \quad \mathbf{Q}_d = \begin{bmatrix} \mathbf{B} & \mathbf{AB} & \mathbf{A}^2\mathbf{B} & \cdots & \mathbf{A}^{d-1}\mathbf{B} \end{bmatrix} \tag{6.25}$$

If the system is completely controllable and observable, the block matrices $\mathbf{P}_q$ and $\mathbf{Q}_d$ are of rank $n$. Therefore, the Hankel matrix and state matrix $\mathbf{A}$ has identical rank $n$.

The ERA first decomposes the Hankel matrix at time step $k$=0 using a SVD procedure. Then the decomposed matrices are manipulated together with the Hankel matrix at time step $k$=1 to estimate $\mathbf{A}$, $\mathbf{B}$ and $\mathbf{C}$. The following steps summarize the minimum rank realization using the ERA.

Step 1: Construct the Hankel matrix $\mathbf{H}_{qd}(k-1)$ at $k$=1 and $k$=2.

$$\mathbf{H}_{qd}(0) = \begin{bmatrix} \mathbf{Y}_1 & \mathbf{Y}_2 & \cdots & \mathbf{Y}_d \\ \mathbf{Y}_2 & \mathbf{Y}_3 & \cdots & \mathbf{Y}_{d+1} \\ \vdots & \vdots & \ddots & \vdots \\ \mathbf{Y}_q & \mathbf{Y}_{q+1} & \cdots & \mathbf{Y}_{q+d-1} \end{bmatrix} \tag{6.26}$$

$$\mathbf{H}_{qd}(1) = \begin{bmatrix} \mathbf{Y}_2 & \mathbf{Y}_3 & \cdots & \mathbf{Y}_{d+1} \\ \mathbf{Y}_3 & \mathbf{Y}_4 & \cdots & \mathbf{Y}_{d+2} \\ \vdots & \vdots & \ddots & \vdots \\ \mathbf{Y}_{q+1} & \mathbf{Y}_{q+2} & \cdots & \mathbf{Y}_{q+d} \end{bmatrix} \tag{6.27}$$

Note that the row dimension of the Hankel matrix should be larger than the column dimension, that is $m \times q \geq r \times d$, to ensure that Equation (6.21) is over-determined.

Step 2: Decompose $\mathbf{H}_{qd}(0)$ using the SVD algorithm.

$$\mathbf{H}_{qd}(0) = \mathbf{R}\Sigma\mathbf{S}^T \tag{6.28}$$

where the column of matrices $\mathbf{R}$ and $\mathbf{S}$ are orthogonal and $\Sigma$ is give as

$$\Sigma = \begin{bmatrix} \Sigma_n & \mathbf{0} \\ \mathbf{0} & \mathbf{0} \end{bmatrix} \tag{6.29}$$

with $\Sigma_n$=$diag[\alpha_1\ \alpha_2\ \ldots\ \alpha_n]$. In theory, the number of nonzero singular values should be equal to the dimension of the system $n$. However, the selection of the right order becomes difficult when the data are corrupted by noise. A conservative solution is to include as many non-zero singular values as possible even if some noise modes are included in the identification. Since noise in data tends to increase the apparent rank of the Hankel matrix, it is recommended to run the ERA by increasing $q$ and $d$ until the number of non-zero singular values converges. Then, with the help of various indications, the quality of the identified modes is assessed in a later step.

Step 3: let $\mathbf{R}_n$ and $\mathbf{S}_n$ be the first $n$ columns of $\mathbf{R}$ and $\mathbf{S}$, respectively. Once the minimum order $n$ is estimated, $\mathbf{A}$, $\mathbf{B}$, $\mathbf{C}$ and $\mathbf{D}$ are estimated as follows:

$$\hat{\mathbf{A}} = \Sigma_n^{-1/2}\mathbf{R}_n^T\mathbf{H}(1)\mathbf{S}_n\Sigma_n^{-1/2},\ \ \hat{\mathbf{B}} = \Sigma_n^{1/2}\mathbf{S}_n^T\mathbf{E}_r,\ \ \hat{\mathbf{C}} = \mathbf{E}_m^T\mathbf{R}_n\Sigma_n^{1/2},\quad \hat{\mathbf{D}} = \mathbf{Y}_0 \tag{6.30}$$

where $\mathbf{E}_m^t = [\ \mathbf{I}\ \mathbf{0}\cdots\mathbf{0}\ ] \in \mathcal{R}^{m\times(m\times d)}$ and $\mathbf{E}_r^t = [\ \mathbf{I}\ \mathbf{0}\cdots\mathbf{0}\ ] \in \mathcal{R}^{r\times(q\times r)}$. The block matrices $\mathbf{I}$ and $\mathbf{0}$ in $\mathbf{E}_m$ and $\mathbf{E}_r$ have the dimension of $m\times m$ and $r\times r$, respectively. The notation $\hat{}$ ("hat") denotes the estimated quantities to distinguish them from the true quantities. Note that the computation of the ERA becomes very storage intensive as the size of the Hankel matrix increases. A recursive version of the ERA is available when the construction of a large Hankel matrix is necessary [100]. Another implementation, which uses a partial eigensolver to extract the singular values, has also been proposed [121].

Step 4: The overall quality of the identification is investigated in this step. There are three indicators developed specifically for use with the ERA [119]: Extended Mode

Amplitude Coherence (EMAC), Modal Phase Collinearity (MPC) and Consistent Mode Indicator (CMI), which is the product of EMAC and MPC. EMAC is a measure of how accurately a particular mode projects forward onto the impulse response data. MPC is a measure of how collinear the phases of the components of a particular complex mode are. If the phases are perfectly in phase or out of phase with each other, this mode exactly has proportional damping and can be completely represented by the corresponding real mode shape. That is, EMAC is a temporal quality measure and MPC is a spatial quality measure. The final step is a visual inspection of the mode shapes. Typically, the values of EMAC=0.7, MPC=0.7 and CMI=0.5 are employed [47].

### 6.1.8 Extraction Procedure of Modal Parameters

From the estimated system matrices, $\hat{\mathbf{A}}$, $\hat{\mathbf{B}}$ and $\hat{\mathbf{C}}$, physical modal properties such as natural frequencies, damping ratios and modal vectors are computed. First, the discrete time system matrices $\hat{\mathbf{A}}$ and $\hat{\mathbf{B}}$ are converted to the continuous time system matrices $\hat{\mathbf{A}}_c$ and $\hat{\mathbf{B}}_c$ using Equation (6.8) where the exponential matrices are computed using a scaling and squaring algorithm with a Pade approximation. Define $\Lambda$ as the diagonal matrix of eigenvalues of the matrix $\hat{\mathbf{A}}_c$ and $\Phi$ as the matrix of eigenvectors, then $\hat{\mathbf{A}}_c$ can be expressed as follows:

$$\hat{\mathbf{A}}_c = \Phi \Lambda \Phi^{-1} \tag{6.31}$$

where

$$\Lambda = diag[\lambda_1, \lambda_2, ..., \lambda_n] \in \mathcal{R}^{n \times n}, \quad \Phi = [\phi_1, \phi_2, ..., \phi_n] \in \mathcal{R}^{n \times n}$$

Note that $\lambda_i$ and $\phi_i$ are complex eigenvalues and eigenvectors, respectively. Complex conjugate pairs appear in $\Lambda$. The real eigenvalues in $\Lambda$ are rejected since they correspond to noise modes. Similar process is applied for complex modal vectors. The physical natural frequency $\omega_i$ and the corresponding damping ratio $\xi_i$ are related to $\lambda_i$ such that $\lambda_i = \xi_i \omega_i + j\omega_i \sqrt{1 - \xi_i^2}$, where $j = \sqrt{-1}$. Note that if a complex conjugate of $\lambda_i$ is $\lambda_{i+1} (= \lambda_i^*)$, the plus sign in the previous equation changes to minus sign, that

is $\lambda_{i+1} = \xi_{i+1}\omega_{i+1} + j\omega_{i+1}\sqrt{1-\xi_{i+1}^2}$. Also $\omega_i = \omega_{i+1}$ and $\xi_i = \xi_{i+1}$. Therefore, only $N$ $(=n/2)$ separate eigenvalues and damping ratios exist.

If we denote $\lambda_i = \lambda_i^R + j\lambda_i^I$ where $\lambda_i^R$ and $\lambda_i^I$ represent the real and imaginary parts, respectively, the physical natural frequency $\omega_i$ and the corresponding damping ratio $\xi_i$ are computed as:

$$\omega_i = \sqrt{\lambda_i^{R2} + \lambda_i^{I2}} \quad \text{and} \quad \xi_i = \frac{\lambda_i^R}{\sqrt{\lambda_i^{R2} + \lambda_i^{I2}}} \tag{6.32}$$

Next, modal vectors in physical coordinate $\mathbf{V}$ is computed as:

$$\mathbf{V} = \hat{\mathbf{C}}\Phi \quad \in \mathcal{R}^{m\times n} \tag{6.33}$$

Again only $N$ $(=n/2)$ number of modal vectors are unique. Note that the experimental modal vectors in Equation (6.33) are *complex* modal vectors. If the structure exhibits nonlinearity and non-proportional damping, the modal vectors in Equation (6.33) are corrupted by out-of-phase components corresponding to the imaginary part of the modal vectors [78]. Since we need *normal* modal vectors, which are the modal vectors of the undamped system, the estimated complex modal vectors must be approximated by equivalent normal modal vectors.

References 30 and 101 describe the concept of complex modes. References 73 and 109 present techniques to isolate normal modal vectors from complex modal vectors. The errors introduced by these methods are addressed in Reference 132. The easiest way is to retain only the real parts of the complex modal vectors. More detailed discussion on this issue can be found in Reference 3.

### 6.1.9 State-Space Based Extraction of Ritz Vectors

The state-space based extraction procedure of experimental Ritz vectors are similar to the generation procedure of analytical Ritz vectors discussed in Section 3.4.1 [28]. The main difference is that the triple set state-space matrices $\hat{\mathbf{A}}_c$, $\hat{\mathbf{B}}_c$ and $\hat{\mathbf{C}}$ are used instead of the system matrices $\mathbf{K}$, $\mathbf{M}$ and the spatial load vector $\mathbf{f}$. Note that the diagonal eigen matrix of $\hat{\mathbf{A}}_c$ (denoted by $\Lambda$ in Equation (6.31)) often contains noise modes as well as true modes in vibration tests. Therefore, the modes corresponding

to the actual response of the test structure should be first distinguished before the Ritz vector extraction. This process requires some engineering judgment and two useful approaches are described in Reference 77.

The static deformation $\bar{\mathbf{x}}_1$ subject to a load at the excitation point is computed by solving the following equation for $\bar{\mathbf{x}}_1$:

$$\hat{\mathbf{A}}_c \bar{\mathbf{x}}_1 = -\hat{\mathbf{B}}_c \quad \text{solve for} \quad \bar{\mathbf{x}}_1 (= \tilde{\mathbf{x}}_1) \tag{6.34}$$

where the input influence matrix $\hat{\mathbf{B}}_c$ contains the information regarding the excitation point. Then, the first Ritz vector is normalized as:

$$\mathbf{x}_1 = \frac{\bar{\mathbf{x}}_1}{\left[\bar{\mathbf{x}}_1^T \ \bar{\mathbf{x}}_1\right]^{\frac{1}{2}}} \tag{6.35}$$

The subsequent Ritz vectors are recursively generated from the following equation:

$$\bar{\mathbf{A}}_c \bar{\mathbf{x}}_s = \mathbf{x}_{s-1} \quad \text{solve for } \bar{\mathbf{x}}_s \tag{6.36}$$

The linear independence of Ritz vectors is achieved using the Gram-Schmidt orthogonalization. That is, the current Ritz vector is orthogonalized with respect to all the previous Ritz vectors:

$$\tilde{\mathbf{x}}_s = \bar{\mathbf{x}}_s - \sum_{t=1}^{s-1} (\mathbf{x}_t^T \bar{\mathbf{x}}_s) \ \mathbf{x}_t \tag{6.37}$$

Finally, the current Ritz vector is normalized:

$$\mathbf{x}_s = \frac{\tilde{\mathbf{x}}_s}{\left[\tilde{\mathbf{x}}_s^T \ \tilde{\mathbf{x}}_s\right]^{\frac{1}{2}}} \tag{6.38}$$

The Ritz vectors in the physical coordinates $\mathbf{r}_s$ are computed at the measurement points as:

$$\mathbf{r}_s = \hat{\mathbf{C}} \mathbf{x}_s \tag{6.39}$$

It should be noted that the normalization and orthogonalization procedures in this state-space method are not identical to those of the analytical generation procedure

in Section 3.4.1. Therefore, the physical Ritz vectors obtained from Equation (6.39) should be again normalized and orthogonalized with the analytical mass matrix $\mathbf{M}$ in order to compare the experimental Ritz vectors with the analytical ones.

### 6.1.10 Flexibility Based Extraction of Ritz Vectors

A close look at the analytical generation procedure in Section 3.4.1 reveals that the generation of Ritz vectors requires the flexibility matrix $\mathbf{F}$ (defined here as the inverse of the stiffness matrix) rather than the stiffness matrix itself. Assuming that the modal vectors are mass-normalized such that

$$\begin{aligned} \mathbf{V}^T\mathbf{K}\mathbf{V} &= \Omega \\ \mathbf{V}^T\mathbf{M}\mathbf{V} &= \mathbf{I} \end{aligned} \tag{6.40}$$

the flexibility matrix can be represented with the modal parameters [44]:

$$\mathbf{F} = \mathbf{K}^{-1} = \mathbf{V}\Omega^{-1}\mathbf{V}^T \tag{6.41}$$

where $\Omega$ is the diagonal eigenvalue matrix and $\mathbf{V}$ is the corresponding eigenvector (modal vector) matrix. In most experimental modal analyses, only a few lower modal frequencies and modal vectors are identified. For this case, the flexibility matrix is divided into the *modal flexibility*, which is formed from the estimated frequencies and modal vectors, and the *residual flexibility* formed from the residual modes:

$$\mathbf{F} = \mathbf{F}_m + \mathbf{F}_r = \mathbf{V}_m\Omega_m^{-1}\mathbf{V}_m^T + \mathbf{V}_r\Omega_r^{-1}\mathbf{V}_r^T \tag{6.42}$$

where the subscript $m$ and $r$ denote the estimated and residual quantities, respectively. Here, the modal flexibility matrix is constructed only from the measured natural frequencies and modal vectors ($\mathbf{F}_m = \mathbf{V}_m\Omega_m^{-1}\mathbf{V}_m^t$). The residual flexibility is the contribution of the unmeasured dynamic modes to the full flexibility matrix. Note that the contribution of lower modes, which are normally estimated in experimental modal analyses, are more significant than those of higher modes because the contribution of each mode is inversely proportional to the magnitude of the corresponding natural frequencies.

From the modal flexibility matrix $\mathbf{F}_m$ and the analytical mass matrix $\mathbf{M}$, the first Ritz vector can be computed as:

$$\bar{\mathbf{r}}_1 = \mathbf{F}_m \mathbf{f} \tag{6.43}$$

where $\mathbf{f}$ is the spatial load distribution vector defined in Equation (3.24). The first Ritz vector is, then, mass-normalized as:

$$\mathbf{r}_1 = \frac{\tilde{\mathbf{r}}_1}{[\tilde{\mathbf{r}}_1^T \mathbf{M} \tilde{\mathbf{r}}_1]^{\frac{1}{2}}} \tag{6.44}$$

The following Ritz vectors are recursively generated. Assuming the mass matrix times the previous Ritz vector $\mathbf{M}\mathbf{r}_{s-1}$ as a load, the recurrence relationship computes the next Ritz vector $\bar{\mathbf{r}}_s$:

$$\bar{\mathbf{r}}_s = \mathbf{F}_m \mathbf{M} \mathbf{r}_{s-1} \tag{6.45}$$

The linear independence of Ritz vectors is achieved using the Gram-Schmidt orthogonalization:

$$\tilde{\mathbf{r}}_s = \bar{\mathbf{r}}_s - \sum_{t=1}^{s-1} (\mathbf{r}_t^T \mathbf{M} \bar{\mathbf{r}}_s) \mathbf{r}_t \tag{6.46}$$

Finally, the current Ritz vector is mass-normalized:

$$\mathbf{r}_s = \frac{\tilde{\mathbf{r}}_s}{[\tilde{\mathbf{r}}_s^T \mathbf{M} \tilde{\mathbf{r}}_s]^{\frac{1}{2}}} \tag{6.47}$$

It's worthwhile to compare the flexibility-based extraction procedure with the state-space procedure. While the flexibility-based method is able to generate Ritz vectors with arbitrary load patterns, the state-space method only identifies the Ritz vectors corresponding to the specific excitation pattern used in the actual modal testing. That is, the spatial load distribution vector $\mathbf{f}$ in Equation (6.43) can be assigned arbitrarily to generate different sets of Ritz vectors. On the other hand, the input influence matrix $\hat{\mathbf{B}}_c$ in Equation (6.34), which retains the loading information, is experimentally estimated. Note that both methods require an appropriate approximation for the mass matrix. However, since stiffness changes are the main concern of

damage detection, the exact estimation of the mass matrix is not necessary.

## 6.2 A Grid-Type Bridge Model

This section presents the experiment results of a grid-type bridge model constructed and tested at the Hyundai Institute of Construction Technology (HICT), Korea. The steel bridge model consists of two parallel girders and six evenly spaced cross beams connecting the two girders as shown in Figure 6.2. The girders are steel rectangular tubes and the cross beams are C-shape members. A detailed dimension of the test structure is shown in Figure 6.2. Using impact excitations, we extract Ritz/modal vectors from the vibration response of the test structure, demonstrate the proposed Bayesian framework, and investigate the relationship between the locations of exciting forces and the observability of damages in various parts. Furthermore, damage diagnosis comparisons using Ritz/modal vectors and other damage detection techniques are conducted.

Figure 6.1: An overview of a grid-type bridge structure

### 6.2.1 Experimental Setup

A SA-390 signal analyzer with four channels is used for the analog to digital conversion of accelerometer signals and the Fast Fourier Transform (FFT) calculation. Data

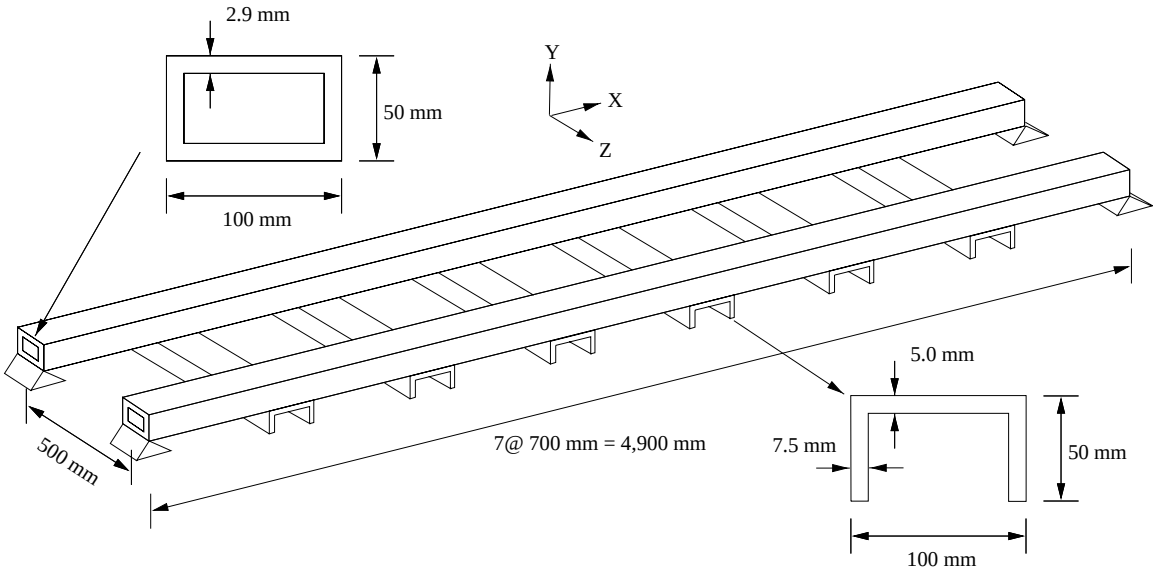


Figure 6.2: Configuration of a grid-type bridge model

acquisition parameters are specified such that a frequency response function (FRF) in the range of 0 to 100 Hz could be estimated. Each spectrum is computed by averaging three 8 seconds long time histories. A total of 2048 points are sampled for a 8 second time period and this sampling rate produces a frequency resolution of 0.125 Hz. An exponential window is applied to all measured time histories prior to the FFT calculation.

For measurements, a Dytran 5801A4 impact hammer and three Dytran 3100B accelerometers with a normal sensitivity of 100mV/g are used. The excitation is applied to nodes 3, 4 and 5 as shown in Figure 6.3. The sensors measure the vertical accelerations at the twelve nodes as indicated in Figure 6.3. Note that since the SA-390 data acquisition system has only four channels and there are three accelerometers, the first channel is always connected to the input hammer and the remaining three channels are connected to three accelerometers. To complete one set of modal test, the hammer excitation is repeated twelve times at one point and the three accelerometers are moved from one set of three nodes to another set of three nodes after every three excitations (note that each FRF is computed by averaging the three response time histories, and there are twelve measurement points and three accelerometers).

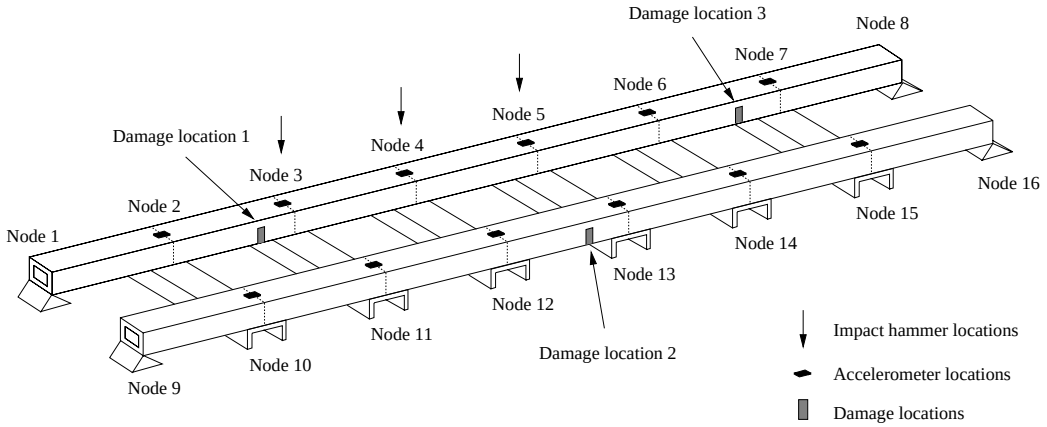


Figure 6.3: Impact, accelerometer and damage locations of the grid-type bridge structure

The DIAMOND [2] software developed by the Los Alamos National Laboratory is employed for the extraction of modal parameters. The ERA and rational polynomial techniques are employed to extract the first six natural frequencies and the corresponding modal vectors from the recorded FRFs. Figure 6.4(a) shows a typical FRF and coherence function of the test structure. Figure 6.4(a) is a FRF obtained at node 5 when the structure is excited at node 4. Figure 6.4(b) presents the corresponding coherence function defined in Equation (6.17). Figure 6.4(b) shows that the value of the coherence function is close to unity at the resonance frequencies. This implies that the output signals from the sensors are reasonably strong compared to the noise levels.

To validate the linearity assumption of the structure response, a reciprocity check is conducted. Figure 6.5 compares the FRFs obtained at node 3 with input at node 14 and at node 14 with excitation at node 3. For an ideal linear structure, these two FRFs should be identical. For the grid structure, the linearity assumption seems valid up to the fourth mode but the difference of the functions becomes noticeable after 40Hz.

[2]The program is available for download from http://esaea-www.esa.lanl.gov/damage_id.

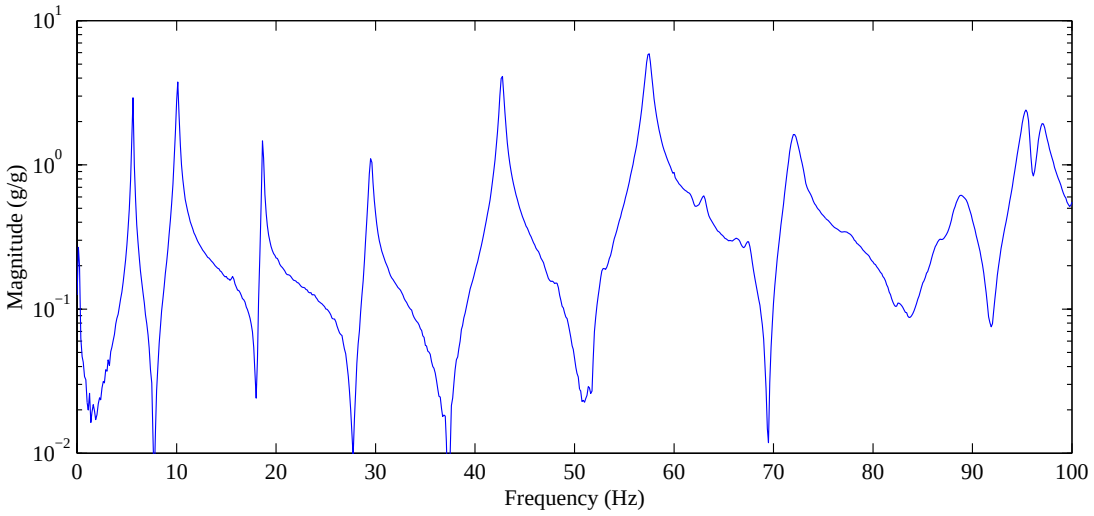


(a) A FRF of node 5 with node 4 input

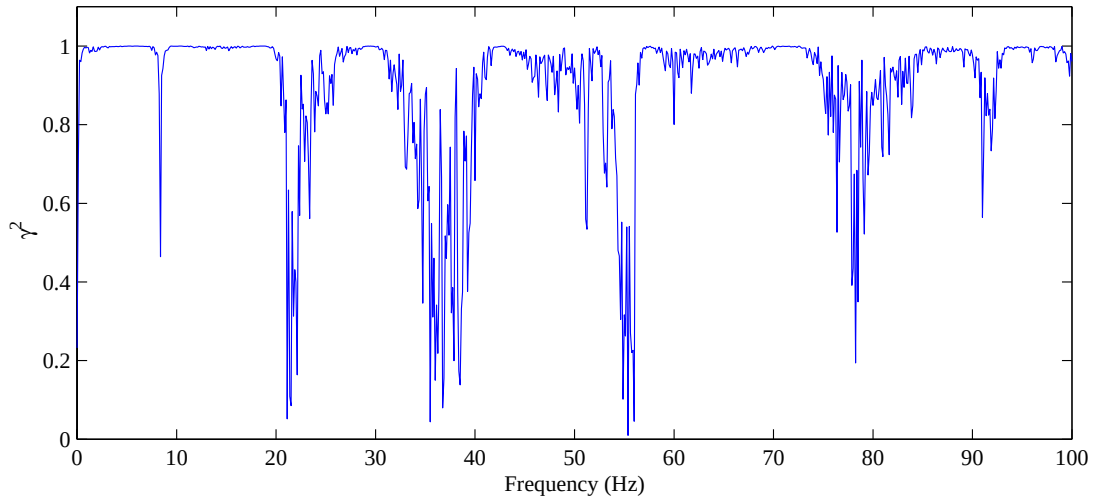


(b) A coherence function of node 5 with node 4 input

Figure 6.4: A typical FRF & coherence function of the grid-type bridge model

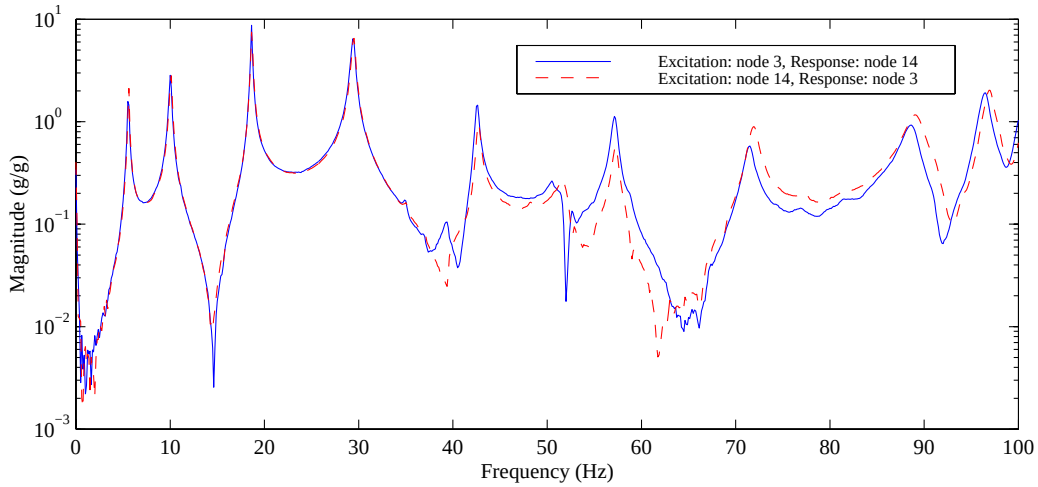


Figure 6.5: A reciprocity check of the grid-type bridge model

### 6.2.2 Analytical Modeling

A FE model is constructed using twenty three-dimensional beam elements. As shown in Figure 6.2, a girder or cross beam is modeled as a single member. An elastic modulus of $2.0\times10^5$ MPa, a mass density of 7850 kg/m$^3$, and a Poission's ratio of 0.2 are specified in this model. Since the accelerometers measure only the vertical movement of the structure, the lateral DOFs are not included in the analytical model. Therefore, each node of an element has two translational DOFs and three rotational DOFs. The model has a total of 64 DOFs including four rotational DOFs at the boundary. Both ends of the beam are modeled as simple pinned connections. A pinned connection is modeled by a ball bearing with a 35mm diameter in the experimental setup. Based on a preliminary vibration test, the boundary conditions appear to be less accurately modeled. The boundary conditions are then modified by introducing rotational springs at the rotational DOFs of the boundaries. Furthermore, additional springs are added to the rotational DOFs at both end of the cross beams to simulate the bolted connection between the girders and the cross beams. After these modifications, the relative errors of the first six natural frequencies between the analytical model and the test structure fall within 4%.

Table 6.1: Comparison of the analytical and experimental natural frequencies

| Mode | Frequency (Hz) | | Relative |
|---|---|---|---|
| | Analytical ($\omega$) | Experimental ($\hat{\omega}$) | Error* (%) |
| 1st Bending | 5.4488 | 5.5635 | 2.06 |
| 1st Torsion | 10.1494 | 10.0406 | 1.08 |
| 2nd Bending | 19.1841 | 18.6410 | 2.91 |
| 2nd Torsion | 30.6216 | 29.4388 | 4.02 |
| 3rd Bending | 41.6086 | 42.5910 | 2.31 |
| 3rd Torsion | 54.9704 | 57.1864 | 3.88 |

* error=$|\omega - \hat{\omega}|/\hat{\omega}$

Table 6.1 compares the values of the analytical and experimental natural frequencies. Here, the experimental frequency ($\hat{\omega}$) is a mean value of the three frequencies estimated with impacts on nodes 3, 4 and 5, respectively. Figure 6.6 displays the analytical and experimental modal vectors of the first six modes. The first six Ritz vectors are also computed following the extraction procedure in Section 6.1.10. Figure 6.7 shows the analytical Ritz vectors and the experimental Ritz vectors with an impulse excitation at node 3. The analytical Ritz vectors in Figure 6.7 are computed from the analytical model following the procedure in Section 3.4.1. It should be noted that the first Ritz vector is equivalent to a deflection pattern observed when a unit load is applied to node 3.

As for the scaling of the Ritz or modal vectors, a mass-normalization is conducted. However, since the DOFs of the analytical model do not coincide with the DOFs of the experimental Ritz or modal vectors, a reduced analytical mass matrix is first computed using the Guyan (static) condensation procedure [61]. Then, both the analytical and experimental vectors are normalized with respect to the reduced mass matrix. Errors arise from the model reduction are found to be minimum since the inertial forces associated with the omitted rotational DOFs (slave DOFs) are negligible in this example.

### 6.2.3 Application to Damage Detection

Continuous deterioration of stiffness is simulated at three different regions of the grid structure and the vibration tests are conducted at six different damage stages

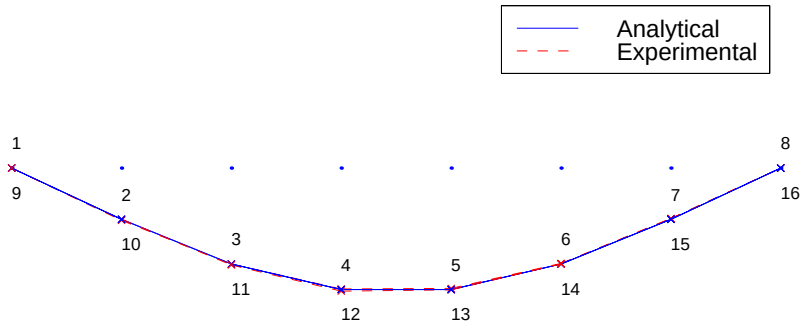


(a) The first mode

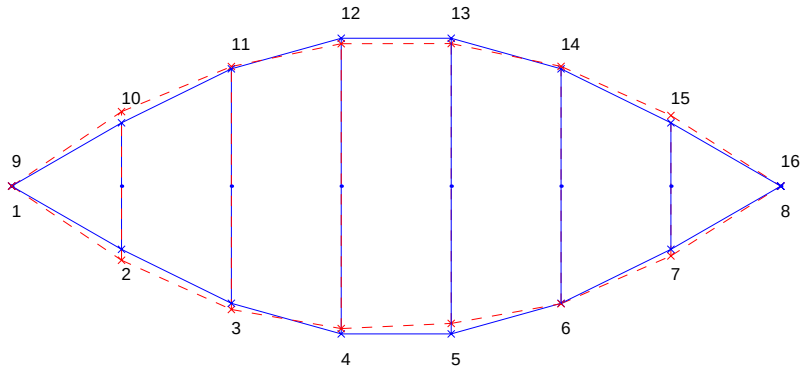


(b) The second mode

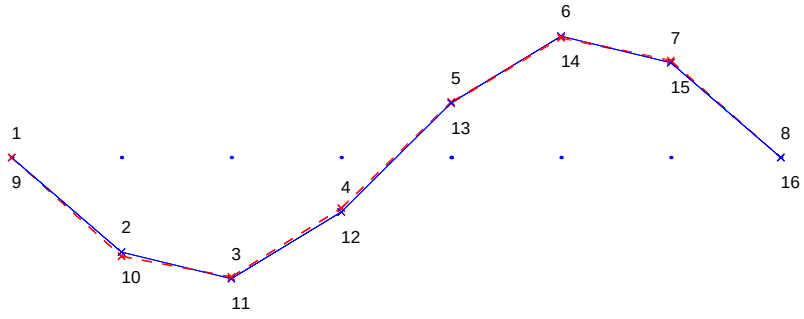


(c) The third mode

Figure 6.6: Comparison of analytical and experimental modal vectors

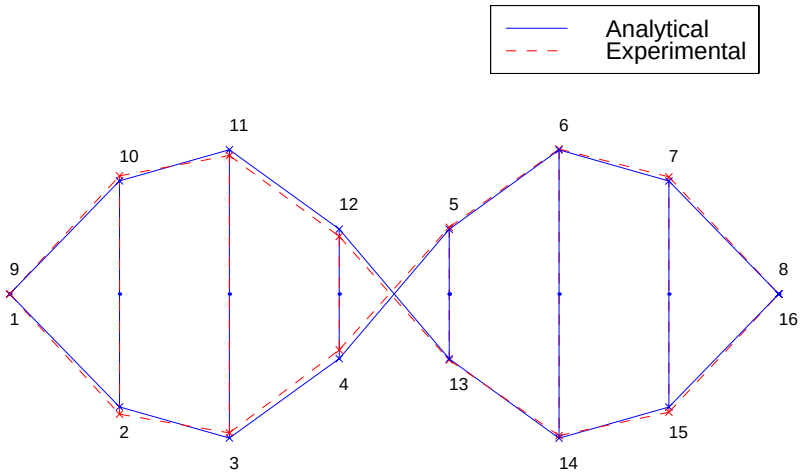


(d) The fourth mode

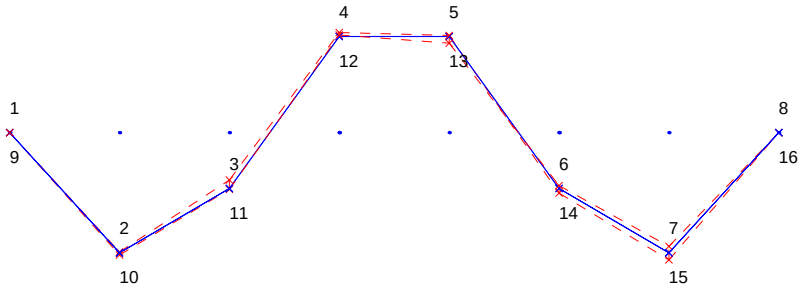


(e) The fifth mode

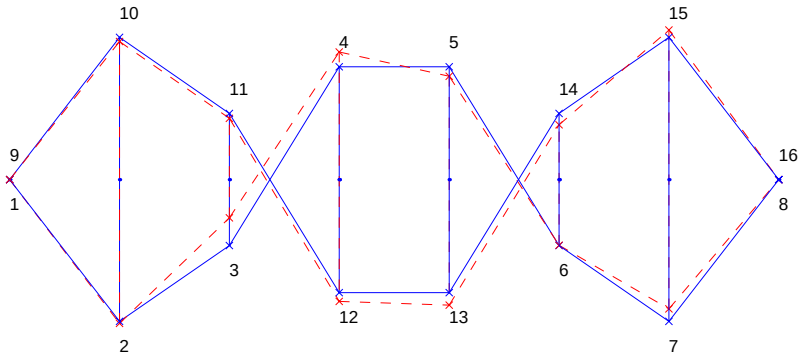


(f) The sixth mode

Figure 6.6: Comparison of analytical and experimental modal vectors (continued)

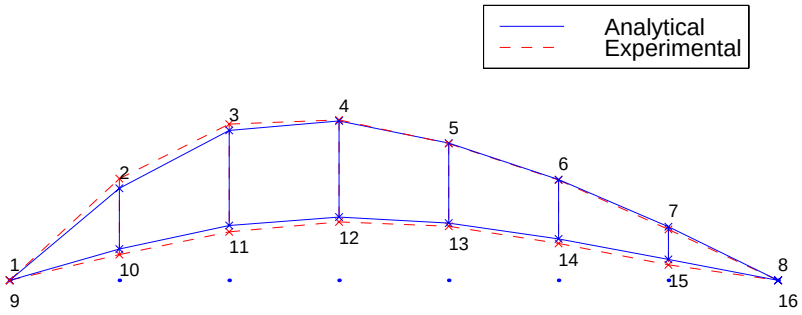


(a) The first Ritz vector

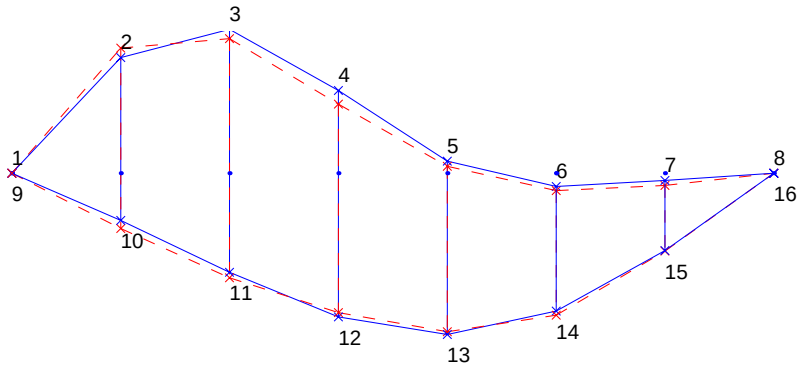


(b) The second Ritz vector

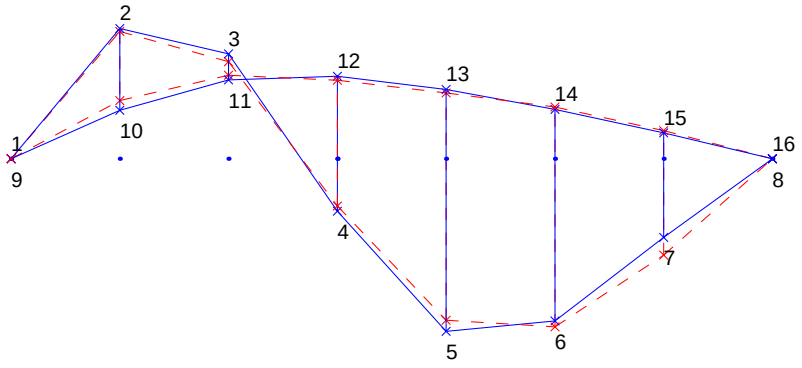


(c) The third Ritz vector

Figure 6.7: Comparison of analytical and experimental modal vectors

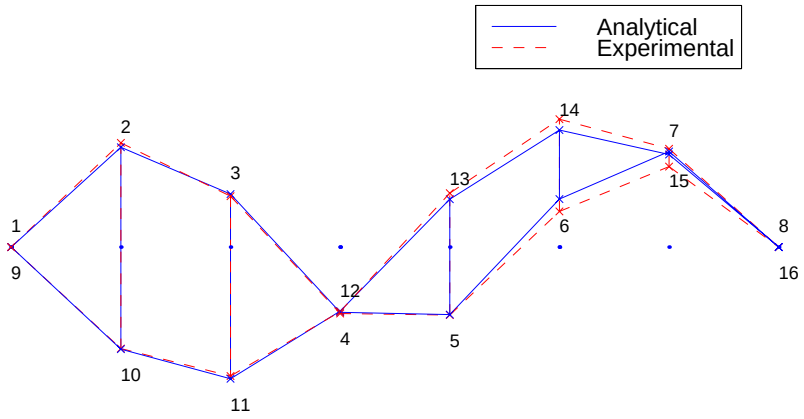


(d) The fourth Ritz vector

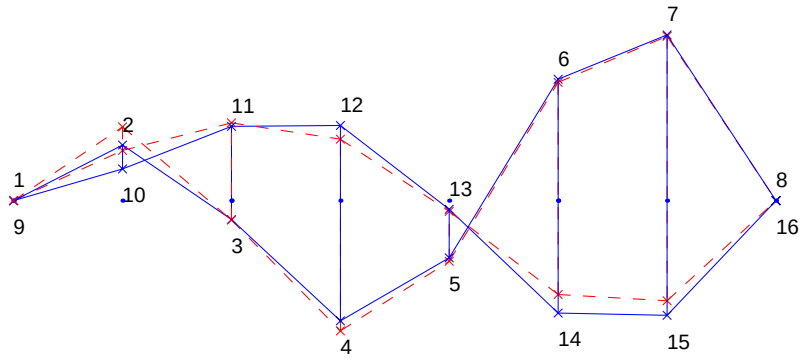


(e) The fifth Ritz vector

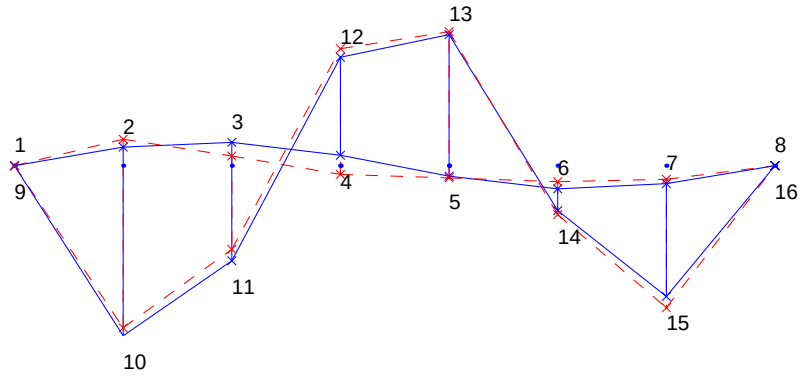


(f) The sixth Ritz vector

Figure 6.7: Comparison of analytical and experimental modal vectors (continued)

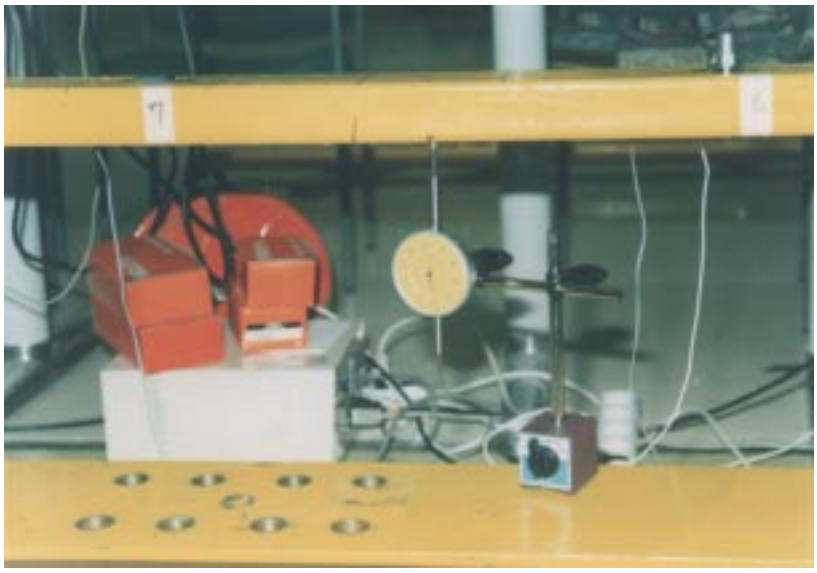

Figure 6.8: Actual damage introduced to the grid-type bridge structure

Table 6.2: Description for six damage cases of a grid-type bridge structure

| Case | Location 1* | Location 2* | Location 3* |
|---|---|---|---|
| 1 | 2.0 cm (40%) | - | - |
| 2 | 3.0 cm (60%) | - | - |
| 3 | 3.0 cm (60%) | 1.5 cm (30%) | - |
| 4 | 3.0 cm (60%) | 2.6 cm (52%) | - |
| 5 | 3.0 cm (60%) | 3.2 cm (64%) | - |
| 6 | 3.0 cm (60%) | 3.2 cm (64%) | 2.5 cm (50%) |

* Damage locations 1, 2 & 3 are shown in Figure 6.3. The first number is the depth of cut and the second number is the ratio of the cut depth to the height of the beam (5 cm).

Table 6.3: Natural frequencies (Hz) estimated at different damage levels

| Damage case | Natural Frequency (Hz) | | | | | |
|---|---|---|---|---|---|---|
| | 1st | 2nd | 3rd | 4th | 5th | 6th |
| Case 0 | 5.5635 | 10.0406 | 18.6410 | 29.4388 | 42.5910 | 57.1864 |
| Case 1 | 5.5325 | 9.8055 | 18.0557 | 29.0354 | 42.0302 | 56.6170 |
| Case 2 | 5.4834 | 9.6725 | 17.2749 | 28.5032 | 41.1840 | 56.1848 |
| Case 3 | 5.3699 | 9.5971 | 17.2364 | 27.6911 | 40.6107 | 55.3881 |
| Case 4 | 5.2398 | 9.5249 | 17.2193 | 27.3410 | 39.7738 | 52.3992 |
| Case 5 | 5.0254 | 9.3938 | 17.1694 | 27.1571 | 38.5939 | 51.6392 |
| Case 6 | 4.9622 | 9.0075 | 16.1835 | 26.6957 | 37.2933 | 49.9543 |

as shown in Table 6.2. Figure 6.3 shows the three damage locations. First, a single damage is introduced at damage location 1 (for cases 1 and 2) and the second damage is formed between nodes 12 and 13 (for cases 3, 4 and 5). Finally, damage case 6 is simulated by adding the third damage at location 3.

For each damage location, a crack is introduced by a saw cutting at a distance of 30cm from the left node. A typical saw cutting is shown in Figure 6.8. For example, the damage location 1 in Figure 6.3 is formed at 30cm left of the node 3. The severity of saw cutting in terms of depth (cm) and the ratio of the cut depth to the height of the beam (%) are tabulated as shown in Table 6.2. In addition, Table 6.3 summarizes the change of frequencies at each damage stage.

Table 6.4: Damage diagnosis results for the grid-type structure using Ritz & modal vectors

| | Damage | Ritz Vectors | | Modal Vectors | |
|---|---|---|---|---|---|
| Case | Location | $\hat{L}_{dam}$ | Rank[1] | $\hat{L}_{dam}$ | Rank[1] |
| 1 | {2} | {2, 3} | 1(2) | {2, 8, 9} | 1(29) |
| 2 | {2} | {2, 3} | 1(12) | {2, 8, 12} | 1(46) |
| 3 | {2, 11} | {2, 3} | 3(9) | {2, 3, 8} | 13(41) |
| 4 | {2, 11} | {2} | 3(3) | {2, 8, 12} | 4(12) |
| 5 | {2, 11} | {2, 11} | 1(1) | {2, 11, 12} | 1(9) |
| 6 | {2, 6, 11} | {2, 6, 11} | 1(1) | {2, 6, 11} | 1(1) |

1. The first number is the highest rank of a damage event which includes all actual damage locations and the second number is the rank of the actual damage event.
2. $\hat{L}_{dam}$ is a set of the most probable damage locations identified by the branch-and- bound search.

First, damage diagnosis is conducted using the six estimated modes. For each damage stage, three sets of modal data, which are obtained from the impulse excitation at nodes 3, 4 and 5, are employed for the proposed Bayesian approach. The diagnosis results are summarized in Table 6.4. The fifth column of the table (the column under $\hat{L}_{dam}$) shows the most likely damage locations identified by the branch-and-bound search scheme. The first number under the title "*Rank*" denotes the rank of the actual damage event, and the second number presents the highest rank among the damage events that include all the actual damage locations. The diagnosis results reveal that as we approach the final damage stage, the diagnosis employing the modal parameters converges to the actual damage locations.

Second, the same six cases are re-diagnosed using the Ritz vectors generated from

different load patterns. A point load is assumed to be applied to the vertical direction of each node (the global Y direction in Figure 6.2) and the first six Ritz vectors are generated from the load pattern. Then, this process is repeated for all twelve vertical DOFs. From these load patterns, a total of 48 (4 Ritz vectors/load $\times$ 12 load patterns) Ritz vectors are generated. Note that, following the extraction procedure in Section 6.1.10, Ritz vectors corresponding to any load pattern can be theoretically extracted with the same amount of test data used to estimate the modal parameters. That is, more information is gained by applying multiple loads.

The diagnosis results using the Ritz vectors are also summarized in Table 6.4. For cases 1 and 2, the actual damage event is ranked as the second and twelfth most likely damage event, respectively. In the first two cases, damage location 1 is included in the most likely damage event estimated by the branch-and-bound search. That is, although the branch-and-bound search fails to pinpoint the actual damage location, the search finds the actual damage location as one of the most likely damage locations. For case 3, the actual damage event is ranked as the ninth most likely event. For case 4, the actual damage case is ranked as the third most likely event, for cases 5 and 6, the branch-and-bound search exactly finds the actual damage events.

Table 6.5: Diagnosis result for damage case 3 of the girder structure

| Rank | $\hat{L}_{dam}$ | Rank | $\hat{L}_{dam}$ | Rank | $\hat{L}_{dam}$ |
|---|---|---|---|---|---|
| 1 | {2, 3 } | 4 | {2, 3, 12} | 7 | {1, 2, 3} |
| 2 | {2, 3, 4} | 5 | {2 } | 8 | {2, 12 } |
| 3 | {2, 3, 11} | 6 | {2, 4 } | 9 | {2, 11 } |

Table 6.5 shows the first nine most probable damage events identified by the branch-and-bound search for damage case 3. The first two most probable events only include damage location 1 and miss damage location 2. However, the third most probable event includes the two damage locations and one extra member 3. That is, although the proposed approach ranks the actual damage event as the ninth most probable event, the third most likely event conservatively includes all the actual damage locations.

Using the test data obtained from case 5, Figure 6.9 illustrates the branch-and-bound search scheme proposed in Section 2.2. The search presented here follows a depth-first/best-first search strategy and the third highest posterior probability, $P^3_{max}$, among all the hypotheses examined so far is employed in Equation 2.27 instead of $P_{max}$. The branch-and-bound search finds the actual damage event as the most likely one after examining 63 different damage scenarios out of 4096 ($=2^{12}$) possible ones.

The results shown in Table 6.4 shows that the Ritz vectors provide better diagnosis results than the modal vectors for all the six damage cases investigated. The sensitivity comparison shown in Figure 6.10 supports the diagnosis results. In Figure 6.10, the sensitivity comparison using the experimental Ritz/modal vectors at different damage stages is conducted. The Ritz vectors are extracted from a point load applied at node 4. From Figure 6.10, we conclude that a careful selection of load patterns can make damage more observable. The better sensitivity of Ritz vectors to damage locations and the increased amount of information employing multiple load patterns seem to improve the damage diagnosis.

### 6.2.4 Application of Other Detection Methods

For comparison, the Minimum Rank Perturbation Theory (MRPT) [85], damage index method [92,143,145], and Sensitivity-Based Element-By-Element (SB-EBE) method [69] are applied to the test data.

The MRPT proposed by Kaouk and Zimmerman consists of two basic steps [85]. First, dynamic residual forces (also know as damage vectors or residual force vectors) are employed to locate the damaged regions which are mathematically expressed in terms of DOFs in the analytical model. Physically, the dynamic residual force in each DOF represents the unbalanced force caused by the discrepancy between the analytical model and the estimated modal parameters. Second, the lowest rank perturbation is introduced to the analytical stiffness matrix such that the residual forces are minimized. This method is computationally efficient and does not require any iteration. However, the measurement points of the experimental modal vectors should coincide with those of the analytical model, and the dimension of the modal vectors should be the same as the dimension of the analytical model. To satisfy these

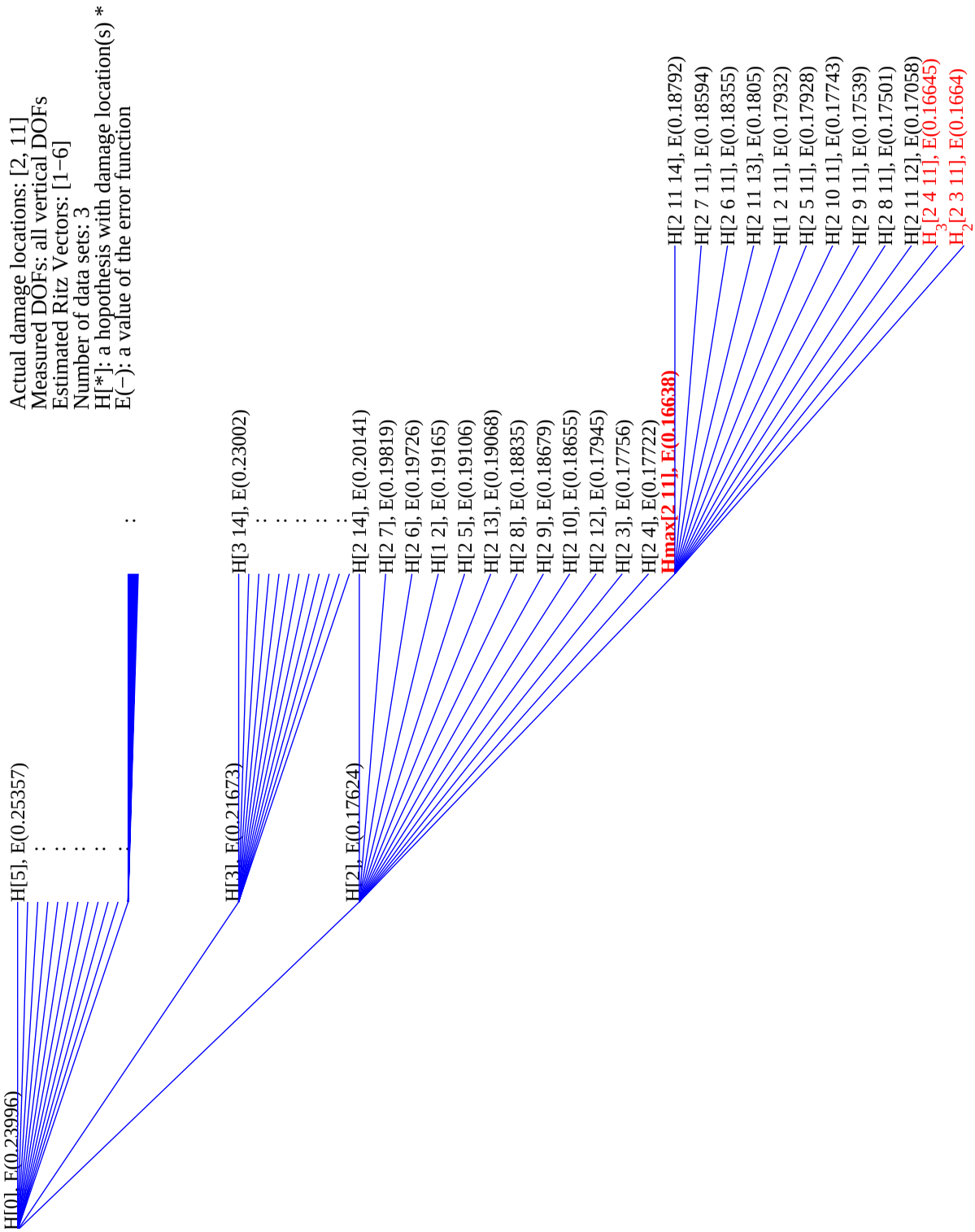


Figure 6.9: A Branch-and-Bound search of a grid-type bridge model

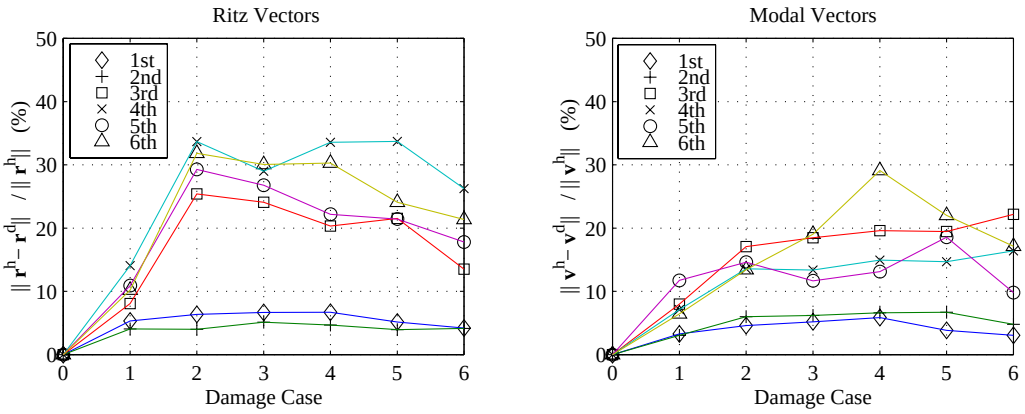


Figure 6.10: Sensitivity comparison of Ritz and modal vectors at different damage stages

conditions, the Guyan condensation is applied to the analytical model. Furthermore, in Reference 157, the MRPT is extended for the case where multiple data sets are available from several static and vibration tests. Since three modal data sets are obtained at each damage stage of the grid structure, this extended MRPT is employed here. The extended MRPT first computes the residual forces similar to the original MRPT. Next, singular value decomposition of the residual force is performed Here, only the singular values above the user-specified threshold value are kept for the stiffness updating. The performance of the MRPT depends greatly on the number of the singular values remained for the updating.

In Figure 6.11, the MPRT is applied to the test data obtained from the grid structure. In this figure, the abscissa shows the node numbers defined in Figure 6.3, and the ordinate displays the diagonal components of the stiffness changes at each damage stage. $\mathbf{K}_h$ and $\mathbf{K}_d$ denote the stiffness matrix before and after damage occurrence, respectively. Note that the stiffness change is normalized such that the maximum component becomes one. The damaged nodes are distinguished by darker color in the figure. In cases 1 and 2, the MPRT locates member 3 ( with end nodes 3 and 4) as potential damage region and the stiffness changes at nodes 2 and 3 (or the residual forces) seem small. In cases 3 and 4, the stiffness changes near the actual damage regions (nodes 2, 3 12 and 13) become larger than the previous two cases, but the stiffness changes are also smeared to the adjacent components. This phenomenon particularly attributes to the error induced by the model condensation. For cases 5

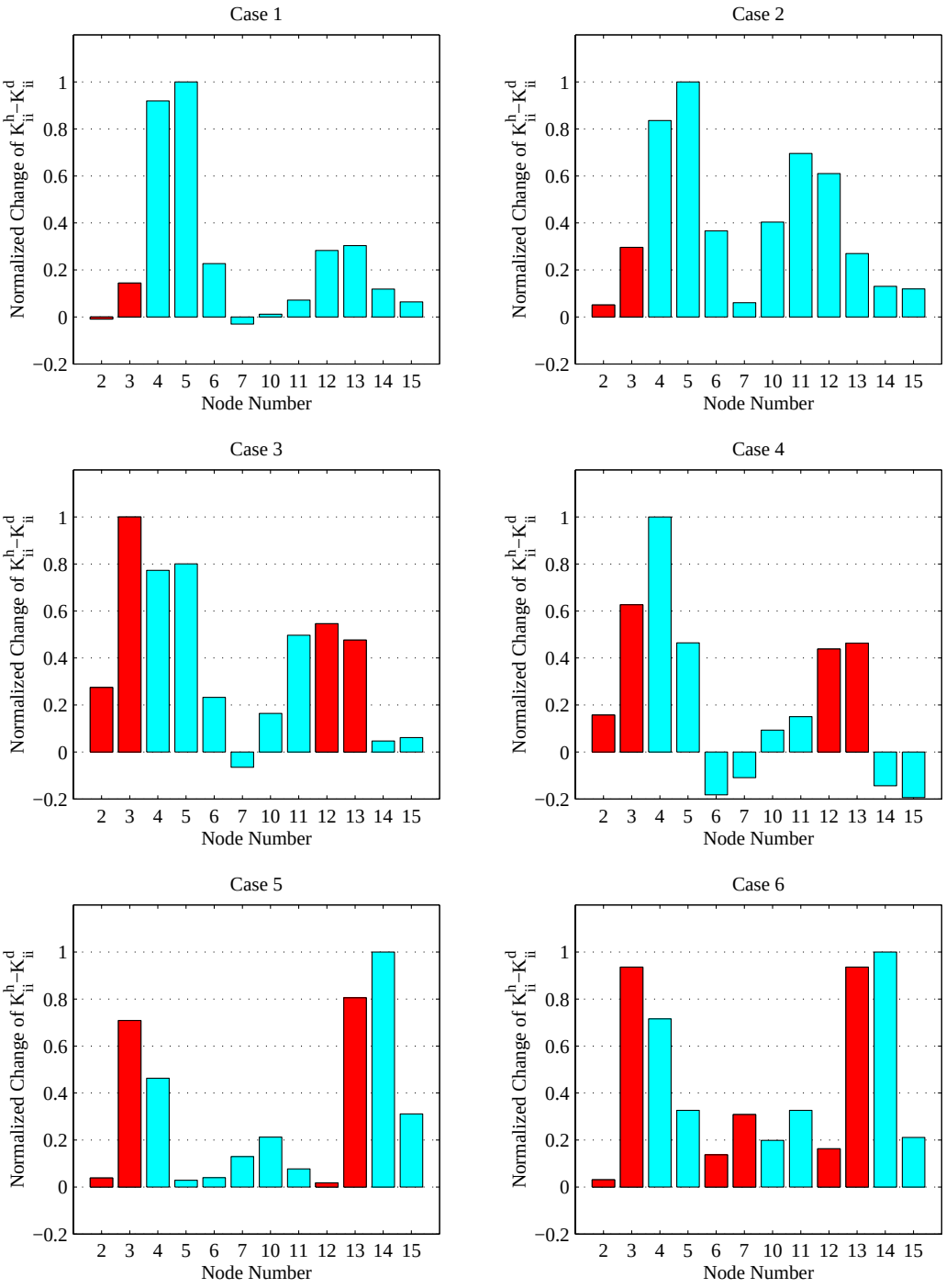


Figure 6.11: Damage diagnosis of a grid-type bridge model using the MRPT method

and 6, the stiffness changes at the actual damage locations becomes more obvious. However, damage location 3 (between nodes 6 and 7) is not successfully identified in case 6.

The SB-EBE method searches for the locations of potential errors between the finite element model and the measured modal data, and then update the analytical model at the element level by adjusting the elements' material properties. This method minimizes the squared norms of the modal dynamic residuals via a two-step iteration: At each iteration, the estimated modal vectors are first expanded, and the parameters of the elements are corrected using the expanded modal vectors and natural frequencies. This approach has demonstrated the potential applicability to the damage detection of truss structures [46]. The SB-EBE method is employed here since the mode shape expansion scheme is built within the updating process and damage can be identified at each structural element level. However, since this method can not employ mutiple data sets for updating (note that, in the experiment presented here, three sets of modal parameters are obtained at each damage stage by exciting the structure at nodes 3, 4 and 5, repeatedly), a single modal parameter set is separately used for the SB-EBE method and the diagnosis is repeated for all three data sets.

Figure 6.12 shows the diagnosis results using the SB-EBE method. Note that, the best diagnosis result among the diagnoses using three different modal data sets is presented for each damage stage. In Figure 6.12, the abscissa represents the substructure number and the ordinate denotes the percent change of the corresponding substructure stiffness. For cases 1 and 2, the actual damaged member has the largest stiffness decrease. The SB-EBE method also correctly indicates the actual damage locations for cases 3 and 4. However, damage locations 2 and damage location 3 are missed in cases 5 and 6, respectively.

The damage index method proposed by Stubbs, Kim and Topole is based on the assumption that the strain energy stored in the structure will decrease in damaged regions [92,143,145]. Basically, the damage index for the $i$th member ($\beta_i$) is the ratio of the bending stiffness between the undamaged element ($EI_i^h$) and the damaged

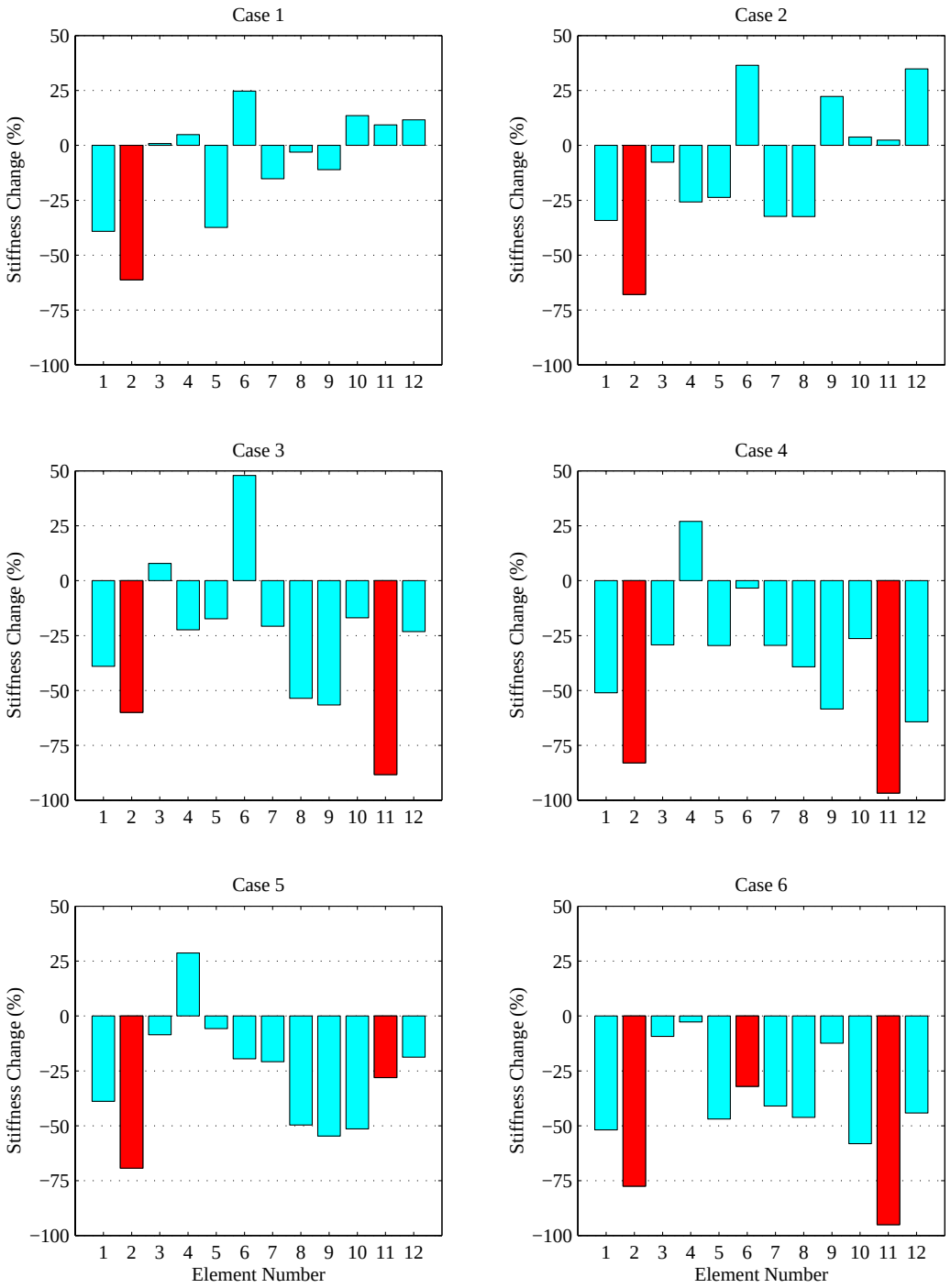


Figure 6.12: Damage diagnosis of a grid-type bridge model using the SB-EBE method

element ($EI_i^d$):

$$\beta_i = \frac{EI_i^h + 1}{EI_i^d + 1} \tag{6.48}$$

where a unity value is added to the numerator and denominator to avoid potential numerical problems. This method requires the discretization of the structure into a sufficient number of small elements and the method is applicable to beam-type structures only. Since the bending stiffness $EI_i^d$ term is unknown, the damage index $\beta_i$ is actually estimated by the curvature of the structure at the $i$th node. However, since the direct measure of the curvature is infeasible, the curvature is approximated as follows [143]: (1) Estimate the unmeasured node amplitudes of the modal vectors by interpolating the measured nodes using cubic-spline functions [125], and (2) take a second derivative of the interpolation function at each node. Finally, treating $\beta_i$ as a realization of a random variable $\beta$, a normalized damage index is computed as follows:

$$Z_i = \frac{\beta_i - \bar{\beta}}{\sigma_\beta} \tag{6.49}$$

$\bar{\beta}$ and $\sigma_\beta$ denote the mean and standard deviation of the damage indices, respectively. The $i$th substructure is defined as damaged when $|Z_i| > 2$, which corresponds to a hypothesis testing with 95% confidence level [57].

Table 6.6: Actual and estimated damage locations for the damage index method

| Case | Members with $\|\beta_i\| > 2$ | Actual damage locations |
|---|---|---|
| 1 | 20-26, 34-39 | 16 |
| 2 | 17-26 | 16 |
| 3 | 17-24, 101-107 | 16, 106 |
| 4 | 22-27, 100-109 | 16, 106 |
| 5 | 20-29 | 16, 106 |
| 6 | 20-29 | 16, 56, 106 |

Figure 6.13 and Table 6.6 show the diagnosis results using the damage index method. Each girder is discretized into seventy 7cm long members and damage locations 1, 2 and 3 correspond to members 16, 56 and 106 in this model, respectively.

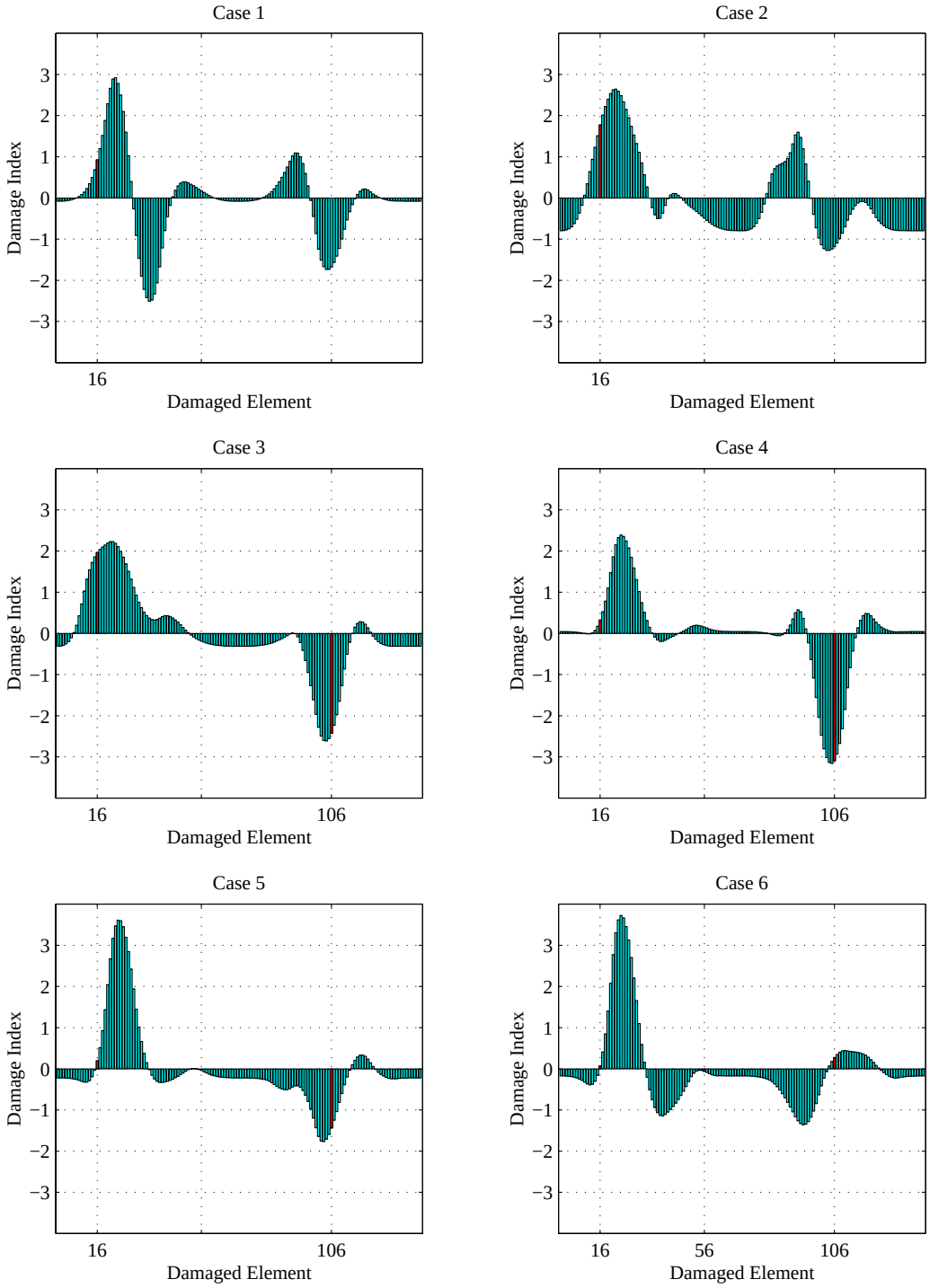


Figure 6.13: Damage diagnosis of a grid-type bridge model using the Damage Index method

For each damage case of Figure 6.13, vertical grid lines are added to display all three damage locations, and the abscissa is labeled only for the actual damaged members at each damage stage. Note that the diagnosis results in Figure 6.13 and Table 6.6 are obtained by using only the first modal vector since the inclusion of higher modes worsens the performance of damage index method. This phenomenon is also reported when the damage index method is applied to the I-40 bridge in Albuquerque, New Mexico [50]. It seems that the interpolation could not approximate the higher modes well and this partially causes the worse diagnosis when the higher modes are included. For cases 1 and 2, the damage index method estimates that the damage is located in members 20-26 or members 17-26 which are near the actual damaged member 16. For cases 3 and 4, the method successfully indicates the actual damage locations. However the damage index method fails to detect the damaged members 106 and 56 for cases 5 and 6.

## 6.3 Summary and Discussions

This chapter first reviews the procedure of typical experimental modal analyses emphasizing the Eigensystem Realization Algorithm. Next, an extraction procedure of Ritz vectors, which is based on the state-space model estimated from the ERA, is presented. Furthermore, we describe a new procedure which extracts Ritz vectors based on the measured flexibility matrix. The main advantage of the flexibility-based extraction procedure is that while the state-space method extracts Ritz vectors only from the actual loading that is applied to the structure, the flexibility-based method can generate Ritz vectors from arbitrary load patterns. The extraction procedures successfully extract the first six Ritz vectors from the grid-type test structure.

For the grid-type bridge model, six different damage cases are investigated using Ritz and modal vectors. Diagnoses of the six damage cases reveal that the employment of Ritz vectors provides better indication of the actual damage locations. The sensitivity comparison of Ritz/modal vectors exhibits that at every level of damage, the changes of Ritz vectors are larger than those of the modal vectors and confirms the diagnosis results. However, the superiority of Ritz vectors is not as well demonstrated

in this example as expected. It attributes to the facts that (1) since the geometry of the grid structure is relatively simple and less redundant system, the load redistribution caused by different load patterns and stiffness deterioration was not significant, and (2) because of the limited frequency range for the experimental modal analysis, the potential contribution of higher modes to Ritz vectors is truncated. We believe that the advantage of Ritz vectors will be more significant for complicated structures because of greater redundancy. The proposed branch-and-bound search scheme is shown to significantly reduce the computational cost of the proposed Bayesian approach. Particularly when damages are localized in a few locations, the computation is quite manageable.

The application of the MRPT, SB-EBE, and damage index method to the test data of the grid structure shows that none of these methods provide better diagnosis results than the Bayesian approach. The MRPT requires a decision on the rank of the stiffness perturbation that is added to the original stiffness matrix and the performance of the MRPT greatly depends on the rank selection. In this study, the rank is decided based on the knowledge of the actual damage locations. However, for real applications, the rank will be selected without the knowledge of damage locations. The SB-EBE method provides better diagnosis result than the MRPT and damage index method, and identifies damage amount as well as damage locations. However, the SB-EBE method can only employ a single modal parameter set at a time and the diagnosis result varies drastically depending on which modal parameter sets are used. Therefore, the SB-EBE method may not be suitable for the continuous monitoring that we are aiming at in this study. The damage index method provides better diagnosis results than the MRPT method. The advantage of this method is that only a few modes are required to obtain reliable results. In our example, the employment of only the first mode resulted in the best diagnosis result. However, this method is applicable only to beam-type structures and requires the model to be discretized into a large number of small elements.

# Chapter 7

# Environmental Effects on Damage Detection

Many vibration-based damage detection techniques attempt to identify the extent and location of damage in large structures using the modal parameters estimated by experimental modal analysis. These vibration-based damage detection is based on the premise that damage in the structure will cause changes in the measured vibration data. Before the proposed Bayesian approach can be reliably applied to global damage diagnosis (level 2 assessment as described in Chapter 1.1), a decision on the presence of damage should be made first (level 1 assessment).

For a civil structure, changes in load, boundary conditions, temperature and humidity can have a significant effect on the underlying dynamic characteristics of the civil structure. Existing methods, however, neglect the important effects of environmental changes on the underlying structure. In fact, the changes in the modal parameters due to environmental factors can be much larger than those caused by structural damage. During damp weather, for example, concrete bridges in the United Kingdom are reported to absorb considerable amount of moisture, which thus increases their masses and alters their natural frequencies [151]. Therefore, these environmental effects need to be filtered out to make a reliable decision on the presence of damage.

This chapter mainly addresses the thermal effects on the non-stationary responses of bridges due to temperature changes. Very few researchers have addressed such a problem. Churchward and Sokal [38] attempted to predict the temperature distribution within bridge sections and to determine longitudinal expansion and vertical

deflection based on a three-year monitoring of a post-stressed concrete section of a bridge. The measured environmental parameters include ambient air temperature, solar radiation, hours of sunshine and the temperature on the top surface of the section. It is found that the temperature profile can be reasonably represented using two design variables, namely maximum differential temperature and base temperature. Wood [151] reported that the changes of bridge responses were closely related to the structural temperature based on the vibration tests of five bridges in the United Kingdom. Analyses based on the data compiled suggested that the variability of the asphalt elastic modulus due to temperature effects was a major contributor to the changes in the structural stiffness.

Askegaard and Mossing [5] tested a three-span RC footbridge to investigate if modal parameters can provide a long term indication of structural deterioration or crack formation. Seasonal changes of modal parameters were also monitored for a three-year period, and about 10% change in frequency was repeatedly observed for each year. The authors concluded that the change was partially attributed to the variation of ambient temperature. Moorty [104] attempted to relate the responses of a bridge to thermal environmental conditions. An analytical model was developed to obtain the temperature-induced movements and the associated stresses in the bridge. A field test was conducted on the Sutton Creek Bridge in Montana, USA. The movements obtained from both the analytical model and the measured values showed significant expansion of the bridge deck as temperature increased. A comprehensive research program on the Confederation Bridge in Eastern Canada has started in the spring of 1997 and will continue over many years to evaluate the effect of temperature on the short term and long term behavior of the bridge [41]. Data on temperature and strain in the various components of the bridge, movement at expansion joints and deformation of the piers have been collected hourly. The extensive data collected will be used to develop computer models for predicting temperature effects in concrete bridges.

This study presents an adaptive filter that accommodates the changes in temperature to the damage detection system of a large-scale bridge. This system determines modal frequencies using conventional modal analyses, but is able to adapt its

prediction of the underlying natural frequencies of the structure based upon a time-temperature profile. This allows the system to discriminate the changes of modal parameters due to temperature changes from those caused by other environmental factors or structural damage. For example, when the measured frequencies move outside the predicted confidence intervals, the system can provide a reliable indication that structural changes are likely caused by factors other than thermal effect.

Actual data collected from the Alamosa Canyon Bridge in New Mexico are used to train and test the system. Results indicate that a linear four-input (two time and two spatial dimensions) filter of temperature can reproduce the natural variability of the frequencies with respect to time of day. Using this simple model, we attempt to establish a confidence interval of the frequencies for a new temperature profile in order to discriminate the natural variation due to temperature from potential damage.

This section is organized as follows. Section 7.1 describes the experimental setup at the Alamosa Canyon Bridge. Sections 7.2 to 7.4 present the training of the adaptive filter and a selection procedure of temperature input variables. Section 7.5 presents the prediction operation with the construction of confidence intervals, and the examination of prediction performance.

## 7.1 Description of Experimental Setup

The Alamosa Canyon Bridge is located near the town of Truth or Consequences in southern New Mexico and is approximately aligned in the north and south direction. This bridge has seven independent spans and each span consists of a concrete deck supported by six W30x116 steel girders. The top flanges of the girders are embedded in the concrete slab. The roadway in a span is approximately 7.3 m (24 ft) wide and 15.2 m (50 ft) long. Along the length of each span, four sets of crossing braces are equally spaced. Figure 7.1 depicts a side view of the Alamosa Canyon Bridge. More detailed description of the bridge can be found in Farrar *et al.* [49].

A new bridge has been constructed adjacent to this *old* Alamosa Canyon Bridge and since that time the tested bridge has not been used for regular traffic. During the past three years, however, the bridge has been tested several times by the Engineering

Analysis Group of the Los Alamos National Laboratory (LANL). An attempt to characterize the natural variability of modal parameters was conducted in 1996 [49]. The inherent uncertainty in the measured modal parameters was also studied using experimental test data from the bridge [42].

This current study uses the results of the vibration tests conducted on July 27-August 2, 1996 and July 21-25, 1997, referred to here as the *first* and *second* data sets, respectively. The test data were provided to the authors by the Engineering Analysis Group of the LANL. The first data set was used to train the adaptive filter while the second data set was used to test the predictor. For both tests, only one span was implemented with sensors and tested. A total of 31 accelerometers were placed on the concrete deck and on the girders below the bridge. Five accelerometers were spaced along the length of each girder. Since there were six girders, a total of 30 accelerometers were placed on the girders. The last accelerometer was placed near the driving point. The time histories of accelerations and an excitation force were recorded, and the frequency response functions (FRFs) were computed from the time histories. The FRFs were calculated for the range of 0 to 50 Hz with the resolution of 0.0625 Hz. Thirty averages were used for all FRFs. An impact hammer which weighted approximately 53.4 N (12 lbs) was used to excite the bridge. The data acquisition for each test took 30 $\sim$ 45 minutes. The modal parameters were extracted using the Eigensystem Realization Algorithm (ERA) [76]. Approximately nine meaningful modes were identified from the ERA within the range of 0 to 30 Hz.

At the same time, temperature measurements were made on nine different locations across the center of the span. Figure 7.2 shows a cross-section view of the bridge and the distribution of the thermometers, as follows: The bottom west outdoor sensor ($T_8$) was attached to the outside of the west-end exterior girder at the mid height of the web. The bottom west indoor sensor ($T_6$) was located on the inside bottom flange of the west-end exterior girder. The bottom center sensor ($T_9$) was taped beneath the concrete deck at the center of the span. The top west outdoor sensor ($T_2$) was located next to the concrete curb at the west-end of the deck. The top west indoor sensor ($T_4$) was placed on the top of the west-end guard rail. The four remaining sensors ($T_1$, $T_3$, $T_5$ and $T_7$) were placed on the east end of the span symmetrically to the

Figure 7.1: A side view of the Alamosa Canyon Bridge (Courtesy of the Los Alamos National Laboratory)

west-end sensors. All sensors were protected from the direct contact with sunshine either by the bridge itself or by the shades made from duct tape and cups. However, the temperature measurements were not the most precise measurements that could have been made. Attempts were made to calibrate the thermometers prior to the tests, but the the accuracy of the readings was not that which could be obtained with typical thermocouples.

The first vibration test was performed every two hours over a 24-hour time period to investigate the change of modal parameters with respect to time of day. The test started on July 31, 1996 at 09:15 and ended on August 1, 1996 at 9:22. The air was dry throughout the test. Farrar *et al.* [49] showed that the measured first mode frequency varied approximately 5% during the 24-hour test period, and the change in the measured fundamental frequency was found to correlate with the temperature difference across the deck. Similar variations and correlation with deck temperature difference were observed for the other modes of the bridge. Table 7.1 summarizes the measured frequencies and temperatures from the first vibration test. The temperature of a given time in Table 7.1 is an average of the thermometer readings before and after each vibration test. In addition to the temperature effect, traffic, winds, deterioration of the bridge and other environmental conditions could produce changes of the modal parameters. However, since the bridge was not used and the weather was calm during the test period, it is assumed that any changes of the modal parameters are mainly the result of the temperature changes.

The second test was conducted about one year after the first test. The second test started on July 22, 1997 at 04:00 and ended at midnight. Vibration tests were performed eleven times every two hours. A note is in order about the weather conditions prior to the second vibration test; it had been raining hard from approximately 10:00 PM the previous night of the testing until 3:00 AM. When the data acquisition was started at 4:00 AM, rain was sufficient to produce ponds of water near the curbs and drainage paths were blocked by debris. The concrete deck was sufficiently cracked such that a fair amount of moisture might have been absorbed by the bridge. When the second vibration test was conducted, no significant stiffness deterioration were observed since the first testing. In the second testing, no temperature sensor was placed at the bottom center. The other thermometers were placed almost in the same locations as those of the first testing. Table 7.2 summarizes the results from the second vibration test.

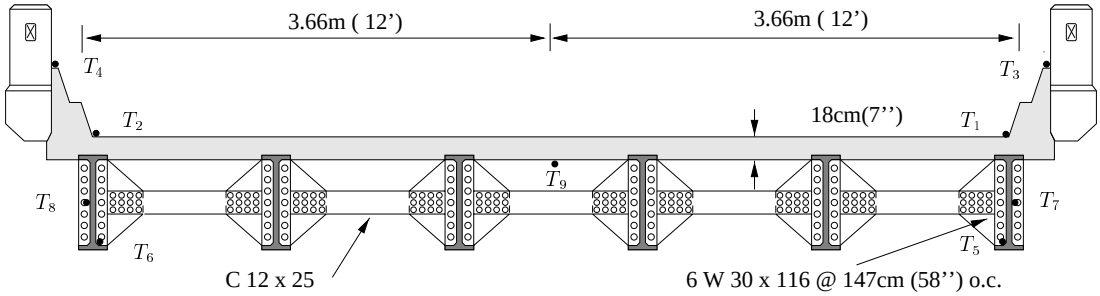


Figure 7.2: A cross section view and thermometer locations of the Alamosa Canyon Bridge

## 7.2 Formulation of a Linear Filter

First, prediction of the fundamental frequency was selected as a target for this study and the same procedure is repeated for the second mode frequency. It was presumed that the temperature changes of the bridge were mainly responsible for the variation of the frequencies. This assumption seems reasonable since the bridge was no longer in service and there was no significant change of weather conditions on the first test day. Observations of the bridge data coupled with some engineering judgment led to three additional assumptions that appear simplistic but are important factors in

Table 7.1: Summary of the first data set (conducted in 1996 Summer)

| Time | Freq. (Hz) | | Temperature ($F^o$) | | | | | | | | |
|---|---|---|---|---|---|---|---|---|---|---|---|
| | 1st | 2nd | $T_1$ | $T_2$ | $T_3$ | $T_4$ | $T_5$ | $T_6$ | $T_7$ | $T_8$ | $T_9$ |
| 09:15 | 7.556 | 8.311 | 76.00 | 90.70 | 93.30 | 95.90 | 83.55 | 77.20 | 103.7 | 75.55 | 77.45 |
| 11:30 | 7.621 | 8.384 | 85.80 | 106.15 | 101.10 | 99.70 | 93.90 | 84.50 | 93.90 | 83.30 | 83.10 |
| 13:12 | 7.475 | 8.084 | 108.15 | 115.60 | 100.65 | 103.00 | 93.55 | 91.20 | 93.20 | 91.85 | 88.60 |
| 15:13 | 7.343 | 7.874 | 109.60 | 110.70 | 102.00 | 102.60 | 92.80 | 93.70 | 93.60 | 95.50 | 94.60 |
| 17:52 | 7.394 | 7.972 | 104.35 | 99.25 | 97.40 | 99.25 | 91.20 | 95.05 | 92.60 | 96.05 | 98.35 |
| 20:09 | 7.376 | 8.042 | 88.00 | 87.00 | 74.40 | 76.05 | 77.80 | 78.90 | 79.50 | 79.50 | 91.35 |
| 21:20 | 7.334 | 8.037 | 85.90 | 86.40 | 76.10 | 77.55 | 79.95 | 80.35 | 80.00 | 79.45 | 89.95 |
| 23:29 | 7.356 | 8.087 | 79.60 | 81.50 | 72.70 | 74.20 | 75.00 | 75.60 | 75.30 | 74.30 | 80.50 |
| 01:21 | 7.328 | 8.071 | 79.55 | 79.35 | 70.05 | 72.05 | 75.20 | 75.10 | 74.85 | 74.75 | 80.70 |
| 03:19 | 7.353 | 8.119 | 74.55 | 75.15 | 65.85 | 66.65 | 70.25 | 71.70 | 72.15 | 70.85 | 77.20 |
| 05:19 | 7.381 | 8.157 | 72.85 | 72.85 | 64.15 | 65.50 | 68.80 | 70.00 | 70.15 | 68.90 | 74.10 |
| 07:03 | 7.389 | 8.178 | 70.85 | 73.85 | 66.90 | 68.10 | 66.70 | 67.85 | 73.80 | 67.35 | 72.10 |
| 09:22 | 7.577 | 8.342 | 74.45 | 92.75 | 94.00 | 93.20 | 83.90 | 77.55 | 102.00 | 75.50 | 76.00 |

Table 7.2: Summary of the second data set (conducted in 1997 Summer)

| Time | Freq. (Hz) | | Temperature ($F^o$) | | | | | | | | |
|---|---|---|---|---|---|---|---|---|---|---|---|
| | 1st | 2nd | $T_1$ | $T_2$ | $T_3$ | $T_4$ | $T_5$ | $T_6$ | $T_7$ | $T_8$ | $T_9$ |
| 04:00 | 7.303 | 8.100 | 79.70 | 76.95 | 80.35 | 76.10 | 70.60 | 70.45 | 69.30 | 69.15 | NA. |
| 06:02 | 7.329 | 8.136 | 79.05 | 76.55 | 81.95 | 80.15 | 68.85 | 69.35 | 68.20 | 67.55 | NA. |
| 08:00 | 7.528 | 8.281 | 79.50 | 87.80 | 88.95 | 94.20 | 74.70 | 71.50 | 68.20 | 71.30 | NA. |
| 10:02 | 7.638 | 8.524 | 79.80 | 111.75 | 96.60 | 109.30 | 67.60 | 77.35 | 68.20 | 77.00 | NA. |
| 12:00 | 7.579 | 8.249 | 100.05 | 121.00 | 113.25 | 109.85 | 67.60 | 82.75 | 68.20 | 83.90 | NA. |
| 14:01 | 7.503 | 8.143 | 113.80 | 120.00 | 112.80 | 100.85 | 67.60 | 88.70 | 68.20 | 91.05 | NA. |
| 16:00 | 7.449 | 8.008 | 104.35 | 102.65 | 102.05 | 97.05 | 88.45 | 91.65 | 90.40 | 91.10 | NA. |
| 18:00 | 7.361 | 8.030 | 92.50 | 90.50 | 82.60 | 81.70 | 82.00 | 82.20 | 82.20 | 84.60 | NA. |
| 20:05 | 7.321 | 8.070 | 80.20 | 81.40 | 72.75 | 73.50 | 74.35 | 73.50 | 73.85 | 73.60 | NA. |
| 21:54 | 7.319 | 8.094 | 78.10 | 77.75 | 71.05 | 71.05 | 72.85 | 73.60 | 72.85 | 71.60 | NA. |
| 24:00 | 7.347 | 8.132 | 75.30 | 74.95 | 68.30 | 66.90 | 70.65 | 71.30 | 70.90 | 69.15 | NA. |

the design of the filter architecture: (1) changes in the modal parameters are *linearly* proportional to changes in temperature; (2) the mass of the bridge forced the change in modal parameters to lag behind the temperature, that is, the bridge takes some time to *warm up* and *cool off*; and (3) the geographical (north-south) orientation of the structure with respect to the sun suggests that the temperature of the west end of the bridge will have a time-lag behind the temperature of the east end.

Given these assumptions, a linear predictor is chosen as a system architecture. A linear filter simply creates a linear one-to-one mapping on input and output pairs. It affords explicit calculation of the filter coefficients using a simple matrix calculation and allows future modification of these coefficients using adaptive least-mean squares error minimization. The filter operates in two modes: *training* and *prediction*. Training is described here. Section 7.5 describes a validation regarding the applicability of the filter for prediction by testing its performance on the second data set.

## 7.3 Training the Linear Filter Model

The architecture of the linear filter takes a subset of the temporal and spatial temperature profiles as inputs and delivers a single output that represents the estimated, or predicted, fundamental frequency. (Later, the same procedure is repeated for the second mode frequency.) In this sense, the filter is also a *multiple linear regression model*, but is more commonly termed a predictor or estimator. Determining the appropriate subset of the available temperature profiles is termed the *variable selection problem* and is discussed in Section 7.4. The method of *Least Mean Squares* (LMS) error minimization is used to estimate the coefficients of the predictor [148].

The filter models the relationship between the selected bridge temperature inputs, $\mathbf{x} = [x_1 \; x_2 \; \ldots \; x_r]^T$, a column vector of $r$ inputs, and its measured fundamental frequency, $y$, at that temperature profile as a linear function:

$$y = w_0 + \mathbf{x}^T\mathbf{w} + \epsilon \tag{7.1}$$

where $w_0$ is bias or offset, $\mathbf{w}$ is a column vector of coefficients that weighs each temperature input, and $\epsilon$ is the *filter error*. Equation (7.1) can be rewritten to

account for the offset term $w_0$ by redefining the input and weight vectors to have $p$ $(= r + 1)$ dimensions:

$$y = \mathbf{x}^T \mathbf{w} + \epsilon \tag{7.2}$$

where $\mathbf{x} = [1 \; x_1 \; x_2 \; \ldots \; x_r]^T$ and $\mathbf{w} = [w_0 \; w_1 \; \ldots \; w_r]^T$. Figure 7.3 depicts the filter to implement this model. In order to consider both the time and spatial variation of temperature, the temperature readings at the current time $T_i$ and the previous time $T_i'$ are used as input variables. That is, $\mathbf{x} = [\; 1 \;\; T_1 \;\; \ldots \;\; T_9 \;\; T_1' \;\; \ldots \;\; T_9' \;]^T$ in Figure 7.3. The filter imposes a strictly linear mapping.

Suppose that $n$ observations are available and let $\mathbf{x}(i)$ and $y(i)$ denote the $i$th input-output pairs. Equation (7.2) can be written in matrix notation:

$$\mathbf{y} = \mathbf{X}\mathbf{w} + \boldsymbol{\epsilon} \tag{7.3}$$

where, with $n$ observations

$$\mathbf{y} = \begin{bmatrix} y(1) \\ y(2) \\ \vdots \\ y(n) \end{bmatrix}, \; \mathbf{X} = \begin{bmatrix} 1 & x_1(1) & x_2(1) & \ldots & x_r(1) \\ 1 & x_1(2) & x_2(2) & \ldots & x_r(2) \\ \vdots & \vdots & \vdots & & \vdots \\ 1 & x_1(n) & x_2(n) & \ldots & x_r(n) \end{bmatrix}, \; \boldsymbol{\epsilon} = \begin{bmatrix} \epsilon(1) \\ \epsilon(2) \\ \vdots \\ \epsilon(n) \end{bmatrix}$$

The LMS error minimization is employed to estimate the filter coefficients. We wish to find the vector of the filter coefficients $\mathbf{w}$ that minimizes the expected value of the square of the filter error:

$$\min_{\mathbf{w}} \; E\left[\, \epsilon(i)^2 \,\right] \tag{7.4}$$

where $E\left[\, \epsilon(i)^2 \,\right]$ is the mean of the filter errors created by $n$ observations. $E\left[\, \epsilon(i)^2 \,\right]$ can be rewritten as follows. The index $i$ is omitted for notational simplicity after the

first line.

$$\begin{aligned} E\,[\,\epsilon(i)^2\,] &= E\,[\,(y(i)-\mathbf{w}^T\mathbf{x}(i))^2\,] \\ &= E\,[\,(y-\mathbf{w}^T\mathbf{x})^2\,] \\ &= E\,[\,y^2+\mathbf{w}^T\mathbf{x}\mathbf{x}^T\mathbf{w}-2y\mathbf{x}^T\mathbf{w}\,] \\ &= E\,[\,y^2\,]+\mathbf{w}^T E\,[\,\mathbf{x}\mathbf{x}^T\,]\mathbf{w}-2E\,[\,y\mathbf{x}^T\,]\mathbf{w} \\ &= E\,[\,y^2\,]+\mathbf{w}^T\mathbf{R}\mathbf{w}-2\mathbf{p}^T\mathbf{w} \end{aligned} \tag{7.5}$$

where $\mathbf{R}$ ($=E[\,\mathbf{x}\mathbf{x}^T]$) is the *auto-correlation* of the random input vector $\mathbf{x}$, and $\mathbf{p}$ ($=E[\,y\,\mathbf{x}^T]$) is the *cross-correlation* between the desired output and the input vector. We note that $E\,[\,\epsilon^2\,]$ is quadratic with $\mathbf{w}$ and thus can be solved for a single extrema (minima) with respect to $\mathbf{w}$. The *estimated* coefficients, $\hat{\mathbf{w}}$, are found by differentiating Equation 7.6 with respect to $\mathbf{w}$ and setting the result equal to zero:

$$\nabla(E\,[\,\epsilon^2\,]) = \frac{\partial E\,[\,\epsilon^2\,]}{\partial \mathbf{w}} = 2(\mathbf{R}\hat{\mathbf{w}}-\mathbf{p}) = 0 \tag{7.6}$$

Solving for $\hat{\mathbf{w}}$,

$$\hat{\mathbf{w}} = \mathbf{R}^{-1}\mathbf{p} \tag{7.7}$$

Equation (7.7) is called the *Wiener-Hopf equation* and is used to determine the estimated coefficients, $\hat{\mathbf{w}}$, for a given set of input-output pairs.

One should note that the actual filter output error that results after applying the Wiener-Hopf equation is dependent upon the number of input-output mappings ($n$) that are used to determine $\hat{\mathbf{w}}$ and the dimension of $\hat{\mathbf{w}}$, $p$. If the filter is under-specified, that is, the number of input-output pairs is less than the dimension of $\hat{\mathbf{w}}$, then the Wiener-Hopf equation will produce an unlimited number of different $\hat{\mathbf{w}}$'s that result in zero error ($\boldsymbol{\epsilon} = \mathbf{0}$). This means that there exists an infinite number of weights that will produce zero error for the given observation sets.

Since the training data set was fixed for this study, we decided to reduce the dimension $p$. In the derivation of Equation (7.1), all input variables are assumed to

be influential in predicting the output response. However, in most practical applications, the analyst must check the significance of each input and determine some optimal subset of inputs from a pool of *candidate* inputs. This variable selection is equivalent to pruning irrelevant or redundant inputs from the filter of Figure 7.3, and the procedure is addressed in the following section.

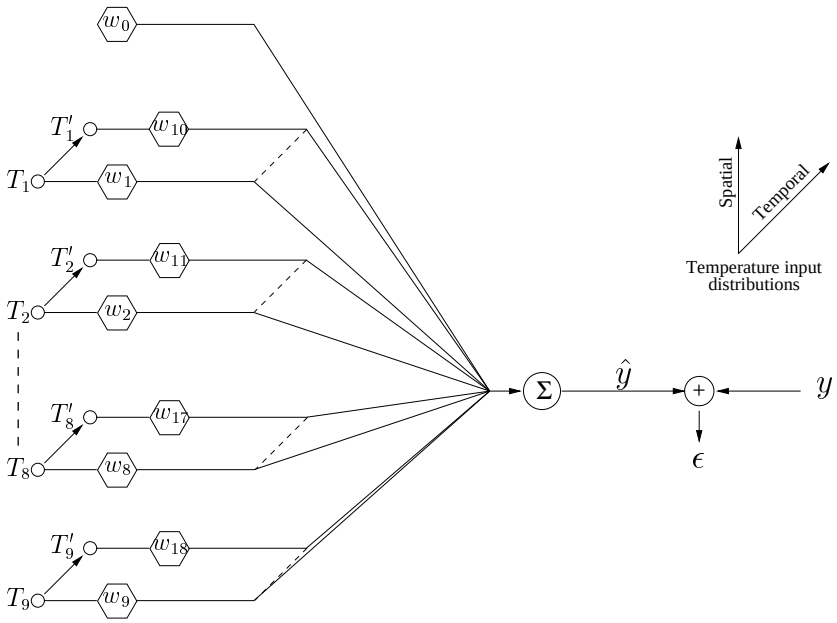


Figure 7.3: A linear adaptive filter

## 7.4 Input Variable Selection

We presume that the changes of the fundamental frequency are related to the spatial and temporal variations of temperatures across the bridge. In order to consider both the time and spatial variations of temperature, we decide to define the temperature readings at the current time $T_i$, and at the previous time $T_i'$ as an initial pool of candidate input variables. Let $k$ denote the size of this input pool. While the number of candidate input variables are eighteen (nine temperature readings at the current time and the other nine from the one step previous time), the number of observations from the first vibration test is thirteen ($n = 13$). Therefore, the selection of input variables should be conducted to reduce the size of the filter before any estimation of

the filter coefficients. In general, a model with smaller number of input variables are more desirable because the variance of the prediction $\hat{y}$ increases as the number of inputs increases. Also, addition of extra inputs increases the costs of data collection and model maintenance.

Table 7.3: Correlation of the measured fundamental frequency and the thermometer readings

| | $y$ | $T_1$ | $T_2$ | $T_3$ | $T_4$ | $T_5$ | $T_6$ | $T_7$ | $T_8$ | $T_9$ |
|---|---|---|---|---|---|---|---|---|---|---|
| $y$ | 1.000 | | | | | | | | | |
| $T_1$ | −0.097 | 1.000 | | | | | | | | |
| $T_2$ | 0.435 | 0.835 | 1.000 | | | | | Sym. | | |
| $T_3$ | 0.608 | 0.684 | 0.941 | 1.000 | | | | | | |
| $T_4$ | 0.580 | 0.707 | 0.943 | 0.997 | 1.000 | | | | | |
| $T_5$ | 0.485 | 0.787 | 0.969 | 0.966 | 0.966 | 1.000 | | | | |
| $T_6$ | 0.130 | 0.949 | 0.901 | 0.839 | 0.853 | 0.916 | 1.000 | | | |
| $T_7$ | 0.741 | 0.396 | 0.750 | 0.910 | 0.909 | 0.807 | 0.605 | 1.000 | | |
| $T_8$ | 0.065 | 0.968 | 0.883 | 0.804 | 0.820 | 0.886 | 0.996 | 0.556 | 1.000 | |
| $T_9$ | −0.232 | 0.886 | 0.641 | 0.518 | 0.540 | 0.668 | 0.870 | 0.283 | 0.889 | 1.000 |

First, the correlation of the nine sensor readings and the measured fundamental frequency is investigated. Table 7.3 presents the resulting correlation matrix. The correlation matrix shows that temperatures at the top east indoor ($T_3$) and at the top west indoor ($T_4$) are very closely related. (Figure 7.2 shows the locations of the thermometers.) The temperature at the bottom west indoor ($T_6$) is also strongly correlated to the temperature at the bottom west outdoor ($T_8$). $T_4$ is deleted from the filter model because $T_3$ has a larger correlation with the observation output $y$ than $T_4$. For the same reason, $T_6$ is kept in the model and $T_8$ is excluded. Since the second data set did not measure the temperature at the bottom center, the variable selection did not include $T_9$. Now, the number of candidate input variables becomes twelve ($k$=12).

Next, an exhaustive search of all possible subsets of the remaining input variables is conducted using the SAS (Statistical Analysis System) program and the exhaustive search took on a SUN ULTRA-2 workstation less than a minute. If the intercept weight $w_o$ is always included, a total of $2^k$ models should be examined. In this example, there are $2^{12}$ (=4096) possible models. This study employs *adjusted* $R^2$

Table 7.4: The best five models for each given number of input variables

| # | r | $\bar{R}^2$ | $R^2_{pred}$ | Selected Input Variables | | | | | | | | | | | | |
|---|---|---|---|---|---|---|---|---|---|---|---|---|---|---|---|---|
| 1* | 9 | 0.99801 | 0.96958 | $T_1$ | $T_2$ | | $T_5$ | $T_6$ | | $T_1'$ | | $T_3'$ | $T_5'$ | $T_6'$ | $T_7'$ |
| 2 | | 0.99718 | 0.98144 | $T_1$ | $T_2$ | $T_3$ | | $T_6$ | | $T_1'$ | | $T_3'$ | $T_5'$ | $T_6'$ | $T_7'$ |
| 3 | | 0.99678 | 0.98716 | $T_1$ | $T_2$ | | | $T_6$ | | $T_1'$ | $T_2'$ | $T_3'$ | $T_5'$ | $T_6'$ | $T_7'$ |
| 4 | | 0.99665 | 0.86686 | $T_1$ | $T_2$ | | | $T_6$ | $T_7$ | $T_1'$ | | $T_3'$ | $T_5'$ | $T_6'$ | $T_7'$ |
| 5 | | 0.99424 | 0.72374 | $T_1$ | $T_2$ | | | $T_6$ | $T_7$ | $T_1'$ | $T_2'$ | $T_3'$ | $T_5'$ | | $T_7'$ |
| 6* | 8 | 0.99747 | 0.99374 | $T_1$ | $T_2$ | | | $T_6$ | | $T_1'$ | | $T_3'$ | $T_5'$ | $T_6'$ | $T_7'$ |
| 7 | | 0.99517 | 0.98352 | $T_1$ | $T_2$ | $T_3$ | | $T_6$ | | $T_1'$ | | $T_3'$ | $T_5'$ | | $T_7'$ |
| 8 | | 0.99324 | 0.97479 | | $T_2$ | $T_3$ | | | $T_7$ | $T_1'$ | $T_2'$ | $T_3'$ | $T_5'$ | $T_6'$ | |
| 9 | | 0.99320 | 0.97169 | $T_1$ | | $T_3$ | | | $T_7$ | $T_1'$ | $T_2'$ | $T_3'$ | $T_5'$ | $T_6'$ | |
| 10 | | 0.99318 | 0.93469 | $T_1$ | $T_2$ | | | $T_6$ | | $T_1'$ | $T_2'$ | $T_3'$ | $T_5'$ | | $T_7'$ |
| 11* | 7 | 0.99373 | 0.98514 | | | $T_3$ | | | $T_7$ | $T_1'$ | $T_2'$ | $T_3'$ | $T_5'$ | $T_6'$ | |
| 12 | | 0.99302 | 0.98485 | | $T_2$ | $T_3$ | | | | $T_1'$ | $T_2'$ | $T_3'$ | $T_5'$ | $T_6'$ | |
| 13 | | 0.99293 | 0.96718 | $T_1$ | | $T_3$ | | | $T_7$ | $T_1'$ | $T_2'$ | $T_3'$ | $T_5'$ | | |
| 14 | | 0.99277 | 0.96203 | $T_1$ | $T_2$ | $T_3$ | | | $T_7$ | | $T_2'$ | $T_3'$ | $T_5'$ | | |
| 15 | | 0.99275 | 0.97943 | | $T_3$ | | $T_5$ | $T_6$ | $T_7$ | | $T_2'$ | $T_3'$ | $T_5'$ | | |
| 16* | 6 | 0.99387 | 0.98804 | $T_1$ | | $T_3$ | | | $T_7$ | | $T_2'$ | $T_3'$ | $T_5'$ | | |
| 17 | | 0.99373 | 0.98639 | | | $T_3$ | | | $T_7$ | $T_1'$ | $T_2'$ | $T_3'$ | $T_5'$ | | |
| 18 | | 0.99369 | 0.98766 | | | $T_3$ | | $T_6$ | $T_7$ | | $T_2'$ | $T_3'$ | $T_5'$ | | |
| 19 | | 0.99360 | 0.98694 | | | $T_3$ | | | $T_7$ | | $T_2'$ | $T_3'$ | $T_5'$ | | $T_7'$ |
| 20 | | 0.99358 | 0.98733 | | | $T_3$ | | | | $T_1'$ | $T_2'$ | $T_3'$ | $T_5'$ | $T_6'$ | |
| 21* | 5 | 0.99428 | 0.99112 | | | $T_3$ | | | $T_7$ | | $T_2'$ | $T_3'$ | $T_5'$ | | |
| 22* | | 0.99414 | 0.99062 | $T_1$ | | $T_3$ | | | $T_7$ | | $T_2'$ | $T_3'$ | | | |
| 23* | | 0.99386 | 0.99054 | | $T_2$ | $T_3$ | | | $T_7$ | | $T_2'$ | $T_3'$ | | | |
| 24 | | 0.99361 | 0.98613 | | | $T_3$ | | $T_6$ | $T_7$ | | $T_2'$ | $T_3'$ | | | |
| 25 | | 0.99351 | 0.98878 | | | $T_3$ | | | $T_7$ | | $T_2'$ | $T_3'$ | | | $T_7'$ |
| 26* | 4 | 0.99410 | 0.99165 | | | $T_3$ | | | $T_7$ | | $T_2'$ | $T_3'$ | | | |
| 27 | | 0.98934 | 0.98275 | | | $T_3$ | | | | $T_1'$ | $T_2'$ | $T_3'$ | | | |
| 28 | | 0.98885 | 0.98131 | | | $T_3$ | | | | | $T_2'$ | $T_3'$ | | $T_6'$ | |
| 29 | | 0.98757 | 0.97702 | | $T_2$ | $T_3$ | | | | | $T_2'$ | $T_3'$ | | | |
| 30 | | 0.98735 | 0.97116 | | | $T_3$ | $T_5$ | | | | $T_2'$ | $T_3'$ | | | |
| 31* | 3 | 0.98809 | 0.97809 | | | $T_3$ | | | | | $T_2'$ | $T_3'$ | | | |
| 32 | | 0.94915 | 0.90774 | | | | | | | $T_1'$ | | $T_3'$ | $T_5'$ | | |
| 33 | | 0.94346 | 0.89520 | | | | $T_5$ | | | | $T_2'$ | $T_3'$ | | | |
| 34 | | 0.93581 | 0.89347 | | | $T_3$ | | | | | $T_2'$ | | | | $T_7'$ |
| 35 | | 0.91828 | 0.87422 | | | $T_3$ | | | | | $T_2'$ | | $T_5'$ | | |

* These models are retained for further comparison and investigation.

*statistic* for comparing different models. To explain adjusted $R^2$ statistic, let $R_p^2$ denote the coefficient of multiple determination for a model with reduced size $p$ ($\leq k+1$). Computationally

$$R_p^2 = \frac{SS_R(p)}{S_{yy}} = 1 - \frac{SS_E(p)}{S_{yy}} \tag{7.8}$$

and

$$S_{yy} = \sum_{i=1}^{n}[y(i) - \bar{y}]^2, \quad SS_R(p) = \sum_{i=1}^{n}[\hat{y}(i) - \bar{y}]^2, \quad SS_E(p) = \sum_{i=1}^{n}[y(i) - \hat{y}(i)]^2 \tag{7.9}$$

where $S_{yy}$, $SS_R(p)$ and $SS_E(p)$ denote the *total sum of squares*, the *regression sum of squares*, and the *residual sum of squares* of a model with $p$ weightings, respectively. Furthermore, $\bar{y}$ denotes the mean of the output observation ($\bar{y} = \sum_{i=1}^{n} y(i)/n$) and $n$ is the number of observations. $R_p^2$ increases as additional input variables are introduced to the model and reaches the maximum when $p = k+1$.

The analyst might use this criterion by adding input variables to the model up to the point where an additional variable is not useful in that it provides only a small increase in $R_p^2$. However, since $R_p^2$ increases as $p$ increases, using $R_p^2$ to determine the optimal models is not straightforward. To avoid this difficulty, this study prefers to use an adjusted $R^2$ statistic defined as [102]:

$$\bar{R}_p^2 = 1 - \left(\frac{n-1}{n-p}\right)(1 - R_p^2) \tag{7.10}$$

Note that $\bar{R}_p^2$ statistic does not necessarily increase as $p$ increases. Consequently, one can consider the model that has the maximum $\bar{R}_p^2$ value an optimum model.

Table 7.4 shows the five best models that maximize $\bar{R}_p^2$ for each given number of inputs, $3 \leq r \leq 9$. The first column of Table 7.4 shows the identification numbers of the examined models. The best models for each given $r$ ($3 \leq r \leq 9$) are retained for further comparison (models 1, 6, 11, 16, 21, 26 and 31). Note that three models (models 21, 22, and 23) with five input variables and model 26 with four inputs have larger $\bar{R}_p^2$ values than the models (models 11 and 16) with the largest $\bar{R}_p^2$ values for $r = 7$ and $r = 6$. Therefore, models 22 and 23 are also retained for further

investigation. The filter system appears to approach the optimal architecture in terms of $\bar{R}_p^2$ statistic, when the size of inputs is about four or five ($4 \leq r \leq 5$).

Furthermore, we want to estimate the prediction performance of the model before future observations become available. A possible procedure is to split the training data into two parts: the *estimation data* and the *prediction data*. The estimation data is used to build the model, and the prediction data is employed to estimate the prediction capability of the model. The basic process is summarized as follows [2]:

1. Select an observation $y(i)$ as prediction data.
2. Fit the model to the remaining $n-1$ estimation data and use the model to predict the withheld observation (denote $\tilde{y}(i)$ as the predicted value corresponding to $y(i)$).
3. Compute the *deleted residual* defined as $e(i) = y(i) - \tilde{y}(i)$.
4. Repeat this procedure for all observations.

The **PR**ediction **E**rror **S**um of **S**quares (PRESS) statistic is then defined as the sum of the deleted residuals. That is, PRESS=$\sum_{i=1}^{n}[y(i)-\tilde{y}(i)]^2$. Finally, an approximate $R^2$ for prediction is computed as

$$R_{pred}^2 = 1 - \frac{\text{PRESS}}{S_{yy}} \tag{7.11}$$

This $R_{pred}^2$ is used as a complementary criterion and shown in the fourth column of Table 7.4.

For the remaining models (models 1, 6, 11, 16, 21, 22, 23, 26 and 31), two hypothesis tests (the $F$- and $t$-statistic tests) are conducted to measure model adequacy. These tests assume that the errors $\epsilon(i)$ in Equation (7.3) are normally and independently distributed with zero mean and variance $\sigma_\epsilon^2$. A detailed description for the $F$- and $t$-statistic tests can be found in Reference 102.

First, the $F$-statistic test determines if there is a linear relationship between the output and any of the input variables. The appropriate hypothesis are

$$\begin{aligned} H_0 : w_i &= 0 \text{ for all } i \\ H_1 : w_i &\neq 0 \text{ for at least one } i \end{aligned} \tag{7.12}$$

The hypothesis $H_0$ is rejected if $F_0 > F_{\alpha,r,n-r-1}$. Here, $F_0$ is a ratio of $SS_R/r$ to $SS_E/(n-r-1)$, and $F_{\alpha,r,n-r-1}$ can be found from a statistical table of the $F$ distribution. $SS_R/\sigma_\epsilon^2$ and $SS_E/\sigma_\epsilon^2$ have $\chi^2$ distributions with $r$ and $(n-r-1)$ degrees of freedom, respectively. Furthermore, $F_0$ $(=(n-r-1)SS_R/kSS_E)$ have a $F$ distribution with $r$ and $n-r-1$ degrees of freedom for numerator and denominator, respectively. Rejection of $H_0$ implies that at least one of the inputs contributes significantly to the model. Table 7.5 presents the LMS estimation of the weighting coefficients and the $F$-statistic of the remaining models (models 1, 6, 11, 16, 21, 22, 23, 26 and 31). The last column of Table 7.5 shows that for all the selected models, the linear relationship between the inputs and output is significant. However, the passing of the $F$-statistic test does not necessarily indicate that the model examined is an appropriate one for predicting the output. Further tests of model adequacy are required.

Next, the $t$-statistic test examines the significance of the individual filter coefficient to the model given the other inputs in the model. The hypotheses for testing the significance of any input, such as $w_i$, are

$$\begin{aligned} H_0 &: w_i = 0 \\ H_1 &: w_i \neq 0 \end{aligned} \tag{7.13}$$

If $|t_0| > t_{\alpha/2,n-r-1}$, the hypothesis $H_0$ is rejected implying that the examined input contributes significantly to the model. Here, $t_0$ $(= w_i/\sqrt{\hat{C}_i\ \sigma_\epsilon^2})$ has a $t$ distribution, $C_i$ is the $i$th diagonal element of $(\mathbf{X}^T\mathbf{X})^{-1}$, and $\hat{\sigma}_\epsilon^2$ is an unbiased estimate of the sum of squared errors of the system:

$$\hat{\sigma}_\epsilon^2 = \sum_{i=1}^{n} \frac{[y(i) - \hat{y}(i)]^2}{n-p} \tag{7.14}$$

The value of $t_{\alpha,r,n-r-1}$ is found from a statistical table of the $t$ distribution. Note that this examines only the marginal contribution of one input given the other inputs are in the model. Table 7.6 shows the results of the $t$-statistic test. Each filter coefficient that does not pass the $t$-statistic test is subscripted by an asterisk * in Table 7.6. Except for models 6, 26 and 31, the hypothesis $H_0 : w_i = 0$ is not rejected. This indicates that the other models contain redundant inputs that can be deleted from

Table 7.5: The estimated weights for the selected models

| # | $r$ | Estimated Weightings | | | | | | |
|---|---|---|---|---|---|---|---|---|
| | | $\hat{w}_o$ | $\hat{w}_{T_1}$ ($\times 10^{-2}$) | $\hat{w}_{T_2}$ ($\times 10^{-3}$) | $\hat{w}_{T_3}$ ($\times 10^{-3}$) | $\hat{w}_{T_5}$ ($\times 10^{-3}$) | $\hat{w}_{T_6}$ ($\times 10^{-2}$) | $\hat{w}_{T_7}$ ($\times 10^{-3}$) |
| 1 | 9 | 7.457 | -1.276 | 7.548 | | -4.179 | 1.419 | |
| 6 | 8 | 7.559 | -1.102 | 5.346 | | | 0.964 | |
| 11 | 7 | 7.530 | | | 6.055 | | | -1.162 |
| 16 | 6 | 7.572 | -0.053 | | 7.832 | | | -2.358 |
| 21 | 5 | 7.580 | | | 7.478 | | | -2.171 |
| 22 | 5 | 7.517 | -0.070 | | 8.105 | | | -2.287 |
| 23 | 5 | 7.527 | | -0.633 | 8.462 | | | -2.367 |
| 26 | 4 | 7.509 | | | 7.694 | | | -1.992 |
| 31 | 3 | 7.429 | | | 5.957 | | | |
| | | $\hat{w}_{T_1'}$ ($\times 10^{-3}$) | $\hat{w}_{T_2'}$ ($\times 10^{-2}$) | $\hat{w}_{T_3'}$ ($\times 10^{-2}$) | $\hat{w}_{T_5'}$ ($\times 10^{-2}$) | $\hat{w}_{T_6'}$ ($\times 10^{-2}$) | $\hat{w}_{T_7'}$ ($\times 10^{-3}$) | $F_o(F_{\alpha,r,n-r-1})$ |
| 1 | 9 | -9.258 | | 1.303 | -1.557 | 1.311 | -5.822 | 670.487(>6.04) |
| 6 | 8 | -8.288 | | 1.427 | -1.475 | 1.029 | -6.454 | 592.828(>4.88) |
| 11 | 7 | -4.049 | -0.997 | 1.047 | -0.785 | 0.628 | | 272.680(>4.28) |
| 16 | 6 | | -1.453 | 1.095 | -0.186 | | | 325.259(>3.97) |
| 21 | 5 | | -1.503 | 1.147 | -0.232 | | | 418.202(>3.84) |
| 22 | 5 | | -1.490 | 1.002 | | | | 408.356(>3.84) |
| 23 | 5 | | -1.573 | 1.050 | | | | 389.600(>3.84) |
| 26 | 4 | | -1.575 | 1.044 | | | | 506.328(>3.86) |
| 31 | 3 | | -1.480 | 1.005 | | | | 332.842(>4.10) |

the models.

Finally, model 26 with inputs $T_3$, $T_7$, $T_2'$ and $T_3'$ is selected as a *satisfactory* model for the prediction of the second data set since (1) the $\bar{R}_p^2$ value of model 26 is comparable to that of model 6 or better than model 31, (2) the $R_{pred}^2$ value of model 26 is higher than the other models (except model 6), (3) this model passes both the $F$- and $t$-statistic tests, and (4) model 26 has only half as many inputs as model 6. From

Equation (7.7), the LMS estimator of $\hat{\mathbf{w}}$ is computed for model 26:

$$\hat{\mathbf{w}} = \begin{bmatrix} \hat{w}_o \\ \hat{w}_{T_3} \\ \hat{w}_{T_7} \\ \hat{w}_{T_2'} \\ \hat{w}_{T_3'} \end{bmatrix} = \begin{bmatrix} 7.509 \\ 0.007694 \\ -0.001992 \\ -0.01575 \\ 0.01044 \end{bmatrix} \tag{7.15}$$

Usually, the selection of an optimal model is not a computationally trivial task. One should also check if the model is physically reasonable. The selection of model 26 and the estimated filter coefficients in Equation (7.15) reveals that (1) the response change of the Alamosa Canyon Bridge lags the temperature of the bridge (the temperatures of two hours before the current time contribute more significantly to the change of the current frequency than the temperatures at the current time: $\hat{w}_{T_2'}$ and $\hat{w}_{T_3'}$ are approximately ten times larger than $\hat{w}_{T_3}$ and $\hat{w}_{T_7}$), and (2) the temperature gradient between the top west outdoor and the top east indoor ($0.01044T_3'$-$0.01575T_2'$) largely influences the variation of the fundamental frequency. This supports the observation in Reference 49 that the changes in modal frequencies are related to the temperature differentials across the deck.

Figure 7.5 shows how well the selected model 26 reproduces the first mode frequency from the first data set which is employed for the training of the filter. Note that only three temperature readings at the top west outdoor, top west indoor and bottom east outdoor out of the total of nine thermometers are necessary to reasonably estimate the change of the fundamental frequency.

## 7.5 Prediction using the Trained Model

The adaptive filter established in the previous subsection was used to predict the fundamental natural frequency of the bridge. The predicted value is then used to discriminate the changes of the fundamental natural frequency caused by temperature effects from changes caused by other environmental effects or potential damage of the structure. For example, let $\mathbf{x}_0$ denote a vector of new temperature readings. A point

Table 7.6: The $t$-statistic test of each weight for the selected models

| ID# | $r$ | t-statistic ($t_o$) | | | | | | |
|---|---|---|---|---|---|---|---|---|
| | | $\hat{w}_o$ | $\hat{w}_{T_1}$ | $\hat{w}_{T_2}$ | $\hat{w}_{T_3}$ | $\hat{w}_{T_5}$ | $\hat{w}_{T_6}$ | $w_{T_7}$ |
| 1 | 9 | 84.166 | -7.548 | 4.629 | | -1.445* | 4.292 | |
| 6† | 8 | 125.900 | -8.255 | 8.156 | | | 8.557 | |
| 11 | 7 | 72.692 | | | 4.313 | | | -1.070* |
| 16 | 6 | 103.642 | -0.729* | | 9.824 | | | -3.339 |
| 21 | 5 | 108.696 | | | 12.248 | | | -3.416 |
| 22 | 5 | 247.207 | -1.030* | | 11.420 | | | -3.338 |
| 23 | 5 | 202.962 | | -0.832* | 7.682 | | | -3.033 |
| 26† | 4 | 254.457 | | | 13.071 | | | -3.188 |
| 31† | 3 | 330.891 | | | 18.800 | | | |

| | | $\hat{w}_{T_1'}$ | $\hat{w}_{T_2'}$ | $\hat{w}_{T_3'}$ | $\hat{w}_{T_5'}$ | $\hat{w}_{T_6'}$ | $\hat{w}_{T_7'}$ | $t_{\alpha,r,n-r-1}$ |
|---|---|---|---|---|---|---|---|---|
| 1 | 9 | -9.612 | | 10.609 | -10.160 | 5.281 | -5.365 | 3.182 |
| 6† | 8 | 10.639 | | 14.386 | -9.184 | 5.943 | -5.763 | 2.776 |
| 11 | 7 | -1.099 | -2.247* | 6.727 | -1.465* | 0.999* | | 2.571 |
| 16 | 6 | | -13.107 | 8.460 | -0.830* | | | 2.447 |
| 21 | 5 | | -17.902 | 11.023 | -1.120* | | | 2.365 |
| 22 | 5 | | -14.985 | 15.724 | | | | 2.365 |
| 23 | 5 | | -27.998 | 20.699 | | | | 2.365 |
| 24 | 5 | | -14.996 | 15.811 | | | | 2.365 |
| 25 | 5 | | -18.894 | 8.911 | | | 0.519* | 2.365 |
| 26† | 4 | | -28.639 | 21.193 | | | | 2.306 |
| 31† | 3 | | -22.566 | 14.820 | | | | 2.262 |

† Only these models pass the t-statistic test. $*$ These coefficients do not pass the $t$-statistic test.

prediction $\hat{y}_0$ of the fundamental natural frequency at the temperature profile becomes

$$\hat{y}_0 = \mathbf{x}_0^T \hat{\mathbf{w}} \tag{7.16}$$

where $\hat{\mathbf{w}}$ is the weight vector determined in Equation (7.15).

One cannot expect a perfect match of the prediction and the measured modal parameters because of incompleteness of the model, insufficient training data sets, uncertainties in actual testing and measurements and so on. Of broader importance, however, one can compute a confidence interval around the point prediction $\hat{y}_0$ to account for the inherent uncertainties. The upper and lower bounds of a $100(1-\alpha)\%$

confidence interval for the predicted output at the given input observation, namely $\hat{y}_0$ in this case, is computed as [102]:

$$\hat{y}_0 \pm t_{\alpha/2,n-p}\sqrt{\hat{\sigma}_\epsilon^2(1+\mathbf{x_0^T}(\mathbf{X^T X})^{-1}\mathbf{x_0})} \tag{7.17}$$

where $\mathbf{X}$ is the collection of training data sets as defined in Equation 7.3.

Once the filter is trained, the newly measured frequency can be compared against the confidence interval. If the fundamental natural frequency falls outside the confidence interval, then one may suspect with the given confidence that some changes in the underlying structural characteristic are caused by damage or other effects. Table 7.7 shows the predicted value of the fundamental frequency and a 95% confidence interval computed at the different time of temperature profiles from the second data set. The first column of the table shows the starting time of each testing, and the second and third columns present the lower and upper bounds of the confidence interval, respectively. These bounds are computed from Equation (7.17). The variables $\hat{y}$ and $y$ in Table 7.7 denote the predicted frequency from Equation (7.16) and the measured frequency from the second testing, respectively.

Table 7.7: Comparison of the measured fundamental frequency and the 95% confidence intervals

| Time | Confidence Bounds | | $y$ | $\hat{y}$ | Relative* | Extrapolation Check |
|---|---|---|---|---|---|---|
| | Lower | Upper | | | Error(%) | $h_0$ ($h_{max}$) |
| 06:02 | 7.592 | 7.669 | 7.630 | 7.329 | 3.95 | 3.6004 ($>$ 0.7686) |
| 08:00 | 7.660 | 7.755 | 7.707 | 7.528 | 2.32 | 5.9233 ($>$ 0.7686) |
| 10:02 | 7.612 | 7.712 | 7.662 | 7.638 | 0.31 | 6.6219 ($>$ 0.7686) |
| 12:00 | 7.435 | 7.550 | 7.493 | 7.579 | 1.15 | 9.0997 ($>$ 0.7686) |
| 14:01 | 7.463 | 7.570 | 7.517 | 7.503 | 0.19 | 8.0356 ($>$ 0.7686) |
| 16:00 | 7.379 | 7.424 | 7.401 | 7.449 | 0.64 | 0.5026 ($<$ 0.7686) |
| 18:00 | 7.407 | 7.451 | 7.429 | 7.361 | 0.92 | 0.4734 ($<$ 0.7686) |
| 20:05 | 7.338 | 7.378 | 7.358 | 7.321 | 0.51 | 0.1836 ($<$ 0.7686) |
| 21:54 | 7.367 | 7.408 | 7.388 | 7.319 | 0.93 | 0.2384 ($<$ 0.7686) |
| 24:00 | 7.389 | 7.431 | 7.410 | 7.347 | 0.85 | 0.3396 ($<$ 0.7686) |

* Relative Error (%)=$100 \times |y - \hat{y}|/\hat{y}$

In predicting new observations, one should be careful not to extrapolate beyond the input variable region containing the training data set. A model that fits well inside

the region of the original data may perform poorly outside that region. In a multi-dimensional input space, it is difficult to decide if an input variable point lies inside or outside the region of the original data. The diagonal elements of the *hat* matrix $\mathbf{H}(= \mathbf{X}(\mathbf{X}^T\mathbf{X})^{-1}\mathbf{X}^T)$ are employed to detect a hidden extrapolation point [102]. Let the largest diagonal value of the hat matrix $\mathbf{H}$ be $h_{max}$, and define the smallest convex surface containing all of the training data points as the input variable hull (IVH). The relative distance of any input variable vector $\mathbf{x}_0$ to the centroid of the IVH is reflected by

$$h_0 = \mathbf{x}_0^T(\mathbf{X}^T\mathbf{X})^{-1}\mathbf{x}_0 \tag{7.18}$$

If $h_0 > h_{max}$, the point is outside the IVH and requires an extrapolation. The value of $h_0$ depends both on the Euclidean distance of the corresponding point from the centroid of the training data and on the density of points in the IVH. In the last column of Table 7.7, the $h_0$ value of each input is compared to $h_{max}$. Only the last five points corresponding to time 16:00, 18:00, 20:05, 21:54 and 24:00 are interpolation points. We presume that only these data points inside the IVH are reliable for the prediction.

The measured fundamental frequency from the second data set, and the upper and lower bounds of the 95% confidence interval are plotted in Figure 7.5. Figure 7.5 reveals that the measured frequencies corresponding to the interpolation points are consistently lower than the associated lower bounds of the 95% prediction interval (except the one at time 16:00). The linear filter was also trained using the second mode frequency from the first data set and tested for prediction of the second mode frequency from the second data set. Figures 7.6 and 7.7 show the reproduction of the training data set and the prediction result for the second mode frequency, respectively. Again we observe that the measured second frequency is lower than or close to the lower bound of the confidence interval.

This result implies that the stiffness of the structure is deteriorated and/or the mass of the structure is increased. Considering the facts that the Alamosa Canyon Bridge is a concrete bridge, it had visible cracks over the deck, and there was a severe rain prior to the second test, and the drainage paths were filled with debris and dirt, it

is very possible that these consistent decreases of the fundamental natural frequency were mainly caused by the increase of the bridge mass as the Alamosa Canyon Bridge absorbed significant amount of moisture and the bridge retained some of the rainfall on its surface. Assuming that the change of the bridge mass is solely responsible for the decrease of the fundamental frequency within the interpolation points, the increase of mass is approximately estimated as 1.62%. Considering the experimental study that several concrete bridges in the United Kingdom absorbed considerable amount of moisture during damp weather, and consequently increased the mass of the bridge approximately by 3 to 6 % [151], the change of the mass estimated in this study falls within a reasonable range.

Note that statistical uncertainty bounds (mean $\pm$ $2\sigma$) are added around the measured frequencies in Figures 7.5 and 7.7 to show that the variation caused by thermal effect is larger than the inherent uncertainties in the measured frequencies. (The measured frequencies in Figures 7.5 to 7.7 are the mean values computed by averaging thirty FRFs.) The standard deviation ($\sigma$) of the frequencies is estimated using the procedure in References 18 and 42.

## 7.6 Summary and Discussions

This chapter presents an adaptive filter for predicting changes in modal parameters of a full-scale bridge due to environmental temperature. Data from the Alamosa Canyon Bridge in New Mexico were employed to demonstrate the applicability of the adaptive filter. The vibration tests were conducted during the summer of 1996 and 1997. The first data set from 1996 test was used to train the adaptive filter while the second data set from 1997 test was used to test the prediction performance. Changes in the frequencies are found linearly correlated with temperature readings from different parts of the bridge. The filter uses spatial and temporal temperature distributions to determine changes in the first and second mode frequencies. A linear filter with two spatially-separated temperature measurements and two temporally-separated temperature measurements reproduces the variation of the frequencies of the first data set. Then, the system defines a confidence interval for future values

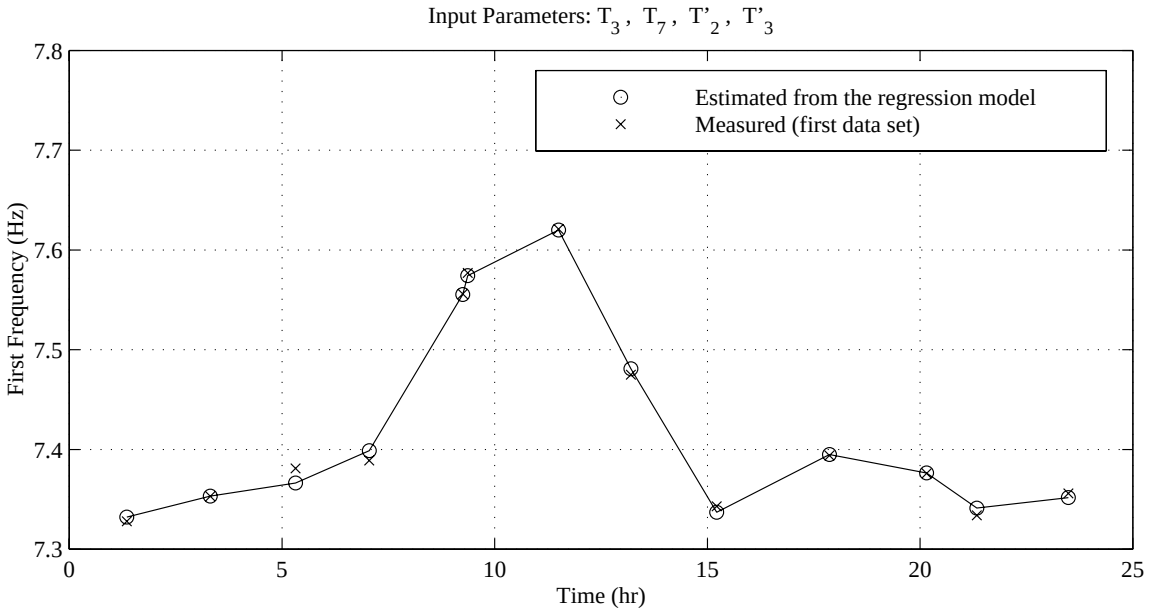


Figure 7.4: Reproduction of the first mode frequency using a linear filter

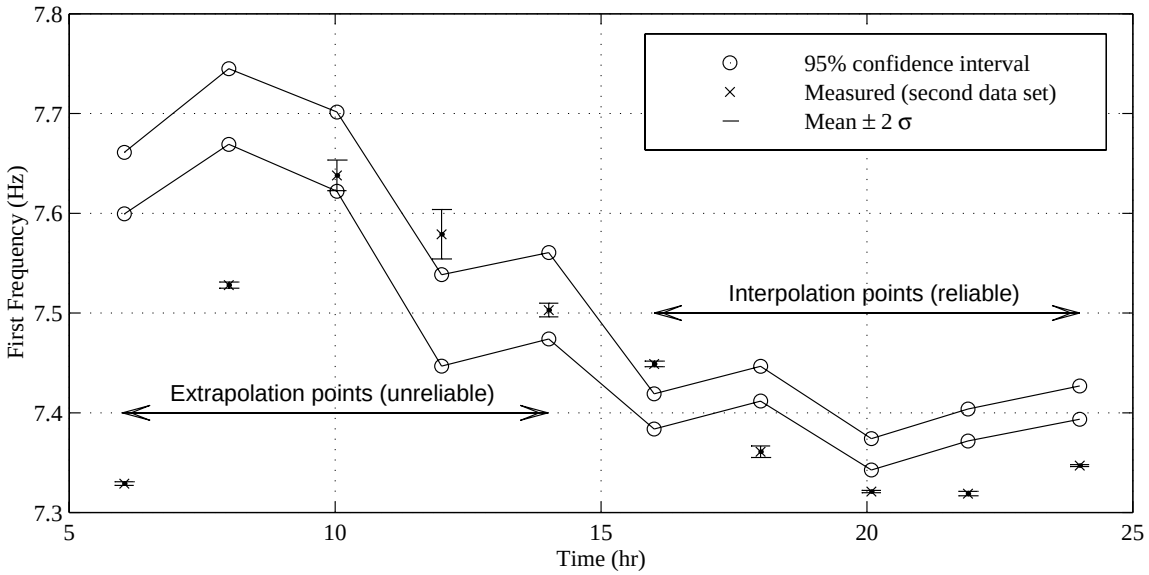


Figure 7.5: Prediction of the first mode frequency using a linear filter

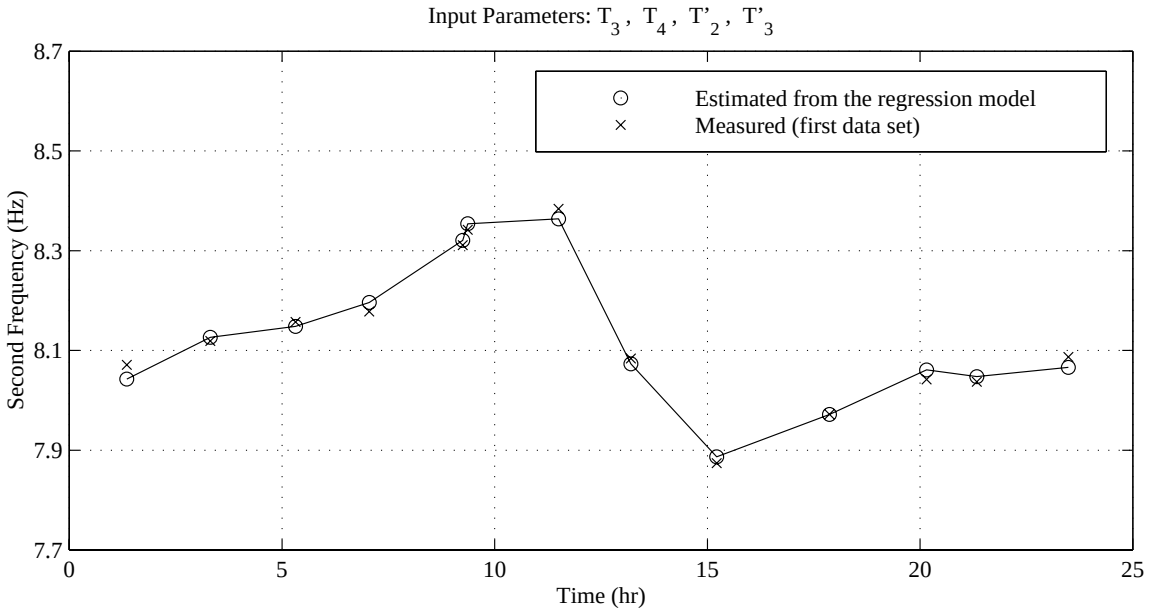


Figure 7.6: Reproduction of the second mode frequency using a linear filter

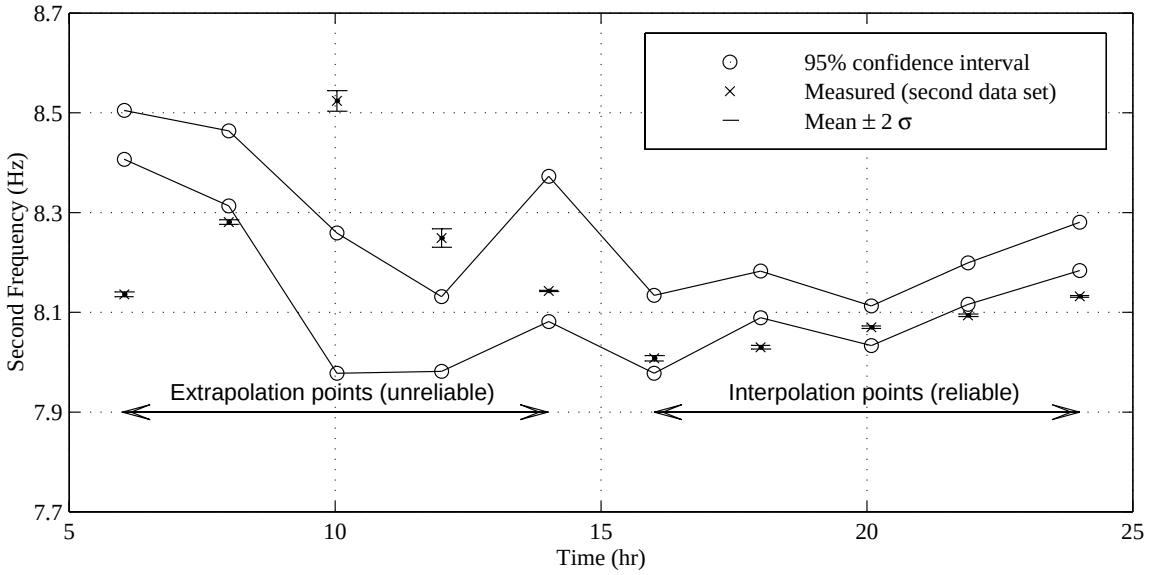


Figure 7.7: Prediction of the second mode frequency using a linear filter

of modal parameters in order to discriminate between variations caused by temperature changes and those indicative of structural change or other environmental effects. The comparison of the prediction intervals obtained from the first data set and the measured frequencies from the second test data reveals that the bridge experienced a statistically significant decrease in the first and second mode frequencies. Considering the severe rain prior to the testing and the drainage system severely blocked by debris, it is very possible that this consistent decrease of the frequencies was mainly caused by the increase of the bridge mass as the Alamosa Canyon Bridge absorbed significant amount of moisture, and the bridge retained much of the rainfall on its surface.

It should be kept in mind that the filter system presented was developed for a particular bridge under particular environmental conditions. Further and well controlled testings are required to fully validate this linear model. Although this study has been limited to a single external variable (temperature), the approach might be extendible to other environmental effects. To control for other environmental conditions and account for larger-scale seasonal variations, tests should be conducted during different times of the year as well as different times of a day, and measurements for other environmental factors should be obtained. Furthermore, a continuous data collection system would allow the filter coefficients to be more reliably updated, and to decrease the size of the confidence intervals. Last but not least, as shown in the test, reliable damage detection must account for the significant non-stationary environmental processes. While the current study focuses on the temperature effect on the frequencies, similar technique may also be applicable for obtaining confidence bounds for other parameters such as modal and Ritz vectors.

# Chapter 8

# Summary and Discussions

A Bayesian probabilistic framework for damage detection is proposed for the continuous monitoring of structures. The idea is to search for the most probable damage event by comparing the relative probabilities for different damage scenarios. The relative probability of a damage event is expressed in terms of the posterior probability of the damage event, given the estimated data sets from vibration tests of the structure. The formulation of the relative posterior probability is based on an output error, which is defined as the difference between the estimated vibration signatures and the theoretical ones from the analytical model. This feature makes the Bayesian approach well suited from long-term health monitoring of a structure. Through the experimental investigations, the Bayesian approach is shown (1) to take into account the uncertainties in the measurement and the analytical modeling, (2) to perform damage diagnosis with a relatively small number of measurement points and a few modes, and (3) to systematically extract information from continuously obtained test data.

The proposed method has many advantages over the deterministic approaches, which produce a single diagnosis result, in that (1) several suspicious damage events are provided with their relative probabilities, (2) a series of measurement data obtained from vibration tests can be included to improve the accuracy of the results, and (3) engineering judgment about possible damage events via system reliability/structural analysis or experience with similar structures can potentially be incorporated into the Bayesian framework as the prior probabilities of the damage

events.

A branch-and-bound search scheme is devised to expedite the search for the most likely damage event without exhaustively examining all possible damage cases. Our experience has shown that the branch-and-bound search can significantly reduce the computational requirements of the Bayesian approach; particularly when damage is localized in a few locations, the computation is quite manageable.

The Bayesian approach, like many other methods using vibration responses, is based on the premise that when the physical properties (such as the mass, stiffness and damping) of a structure change due to damage, these changes can be revealed by measuring the dynamic response of the structure. Therefore, the sensitivity of damage with respect to the measured quantities is critical to the success of the method. Furthermore, this method might have the drawback that the damage locations and amount may not be uniquely determined from the estimated modal data when the vibration measurements are obtained at limited points and only a few fundamental modes are estimated. Particularly, in the presence of the modeling error and the measurement noise, some erroneous models could have modal parameters closer to the estimated modal parameters than the model with the correct damage locations and amount.

As an alternative to modal vectors, load-dependent Ritz vectors are incorporated into the Bayesian framework. Advantages of Ritz vectors over modal vectors are shown through experimental and numerical examples: (1) in general, load-dependent Ritz vectors are more sensitive to damage than the corresponding modal vectors particularly for complicated, highly redundant systems, and (2) by a careful selection of load patterns, substructures of interest can be made more observable by imposing particular load patterns. Furthermore, a procedure to extract Ritz vectors from vibration tests is proposed, and the procedure is successfully demonstrated using the test data from a grid-type bridge structure. It is believed that the advantage of Ritz vectors will be more salient for structures with complicated geometry because load redistribution caused by different load patterns will be significant for the complex structures. It would be worthwhile to develop a systematic scheme to find appropriate load patterns, which yield better detection of damage in substructures of interest.

Data from vibration tests of civil structures indicate that the environmental effects such as temperature, traffic loading, humidity can often mask subtle structural changes caused by damage. We examined a linear adaptive model to discriminate the changes of modal parameters due to temperature changes from those caused by structural damage or other environmental effects. Data from the Alamosa Canyon Bridge in New Mexico were used to demonstrate the effectiveness of the adaptive filter for this problem. Results indicate that a simple linear filter of temperature can reproduce the natural variability of the frequencies with respect to time of day. A confidence interval of the frequencies is established for a new temperature profile in order to discriminate the changes of modal parameters due to temperature changes from those caused by other environmental effects or potential structural damage. It should be noted that the adaptive filter system presented was developed for a particular bridge under particular environmental conditions. To fully validate this linear model, tests should be conducted during different times of the year as well as different times of a day, and measurements for other environmental factors should be obtained.

Finally, the application of the Bayesian approach to real structures will be the utmost important task to fully validate the proposed approach and to demonstrate the viability of the approach and its implementation. Furthermore, recent advances in wireless communication and information technologies will have significant impacts on the development of sensing devices for structural monitoring [142]. The development of a cost effective, large scale instrumentation based on these technologies must be carried out in parallel to make the monitoring of civil structures a reality.

# Bibliography


[1] A. K. Ahmadi. *Application of System Identification in Mathematical Modeling of Buildings*. PhD thesis, Department of Civil Engineering, University of Pittsburgh, Pittsburgh, PA, 1986.

[2] D. M. Allen. The relationship between variable selection and data augmentation and a method for prediction. *Technometrics*, 16:125–127, 1974.

[3] K. A. Alvin, K. C. Park, and W. K. Belvin. A second-order structural identification procedure via state space-based system identification. Technical Report AIAA-92-4387-CP, American Institute of Aeronautics and Astronautics, 1992.

[4] K. F. Alvin. Finite element model update via Bayesian estimation and minimization of dynamic residuals. *American Institute of Aeronautics and Astronautics*, 35:879–886, 1997.

[5] V. Askegaard and P. Mossing. Long term observation of RC-bridge using changes in natural frequencies. *Nordic Concrete Research*, 7:20–27, 1988.

[6] P. Avitabile, J. O'Callahan, and J. Milani. Comparison of system characteristics using various model reduction techniques. In *Proceedings of the 7th International Modal Analysis Conference*, pages 1109–1115, Las Vegas, NV, 1989.

[7] P. Avitabile, F. Pechinsky, and J. O'Callahan. Study of vector correlation using various techniques for model reduction. In *Proceedings of the 10th International Modal Analysis Conference*, pages 572–583, San Diego, CA, 1992.

[8] M. Baruch. Optimization procedure to correct stiffness and flexibility matrices using vibration tests. *American Institute of Aeronautics and Astronautics*, 16:1208–1210, 1978.

[9] M. Baruch. Optimal correction of mass and stiffness matrices using measured modes. *American Institute of Aeronautics and Astronautics*, 20:1623–1626, 1982.

[10] M. Baruch. Methods of reference basis for identification of linear dynamic structures. *American Institute of Aeronautics and Astronautics*, 22:561–564, 1984.

[11] M. Baruch and I.Y. Bar Itzhack. Optimal weighted orthogonalization of measured modes. *American Institute of Aeronautics and Astronautics*, 16:346–351, 1978.

[12] M. Baruch and Y. Zemel. Mass conservation in the identification of space structures. In *Proceedings of the 30th AIAA/ASME/ASCE/AHS/ASC Structures, Structural Dynamics, and Materials Conference*, pages 710–712, Mobile, AL, 1989.

[13] H. Baruh. Identification of boundary conditions in flexible structures. In *Proceedings of the 2nd USAF/NSAS Workshop on System Identification and Health Monitoring of Precision Space Structures*, pages 193–211, Pasadena, CA, 1990.

[14] C. A. Beattie and S. W. Smith. Secant methods for structural model identification. Technical Report TR-ICAM-TR-88-09-01, Center for Applied Mathematics, Virginia Polytechnic Institute and State University, 1988.

[15] J. L. Beck and L. S. Katafygiotis. Probabilistic system identification and health monitoring of structures. In *Proceedings of the 10th World Conference on Earthquake Engineering*, pages 3721–3726, Balkema Rotterdam, 1992.

[16] J. L. Beck, M. W. Vanik, and L. S. Katafygiotis. Determination of stiffness changes from modal parameter changes for structural health monitoring. In

*Proceedings of the First World Conference on Structural Control*, Pasadena, CA, 1994.

[17] R. T. Beck. *Fundamental Problems in the Application of Structural Identification Procedures to Damage Detection.* PhD thesis, Department of Civil Engineering, California Institute of Technology, Pasadena, CA, 1991.

[18] J. S. Bendat and A. G. Piersol. *Engineering Applications of Correlation and Spectral Analysis.* John Wiley and Sons Inc., New York, 1980.

[19] J. S. Bendat and A. G. Piersol. *Random Data: Analysis and Measurement procedures, Second Edition.* John Wiley and Sons Inc., New York, 1986.

[20] H. Berger, L. Barthe, and R. Ohayon. Parametric updating of a finite element model from experimental modal characteristics. In *Proceedings of the 1989 European Forum on Aeroelasticity and Structural Dynamics*, Aachen, Germany, 1989.

[21] H. Berger, J. P. Chaquin, and R. Ohayon. Finite element model adjustment using experimental data. In *Proceedings of the 2nd International Modal Analysis Conference*, pages 638–642, Orlando, FL, 1984.

[22] A. Berman. Mass matrix correction using an incomplete set of measured modes. *American Institute of Aeronautics and Astronautics*, 17:1147–1148, 1979.

[23] A. Berman and W. G. Flannelly. Theory of incomplete models of dynamic structures. *American Institute of Aeronautics and Astronautics*, 9:1481–1487, 1971.

[24] A. Berman and E. J. Nagy. Improvements of a large analytical model using test data. *American Institute of Aeronautics and Astronautics*, 21:1168–1173, 1983.

[25] A. Berman, F. S. Wei, and K. V. Rao. Improvement of analytical dynamic models using modal test data. In *Proceedings of the 21th AIAA/ASME/ASCE/AHS/ASC Structures, Structural Dynamics, and Materials Conference*, pages 809–814, Seattle, WA, 1980.

[26] M. M. Bernitsas and R. L. Tawekal. Structural model correlation using large admissible perturbations in cognate space. *American Institute of Aeronautics and Astronautics*, 29:2222–2232, 1991.

[27] T. T. Cao and D. C. Zimmerman. Application of load-dependent Ritz vectors in structural damage detection. In *Proceedings of the 15th International Modal Analysis Conference*, pages 1319–1324, Orlando, FL, 1997.

[28] T. T. Cao and D. C. Zimmerman. A procedure to extract Ritz vectors from dynamic testing data. In *Proceedings of the 15th International Modal Analysis Conference*, pages 1036–1042, Orlando, FL, 1997.

[29] D. Capecchi and F. Vestroni. Identification of finite element models in structural dynamics. *Engineering Structure*, 15:21–30, 1993.

[30] T. K. Caughey and M. M. J. O'Kelly. Classical normal modes in damped linear dynamic systems. *Journal of Applied Mechanics*, 32:583–588, 1965.

[31] J. C. Chen and J. A. Garba. Matrix perturbation for analytical model improvement. In *Proceedings of the 20th AIAA/ASME/ASCE/ AHS/ASC Structures, Structural Dynamics, and Materials Conference*, pages 428–436, St. Louis, MO, 1979.

[32] J. C. Chen and J. A. Garba. Analytical model improvement using modal test results. *American Institute of Aeronautics and Astronautics*, 18:684–690, 1980.

[33] J. C. Chen and J. A. Garba. On-orbit damage assessment for large space structures. *American Institute of Aeronautics and Astronautics*, 26:1119–1126, 1988.

[34] J. C. Chen and D. L. Hunt. Application of multiple input random and Polyreference analysis techniques to the Galileo spacecraft modal test. In *Proceedings of the 25th AIAA/ASME/ASCE/AHS/ASC Structures, Structural Dynamics, and Materials Conference*, pages 554–560, Palm Springs, CA, 1984.

[35] A. K. Chopra. *Dynamics of Structures.* Prentice-Hall, New Jersey, 1995.

[36] C. M. Chou, J. C. O'Callahan, and C. H. Wu. Localization of test/analysis structural model errors. In *Proceedings of the 30th AIAA/ASME/ASCE/ AHS/ASC Structures, Structural Dynamics, and Materials Conference*, pages 748–752, Mobile, AL, 1989.

[37] C. M. Chou and C. H. Wu. System identification and damage localization of dynamic structures. In *Proceedings of the 31st AIAA/ASME/ASCE/ AHS/ASC Structures, Structural Dynamics, and Materials Conference*, pages 113–120, Long Beach, CA, 1990.

[38] A. Churchward and Y. J. Sokal. Prediction of temperatures in concrete bridges. *Journal of Structural Division, ASCE*, 107:2163–2176, 1981.

[39] J. D. Collins, G. C. Hart, T. K. Hasselman, and B. Kennedy. Statistical identification of structures. *American Institute of Aeronautics and Astronautics*, 12:185–190, 1974.

[40] J. D. Collins and W. T. Thomson. The eigenvalue problem for structural systems with statistical properties. *American Institute of Aeronautics and Astronautics*, 7:642–648, 1969.

[41] W. H. Dilger and S. A. Loptson. Temperature monitoring of the Confederation Bridge. In *The Annual Conference of the Canadian Society for Civil Engineering*, pages 151–160, Quebec, Canada, 1997.

[42] S. W. Doebling, C. R. Farrar, and R. S. Goodman. Effects of measurement statistics on the detection of damage in the Alamosa Canyon Bridge. In *Proceedings of the 15th International Modal Analysis Conference*, pages 918–929, Orlando, FL, 1997.

[43] S. W. Doebling, C. R. Farrar, M. B. Prime, and D. W. Shevitz. Damage identification and health monitoring of structural and mechanical systems from changes in their vibration characteristics: A literature reviews. Technical Report LA-13070-MS, Los Alamos National Laboratory, Los Alamos, NM, 1996.

[44] S. W. Doebling, F. M. Hemez, M. S. Barlow, L. D. Peterson, and C. R. Farhat. Selection of experimental modal data sets for damage detection via model update. Technical Report AIAA-93-1481-CP, American Institute of Aeronautics and Astronautics, 1993.

[45] D. J. Ewins. *Modal Testing: Theory and Practice*. John Wiley and Sons Inc., New York, 1995.

[46] C. Farhat and F. M. Hemez. Updating finite element dynamic model using an element-by-element sensitivity methodology. *American Institute of Aeronautics and Astronautics*, 31:1702–1711, 1993.

[47] C. R. Farrar, W. E. Baker, T. M. Bell, K. M. Cone, T. W. Darling, T. A. Duffey, A. Eklund, and A. Migliori. Dynamic characterization and damage detection in the I-40 bridge over the Rio Grande. Technical Report LA-12767-MS, Los Alamos National Laboratory, Los Alamos, NM, 1994.

[48] C. R. Farrar and K. M. Cone. Vibration testing of the I-40 bridge before and after the introduction of damage. In *Proceedings of the 13th International Modal Analysis Conference*, pages 203–209, Nashville, TN, 1995.

[49] C. R. Farrar, S. W. Doebling, P. J. Cornwell, and E. G. Straser. Variability of modal parameters measured on the Alamosa Canyon Bridge. In *Proceedings of the 15th International Modal Analysis Conference*, pages 257–263, Orlando, FL, 1997.

[50] C. R. Farrar and D. Jauregui. Damage detection algorithms applied to experimental and numerical modal data from the I-40 bridge. Technical Report LA-13074-MS, Los Alamos National Laboratory, Los Alamos, NM, 1996.

[51] A. J. Felber and R. Cantieni. Introduction of a new ambient vibration testing system. Technical Report EMPA-Report-No-156'521, EMPA, Dübendorf, Switzerland, 1996.

[52] R. L. Fox and M. P. Kapoor. Rates of changes of eigenvalues and eigenvectors. *American Institute of Aeronautics and Astronautics*, 6:2426–2429, 1968.

[53] M. I. Friswell and J. E. Mottershead. *Finite Element Model Updating in Structural Dynamics*. Kluwer Academic Publishers, London, UK, 1995.

[54] M. I. Friswell and J. E. T. Penny. Is damage locating using vibration measurements practical? In *Proceedings of the DAMAS 97 Workshop*, pages 351–362, Sheffield, UK, 1997.

[55] K. Fukunaga. *Introduction To Statistical Pattern Recognition*. Academic Press, New York, NY, 1990.

[56] G. V. Garcia and N. Stubbs. Relative performance evaluation of pattern recognition models for nondestructive damage detection (NDD). In *Proceedings of the 15th International Modal Analysis Conference*, pages 1822–1830, Orlando, FL, 1997.

[57] J. D. Gibson and J. L. Melsa. *Introduction To Nonparametric Detection with Applications*. Academic Press, New York, NY, 1996.

[58] A. Girard, K. Chatelain, and N. A. Roy. Efficient sensitivity analysis of frequency response functions. In *Proceedings of the 9th International Modal Analysis Conference*, pages 1100–1104, San Diego, CA, 1992.

[59] R. J. Glaser, C. P. Kuo, and B. K. Wada. Improvement of structural models using covariance analysis and nonlinear generalized least squares. *American Institute of Aeronautics and Astronautics*, 30:226–233, 1992.

[60] E. L. Goh and J. E. Mottershead. On model reduction techniques for finite element updating. In *NAFEMS/DTA international Conference on Structural Dynamics, Modeling, Test, Analysis and Correlation*, pages 421–432, Milton, Keynes, 1993.

[61] R. J. Guyan. Reduction of stiffness and mass matrices. *American Institute of Aeronautics and Astronautics*, page 380, 1965.

[62] H. Gysin. Comparison of expansion methods for fe modeling error localization. In *Proceedings of the 8th International Modal Analysis Conference*, pages 195–204, Kissimmee, FL, 1990.

[63] P. Hajela and F. J. Soeiro. Structural damage detection based on static and modal analysis. In *Proceedings of the 30th AIAA/ASME/ASCE/ AHS/ASC Structures, Structural Dynamics, and Materials Conference*, pages 1172–1182, Mobile, AL, 1989.

[64] P. Hajela and F. J. Soeiro. Recent developments in damage detection based on system identification methods. *Structural Optimization*, 2:1–10, 1990.

[65] T. K. Hasselman and G. C. Hart. Modal analysis of random structural systems. *Engineering Mechanics Division, ASCE*, pages 561–579, 1972.

[66] T. K. Hasselman and G. C. Hart. Solution of the structural dynamics eigenproblem by modal synthesis: Sensitivity to coordinate selection and parameter variation. Technical Report TR-7239, University of California at Los Angeles, Los Angeles, CA, 1972.

[67] E. F. Haug and K. K. Choi. Structural design sensitivity analysis with generalized global stiffness and mass matrices. *American Institute of Aeronautics and Astronautics*, 22:1299–1303, 1984.

[68] J. He and D. J. Ewins. Compatibility of measured and predicted vibration modes in model improvement studies. *American Institute of Aeronautics and Astronautics*, 29:798–803, 1991.

[69] F. M. Hemez. *Theoretical and Experimental Correlation between Finite Element Models and Modal Tests in the Context of Large Flexible Space Structures.* PhD thesis, Aerospace Engineering Sciences, University of Colorado, Boulder, CO, 1993.

[70] M. Henrion. *Towards Efficient Probabilistic Diagnosis in Multiply Connected Belief Networks*, pages 385–409. John Wiley and Sons Inc., 1990.

[71] B. L. Ho and R. E. Kalman. Effective construction of linear state-variable models from inputoutput data. In *Proceedings of the 3th Annual Allerton Conference on Circuit and Systems Theory*, pages 449–459, Monticello, IL, 1965.

[72] M. Hoshiya and E. Saito. Structural identification by extended Kalman filter. *Journal of Engineering Mechanics, ASCE*, 110:1757–1770, 1984.

[73] S. R. Ibrahim. Computation of normal modes from identified complex modes. *American Institute of Aeronautics and Astronautics*, 21:446–451, 1983.

[74] M. Imregun and D. J. Ewins. An investigation into mode shape expansion techniques. In *Proceedings of the 11th International Modal Analysis Conference*, pages 168–175, Kissimmee, FL, 1993.

[75] G. H. James, D. C. Zimmerman, C. R. Farrar, and S. W. Doebling. Current horizon for structural damage detection course. In *SEM short course held at the 15th IMAC conference*, Orlando, FL, 1997.

[76] J. N. Juang. An Eigensystem Realization Algorithm for modal parameter identification and model reduction. *Journal of Guidance, Control, and Dynamics*, 8:620–627, 1985.

[77] J. N. Juang. *Applied System Identification.* Prentice Hall, Englewood Cliffs, New Jersey, 1994.

[78] J. N. Juang and R. S. Pappa. Effects of noise on modal parameters identified by the Eigensystem Realization Algorithm. *Journal of Guidance, Control, and Dynamics*, 9:620–627, 1986.

[79] J. N. Juang, M. Phan, L. G. Horta, and R. W. Longman. Identification of Observer/Kalman filter Markov parameters: Theory and experiments. *Journal of Guidance, Control, and Dynamics*, 16:320–329, 1993.

[80] A. M. Kabe. Stiffness matrix adjustment using mode data. *American Institute of Aeronautics and Astronautics*, 23:1431–1436, 1985.

[81] A. M. Kabe. Constrained adjustment of analytical stiffness matrices. Technical Report Paper 851932, Society of Automotive Engineers, 1986.

[82] D. C. Kammer. Test-analysis-model development using an exact modal reduction. *Journal of International Analytical and Experimental Modal Analysis*, 2:174–179, 1987.

[83] D. C. Kammer. Optimum approximation for residual stiffness in linear system identification. *American Institute of Aeronautics and Astronautics*, 26:104–112, 1988.

[84] M. Kaouk and D. C. Zimmerman. Evaluation of the minimum rank update in damage detection: An experimental study. In *Proceedings of the 11th International Modal Analysis Conference*, pages 1061–1068, Orlando, FL, 1993.

[85] M. Kaouk and D. C. Zimmerman. Structural damage assessment using a generalized minimum rank perturbation theory. *American Institute of Aeronautics and Astronautics*, 32:836–842, 1994.

[86] M. Kaouk and D.C. Zimmerman. Structural damage assessment using a generalized minimum rank perturbation theory. In *Proceedings of the 34th AIAA Structures, Structural Dynamics and Materials Conference*, La Jolla, CA, 1993.

[87] T. A-L. Kashangaki. Ground vibration tests of a high fidelity truss for verification of on-orbit damage location techniques. Technical Report NASA-TM-107626, National Aeronautics and Space Administration, 1992.

[88] T. A-L. Kashangaki, S. W. Smith, and T. W. Lim. Underlying modal data issues for detecting damage in truss structures. Technical Report AIAA-92-2264-CP, American Institute of Aeronautics and Astronautics, 1992.

[89] L. S. Katafygiotis. Treatment of model uncertainties in structural dynamics. Technical Report EERL 91-01, Earthquake Engineering Research Laboratory, California Institute of Technology, Pasadena, CA, 1991.

[90] R. L. Kidder. Reduction of structural frequency equations. *American Institute of Aeronautics and Astronautics*, 11:892, 1973.

[91] H. M. Kim and R. R. Craig. Application of unsymmetric block Lanczos vectors in system identifications. *International Journal of Analytical and Experimental Modal Analysis*, 7:227–241, 1992.

[92] J. T. Kim and N. Stubbs. Damage detection in offshore jacket structures from limited modal information. *International Journal of Offshore and Polar Engineering*, 5:58–66, 1995.

[93] P. Ladeveze and M. Reynier. A localization method of stiffness errors for the adjustment of FE models. In *Proceedings of the 12th ASME Mechanical Vibration and Noise Conference*, Quebec, Canada, 1989.

[94] P. Leger, E.L. Wilson, and R.W. Clough. The use of load-dependent Ritz vectors for dynamic and earthquake analyses. Technical Report UCB/EERC-86/04, Earthquake Engineering Research Center, University of California Berkeley, Berkeley, CA, 1986.

[95] N.A.J. Lieven and D.J. Ewins. Spatial correlation of mode shapes, the coordinate modal assurance criterion (COMAC). In *Proceedings of 6th Modal Analysis Conference*, pages 690–695, Kissimme, FL, 1988.

[96] T. W. Lim. A submatrix approach to stiffness matrix correction using modal test data. *American Institute of Aeronautics and Astronautics*, 28:1123–1130, 1990.

[97] T. W. Lim. Structural damage detection using modal test data. *American Institute of Aeronautics and Astronautics*, 29:2271–2274, 1991.

[98] C. S. Lin. Location of modeling errors using modal test data. In *Proceedings of the 30th AIAA/ASME/ASCE/ AHS/ASC Structures, Structural Dynamics, and Materials Conference*, pages 713–720, Mobile, AL, 1989.

[99] K. Lin and R. E. Skelton. Q-Markov covariance equivalent realization and its application to flexible structure identification. *Journal of Guidance, Control, and Dynamics*, 16:308–319, 1993.

[100] R. W. Longman and J. N. Juang. Recursive form of the eigensystem realization algorithm for system identification. *Journal of Guidance, Control and Dynamics*, 12:647–652, 1989.

[101] L. D. Mitchell. Complex modes: A review. In *Proceedings of the 8th International Analysis Conference*, pages 891–899, Kissimmee, FL, 1990.

[102] D. C. Montgomery and E. A. Peck. *Introduction to Linear Regression Analysis.* John Wiley and Sons Inc., New York, 1991.

[103] D. J. Mook and J. S. Lew. A combined ERA/MME algorithm for robust system realization/identification. In *Proceedings of the 29th AIAA/ ASME/ASCE/AHS/ASC Structures, Structural Dynamics, and Materials Conference*, pages 1556–1564, Williamsburg, VA, 1988.

[104] S. Moorty and C. W. Roeder. Temperature-dependent bridge movements. *Journal of Structural Engineering*, 118:1090–1105, 1992.

[105] J. E. Mottershead and M. I. Friswell. Model updating in structural dynamics: A survey. *Journal of Sound and Vibration*, 167:347–375, 1993.

[106] N. G. Nalitolela, J. E. T. Penny, and M. I. Friswell. Updating structural parameters of a finite element model by adding mass or stiffness to the system. In *Proceedings of the 8th International Modal Analysis Conference*, pages 836–842, Kissimmee, FL, 1990.

[107] R. B. Nelson. Simplified calculation of eigenvector derivatives for large dynamic systems. *American Institute of Aeronautics and Astronautics*, 14:1201–1205, 1976.

[108] D. E. Newland. *An Introduction to Random Vibrations and Spectral Analysis.* Longman, London & New York, 1981.

[109] N. Niedbal and E. Klusowski. Optimal exciter placement and force vector tuning required for experimental modal analysis. In *Proceedings of the 31st AIAA/ ASME/ASCE/AHS/ASC Structures, Structural Dynamics, and Materials Conference*, pages 130–141, Long Beach, CA, 1990.

[110] M. A. Norris and L. Meirovitch. On the problem of modeling for parameter identification in distributed structures. *International Journal for Numerical Methods in Engineering*, 28:2451–2463, 1989.

[111] B. Nour-Omid and R. W. Clough. Dynamics analysis of structures using Lanczos coordinates. *Earthquake Engineering and Structural Dynamics*, 12:565–577, 1984.

[112] J. C. O'Callahan. A procedure for an improved reduced system (IRS) model. In *Proceedings of the 7th International Modal Analysis Conference*, pages 17–21, Las Vegas, NV, 1989.

[113] J. C. O'Callahan, P. Avitabile, and R. Riemer. System equivalent reduction expansion process. In *Proceedings of the 7th International Modal Analysis Conference*, pages 29–37, Las Vegas, NV, 1989.

[114] J. C. O'Callahan and R. Leung. Optimization of mass and stiffness matrices using a generalized inverse technique on the measured modes. In *Proceedings of the 3rd International Modal Analysis Conference*, pages 75–79, Orlando, FL, 1985.

[115] J. C. O'Callahan, I. W. Lieu, P. Avitabile, and R. Madden. An efficient method of determining rotational degrees of freedom from analytical and experimental modal data. In *Proceedings of the 4th International Modal Analysis Conference*, pages 50–58, Los Angeles, CA, 1986.

[116] I. U. Ojalvo. A consistent first-order theory for structural model parameter improvement based upon dynamic test data. In *Proceedings of the 33rd AIAA/ASME/ASCE/AHS/ASC Structures, Structural Dynamics, and Materials Conference*, pages 2286–2294, Dallas, TX, 1992.

[117] N. Olhoff and J. Rasmussen. Method of error elimination of a class of semi-analytical sensitivity analysis problems. *Optimization on Engineering*, 6:193–200, 1991.

[118] A. V. Oppenheim and R. W. Schafer. *Discrete-Time Signal Processing*. Prentice Hall, New Jersey, 1989.

[119] R. Pappa. A Consistent-Mode Indicator for ERA. In *Proceedings of the 33rd AIAA Dynamics Specialist Conference*, Dalas, TX, 1992.

[120] M. Paz. Dynamic condensation. *American Institute of Aeronautics and Astronautics*, 22:724–727, 1984.

[121] L. D. Peterson. Efficient computation of the eigensystem realization algorithm. In *Proceedings of the 10th International Modal Analysis Conference*, pages 1122–1131, Kissimmee, FL, 1993.

[122] L. D. Peterson, R. E. Skelton, and K. T. Liu. Comparison of the Eigensystem Realization Algorithm with the Q-Markov COVER algorithm for model realization. In *Proceedings of the 2nd NASA/USAF Workshop on System Identification and Health Monitoring of Precision Space Structures*, pages 371–417, Pasadena, CA, 1990.

[123] M. Phan, J. N. Juang, and R. W. Longman. Identification of linear systems from one set of input-output data via an asymptotically stable ARMA model by eigenvalue assignment. In *Proceedings of the 2nd NASA/USAF Workshop on System Identification and Health Monitoring of Precision Space Structures*, Pasadena, CA, 1990.

[124] J. Piranda, G. Lallement, and S. Cogan. Parametric correction of finite element models by minimization of an output residual: Improvement of the sensitivity method. In *Proceedings of the 8th International Modal Analysis Conference*, pages 363–368, Firenze, Italy, 1991.

[125] W. H. Press, B. P. Flannery, S. A. Teukolsky, and W. T. Vetterling. *Numerical Recioes.* Cambridge University Press, New York, 1990.

[126] M. Reynier and D. Nedjar. Control of finite element models: The model adjustment technique (MAT) software. In *Proceedings of the 1991 European Conference on New Advances in Computational Structural Mechanics*, Giens, Frances, 1991.

[127] J. M. Ricles and J. B. Kosmatka. Damage detection in elastic structures using vibratory residual forces and weighted sensitivity. *American Institute of Aeronautics and Astronautics*, 30:2310–2316, 1992.

[128] N. A. Roy, A. Girard, and P. E. Dupuis. A direct energy approach for updating dynamic finite element models. In *Proceedings of the 8th International Modal Analysis Conference*, pages 51–57, Firenze, Italy, 1991.

[129] A. Rytter. *Vibration Based Inspection of Civil Engineering Structures.* PhD thesis, Department of Building Technology and Structural Engineering, University of Aalborg, Aalborg, Denmark, 1993.

[130] M. Sanayei and O. Onipede. Damage assessment of structures using static test data. *American Institute of Aeronautics and Astronautics*, 29:1174–1179, 1991.

[131] M. Sanayei, O. Onipede, and S. R. Babu. Selection of noisy measurement locations for error reduction in static parameter identification. *American Institute of Aeronautics and Astronautics*, 30:2299–2309, 1992.

[132] A. Sestieri and S. R. Ibrahim. Analysis of errors and approximations on the use of modal coordinates. *Journal of Sound and Vibration*, 177:145–157, 1994.

[133] S. W. Smith. *Damage Detection and Location in Large Space Trusses.* PhD thesis, Department of Aerospace and Ocean Engineering, Virginia Polytechnic Institute and State University, Blacksburg, VA, 1988.

[134] S. W. Smith. Iterative use of direct matrix updates: Connectivity and convergence. Technical Report AIAA-92-2384-CP, American Institute of Aeronautics and Astronautics, 1992.

[135] S. W. Smith and C. A. Beattie. Simultaneous expansion and orthogonalization of measured modes for structure identification. Technical Report AIAA-90-1218-CP, American Institute of Aeronautics and Astronautics, 1990.

[136] S. W. Smith and C. A. Beattie. Optimal identification using inconsistent modal data. In *Proceedings of 32nd AIAA/ASME/ASCE/AHS/ASC Structures, Structural Dynamics, and Materials Conference*, pages 2319–2324, Baltimore, MD, 1991.

[137] S. W. Smith and C. A. Beattie. Secant-method adjustment for structural models. *American Institute of Aeronautics and Astronautics*, 29:119–126, 1991.

[138] F. J. Soeiro and P. Hajela. Damage detection in composite materials using identification techniques. In *Proceedings of the 31st AIAA/ ASME/ASCE/AHS/ASC Structures, Structural Dynamics, and Materials Conference*, pages 950–960, Long Beach, CA, 1990.

[139] H. Sohn, M. J. Dzwonczyk, E. G. Straser, A. S. Kiremidjian, K. H. Law, and T. H. Meng. An experimental study of temperature effect on modal parameters of the Alamosa Canyon Bridge. *Submitted for publication of Earthquake Engineering and Structural Dynamics.*

[140] H. Sohn and K. H. Law. Application of load-dependent Ritz vectors to Bayesian probabilistic damage detection. *Probabilistic Engineering Mechanics.* (in print).

[141] H. Sohn and K. H. Law. Bayesian probabilistic approach for structure damage detection. *Earthquake Engineering and Structural Dynamics*, 26:1259–1281, 1997.

[142] E. G. Straser. *A Modular, Wireless Damage Monitoring System for Structures.* PhD thesis, Department of Civil and Environmental Engineering, Stanford University, Stanford, CA, 1998.

[143] N. Stubbs and J. T. Kim. Damage localization in structures without baseline modal parameters. *American Institute of Aeronautics and Astronautics*, 34:1644–1649, 1996.

[144] W. P. Targoff. Orthogonality check and correction of measured modes. *American Institute of Aeronautics and Astronautics*, 14:164–167, 1976.

[145] K. G. Topole and N. Stubbs. Nondestructive damage evaluation of a structure from limited modal parameters. *Earthquake Engineering and Structural Dynamics*, 24:1427–1436, 1995.

[146] M. A. M. Torkamani and A. K. Ahmadi. Stiffness identification of two- and three-dimensional frames. *Earthquake Engineering and Structural Dynamics*, 16:1157–1176, 1988.

[147] F. E. Udwadia, D. K. Sharma, and P. C. Shah. Uniqueness of damping and stiffness distributions in the identification of soil and structural systems. *Journal of Applied Mechanics*, 45:180–187, 1978.

[148] B. Widrow and S. D. Stearns. *Adaptive Signal Processing*. Prentice-Hall, Englewood Cliffs, New Jersey, 1985.

[149] E. J. Williams and J. S. Green. A spatial curve-fitting technique for estimating rotational degrees of freedom. In *Proceedings of the 8th International Modal Analysis Conference*, pages 376–381, Kissimmee, FL, 1990.

[150] E. L. Wilson, M. W. Yuan, and J. M. Dicken. Dynamic analysis by direct superposition of Ritz vectors. *Earthquake Engineering and Structural Dynamics*, 10:813–821, 1982.

[151] M. G. Wood. *Damage Analysis of Bridge Structures Using Vibrational Techniques*. PhD thesis, Department of Mechanical and Electrical Engineering, University of Aston, Birmingham, Birmingham, UK, 1992.

[152] D. W. Zhang and L. Zhang. Matrix transformation method for updating dynamic models. *American Institute of Aeronautics and Astronautics*, 30:1440–1443, 1992.

[153] L. Zhang, H. Kanda, D. L. Brown, and R. G. Allemang. A Polyreference frequency domain method for modal parameter identification. Technical Report ASME-85-DEC-106, American Society of Mechanical Engineering, 1985.

[154] D. C. Zimmerman and T. T. Cao. Effects of noise on measured Ritz vectors. In *Proceedings of 1997 ASME Design Engineering Technical Conferences*, Sacramento, CA, 1997.

[155] D. C. Zimmerman and M. Kaouk. Eigenstructure Assignment Approach for structural damage detection. *American Institute of Aeronautics and Astronautics*, 30:1848–1855, 1992.

[156] D. C. Zimmerman and M. Kaouk. Structural damage detection using a subspace rotation algorithm. In *Proceedings of the 33rd AIAA Structure, Structural Dynamics and Materials Conference*, pages 2341–2350, Dallas TX, 1992.

[157] D. C. Zimmerman and T. Simmermacher. Model correlation using multiple static load and vibration tests. *American Institute of Aeronautics and Astronautics*, 33:2182–2188, 1995.

[158] D. C. Zimmerman and M. Widengren. Correcting finite element models using a symmetric eigenstructure assignment technique. *American Institute of Aeronautics and Astronautics*, 28:1670–1676, 1990.